Suche nach Kaluza-Klein Dunkle Materie Kandidaten mit dem CDMS Experiment
-
Searching for Kaluza-Klein Dark Matter Candidates with the CDMS experiment

von

Sebastian Arrenberg

Diplomarbeit in PHYSIK
vorgelegt der

Fakultät für Mathematik, Informatik und Naturwissenschaften
der RWTH Aachen

im Oktober 2007

angefertigt im

I. Physikalischen Institut der RWTH Aachen
Prof. Dr. Laura Baudis

October 2, 2007

Contents

List of Figures

List of Tables

Chapter 1

Introduction

The determination of the nature of dark matter which is one of the most important ingredients of the universe considering the evolution of its structure remains among the most important questions in astrophysics. Though there are several proposals available in the literature to solve this problem the most promising candidate is a Weakly Interacting Massive Particle or WIMP. The most extensively studied candidate is the neutralino arising from a supersymmetric extension of the standard model. However there are several other theories giving rise to appropriate candidates like the model of Universal Extra Dimensions which drew a lot of attention recently.

It is this model which is investigated in great detail in this diploma thesis with special emphasis on the direct detection of the $B^{(1)}$ which is supposed to be the lightest stable particle arising from this theory. Theoretical predictions on its cross sections are investigated considering both spin-independent and spin-dependent interactions. Moreover predictions on differential and total event rates are computed as well. Finally limits on the cross sections and WIMP-nucleon couplings are analyzed using data from the CDMS and XENON10 experiments.

Both experiments are so-called direct detection experiments which seek to measure the energy deposited when a WIMP interacts with a nucleus in the detector.

For example CDMS is an experiment using semiconductor crystals which are cooled down to a temperature of a few millikelvin. Avoiding unwanted background in these experiments is usually one of the most important subjects. Therefor they are usually installed deep underground and surrounded by shields of lead and polyethylene.

CDMS uses so-called ZIP (=Z-sensitive Ionization and Phonon) detectors in order to discriminate between electron recoils which constitute most of the background and nuclear recoils arising from neutrons and hopefully WIMPs on an event-by-event basis by simultaniously measuring an ionization and a phonon signal. Moreover the detectors also provide timing information which can be used to reject surface events. These events are problematic since they yield poor ionization collection and hence mimic nuclear recoils.

The used data from CDMS was obtained during the run 118 from October 11, 2003 until January 11, 2004 and the run 119 from March 25, 2004 to August 8, 2004 using two towers each with 6 detectors. The data from XENON10 was taken between October 6, 2006 and February 14, 2007.

Chapter 2

UEDs - Theoretical Background

In everyday life people experience the existence of only three space dimensions and of course one time dimension. Since this seems to be so natural the question arises why physicists consider additional dimensions at all. To understand these thoughts it is the best to start with the first occurance of extra dimensions in the literature which means taking a look at the work of Theodor Kaluza and Oscar Klein[1] who released their determinations intended to combine General Relativity and Electrodynamics in the 20s of the last century only a few years after Albert Einstein developed General Relativity.

So since General Relativity plays such a crucial role in the context of extra dimensions this chapter is about to start with a short introduction to Special Relativity and this intellectual masterpiece.

2.1 Special Relativity

In 1905 Albert Einstein published Special Relativity a theory based on two main concepts:

- *The special principle of relativity*
  All laws of physics remain the same in all inertial frames which means that no privileged frames of reference exist.

- *Invariance of the speed of light*
  The speed of light in a vacuum is a universal constant which is especially independent of the motion of the source.

[1]In fact there even was an earlier attempt by Nordström in 1914 but this efford did not achieve so much attention especialy because he used his own (wrong) theory of Gravitation. Anyway Kaluza and Klein were influenced by his work.

The resulting concept revolutionized physics by combining space and time into a four-dimensional vector space the so-called Minkowski space breaking down the idea of an absolute time. In this Minkowski space the differential of distance $\mathrm{d}s$ is given by

$$\mathrm{d}s^2 = \mathrm{d}t^2 - \mathrm{d}\vec{r}^{\,2} = \eta_{\alpha\beta}\, \mathrm{d}x^\alpha \mathrm{d}x^\beta \tag{2.1}$$

with the metric

$$\eta_{\alpha\beta} = \begin{pmatrix} +1 & 0 & 0 & 0 \\ 0 & -1 & 0 & 0 \\ 0 & 0 & -1 & 0 \\ 0 & 0 & 0 & -1 \end{pmatrix} . \tag{2.2}$$

The fact that all of its components are constant reflects that the space considered in Special Relativity is flat.

One of the most important improvements was the replacement of Galilei transformations with Lorentz transformations switching from one inertial frame to another one. So physical laws need to be expressed in a new form reflecting their abidance to Lorentz invariance. In other words they have to be written as a tensor equation. For example Electrodynamics which will be discussed in more detail below is a theory which is intrinsically covariant. Other theories however are not which means that they have to be generalized to fit in the frame work of Special Relativity.

Consider for example a pointlike particle of mass m neglecting all forces. Then Newton's Law yields

$$m \frac{\mathrm{d}\vec{v}}{\mathrm{d}t} = \vec{0} \tag{2.3}$$

which is easily generalized to

$$m \frac{\mathrm{d}u^\alpha}{\mathrm{d}\tau} = 0 \tag{2.4}$$

where

$$u^\alpha = \frac{\mathrm{d}x^\alpha}{\mathrm{d}\tau} \tag{2.5}$$

is the four velocity and τ a quantity parameterizing the world line of the particle for example the proper time in the case that it is not massless.

This equation is correct because it is covariant and yields (2.3) in the non-relativistic limit. In fact these two conditions generally define the way theories are made relativistic.

In the case that forces have an impact on the particle a force $\vec{F}$ in (2.3) and F^α in (2.4) has to be introduced on the right side of these equations. An example will be given immediately.

Finding a form for Electrodynamics which is invariant under Lorentz transformations is a quite easy task because the Maxwell equations are covariant by design. This can be shown by introducing the antisymmetric field strength tensor

$$F^{\alpha\beta} = \partial^\alpha A^\beta - \partial^\beta A^\alpha = \begin{pmatrix} 0 & -E_X & -E_Y & -E_Z \\ E_X & 0 & -B_Z & B_Y \\ E_Y & B_Z & 0 & -B_X \\ E_Z & -B_Y & B_X & 0 \end{pmatrix} \tag{2.6}$$

with the gauge potential A^α and the components of the elecrtric field E_i and the Magnetic Field B_i. Now the homogenous and inhomogeneous Maxwell equations can be written as

$$\epsilon^{\alpha\beta\gamma\delta}\partial_\beta F_{\gamma\delta} = 0 \tag{2.7}$$

and

$$\partial_\alpha F^{\alpha\beta} = 4\pi j^\beta \tag{2.8}$$

respectively which are manifest covariant and where the fully antisymmetric Levi-Cività-Pseudotensor ϵ has been introduced. Using this convention the equation of motion for a pointlike particle with charge q is given by

$$m\frac{\mathrm{d}u^\alpha}{\mathrm{d}\tau} = qF^{\alpha\beta}u_\beta \,. \tag{2.9}$$

Again the validity can be checked by showing that this equation yields the known non-relativistic result. Moreover the energy-momemtum tensor

$$T^{\alpha\beta} = \frac{1}{4\pi}\left(F^\alpha{}_\gamma F^{\gamma\beta} + \frac{1}{4}\eta^{\alpha\beta}F_{\gamma\delta}F^{\gamma\delta}\right) \tag{2.10}$$

is of importance considering Generel Relativity because due to the mass energy equivalence it occurs as a source term in Einstein's field equation.

After finishing his Special Relativity Einstein continued his work trying to find a covariant form for Newton's theory of Gravitation which is basically given by the equation of motion for a pointlike particle with mass m

$$m\frac{\mathrm{d}^2\vec{r}}{\mathrm{d}t^2} = -m\nabla\phi(\vec{r}) \tag{2.11}$$

and the field equation for the gravitational potential ϕ

$$\triangle\phi(\vec{r}) = 4\pi G\rho(\vec{r}) \tag{2.12}$$

where the matter density ρ appears as the source of ϕ. These equations look very similar to the field equation of Electrostatics and the corresponding non-relativistic equation of motion of a charged particle given by

$$\triangle\phi_{el}(\vec{r}) = -4\pi\rho_{el}(\vec{r}) \qquad \text{and} \qquad m\frac{\mathrm{d}^2\vec{r}}{\mathrm{d}t^2} = -q\nabla\phi_{el}(\vec{r}) \tag{2.13}$$

respectively. However the underlying truth is much more complicated. This can be seen by realizing that the source ρ_{el} transforms like the 0-component of a four-vector (the current j^α) whereas ρ transforms like the 00-component of a Lorentztensor namely the energy-momentum tensor describing the mass density.

Nevertheless Einstein succeeded in overcoming all appearing problems and eventually published General Relativity which is described in the next section in 1916.

2.2 General Relativity

Dealing with General Relativity means to abandon the restriction of considering solely inertial frames. Similar to Special Relativity there are some important concepts the whole theory is based on.

- *The equivalence of inertial and gravitational mass*
- *The principle of equivalence*
  There is a local inertial frame for every point in spacetime even in the presence of a gravitational field.

The last topic makes it possible to start with a theory which form is known in the framework of Special Relativity and accordingly in a local inertial frame to derive the general form including gravitation. The basic principle to do this is rather easy.

Consider for example a free falling satellite in orbit with respect to the earth. In case that this satellite laboratory with coordinates ξ is small enough that the inhomogeneity of the earth's gravitational field can be neglected it constitutes a local inertial frame (Minkowski space) where the differential of distance $\mathrm{d}s$ is given by

$$\mathrm{d}s^2 = \eta_{\alpha\beta}\,\mathrm{d}\xi^\alpha \mathrm{d}\xi^\beta \tag{2.14}$$

with the constant metric $\eta_{\alpha\beta}$ given in (2.2). The changeover from this local inertial frame to a different arbitrary frame (Riemann space) is accomplished by introducing a coordinate transformation

$$\xi^\alpha = \xi^\alpha(x) \tag{2.15}$$

which yields

$$\mathrm{d}s^2 = g_{\mu\nu}(x)\mathrm{d}x^\mu \mathrm{d}x^\nu \tag{2.16}$$

with the metric tensor

$$g_{\mu\nu}(x) = \eta_{\alpha\beta}\,\frac{\partial\xi^\alpha}{\partial x^\mu}\frac{\partial\xi^\beta}{\partial x^\nu}\,. \tag{2.17}$$

This transformation leaves its marks in the functional dependence of the metric from the coordiantes x. So in fact this represents the mathematical form of the gravitational field.

Even though this way of generalizing physical laws to a world where gravitation is included is in principle rather simple in most cases the actual computations are quite difficult and tedious. Fortunately there is another solution for this problem provided by the so-called covariance principle which has actually already been used to achieve physical laws in Special Relativity from their Newtonian counterparts. But before proceeding with this two definitions have to be made.

First of all, tensors have to be introduced which are invariant under general coordinate transformations. These so-called Riemann tensors can be easily defined by setting

$$A^\mu = \frac{\partial x^\mu}{\partial\xi^\alpha}A^\alpha \tag{2.18}$$

where A^α denotes the familiar Lorentz tensor and A^μ the Riemann tensor. Moreover special attention has to be paid dealing with derivatives because the familiar expression is not very helpful in the context of General Relitivity. Nevertheless the following definition provides a suitable candidate:

$$\frac{\mathrm{D}A^\mu}{\mathrm{D}x^\nu} = \frac{\mathrm{d}A^\mu}{\mathrm{d}x^\nu} + \Gamma^\mu_{\nu\kappa}A^\kappa \tag{2.19}$$

where the Christoffel symbols have been used which are related to the metric tensor by

$$\Gamma^\kappa_{\lambda\mu} = \frac{1}{2}g^{\kappa\nu}\left(\frac{\partial g_{\mu\nu}}{\partial x^\lambda} + \frac{\partial g_{\lambda\nu}}{\partial x^\mu} + \frac{\partial g_{\mu\lambda}}{\partial x^\nu}\right) \tag{2.20}$$

It is quite easy to show that both (2.19) and (2.20) have the demanded transformation property. These definitions will prove to be very useful pretty soon.

Looking back promoting Newton's laws to obey the framework of Special Relativity has been accomplished by trying to find equations which are covariant or rather made of Lorentz tensors and yield the original law in the non-relativistic limit.

The generalization from Special Relativity to General Relativity is quite similar. In this case equations have to be found which are invariant with respect to general coordinate transformations which means that they have to be established using only Riemann tensors. Moreover these laws have to simplify to the appropriate equations considering Special Relativity. This last condition can be checked by making the replacement $g_{\mu\nu}(x) \to \eta_{\mu\nu}$. The just explained method is also know as the *covariance principle*.

The two following examples are quite useful to show its appropriateness. The equation of motion for a particle with mass m without considering any forces is given in (2.4). Taking the definition of the covariant derivative into account this is easily generalized to

$$m\frac{\mathrm{D}u^{\mu}}{\mathrm{D}\tau} = 0 \tag{2.21}$$

or rather

$$\frac{\mathrm{d}u^{\mu}}{\mathrm{d}\tau} = -\Gamma^{\mu}_{\nu\lambda}u^{\nu}u^{\lambda} \tag{2.22}$$

which is correct because from (2.21) it is obvious that the equation is covariant and from (2.22) it is clear that it yields (2.4) for $g_{\mu\nu}(x) \to \eta_{\mu\nu}$ because the Christoffel symbols (2.20) vanish for a constant metric. They obviously incorporate the impact from the gravitational field on the particle. Anyway it should be kept in mind that u^{μ} denotes a Riemann tensor at this stage. Of course this can also be derived by brute force considering a general coordinate transformation and inserting this approach into (2.4).

The second example is of particular importance in the context of Kaluza-Klein Theory. It is the generalization of Electrodynamics. So the Maxwell equations and the equation of motion for a charged particle have to be promoted converting (2.7), (2.8) and (2.9) to

$$\epsilon^{\alpha\beta\gamma\delta}\partial_{\beta}F_{\gamma\delta} = 0 \tag{2.23}$$

$$\frac{1}{\sqrt{-g}}\partial_{\alpha}\left(\sqrt{-g}F^{\alpha\beta}\right) = 4\pi j^{\beta} \tag{2.24}$$

$$m\frac{\mathrm{d}u^\mu}{\mathrm{d}\tau} = -m\Gamma^\mu_{\nu\lambda}u^\nu u^\lambda + qF^{\mu\nu}u_\nu \tag{2.25}$$

where g denotes the determinante of the metric tensor. Apparently the form of the homogenous Maxwell equations has not changed.

Up to now nothing has been said about the origin of the metric $g_{\mu\nu}$. Before coming to this point where the Einstein equations will be discussed briefly there are three more quantities which have to be introduced in order to deal with the core of General Relativity. These quantities are the Riemann curvature tensor, the Ricci tensor and the scalar curvature whereof the latter two are derived from the first one. The Riemann curvature is a tensor of fourth order which can be written in terms of the Christoffel symbols:

$$R^\kappa{}_{\lambda\mu\nu} = \partial_\nu\Gamma^\kappa_{\lambda\mu} - \partial_\mu\Gamma^\kappa_{\lambda\nu} + \Gamma^\rho_{\lambda\mu}\Gamma^\kappa_{\rho\nu} - \Gamma^\rho_{\lambda\nu}\Gamma^\kappa_{\rho\mu} \tag{2.26}$$

Therefor it is clear that it is basically a functional of the metric tensor. It can be shown that the components of this tensor vanish exactly in the case when the considered space is flat which is its most important property. After this the Ricci tensor and the scalar curvature can be defined by

$$R_{\mu\nu} = R^\kappa{}_{\mu\kappa\nu} = g^{\rho\kappa}R_{\rho\mu\kappa\nu} \tag{2.27}$$

and

$$R = R^\mu{}_\mu = g^{\mu\nu}R_{\mu\nu} \tag{2.28}$$

respectively.

After these last definitions it is possible to take a look at the Einstein equations which are differential equations for the still unknown metric $g_{\mu\nu}$. It is clear that these equations must depend on an overall energy momentum tensor $T_{\mu\nu}$ because according to the famous mass-energy equivalence

$$E = mc^2 \tag{2.29}$$

all kinds of energy contribute to the mass of the universe and therefor constitute a source for the gravitational field. Moreover the functional dependence on the metric cannot be just linear because the field itself carries energy. Hence higher order terms are necessary in order to take care of self interaction. Finally it is clear that the field equations should yield the Newtonian limit (2.12) in the case of a static and weak gravitational field.

The actual field equations cannot be derived. They can only be made plausible based on the just made assumptions. However it can be shown that the following four conditions are sufficent to completely determine the Einstein equations given below.

- The equations should be written as tensor equations depending only on the unknown metric $g_{\mu\nu}$ and the energy momentum tensor $T_{\mu\nu}$.
- The dependence on the metric should be only linear in the second derivatives and linear and quadratic in the first derivatives.
- Overall energy momentum conservation should hold which means that the covariant derivative of the energy momentum tensor should vanish.
- The field equations should yield the Newtonian limit considering a static and weak gravitational field.

Using these assumptions finally leads to the famous Einstein equations

$$R_{\mu\nu} - \frac{1}{2} R g_{\mu\nu} = -8\pi G T_{\mu\nu} \, . \tag{2.30}$$

Their most important properties have already been discussed. Anyway it should be pointed out that these equations do not completely determine the metric because general gauge transformations are still possible which is similar to the case of Electrodynamics.

Later on Einstein introduced yet another term linear in the metric in order to obtain a(n archaic) stationary universe.

$$R_{\mu\nu} - \frac{1}{2} R g_{\mu\nu} + \Lambda g_{\mu\nu} = -8\pi G T_{\mu\nu} \tag{2.31}$$

introducing the so-called cosmological constant Λ. However this term is in conflict with the Newtonian limit which constrains its value to a maximum of 10^{-46} km^{-2}. Therefor it is only of interest on cosmological scales especially considering the expansion of the universe.

Finally it should be emphasized that these field equations give a geometrical intepretation of the energy distribution of the universe which is a really remarkable result.

A topic that concerned Einstein and others is the fact that the energy momentum tensor is not determined by the theory but an input which must be derived elsewhere. An example for the energy momentum tensor of the electromagnetic field is given in (2.10).[2] An attempt to come to grips with this problem undertaken by Theodor Kaluza and Oscar Klein implementing additional space dimensions is explained in the next chapter.

[2] Of course this Lorentz tensor has to be promoted to a Riemann tensor first.

2.3 Kaluza-Klein Theory

In the 20s of the last century only two fundamental interactions were known namely Gravitation and Electrodynamics including their respective theoretical frameworks. In these days the discovery of the Weak and Strong interactions was yet to come.

Since unification of certain interactions has always been interesting especially from a theoretical point of view it was only a matter of time until the first approaches were puplished pursueing the work done by combining Electricity and Magnetism leading to the Maxwell equations.

So neglecting Nordström's idea because he used the wrong theory of Gravitation Kaluza was the first who tried to combine Gravitation and Electrodynamics.[3]

In 1919 he submitted a paper [1] about his work to Einstein which he really appreciated. It was finally published in 1921 and contained an approach combining the Einstein equations and Maxwell Equations by proposing an additional space dimension.

The basic idea behind this and accordingly Klein's approach is rather easy to understand. To come to grips with this topic consider the Einstein equations (2.30) in a vacuum which means setting $T_{\mu\nu} = 0$. In this case contracting with $g_{\mu\nu}$ yields $R = 0$ which finally leads to the Einstein equations in vacuum

$$R_{\alpha\beta} = 0\,. \tag{2.32}$$

Now comes the important step of adding another space dimension. To do this it should be remembered that the Ricci tensor and the scalar curvature have been defined starting with the curvature tensor and summing over indices. So adding another space dimension lets the sum run over the indices 0 to 4 instead of from 0 to 3. Splitting the summation into one part again summing only over 0 to 3 and shuffling the rest to the other side of the equation obviously generates a source term for the four dimensional part. Moreover additional equations arise from the fifth dimension which have to be interpreted in an appropriate way.

So anticipating the result of the Kaluza-Klein Theory is that the just mentioned generated sources indeed have the exact form of the energy momentum tensor of the electromagnetic field assumed that the metric is interpreted in an adequate way. Besides the additional equations yield the source free Maxwell equations and the geodesic equation of a point like particle in an elctromagnetic field (2.25) is recovered as well.

But in order to get a better understanding of how this beautiful theory works it is necessary to go a bit further into detail.

So proceeding with the idea of Kaluza means considering the Ansatz

[3] The Kaluza-Klein theory is reviewed with a lot of historical anecdotes in [2] and [3].

$$g_{IJ}^{(5)} = \begin{pmatrix} g_{\mu\nu}^{(4)} & \sqrt{16\pi G}A_\nu \\ \sqrt{16\pi G}A_\mu & 2\phi \end{pmatrix} \tag{2.33}$$

with the four dimensional familiar metric $g_{\mu\nu}$, the gauge field from electrodynamics A_μ, the new so-called dilaton field ϕ and the expanded five dimensional metric g_{IJ}.[4] Moreover he imposed the so-called cylinder condition which means that the metric should be independent of the fifth dimension or rather

$$\partial_5 g_{IJ} = 0 \tag{2.34}$$

which is related to the fact that this dimension does not lead to any effects in existing experiments. However it should be emphasized that Kaluza did not impose any kind of compactification which will be of importance pretty soon. Especially because Kaluza only used the linearized aproximation of the Einstein equations and the final equation of motion of a particle depends crucially on the new dilaton field this idea is rather unaesthetic.

In 1926 Klein [4] published another proposal influenced by Kaluza's ideas. The most important difference however is a different definition of the five-dimensional metric

$$g_{IJ}^{(5)} = \begin{pmatrix} g_{\mu\nu}^{(4)} + \phi A_\mu A_\nu & \phi A_\nu \\ \phi A_\mu & \phi \end{pmatrix} \tag{2.35}$$

which is a much more fruitable approach. Moreover he dropped the cylinder condition and replaced it by compactifying the fifth dimension on a circle. This approach will be explained in a little bit more detail in the next paragraph. In fact it is also pointed out below that the compactification approximately yields the cylinder condition which is the reason why the cylinder condition is used again in the upcoming derivation. Moreover he set the dilaton field to a constant which is a little bit tricky because this actually yields $F_{\mu\nu}F^{\mu\nu} = 0$. However this problem will not be discussed here.

To explain the just stated arguments it is the best to start with the determination of the geodesic equation. To do this it is necessary to evalute

$$\frac{\mathrm{d}u^I}{\mathrm{d}\tau} = -\Gamma^I_{JK} u^J u^K \tag{2.36}$$

which is obviously nothing but the five dimensional generalization of (2.22). A straight forward computation using the cylinder condition yields

[4]Greek indices still run from 0 to 3 whereas capital Latin indices run from 0 to 4 including summing over the added dimension.

$$\frac{\mathrm{d}u^\mu}{\mathrm{d}\tau} = -\Gamma^\mu_{\nu\lambda} u^\nu u^\lambda + \left(A_\alpha u^\alpha + u^5\right) F^{\mu\beta} u_\beta \tag{2.37}$$

and

$$\frac{\mathrm{d}u^5}{\mathrm{d}\tau} = \left(\Gamma^\mu_{\nu\lambda} A^\mu - \partial_\nu A_\lambda\right) u^\nu u^\lambda - \left(A_\alpha u^\alpha + u^5\right) F_\beta A^\mu u^\beta \,. \tag{2.38}$$

Comparing (2.37) and the geodesic equation of a charged particle in a gravitational and electromagnetic field (2.25) the similarity is really striking and it can be seen that they are equal if the following identification is made

$$q = m\left(A_\alpha u^\alpha + u^5\right) \,. \tag{2.39}$$

Indeed a more proper analysis reveals that the right side of (2.39) is proportional to the canonical conjugated momentum in the fifth dimension p^5 and that this momentum is conserved due to the cylinder condition which makes this identification valid. To be more precise the following relation between p^5 and the charge q holds:

$$p^5 = \frac{q}{\sqrt{16\pi G}} \tag{2.40}$$

This is of crucial importance since it is well known that the charge q is always a multiple of the electron charge e or rather $q = ne$ with $n \in \mathbb{Z}$. So (2.40) implies that the momentum in the fifth dimension is quantized as well. This is the stage where quantum theory emerges ...

In quantum theory quantized momenta occur when periodic boundary conditions are imposed. Dropping the convention $\hbar = c = 1$ which is implicitely used throughout this whole thesis and denominating the period length L the following well known formula holds imposing periodic boundary conditions in the fifth dimension:

$$p^5 = n\frac{2\pi\hbar}{L} \qquad \text{with} \qquad n \in \mathbb{Z} \tag{2.41}$$

Comparing (2.40) and (2.41) yields an estimate for L

$$L = \frac{hc}{e}\sqrt{16\pi G} \approx 0.8 \cdot 10^{-30} \text{ cm} \tag{2.42}$$

which is obviously quite close to the Planck length

$$L_P = \sqrt{\frac{\hbar G}{c^3}} \approx 1.6 \cdot 10^{-33} \text{ cm}\,. \tag{2.43}$$

This really small value is supporting the idea of compactifying the fifth dimension and also the non-appearance of effects related to this dimension in ordinary experiments. It seems like all experiments might only see effects obtained by averaging over the additional dimension.

Additionally it should be pointed out that the compactification together with the just estimated extremely small period length directly yields the cylinder condition. This can be seen by expanding the five dimensional metric in a Fourier series:

$$g_{IJ}(x_K) = \sum_{n=-\infty}^{\infty} g_{IJ}(x_\mu) \mathrm{e}^{\frac{inx^5}{L}} \tag{2.44}$$

Considering that it has just been shown that the period length L is really small yields that all modes with $n \neq 0$ can be neglected. However the special case of $n = 0$ has the property that the metric does not depend on the compactified extra dimension or rather $\partial_5 g_{IJ} = 0$ which is nothing but the cylinder condition (2.34). So considering quantization leads to a physical justification of the compactification procedure and shows that this constraint is not just "falling from the sky".

After discussing the geodesic equation and the compactification in so much detail a few information about the field equations are to come. As stated above it is possible to derive these equations by using the metric (2.35) separating the fraction related to the summation over the four usual dimensions from the rest and interpreting the latter as a source term. This yields the Maxwell equations and the Einstein equations with the energy momentum tensor of the electromagnetic field as the the source. However another way is to take a closer look at the Einstein-Hilbert action which gives raise to the vacuum equations

$$S[g] = \frac{1}{16\pi G} \int R\sqrt{-g}\mathrm{d}^5 x \tag{2.45}$$

with the scalar curvature R which in this case is derived by contracting over all five dimensions. However after a long tedious computation it is possible to write R in a very convenient form

$$R = R^{(4)} + \frac{1}{4} F^{\mu\nu} F_{\mu\nu} \tag{2.46}$$

which shows the aspired result since one immediately recognizes the Lagrangian of the Einstein equations and Maxwell equations. Of course varying the Einstein-Hilbert action (2.45) using (2.46) leads to the advertised result.

Before finishing this chapter about classical Kaluza-Klein Theory it should be pointed out that it is possible to leave the scope of Gravitation and Electrodynamics. Looking at this unification from a more technical point of view it can be summarized by expanding the familiar spacetime adding another dimension and interpreting the additional new parts of the metric as the gauge potentials. However it is possible to expand this approach from abelian gauge theories like Electrodynamics which obeys a U(1) symmetry to non-abelian gauge theories. So in particular it is possible to incorporate Yang-Mills theories which is really interesting because the Strong and the Weak interaction are described in this frame work. Nevertheless this requires more extra dimensions and more complicated geometric compactifications than the circle-compactification considered here and it is still on a classical level. The quantization of Gravitation is still an unsolved problem. Moreover it is problematic to obtain a chiral gauge theory which means that fermions must be introduced in an artificial way.

However the interest in the idea of adding new dimension to space time has grown within the last years especially due to the establishment of string theory as the leading candidate for quantum gravity. But there are also other approaches for theories beyond the standard model considering extra dimension like the ADD model, the Randall-Sundrum model and Universal Extra Dimensions (UED). The latter is of particular interest for astrophysics because it leads to a possible dark matter candidate in a quite easy and aesthetic way. This theory and especially its implications for dark matter will be discussed pretty soon. Of course this will also make it necessary to leave the classical approaches and start considering quantum field theory.

2.4 The Compactification of Extra Dimensions

Before starting with a discussion of the concept of Universal Extra Dimensions in the next section it seems reasonable to take a closer look at the way extra dimensions are compactified which is exceedingly well described in [5]. Thereby a very instructive example is given revealing all of the most important aspects of this expansion especially the generation of new particles which might constitute a dark matter candidate.

The rest of this thesis does not deal with General Relativity anymore. Therefor the four dimensional familiar space is considered to be a Minkowski space $\mathcal{M}_4$ not a Riemann space. Accordingly the transformations of interest are just Lorentz transformations.

For a short general discussion at the beginning a d-dimensional space is considered. The coordinates in $\mathcal{M}_4$ are labeled x^μ whereas the coordinates in the additional dimensions are labeld y^i. In this space the d-dimensional action $S^{(d)}$ has to be written down including all fields of interest and obeying all apropriate symmetries, e.g. d-dimensional Lorentz invariance.

At this stage it should be pointed out that imposing d-dimensional Lorentz invariance seems weird because the compactification constraint considered below breaks this invariance anyway. However higher-dimensional Lorentz invariance is necessary for many application. This can be made feasible by taking a look at the

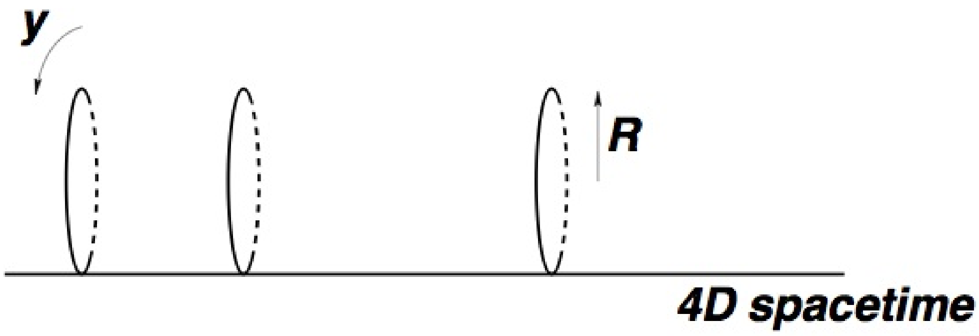

Figure 2.1: 5-dimensional space time with the topology $\mathcal{M}_4 \times S_1$. The extra dimension is compactified on a circle orthogonal to the 4-dimensional Minkowski space represented by a straight line. (Figure taken from [5].)

ultraviolet limit. In this case the particles have very small Compton wavelengths even compared to the compactification scale and therefor the extra dimensions seem to be uncompactified for them.

To proceed with the examination of the action the effective four dimensional action $S^{(4)}$ has to be obtained. Therefor it is necessary to make a mode expansion for all fields, substitute them into the d-dimensional action, choose an appropriate compactifiction and integrate over this compactified space K.

So after writting $S^{(d)}$ the compactification has to be specified. In fact there are a lot of possibilities. Usually a compactification of the form $\mathcal{M}_4 \times K$ is choosen which means that the properties of K are independent of its actual location with respect to $\mathcal{M}_4$. However there are still many ways to compactify the extra dimensions. In the case of only one extra dimension which is studied in more detail below it is useful to compactify the added space on a circle meaning that space time has the topology $\mathcal{M}_4 \times S_1$. This example illustrated in figure 2.1 is quite easy to deal with. Moreover it is very instructive revealing the most important properties of extra dimensions which in fact is the reason why it is so popular as an introduction to this topic. Important topologies in the context of two added dimensions are for example $\mathcal{M}_4 \times T_2$ and $\mathcal{M}_4 \times S_1 \times S_1$. In the first case the compactified space has the topology of a two-torus whereas it consists of two independent spheres in the latter.

At this stage the just mentioned example of one extra dimension compactified on a sphere with radius R is about to be discussed. So in this case the 5-dimensional space time can be described by a four-vector x^μ denoting the coordinates in the familiar Minkowski space and another coordinate y representing the extra dimension. The compactification can be easily implemented by imposing a periodic boundary condition or rather

$$y \leftrightarrow y + 2\pi R \ . \tag{2.47}$$

In order to discuss this kind of compactification a field has to be choosen which is about to be examined. Obviously the easiest possibility is a complex scalar field Φ obeying the Klein-Gordon equation in five dimensions

$$(\partial^K \partial_K + m^2)\Phi(x^\mu, y) = 0 \tag{2.48}$$

with the Lagrangian

$$\mathcal{L} = \frac{1}{2}\Big(\partial_K \Phi(x^\mu, y)\Big)^* \Big(\partial^K \Phi(x^\mu, y)\Big) + \frac{1}{2}m^2 \Big|\Phi(x^\mu, y)\Big|^2 . \tag{2.49}$$

Just as a reminder the capital Latin K runs from 0 to 4 as established on page 12. The 5-dimensional action is given by

$$S^{(5)} = \int \mathrm{d}x^4 \int_0^{2\pi R} \mathrm{d}y \, \mathcal{L} . \tag{2.50}$$

Incorporating the boundary condition (2.47) gives rise to the mode expansion

$$\Phi(x^\mu, y) = \frac{1}{\sqrt{2\pi R}} \sum_{n=-\infty}^{\infty} \phi_n(x^\mu) \mathrm{e}^{\frac{iny}{R}} . \tag{2.51}$$

Inserting this expansion in the Lagrangain (2.49) and correspondingly (2.49) in (2.50) makes it very easy to evaluate the integration over the compactified dimension. Using the well known orthogonality relation

$$\int_0^{2\pi R} \mathrm{d}y \; \mathrm{e}^{\frac{i(n-m)y}{R}} = 2\pi \delta_{nm} \tag{2.52}$$

immediately yields the effective 4-dimensional action

$$S^{(4)} = \int \mathrm{d}x^4 \sum_{n=-\infty}^{\infty} \left[\frac{1}{2}\Big(\partial_\nu \phi_n(x^\mu)\Big)^* \Big(\partial^\nu \phi_n(x^\mu)\Big) + \frac{1}{2}(m^2 + \frac{n^2}{R^2})\Big|\phi_n(x^\mu)\Big|^2 \right] . \tag{2.53}$$

Obviously the effective 4-dimensional theory describes nothing but an inifinite number often called Kaluza-Klein tower of Klein-Gordon fields $\phi(x^\mu)$ with the masses

$$m_n^2 = m^2 + \frac{n^2}{R^2} . \tag{2.54}$$

Taking a look at the expansion (2.51) it is evident that the additional contribution to the mass of the states with $n \neq 0$ is related to the momentum in the fifth dimension p_5:

$$p_5 = \frac{n}{R} \tag{2.55}$$

So assuming translation invariance in this dimension[5] the corresponding quantized momentum and accordingly the quantum number n is conserved which means that the mode is stable. Upgrading this idea is of crucial importance searching for a stable particle which might lead to a dark matter candidate.

Moreover there are some more properties of this theory which are noticable from (2.53) and (2.54). First of all $\phi_0(x^\mu)$ is the field with the lightest mass and it is also the only one which is not degenerate. Therefor this zero mode which is also called the ground state is identified with the usual 4-dimensional state. So for example they are interpreted as the Standard Model particles whereas the excited modes are supposed to be new particles which have not been observed yet. However it is obvious that the accessible energy in an experiment should have a magnitude of about $\sim R^{-1}$ in oder to excite these modes.

Another interesting feature of this theory is the fact that all modes of a certain Kaluza-Klein tower have exactly the same quantum numbers, e.g. spin, couplings. This is of striking difference to Supersymmetry where the new particles have different spins from their Standard Model counterparts. Moreover this implies that only a few new parameters have to be introduced. To be more precise the UED model depends on four unknown parameters: The Higgs mass m_H, the compactification radius R, the number of extra dimensions and the cut-off scale since it turns out that this can only be an effective field theory. This is explained in little bit more detail in section 2.5.

However even though the just investigated compactification seems so appealing this cannot be the whole truth. The problem is that it is impossible to gain a chiral gauge theory from a simple compactification on a topological smooth space like the just investigated sphere because this theory would still contain undesirable fermionic degrees of freedom. Fortunatelly it is possible to remove them. Two frequently discussed choices are the restriction of fermions to branes and the imposition of boundary conditions switching the space containing the added dimensions from a manifold to a so-called orbifold. The latter case is of special importance in the case of the UED model investigated here which is the reason for discussing it in a little bit more detail.

From a mathematical point of view the correct way to introduce these boundary conditions is to start with a manifold and impose an additional discrete symmetry. A convenient way to take a closer look at this approach is to go back to the Klein-Gordon field from the just examined example.

[5]Translation invariance is actually already broken by the compactification. However a related problem has already been discussed on page 15.

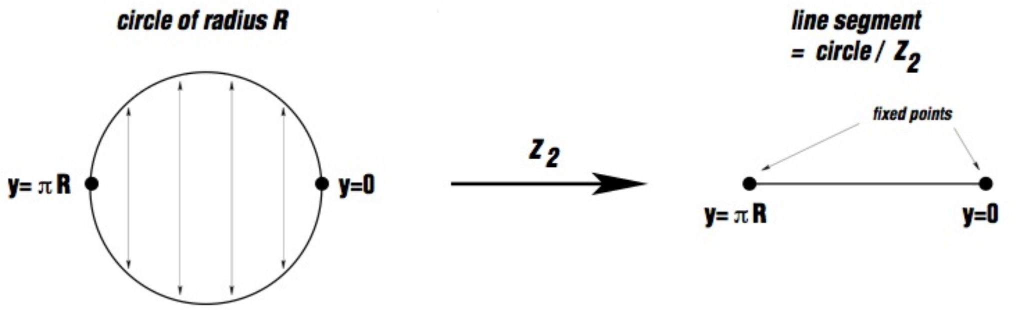

Figure 2.2: The additional constrained $y \leftrightarrow -y$ folds one half of the sphere defined by $y \leftrightarrow y+2\pi R$ on the other one yielding a line segment. (Figure taken from [5].)

In this example the topology or rather the compactification of the added dimension is defined in (2.47). Considering starting with a line segment this requirement effectively leads to identifying its two endpoints. Therefor it is possible to restrict the parameter y of this dimension to the interval $[0, 2\pi)$.

But what if the topology of the extra dimension should just be a straight line segment again? This goal can be achieved by imposing the additional discrete $\mathbb{Z}_2$ symmetry

$$y \leftrightarrow -y \tag{2.56}$$

which yields

$$y \leftrightarrow 2\pi R - y \tag{2.57}$$

if combined with (2.47). The net effect of this constraint is shown in figure 2.2. Obviously it leads to folding one half of the circle on the other half yielding a line segment. So the extra dimension compactified in this way gains two special endpoints at $y = 0$ and $y = \pi R$. The topological space defined here is often denoted as being $S^1/\mathbb{Z}_2$ compactified.

The most important consequence of this construction can be understood by taking a closer look at the mode expansion (2.51). Since the condition $y \leftrightarrow -y$ has been added it seems reasonable to rewrite it in terms of eigenfunctions of the parity operator acting on the extra dimension

$$\Phi(x^\mu, y) = \frac{1}{\sqrt{\pi R}}\left[\frac{1}{\sqrt{2}}\phi_0^{(+)}(x^\mu) + \sum_{n=1}^{\infty}\phi_n^{(+)}(x^\mu)\cos(\frac{ny}{R}) + \sum_{n=1}^{\infty}\phi_n^{(-)}(x^\mu)\sin(\frac{ny}{R})\right] \tag{2.58}$$

with the new functions $\phi_0^{(+)}$, $\phi_n^{(+)}$ and $\phi_n^{(-)}$ being related to the formerly used functions ϕ_n by

$$\phi_0^{(+)} = \phi_0 \,, \qquad \phi_n^{(+)} = \frac{1}{\sqrt{2}}(\phi_n + \phi_{-n}) \,, \qquad \phi_n^{(-)} = \frac{i}{\sqrt{2}}(\phi_n - \phi_{-n}) \,. \tag{2.59}$$

As already stated this is just a rewriting of the former ansatz and therefor it is still valid in the case of a compactification on a circle. However considering the additional constraint (2.56) it is necessary to demand Φ to have a certain parity in order to obtain a good parity symmetry in the fifth dimension. Taking a look at (2.58) achieving this goal is rather easy. If Φ is taken to be even all $\phi_n^{(-)}$ must vanish and accordingly if Φ is taken to be odd all $\phi_n^{(+)}$ including $\phi_0^{(+)}$ must vanish. So the discrete symmetry (2.56) removes roughly half of the Kaluza-Klein modes and moreover also the degeneracy of the excited modes.[6] So as already stated this orbifold compactification makes it possible to obtain a chiral gauge theory by removing unwanted fermionic degrees of freedom.

After all these abstract discussions it is necessary to take a look at the so-called UED expansion of the Standard Model which is the topic of the next section.

2.5 Universal Extra Dimensions

Within the last few years three interesting models have been proposed which have drawn quite some attention in the particle physics community. These are the already mentioned ADD model submitted by Arkani-Hamad, Dimopoulos and Dvali in 1998, the Randall-Sundrum model and Universal Extra Dimensions.

The first two ideas were mainly intended to address the hierarchy problem or rather the question why gravitation is so much weaker than the three Standard Modelf interactions. Important properties of those models in contrast with Universal Extra Dimensions are that the Randall-Sundrum model introduces warped extra dimensions and in the ADD model only gravity is allowed to propagate in the extra dimensions. In other words in the latter all forces except gravity are bound to the familiar four dimensional space called a brane in this context whereas gravity is admitted to the whole bulk.

After all this pre-banter the concept of Universal Extra Dimensions can be attacked. Great reviews on this topic are [6] and [7] with the later contrasting all three introduced models. Apart from these review articles [8] and [9] have been used for this chapter about the properties of Universal Extra Dimensions.

As expected this theory is distinguished by the fact that all Standard Model particles are promoted to the added extra dimensions.

[6] In fact the degeneracy is already broken by higher order mass corrections and therefor it is only valid at tree level which will be shortly discussed in the next section.

At first sight this does not seem like a very appealing idea first of all because fermions receive unwanted degrees of freedom using only a plain compactification on a sphere. However as already addressed in section 2.4 this problem can be avoided by imposing an orbifold compactification. In order to understand why it is impossible to gain a chiral gauge theory without additional constraints just consider the projection operators used in the Standard Model to obtain left-handed and right-handed fermions

$$P_L = \frac{1-\gamma^5}{2}\ , \qquad P_R = \frac{1+\gamma^5}{2} \tag{2.60}$$

leading to

$$\psi_L = P_L\psi\ , \qquad \psi_R = P_R\psi\ . \tag{2.61}$$

Obviously the definition of γ^5 is necessary. However for example in five dimensions γ^5 becomes a part of the group structure which can be seen by promoting the Clifford algebra $\{\gamma^\mu, \gamma^\mu\} = 2g^{\mu\nu}$ to five dimensions with Γ^A denoting the five dimensional generalization of the Gamma matrices. An easy definition making the just stated argument clear is $\Gamma^\mu = \gamma^\mu$ and $\Gamma^4 = i\gamma^5$. So to sumarize this argument it is not possible to define a matrix in five dimensions with the properties of γ^5 in four dimensions which in turn makes it impossible to construct appropriate projection operators.

So consider for example the $S^1/\mathbb{Z}_2$ compactification already discussed before. The effective four dimensional Lagrangian of the Standard Model is easily derived by writing down the five dimensional Lagrangian and integrating over the fifth dimension which in fact is the same approach used in section 5.3. The rather lenghty result can be found for example in [6]. However it should be pointed out which kind of mode expansion is used for Standard Model fields. Considering the result from the former section that wave functions are expected to have a certain parity with respect to the discrete $\mathbb{Z}_2$ symmetry the question arises which fields are supposed to be taken even and which ones odd. In the case of Gauge Bosons and the Higgs Boson this choice is rather obvious. Since the zero modes which correspond to the Standard model fields are removed from all odd fields it is clear that all of these Standard Model particles have to be described by even wave functions. This gives rise to the expansions

$$\begin{aligned}
A^\mu(x^\mu, y) &= \frac{1}{\sqrt{\pi R}}\left[\frac{1}{\sqrt{2}}A_0^\mu(x^\mu) + \sum_{n=1}^{\infty} A_n^\mu(x^\mu)\cos(\frac{ny}{R})\right] \\
A^5(x^\mu, y) &= \frac{1}{\sqrt{\pi R}}\sum_{n=1}^{\infty} A_n^5(x^\mu)\sin(\frac{ny}{R}) \\
H(x^\mu, y) &= \frac{1}{\sqrt{\pi R}}\left[\frac{1}{\sqrt{2}}H_0(x^\mu) + \sum_{n=1}^{\infty} H_n(x^\mu)\cos(\frac{ny}{R})\right]\ .
\end{aligned} \tag{2.62}$$

As already mentioned this expansion is a little bit more tricky in the case of fermions. However in this case the ansatz

$$\psi(x^\mu, y) = \frac{1}{\sqrt{\pi R}}\left[\frac{1}{\sqrt{2}}\psi_0(x^\mu) + \sum_{n=1}^{\infty} P_L\psi_{L,n}(x^\mu)\cos(\frac{ny}{R}) + \sum_{n=1}^{\infty} P_R\psi_{R,n}(x^\mu)\sin(\frac{ny}{R})\right] \tag{2.63}$$

is possible. In this formula ψ_0 denotes the familiar Standard Model spinor chiral in four dimensions whereas ψ_L and ψ_R turn out to be vector-like in the effective theory. This rather complicated construction will not be explained here. However it should be pointed out that the projection operators introduced here are the familiar four dimensional ones defined in (2.60).

At this stage a very important property of Universal Extra Dimensions should be pointed out which is especially interesting in the context of dark matter. It is the conservation of Kaluza-Klein parity. The basics have been already discussed in section 2.4. Nevertheless it is interesting to take a look at this property in more detail.

First of all the UED model is the only theory introducing extra dimensions giving rise to a stable particle and hence to a viable dark matter candidate. From a theoretical point of view this can be understood as follows:

Consider a theory assuming that some particles are allowed to propagate in the bulk whereas other particles are trapped brane fields which means that they cannot leave the familiar four dimensional space time. Supposing that trapping particles to the branes can be described by introducing Dirac δ-functions which is equal to neglecting the thickness of the brane the full five dimensional action S_5 is given by

$$S^{(5)} = \int \mathrm{d}x^4 \int \mathrm{d}y \, \left[\mathcal{L}_{bulk} + \mathcal{L}_{brane}\delta(y)\right] \tag{2.64}$$

with the five dimensional Lagrangian $\mathcal{L}_{bulk}$ and the four dimensional $\mathcal{L}_{brane}$ for the particles traped on the brane. For example actions of this form are used in the ADD model mentioned above. Of course, however there are no δ-functions present in the action describing the UED model. This lacking of δ-functions has a very important consequence for the kinds of Kaluza-Klein modes which are allowed to participate in an interaction.

Ignoring for example again the case of orbifolds for a moment it turns out that only vertices with an even number of same-level excited Kaluza-Klein modes are allowed whereas there is no restriction for the zero modes. In this context Figure 2.3 shows some allowed and forbidden vertices of fermions and gauge fields related to the absence of δ-functions in the Lagrangian. This result which in fact arises from momentum conservation due to Translation invariance[7] has already

[7]Remember that compactification on a manifold is considered in this short passage. No additional discrete symmetries are imposed. Moreover Lorentz invariance and hence translation

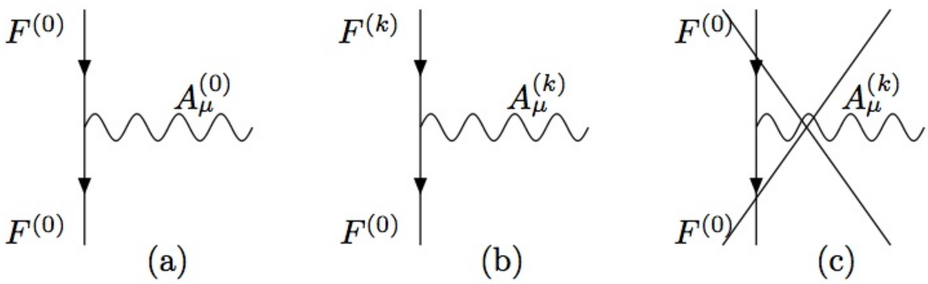

Figure 2.3: A few allowed and forbidden vertices due to the absence of δ-functions in the Lagrangian of the UED model which can arise in models incorporating branes. (Figure taken from [7].)

been obtained in section 4.6. To sum it up the Kaluza-Klein number is conserved with respect to all interactions neglecting branes and orbifolds.

However as discussed before *orbifolding* is necessary to gain a more realistic model. Obviously this approach breaks translation invariance explicitely by introducing for example two fixed points in the case of $S^1/\mathbb{Z}_2$ which in fact is the only valid compactification assuming one extra dimension.[8] These fixed points give rise to localized interactions emerging via radiative corrections which turn out to be of crucial importance in the case of Universal Extra Dimensions as described later in this section. Nevertheless a discrete subgroup called Kaluza-Klein parity defined by $P_{KK} = (-1)^n$ remains unbroken so that at least the lightest Kaluza-Klein mode is stable. It is this candidate which is specified below that gives rise to an important dark matter candidate.

Another implication which is not so significant considering direct detection of dark matter but collider physics is the fact that all odd-level Kaluza-Klein modes can only be pair-produced. Anyway it should be pointed out that this breaking from Kaluza-Klein number conservation to Kaluza-Klein parity conservation is due to radiative corrections which means that the former is still valid at tree level and hence leads to loop-suppression of direct couplings to an even number of Kaluza-Klein modes. Moreover it might be possible that renormalization gives rise to Kaluza-Klein parity breaking. However since this is rather unlikely and cannot be veryfied without having a full ultraviolet completion of the theory it is always assumed that Kaluza-Klein parity is a good symmetry.

Another problem is the fact that the quantum field theory used to describe the Standard Model is not renormalizable in more than four dimensions. This can be noticed by observing that the dimensions of the gauge couplings are negative in the case of added extra dimensions. This makes it necessary to introduce

invariance is supposed to be respected in the UV-limit or in other words by the short-length physics as discussed on page 15.

[8]There are various possibilities considering six or more dimensions.

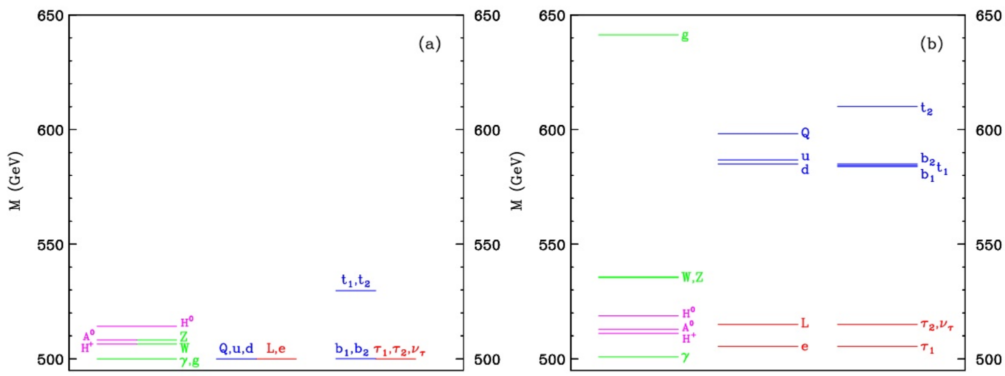

Figure 2.4: The mass spectrum of the level one Kaluza-Klein particles without (a) and with (b) considering first order radiative corrections. Asumed values are $R^{-1} = 500$ GeV, $\Lambda R = 20$ and $m_H = 120$ GeV. (Figure taken from [9].)

another paramter except for the compactification radius R namely the cut-off scale Λ indicating that this is just an effective field theory. So all in all the UED model depends on four unknown parameters: The Higgs mass m_H, the compactification radius R, the number of extra dimensions and the cut-off scale Λ. Some more information about this problem is given immediately in the context of mass corrections.

This sections deals with the mass spectrum of the Kaluza-Klein modes. In the case of promoting the Standard model to five dimensions the formula for masses of the excited modes given in (2.54) still holds at tree level:

$$m_n^2 = m^2 + \frac{n^2}{R^2} \tag{2.65}$$

(2.65) where m is again just the mass of the corresponding Standard model particle suggests a high degree of degeneracy considering the low value of R discussed below. However it turns out that radiative corrections are really important considering this UED model.

Radiative corrections are given rise to in two different ways. First of all there are the already mentioned corrections localized on the fix points of the orbifold. Computing the corresponding contributions reveals that they all diverge logarithmic with respect to the cut-off parameter Λ.

The second kind of radiative corrections is due to loop diagramms which are usually difficult to deal with especially in higher dimensional theories since in this case the Standard model is not supposed to be renormalizeable as already pointed out before. In this case though the loops include propagation in the compactified extra dimensions leading to an exponential suppression for momenta which are large in comparison to the scale of the extra dimension. Therefor the obtained results in this second case are finite.

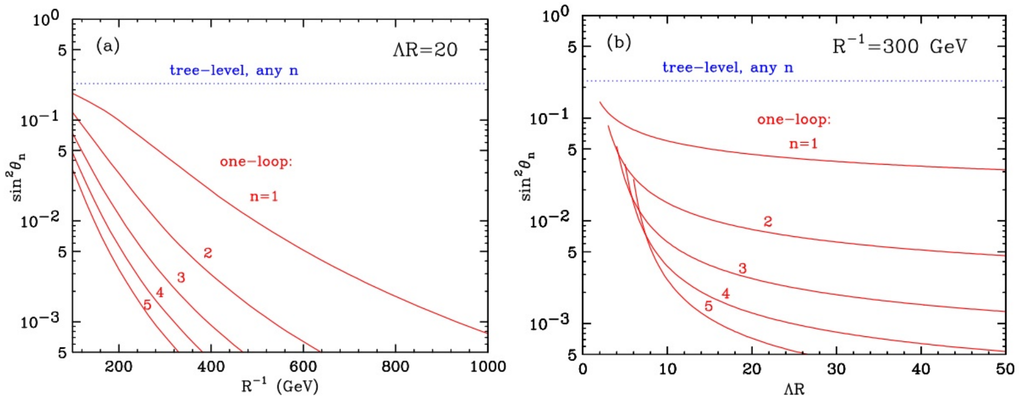

Figure 2.5: Dependence of the Weinberg angle for the first five Kaluza-Klein modes using appropriate values for the parameters R and ΛR. In (a) the latter is fixed whereas the former is fixed in (b). (Figure taken from [9].)

The complete spectrum of Kaluza-Klein particles has been computed and is given in [9]. Instead of quoting the results it is more instructive to take a look at figure 2.4 which shows the spectrum without (a) and with (b) radiative corrections of first order. Appropriate values given in the caption are explained hereafter. As expected neglecting all radiative corrections yields a quite degenerated spectrum which is broken by the incorporation of first order contributions. So higher order terms change the spectrum in a way that will make its distinction from Supersymmetry models rather difficult. However it should be kept in mind that this computation is based on some assumptions which do not necessarily need to be true though they are quite suggesting. Without examining the details it should be mentioned that the spectrum could possibly be quite different especially insofar that the lightest Kaluza-Klein particle is not essentially the first excited mode of the photon. So even though an appropriate dark matter candidate could also be given by the first Kaluza-Klein mode of a neutrino, the Higgs boson or even the graviton this work has been focused on the photon since this is widely believed to be the most probable candidate within the dark matter community. To underpin this assumption it should be pointed out that gravitons would probably not anihilate very effective due to the weakness of gravitational interactions and hence lead to an overclosure of the universe. Moreover consideration of the $\nu^{(1)}$ has led to the result that expected cross sections would probably be so high that they should have already been detected. The corresponding computations are published in [10].

Finally consider the identification of the lightest Kaluza-Klein particle in more detail. It is well known that electroweak symmetry-breaking mixes the bosons B and W_3 to gain the Z and the γ. The mixing is determined by the Weinberg angle θ_W given by $\sin^2\theta_W = 0.23$. Examining the corresponding matrix mixing the first level Kaluza-Klein modes and incorporating the first level radiative corrections the result

$$\begin{pmatrix} Z^{(1)} \\ \gamma^{(1)} \end{pmatrix} = \begin{pmatrix} \frac{1}{R^2} + \frac{1}{4}g_1^2v^2 + \delta M_1^2 & \frac{1}{4}g_1g_2v^2 \\ \frac{1}{4}g_1g_2v^2 & \frac{1}{R^2} + \frac{1}{4}g_2^2v^2 + \delta M_2^2 \end{pmatrix} \begin{pmatrix} W_3^{(1)} \\ B^{(1)} \end{pmatrix} \tag{2.66}$$

with the U(1) and SU(2) gauge couplings g_1 and g_2 repectively, the Higgs vacuum expectation value $v \approx 174$ GeV and the radiative corrections δM_1^2 and δM_2^2 to the $B^{(1)}$ and $W^{(3)}$ is obtained. Evaluating the already mentioned corrections given in [9] reveals that the Weinberg angle for excited Kaluza-Klein modes is shifted to quite small values for reasonable parameters as cognizable from figure 2.5. Therefor according to

$$\gamma^{(1)} = B^{(1)} \cos\theta_W^{(1)} + W_3^{(1)} \sin\theta_W^{(1)} \tag{2.67}$$

it is an appropriate approximation to consider $\gamma^{(1)}$ as being entirely $B^{(1)}$ in order to simplify the upcoming computations.

Before proceeding with considerations of the $B^{(1)}$ as a dark matter candidate just a few annotations about the magnitudes of the compactification radius R and the cutoff scale Λ. An estimate on R is given in [8]. In this paper the authors discuss their evaluation of electroweak precision observables and corrections related to one-loop contributions from Kaluza-Klein modes. They argue that constrains related to these modes are rather weak because as already discussed there are no additional contributions from the UED model at tree level. Finally they place an upper bound of

$$\frac{1}{R} \gtrsim 300 \text{ GeV} \tag{2.68}$$

on the compactification radius considering one added extra dimension and a bound of

$$\frac{1}{R} \gtrsim 400 \text{ to } 800 \text{ GeV} \tag{2.69}$$

for two extra dimensions. The reason for giving an interval in the latter case is the fact that the result is logarithmically divergent and therefor depends on the cutoff which is an unknown parameter as well. This problem does not occur for five dimensions. So considering one extra dimension the bounds can be reliably computed in the framework of the effective theory whereas this is rather difficult assuming more extra dimensions. However it is obvious that the bounds seem to be in a range of a few hundred GeV which makes this theory testable at the Tevatron and the LHC. As already mentioned for example the ADD model includes trapping some particles on the brane which leads to tree-level corrections to electroweak observables in turn yielding upper bounds on R in the range of a few TeV. It is especially this pleasant property and the occurance of a viable dark matter candidate which drew a lot of attention to the UED model in recent years.

Considering the cutoff scale a simple estimate is given in [7]. There an upper bound on ΛR is estimated to be around 30 for five dimensions and about 10 for six dimensions. Therefor in general the cutoff is estimate to have a magnitude of about

$$\Lambda \sim \frac{10}{R} \,. \tag{2.70}$$

The last part of this section on the UED model deals with some properties of a viable dark matter candidate.

In order to really decide if a theory gives rise to a possible dark matter candidate a stable particle is needed which in turn yields an appropriate value for the dark matter relic density of our universe Ω_{DM}. So according to [11] it should be in the range of

$$0.095 < \Omega_{DM} h^2 < 0.129 \tag{2.71}$$

with the Hubble expansion rate given approximately by $h = 0.71$.

As already discussed the particle of interest is the $B^{(1)}$ which is expected to be in thermal equilibrium in the early universe and non-relativistic when it comes to the freeze-out. In this case calculating the relic density of a particle is relatively easy if no coannihilation processes need to be considered. Assuming the validity of the just made assumptions it is justified to expect that the number density n of the $B^{(1)}$ which is its own antiparticle is governed by the Boltzmann equation

$$\frac{\mathrm{d}n}{\mathrm{d}t} + 3Hn = -\langle \sigma v \rangle \left(n^2 - n_{eq}^2 \right) \tag{2.72}$$

with the Hubble paramter H, the relative velocity v, the annihilation cross section σ and the Boltzmann supressed number density n_{eq} in thermal equilibrium given by

$$n_{eq} = g \left(\frac{mT}{2\pi} \right)^{\frac{3}{2}} e^{-\frac{m}{T}} \,. \tag{2.73}$$

Clearly m is the mass of the $B^{(1)}$, g the number of its internel degrees of freedom and T the temperature of the universe. Moreover it should be mentioned that $\langle \ldots \rangle$ in (2.72) denotes thermal averaging. As a reminder the freeze-out takes place when the annihilation rate $\Gamma = n\langle \sigma v \rangle$ drops below the Hubble parameter H.

However as pointed out and executed in [12] in the case of the UED model it is absolutely necessary to include coannihilation processes to obtain results that are trustworthy. As already described in detail the mass spectrum is exceedingly degenerate at tree level. However taking a look Figure 2.4 might give reason to the assumption that coannihilation processes could be neglected because the degeneracy is broken by radiative corrections. Nevertheless it was already indicated that these corrections depend on assumptions about unknown physics at the cutoff scale so that these computations are not necessarily correct. Therefor in order to be safe from possible mistakes it seems much more reliable to take coannihilations into account. Moreover it is obvious from Figure 2.4 that the degeneracy is not completely broken at least not for certain particles.

Thus the authors of [12] incorporated coannihilation processes with all other first level Kaluza-Klein particles. This is accomplished by generalizing (2.72) taking the occurance of other particles into account. Consider an ensemble of N nearly degenerated particles χ_i with masses m_i and $\chi_1 = B^{(1)}$. Then it can be shown that the number density of the lightest of these particles is given by

$$\frac{\mathrm{d}n}{\mathrm{d}t} + 3Hn = -\langle \sigma_{eff} v \rangle \left(n^2 - n_{eq}^2 \right) \ . \tag{2.74}$$

So σ in (2.74) has to be replaced by an effective cross section σ_{eff} which is given by

$$\sigma_{eff} = \sum_{i,j=1}^{N} \sigma_{ij} \frac{g_i g_j}{g_{eff}^2} (1+\Delta_i)^{\frac{3}{2}} (1+\Delta_j)^{\frac{3}{2}} e^{-x(\Delta_i - \Delta_j)} \tag{2.75}$$

with

$$g_{eff} = \sum_{i=1}^{N} g_i (1+\Delta_i)^{\frac{3}{2}} e^{-x\Delta_i} \tag{2.76}$$

and the degeneracy parameter

$$\Delta_i = \frac{m_i - m_1}{m_i} \tag{2.77}$$

describing the fractional mass splitting between the particle χ_i and the $B^{(1)}$ which is also of importance as a paramter in investigations described in chapters below. After solving the Boltzmann equation the relic density ρ_{DM} of the possible dark matter candidate is easily obtained by $\rho_{DM} = nm_1$ which in turn yields Ω_{DM} using

$$\Omega_{DM} = \frac{\rho_{DM}}{\rho_c} \tag{2.78}$$

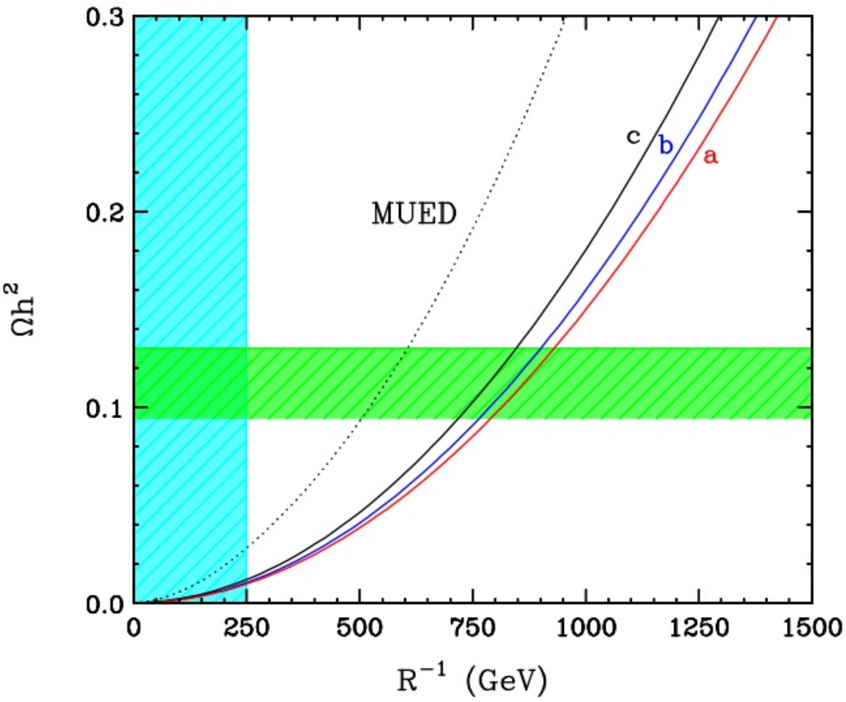

Figure 2.6: Relic density of the $B^{(1)}$ as a function of R^{-1} considering several assumptions about coannihilation. "a" labels the case neglecting coannihilations whereas "MUED" labels the one considering coannihilations with all level one Kaluza-Klein modes. Comparison of the latter with the interval allowed by WMAP data yields a mass range of $500-600$ GeV. (Figure taken from [12].)

with the critical density of a flat universe given by

$$\rho = \frac{3H_0^2}{8\pi G} \approx 1.054 \cdot 10^{-5} \frac{h^2 \mathrm{GeV}}{\mathrm{cm}^3} \ . \tag{2.79}$$

The results from [12] can be seen in figure 2.6 which shows the relic density of the $B^{(1)}$ as a function of R^{-1} and as already explained this is quite similar to the uncorrected mass of the particle. The two most interesting lines are those labeled "a" and "MUED" with the former representing the case where all coannihilation processes are neglected and the latter the one where coannihilation with all other level one Kaluza-Klein modes is allowed. In this case the particle spectrum computed in [9] and shown in Figure 2.4 was used.

Obviously taking coannihilations into account leads to a decrease in the expected mass range which is obtained by the intersection of the appropriate line and the horizontal bound representing the WMAP restrictions for the dark matter density given in (2.71). So it is obvious that the $B^{(1)}$ with a mass in the range of about 500 - 600 Gev indeed provides a possible dark matter candidate. Lighter masses would lead to over-annihilating and hence to under-producing of the relic abundance of dark matter whereas heavier values would give rise to more dark matter than observed. However it should be kept in mind that this result was obtained assuming that only the $B^{(1)}$ contributes to dark matter whereas it is possible and even very likely that the dark matter is generated by more than one particle. In this case the $B^{(1)}$ would be even lighter. Moreover there are also other possible mechanisms which could produce dark matter apart from the thermal production discussed here like gravitational entropy injection. However the 500 - 600 Gev interval will be used as a benchmark here.

In a later chapter it will be shown that current experiments are just starting to probe this interesting mass range. So considering previous annotations it looks like the UED model is about to be testable pretty soon using direct detection experiments like the one described here as well as colliders. Therefor and due to the fact that the theory is quite aestethic and rather simple it is really justified that it has drawn so much attention recently.

The following chapters will deal with considerations about the direct detection of the $B^{(1)}$.

Chapter 3

Cross sections of the $B^{(1)}$ and nuclei

After this extensive discussion about general properties of the UED model this and the following chapters are about to deal with considerations regarding direct detection with earth bound detectors like those used by the CDMS and XENON10 collaboration.

Obviously one of the most important properties in this context is the cross section of the WIMP candidate considered and the used target nuclei. Therefor this chapter is devoted to theoretical predictions on these cross sections. Even though as already stated the focus is set on the $B^{(1)}$ as the dark matter candidate most of the following methods are completely general and independent of the kind of WIMP and target nuclei.

Taking a closer look at the mentioned cross sections it is essential to have a certain idea about some basic nuclear physics. Great reviews especially focussing on direct dark matter detection are given in [13] and [14].

So first of all the question arises whether the cross sections are actually expected to be high enough to be detectable. Without going into the details at this stage the answer to this question is probably "yes". This can be understood by realizing that the considered dark mattar candidate has to have a certain coupling to ordinary matter. Of course this interaction is expected to be quite small but not neglectable since otherwise there would not have occured enough annihilation in the early universe and the abundance would have to significantly exceed the measured value given for example in (2.71). To conclude it is a well known fact from quantum field theory that certain Feynman diagramms contributing for example to pair annihilation are related to scattering amplitudes by the so-called crossing symmetry. Therefor a non-vanishing pair annihilation cross section from dark matter particles to quarks gives rise to a non-vanishing dark matter candidate-quark scattering cross section. This simple argument is quite encouraging.

In order to attack the problem of cross sections three steps have to be accomplished which all have their own subtlety.

First of all the corresponding Feynman amplitudes at the particle physics level have to be computed. Of course this means that a theoretically motivated Lagrangian is available describing the interaction of the considered WIMP and the quarks and gluons which constitute the nucleons and hence the nuclei. Obtaining an effective four dimensional Lagrangian in the framework of UEDs has been decribed extensively in the previous chapter. Even though the number of newly introduced parameters in this model is quite small compared for example to Supersymmetry all of these models generally have large uncertainties which are in fact of crucial importance to the predicions for expected event rates.

Moreover it should be mentioned that these considerations usually need to incorporate interactions with internal quark loops in the nuclei which means that the couplings to all quarks and gluons need to be taken into account.

Besides this step usually only deals with the zero-momentum transfer limit. Unfortunatelly this assumption is not sufficient which is one of the reasons for introducing form factors later on.

The second step is about leaving the quark-gluon content of the nucleons behind. In order to obtain WIMP-nucleon cross sections the matrix elements of the quark and gluon operators sandwiched between nucleon states are needed. These so-called hadronic matrix elements can be provided by physicist investigating appropriate scattering processes.

As expected the next step deals with the upgrade from the nucleon to the nucleus level. The way this is done is similar to the former step sandwiching the nucleon operators obtained before between two nucleon states. This effectively yields a suppression of the cross sections incorporated by introducing a form factor which also takes care of finite momentum transfer as mentiond before.

The first two steps will be explained in this chapter whereas the third step is the main subject of the next one.

An important simplification when dealing with the direct detection of dark matter arises from the fact that these interactions happen in the non-relativistic limit which is appropriate for halo velocities with a magnitude of about $10^{-3}c$. This limit is discussed in great detail in [15] where an effective WIMP-nucleon Lagrangian is considered. So the first two steps of the just explained accomplishment are studied. The authors argue that in the non-relativistic limit the interaction of a WIMP and a nucleon can be effectively described by a Lagrangian of the form

$$\mathcal{L}_{int} = 4\chi^\dagger\chi\left(f_p\eta_p^\dagger\eta_p + f_n\eta_n^\dagger\eta_n\right) + 16\sqrt{2}G_F\chi^\dagger\frac{\vec{\sigma}}{2}\chi\left(a_p\eta_p^\dagger\frac{\vec{\sigma}}{2}\eta_p + a_n\eta_n^\dagger\frac{\vec{\sigma}}{2}\eta_n\right) + \mathcal{O}(\frac{q}{m_{p,W}}) \tag{3.1}$$

where χ denotes the WIMP spinor and η_n and η_p denote the two-component Weyl spinors of the neutron and proton respectively. Moreover $G_F = 1.16637 \cdot 10^{-5}\mathrm{GeV}^{-2}$ refers to Fermi's constant and m_p to the proton mass. All in all the whole process can be parameterized using only five quantities namely the Wimp mass m_W

and the spin-independent (SI) WIMP-nucleon couplings f_p and f_n and the spin-dependent (SD) WIMP-nucleon couplings a_p and a_n. So obviously only a scalar and an axial-vector interaction remain whereas all other parts can either be neglected or rewritten and incorporated in one of the two forms just mentioned.[1]

This result is really remarkable considering that it has been derived using only very general assumptions like general Lorentz invariance of the interaction Lagrangian. Especially it should be pointed out that no constraints were imposed considering the framework of the theory so for example (3.1) holds for the non-relativistic limit of UED and Supersymmetry models as well.

But in order to take a look at the cross sections relevant to the investigations made here it is more convenient to go back to the quark level. Of course for a discussion of the UED model the interaction of the $B^{(1)}$ and the quarks has to be considered. The interaction Lagrangian for this example is given in [15], too:

$$\mathcal{L}_{int} = -\frac{1}{4}(\beta_q + \gamma_q)B_1^{\dagger\mu}B_{1\mu}\bar{q}q - \frac{i}{4}\alpha_q B_{1\mu}^{\dagger}B_{1\nu}\epsilon^{0\mu\nu\rho}\bar{q}\gamma_\rho\gamma_5 q \tag{3.2}$$

with

$$\alpha_q = 2g_1^2 m_{B^{(1)}}\left(\frac{Y_{qL}^2}{m_{q_L^{(1)}}^2 - m_{B^{(1)}}^2} + \frac{Y_{qR}^2}{m_{q_R^{(1)}}^2 - m_{B^{(1)}}^2}\right) \tag{3.3}$$

$$\beta_q = 2E_q g_1^2\left(Y_{qL}^2\frac{m_{q_L^{(1)}}^2 + m_{B^{(1)}}^2}{(m_{q_L^{(1)}}^2 - m_{B^{(1)}}^2)^2} + Y_{qR}^2\frac{m_{q_R^{(1)}}^2 + m_{B^{(1)}}^2}{(m_{q_R^{(1)}}^2 - m_{B^{(1)}}^2)^2}\right) \tag{3.4}$$

$$\gamma_q = g_1\frac{m_q}{2m_H^2} \tag{3.5}$$

In (3.3), (3.4) and (3.5) $m_{q_L^{(1)}}$ and $m_{q_R^{(1)}}$ denote the masses of the first Kaluza-Klein modes of the left- and right-chiral quarks and g_1 the hypercharge coupling defined by

$$g_1 = \frac{e}{\cos\theta_W} = \frac{\sqrt{4\pi\alpha}}{\cos\theta_W} \approx 0.34537 \tag{3.6}$$

where the Weinberg angle $\theta_W \approx 28.741°$ and the Sommerfeld fine-structure constant $\alpha \approx \frac{1}{137.036}$ is used. Moreover the Higgs mass is abreviated m_H and m_q obviously represents the masses of the Standard model quarks and Y_{qL} and Y_{qR} their hypercharges distinguishing between right-handed and left-handed particles. In the used convention the hypercharge is given by

[1]Even though this result seems so appealing it should be kept in mind that a possible suppression of the four used couplings relative to other occuring couplings has been prohibited which seems reasonable but is not completely secure.

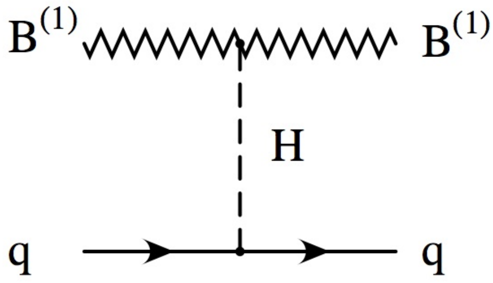

Figure 3.1: Feynman diagram contributing to the $B^{(1)}$-quark scattering at tree level via Higgs boson exchange. (Figure taken from [10].)

$$Y_{qL,R} = Q - I_{z_{L,R}} \tag{3.7}$$

with the charges of the quarks Q in times of the elementary charge e and the z-components of their isospin $I_{z_{L,R}}$ where again the subscript L, R denotes the chirality of the quark considered. A summary of the used values is given in table 3.1.

Further evaluation of the interaction Lagangian (3.2) reveals as shown in [10] and [17] that scattering of a $B^{(1)}$ of a quark at tree level can occur via exchange of a Higgs boson H and a first level Kaluza-Klein quark $q^{(1)}$. The Feynman diagram corresponding to the former interaction is given in figure 3.1 and those two related to the latter are given in figure 3.2.

Evaluating these three amplitudes in the non-relativistic limit indeed leads to the occurance of only two types of interaction one spin-independent and the other one spin-dependent as predicted. Direct translation from the quark to the nucleus level but considering only the case of zero-momentum transfer yields the results which are about to be discussed right now given in this form in [6]. So first of all the total cross section is given by

quark	m_q in GeV	Q in times of e	I_{z_L}	I_{z_R}	Y_L	Y_R
u	0.00225	$\frac{2}{3}$	$\frac{1}{2}$	0	$\frac{1}{6}$	$\frac{2}{3}$
d	0.005	$-\frac{1}{3}$	$-\frac{1}{2}$	0	$\frac{1}{6}$	$-\frac{1}{3}$
s	0.095	$-\frac{1}{3}$	$-\frac{1}{2}$	0	$\frac{1}{6}$	$-\frac{1}{3}$
c	1.25	$\frac{2}{3}$	$\frac{1}{2}$	0	$\frac{1}{6}$	$\frac{2}{3}$
b	4.2	$-\frac{1}{3}$	$-\frac{1}{2}$	0	$\frac{1}{6}$	$-\frac{1}{3}$
t	173	$\frac{2}{3}$	$\frac{1}{2}$	0	$\frac{1}{6}$	$\frac{2}{3}$

Table 3.1: Summary of quark properties used for computing cross sections from [16].

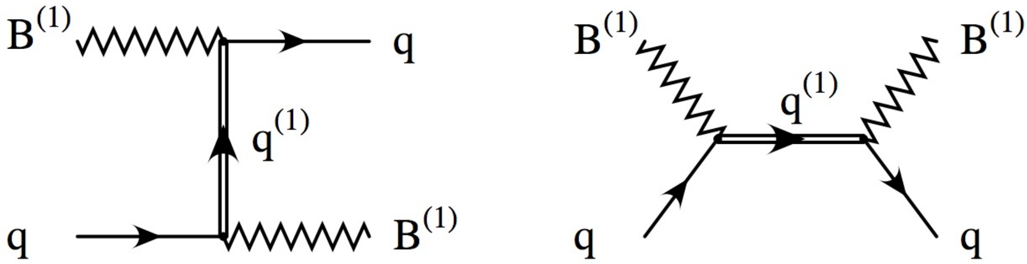

Figure 3.2: Feynman diagrams contributing to the $B^{(1)}$-quark scattering at tree level via exchange of a level one Kaluza-Klein quark. (Figure taken from [10].)

$$\sigma = \sigma_{SI} + \sigma_{SD} \tag{3.8}$$

where σ_{SI} denotes the spin-independent and σ_{SD} the spin-dependent part of the cross section.

The spin-independent part is given by

$$\sigma_{SI} = \frac{4}{\pi}\mu_T^2\Big(Zf_p + (A-Z)f_n\Big)^2 \tag{3.9}$$

with the reduced mass

$$\mu_T = \frac{m_{B^{(1)}} m_T^2}{m_{B^{(1)}} + m_T} \tag{3.10}$$

m_T being the mass of the target nuclei and Z and A representing its atomic number and atomic mass respectively. The translation to the nucleus level[2] is obvious since (3.9) amounts to summing all amplitudes coherently over all nucleons in the target nucleus. However (3.9) only incorporates the zero-momentum transfer limit which is not sufficent for general considerations. This will be explained soon.

The WIMP-nucleon couplings on their parts can be evaluated using

$$f_{p,n} = \sum_{q=u,d,s} f_{T_q}^{(p,n)} a_q \frac{m_{p,n}}{m_q} + \frac{2}{27} f_{TG}^{p,n} \sum_{q=c,b,t} a_q \frac{m_{p,n}}{m_q} \tag{3.11}$$

with the proton and neutron masses $m_p \approx 0.9383$ GeV and $m_n = 0.9396$ GeV and the WIMP-quark couplings a_q given by

[2]This is the third step necessary for computing WIMP-nucleus cross sections mentioned before.

quark	u	d	s
$f_{T_q}^{(p)}$	0.020 ± 0.004	0.026 ± 0.005	0.118 ± 0.062
$f_{T_q}^{(n)}$	0.014 ± 0.003	0.036 ± 0.008	0.118 ± 0.062

Table 3.2: Hadronic matrix elements for the light quarks u, d and s necessary for the computation of WIMP-nucleon cross sections. (Values taken from [6].)

$$a_q = \begin{cases} \frac{m_q g_1^2 \left(Y_{qR}^2 + Y_{qL}^2\right)\left(m_{q^{(1)}}^2 + m_{B^{(1)}}^2\right)}{4 m_{B^{(1)}} \left(m_{B^{(1)}}^2 - m_{q^{(1)}}^2\right)^2} + \frac{m_q g_1^2}{8 m_{B^{(1)}} m_H^2} & , \ q = u, d, s \\ \frac{m_q g_1^2}{8 m_{B^{(1)}} m_H^2} & , \ q = c, b, t \end{cases} \tag{3.12}$$

where a possible mass difference between the left- and right-chiral quarks has already been neglected. Obviously both types of exchanges contribute to the spin-independent interaction.

The mentioned translation from the quark to the nucleon level is hidden in the just introduced parameters $f_{T_q}^{(p,n)}$ and $f_{TG}^{p,n}$. The former is defined by the matrix elements of the quark operators sandwiched between two nucleon states.

$$f_{T_q}^{(p,n)} = \frac{m_q}{m_n} \langle n | \bar{q} q | n \rangle \tag{3.13}$$

These hadronic matrix elements need to be determined not only for the u and d valence quarks constituting the nucleons but also for the s quark which contributes significantly to the cross section. Their values are usually determined experimentally from π-nucleon interactions however burdened with significant uncertainty. Current values are given in table 3.2. There are two interesting observations taking a closer look at these values. First of all it looks like the contribution from the seaquark s dominates reflecting the mass dependence of the spin-independent interaction. Moreover there does not seem to be a great difference between these matrix elements for protons and neutrons. In other words it looks like at least an approximate isospin invariance holds and therefor $f_n \approx f_p$. In this case it is obvious from (3.9) that the spin-independent cross section scales $\sim A^2$ advocating the use of heavy target nuclei.

The heavier quarks c, b and t only lead to contributions included in $f_{TG}^{p,n}$ arising from gluon loops which can be evaluated using

$$f_{TG}^{p,n} = 1 - f_{T_u}^{(p,n)} - f_{T_d}^{(p,n)} - f_{T_s}^{(p,n)} \tag{3.14}$$

A few more important annotations have to be made before showing the results of these computations.

First of all an assumption about the masses of the level one Kaluza-Klein quarks has to be made since their values are at most vaguely known. It is a common procedure to assume a quite high degree of degeneracy of these quark modes and introduce the so-called degeneracy parameter Δ

$$\Delta = \frac{m_{q^{(1)}} - m_{B^{(1)}}}{m_{B^{(1)}}} \tag{3.15}$$

to impose a relation between these assumed to be totally degenerate level one quark masses and the mass of the $B^{(1)}$.

In fact this parameter and the Higgs mass m_H are considered as additional parameters apart from the WIMP mass $m_{B^{(1)}}$ evaluating the spin-independent cross section σ_{SI}. They enter the computation in (3.12) determining the WIMP-quark coupling. Obviously the occurance of a factor $(m^2_{B^{(1)}} - m^2_{q^{(1)}})^2$ in the denominator in (3.12) considering the light quarks leads to a striking enhancement of the WIMP-quark coupling in the case that Δ is extremly small. Such a degeneracy is usually not well motivated but it might be possible especially considering theories like the UED model where a general high degree of degeneracy occurs naturally. In the computations executed here Δ is varied inside an interval from 0.01 to 0.5 which seems quite reasonable taking the high degeneracy of the model into account but omiting unexpected resonances. The other mentioned parameter the Higgs boson mass is varied from 114.4 to 200 GeV.

Moreover it is a useful procedure to normalize the cross sections obtained from (3.9) σ_{SI} to cross sections on a nucleon $\sigma^{p,n}_{SI}$. This is of special importance considering comparisons between different target nuclei. So evaluating (3.9) assuming that the target solely consists of a proton or a neutron yields

$$\sigma^{p,n}_{SI} = \frac{4}{\pi}\mu_{p,n} f^2_{p,n} \tag{3.16}$$

with

$$\mu_{p,n} = \frac{m_{B^{(1)}} m_{p,n}}{m_{B^{(1)}} + m_{p,n}} \; . \tag{3.17}$$

Comparing this result to the original expression (3.9) directly yields the relation

$$\sigma^{p,n}_{SI} = \frac{f^2_{p,n}}{\Big(Zf_p + (A-Z)f_n\Big)^2} \frac{\mu^2_{p,n}}{\mu^2_T} \sigma_{SI} \tag{3.18}$$

which reduces to

$$\sigma^{p,n}_{SI} = \frac{1}{A^2} \frac{\mu^2_{p,n}}{\mu^2_T} \sigma_{SI} \tag{3.19}$$

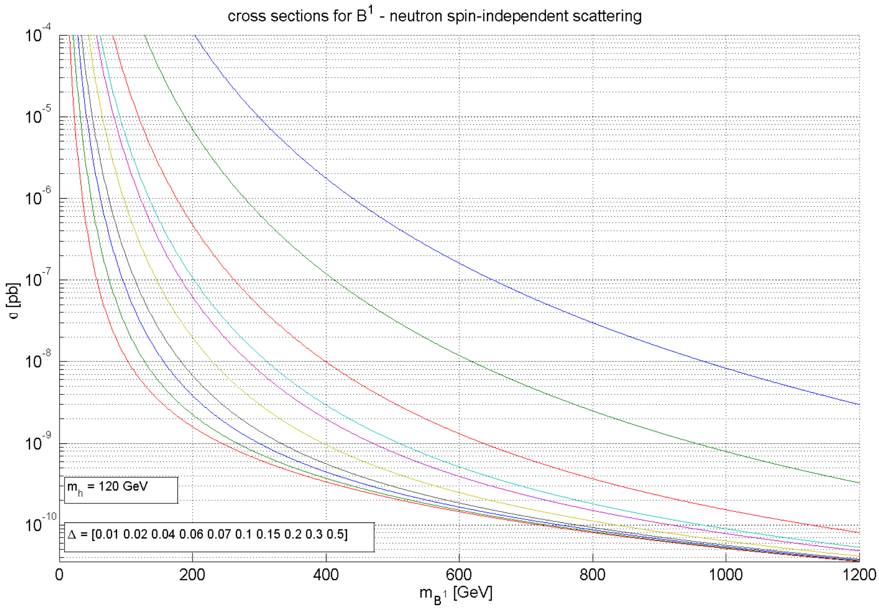

Figure 3.3: Spin-independent $B^{(1)}$-neutron cross sections for a Higgs mass of $m_H = 120$ GeV and various values of the degeneracy parameter Δ in the σ_{SI} vs. $m_{B^{(1)}}$-plane. Within this thesis the highest curve in a plot always belongs to the first value listed in it. So for example the upper blue curve belongs to $\Delta = 0.01$. The cross sections increase significantly for low masses and are enhanced for small degeneracy parameters.

assuming that isospin invariance of the interaction holds. Obviously there is only a slight difference between normalizing to a neutron and a proton. So here the former case is chosen. Considering very heavy WIMP masses assuming $m_{B^{(1)}} \gg m_T$ equation (3.19) even yields

$$\sigma_{SI}^{p,n} = \frac{1}{A^4}\sigma_{SI} \tag{3.20}$$

emphasizing the expected enhancement of a signal using heavy target nuclei. Evaluating all of these formulae yields the result shown in figure 3.3 which represents the most common way these cross sections are displayed namely for a fixed Higgs mass and various values of the degeneracy parameter. Similar plots using different values of the Higgs mass can be found in section A.1 of the apendix.

Moreover it is instructive to show these plots the other way around using a fixed value for Δ and various values for m_H. It is obvious from figure 3.4 that the dependence on the Higg mass is less severe than the dependence on Δ especially for small values of Δ which can be realized by taking a look at A.2 showing similar

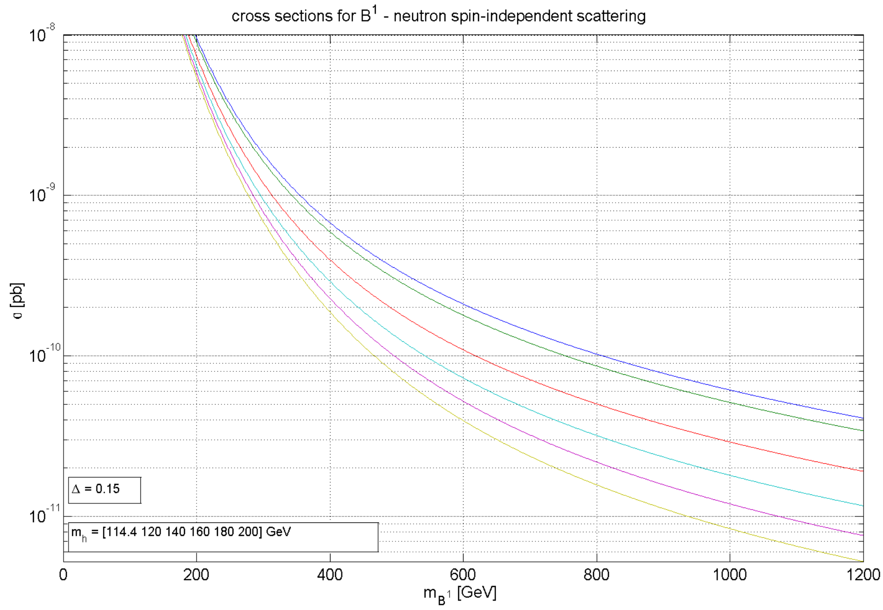

Figure 3.4: Spin-independent $B^{(1)}$-neutron cross sections for a degeneracy paramter given by $\Delta = 0.15$ and various values of the Higgs mass m_H in the σ_{SI} vs. $m_{B^{(1)}}$-plane. Comparing the scale of the y-axis with the corresponding scale in Figure 3.3 it is obvious that the dependence of σ_{SI} on m_H is much less severe than the dependence on Δ.

plots for different values of the degeneracy parameter.

A third plot considering the spin-independent Wimp-neutron cross section is shown in figure 3.5 where the σ_{SI} vs. m_h plane is used incorporating a fixed WIMP mass of 500 GeV and various values for Δ. This WIMP mass is chosen in accordance with the relic density computations as explained on page 30. Again it is obvious that the dependence on the Higgs mass is only slight especially for low values of Δ.

However as already mentioned before the presented accomplishment must be modified by taking the finiteness of the used target nucleus and details of its structure into account. This eventually leads to the multiplication of σ_{SI} with the square of a yet to define form factor F depending on the target nucleus. Therefor the substitution

$$\sigma_{SI} \rightarrow \sigma_{SI} F^2 \tag{3.21}$$

has to be implemented. Details about form factors are given in the next chapter.

Finally before proceeding with the spin-dependent part of the cross section σ_{SD} it is interesting to know that the whole framework dealing with the com-

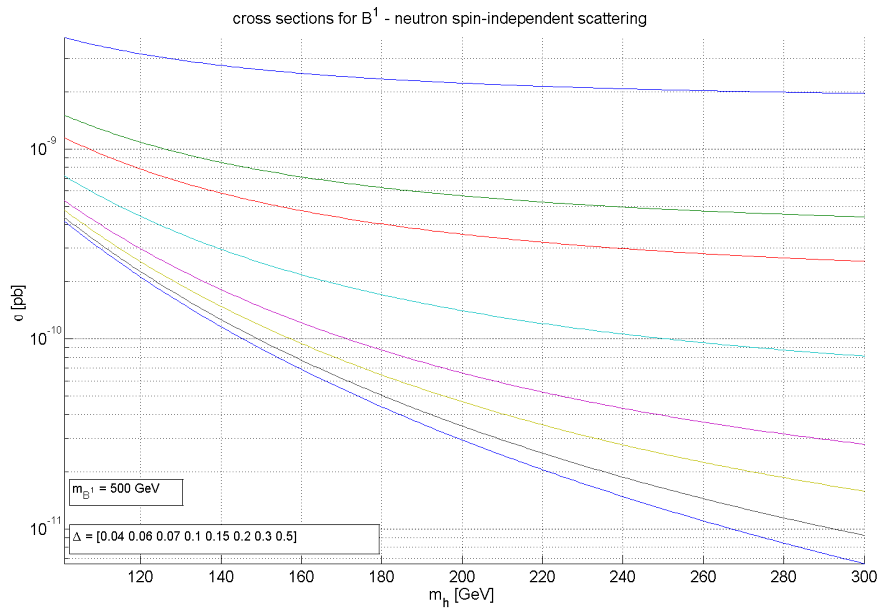

Figure 3.5: Spin-independent $B^{(1)}$-neutron cross sections for a WIMP mass given by $m_{B^{(1)}} = 500$ GeV and various values of Δ in the σ_{SI} vs. m_H-plane.

putation of spin-independent cross sections presented here is completely general and not even dependent of the kind of theory considered except for the expression determining the WIMP-quark couplings given for the case of the UED model in (3.12). So particularly the ansatz for the spin-independent cross section σ_{SI} given in (3.9) and the corresponding WIMP-nucleon couplings $f_{p,n}$ given in (3.11) are model independent. As an example in [18] the authors compare the possible distinguishing of three different possible extensions of the Standard model namely Supersymmetry, Universal Extra Dimensions and Little Higgs Models using direct detection methods all based on (3.9) and (3.11). However the ansatz for the WIMP-quark coupling is different in each case.

After this extensive discussion of the spin-independent cross section σ_{SI} the rest of this chapter is devoted to the spin-dependent cross section σ_{SD}. Like in the spin-independent case the result arises from the evaluation of the Feynman diagrams shown in figure 3.2. The Higgs exchange contributes only to the scalar interaction which means that the Feynman diagram shown in figure 3.1 does not need to be considered here. Thus this type of interaction is also independent of the Higgs mass. The result which is only valid in the zero-momentum transfer limit as well is given by

$$\sigma_{SD} = \frac{2}{3\pi}\mu_T^2 g_1^4 \frac{\Lambda^2 J(J+1)}{(m_{B^{(1)}}^2 - m_{q^{(1)}}^2)^2} \tag{3.22}$$

with

$$\Lambda = \frac{a_p\langle S_p\rangle + a_n\langle S_n\rangle}{J} \tag{3.23}$$

where J denotes the total nuclear spin and $\langle S_{p,n}\rangle$ the expectation values of the proton and neutron spins within the nucleus. Since these last quantities have to be computed using nuclear structure calculations which is usually accomplished in connection with the analysis of form factors a discussions of these quantities is deferred to the next chapter. a_p and a_n are the WIMP-proton and WIMP-neutron couplings respectively containing details of the UED model and the quark spin content ot the nucleons.

What makes the investigation of spin-dependent cross sections comparatively difficult is the fact that in this case the WIMP does not just couple to the number of nucleons in the nucleus but to their spins. So even though the interaction with the nucleus is coherent as in the spin-independent case in the sense that the scattering amplitudes are still summed the strength of the interaction vanishes for paired nucleons in the same energy state since the sign of the interaction amplitude switches together with the nucleon spin. If their energy states are different the effective interaction rate is highly suppressed but still finite. Nevertheless this means that only nuclei with an odd number of nucleons yield a significant cross section and that other nuclei can be neglected. The WIMP-nucleon couplings are given by

$$a_{p,n} = \sum_{q=u,d,s} (Y_{qL}^2 + Y_{qR}^2)\Delta^{p,n} q \tag{3.24}$$

where the parameters $\Delta^{p,n}q$ represent the translation from the quark to the nucleon level. An important difference to the spin-independent case is that these couplings are generally not even approximately equal and that they may even vary by several orders of magnitude. Similar to the quantities $f_{T_q}^{(p,n)}$ defined in (3.13) the $\Delta^{p,n}q$'s are given by the matrix element of the quark axial-vector current or rather

$$s_\mu^{p,n}\Delta^{p,n}q = \frac{1}{2}\langle n|\overline{q}\gamma_\mu\gamma_5 q|n\rangle \tag{3.25}$$

with the nucleon spin $s_\mu^{p,n}$. Obviously the quantity $\Delta^{p,n}q$ parameterizes the contribution of each quark q to the total spin of the nucleon n. The corresponding values are experimentally determined from investigations of polarized lepton-nucleon deep inelastic scattering. Current values are given in table 3.3. Especially comparing the errors of these values to those for the parameters $f_{T_q}^{(p,n)}$ given in table 3.2 shows that they cannot be measured to a great precision and hence that they are a large source of uncertainty in the calculations.

Inserting the values from Table 3.3 and the hypercharges given in Table 3.1 into (3.24) yields

$$\begin{aligned} a_p &= 0.281 \\ a_n &= -0.139\ . \end{aligned} \tag{3.26}$$

Obviously the WIMP-nucleon couplings in the spin-dependent case are independent of the model parameters Δ and m_H which is totally different from the spin-independent case cp. (3.11) with (3.12). However the expression (3.22) for the spin-dependent cross section σ_{SD} is directly dependent on Δ via the mass of the level one Kaluza-Klein quarks. Therefor it is clear that this formula is model dependet. This should be contrasted to the spin-independent case where it was pointed out that the expression (3.9) yielding σ_{SI} is model independent and for example valid in the case of an UED and supersymmetric model as well.

However the normalization to a nucleon analogue to (3.20) is again model independent. To accomplish this normalization (3.22) has to be evaluated for a single nucleon. In this case $J = \frac{1}{2}$ holds and the nucleon spin expectation values are given by $\langle S_p \rangle = \frac{1}{2}$ and $\langle S_n \rangle = 0$ whether a proton is considered or by $\langle S_p \rangle = 0$ and $\langle S_n \rangle = \frac{1}{2}$ in the case of a neutron. Using these values directly yields

$$\sigma_{SD}^{p,n} = \frac{1}{2\pi} g_1^4 \frac{\mu_{p,n}^2 a_{p,n}^2}{(m_{B^{(1)}}^2 - m_{q^{(1)}}^2)^2}\ . \tag{3.27}$$

Comparing this result to (3.22) gives rise to the normalization

$$\sigma_{SD}^{p,n} = \frac{3}{4} \frac{\mu_{p,n}^2}{\mu_T^2} \frac{J}{J+1} \frac{1}{\langle S_{p,n} \rangle^2} \sigma_{SD} \tag{3.28}$$

which is analogue to (3.19) and as already mentioned model independent as well.

However as already mentioned another important difference to the spin-independent case can be realized by evaluating (3.27) for a proton and a neutron which is shown in figure 3.6 and figure 3.7 respectively: Obviously there is a large difference between both cases which in fact is not really surprising since the WIMP-proton and WIMP-neutron couplings given in (3.26) differ a lot. This should be contrasted

quark	u	d	s
$\Delta^p q$	0.78 ± 0.02	-0.48 ± 0.02	-0.15 ± 0.07
$\Delta^n q$	-0.48 ± 0.02	0.78 ± 0.02	-0.15 ± 0.07

Table 3.3: Matrix elements of the quark axial-vector current for the light quarks u, d and s necessary for the computation of WIMP-nucleon cross sections. The values corresponding to the proton and neutron are connected by flavor isospin rotation. (Values taken from [6].)

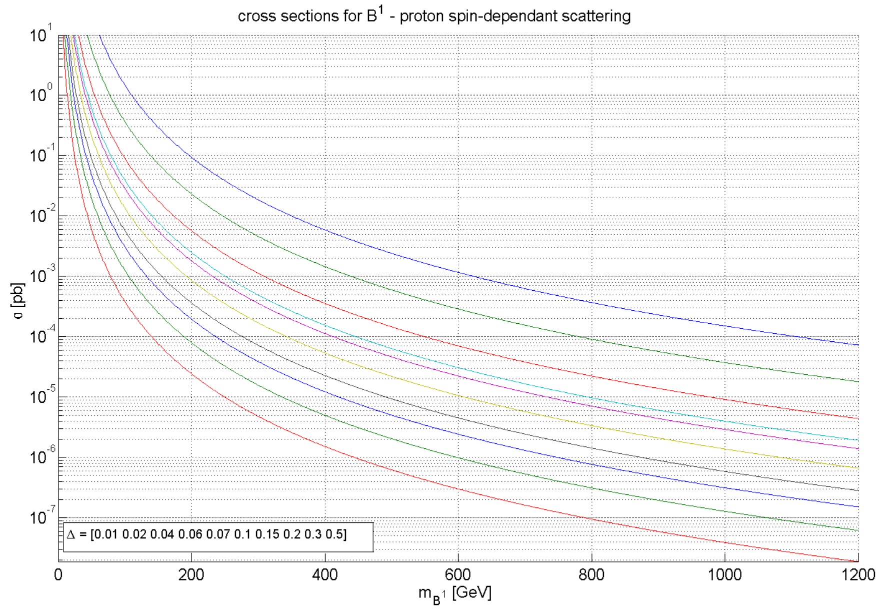

Figure 3.6: Spin-dependent $B^{(1)}$-proton cross sections for various values of Δ in the σ_{SD} vs. $m_{B^{(1)}}$-plane. As argued in the text there is no dependence on the Higgs mass m_H as in the spin-independent case.

to the spin-independent case where it was pointed out that the corresponding couplings can usually be assumed to be almost equal.

Moreover a general comparison between spin-dependent and spin-independent cross sections considering scattering off individual nucleons reveals that the latter are generally supressed to the former. This can be understood by comparing (3.27) and (3.16) yielding

$$\frac{\sigma_{SD}^{p,n}}{\sigma_{SI}^{p,n}} = \frac{1}{8} g_1^4 \frac{a_{p,n}^2}{f_{p,n}^2} \frac{1}{(m_{B^{(1)}}^2 - m_{q^{(1)}}^2)^2} \quad . \tag{3.29}$$

So obviously the high degree of degeneracy or rather the small value of Δ is the main reason for this difference of the magnitudes of both types of interaction. However it should be kept in mind that the spin-independent scattering from a heavier nucleus benefits from coherent enhancement implemented by the $\sim A^2$ scaling of the cross section. Thus experiments are usually assumed to be much more sensitive to spin-independent interactions.

Moreover it is clear that a form factor has to be introduced in the spin-dependent case as well in order to incorporate the possibility of finite momentum transfer. This is done similarly to the spin-independent case by substituting

$$\sigma_{SD} \to \sigma_{SD} F^2 \tag{3.30}$$

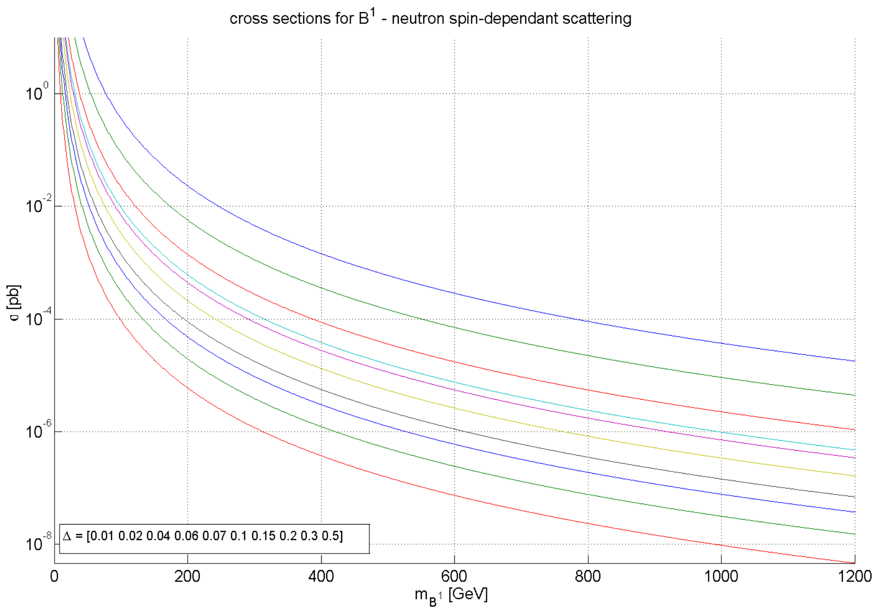

Figure 3.7: Spin-dependent $B^{(1)}$-neutron cross sections for various values of Δ in the σ_{SD} vs. $m_{B^{(1)}}$-plane. Obviously there is a large difference between the spin-dependent scattering from a neutron and a proton as shown in figure 3.6.

with an appropriate form factor F. However determining these form factors is much more complicated in the spin-dependent case involving extensive investigations of nuclear shell models. This will be explained in some detail in the next chapter.

To finish the analysis of cross sections there are two more short topics to be discussed in this chapter.

First of all a short overview of the target nuclei considered is useful at this stage. Since a huge of the workgroup at the institute was involved in the XENON10 experiment using liquid xenon as the target described shortly for example in [19] and [20] both the CDMS and the XENON10 experiments are considered. Therefor germanium, silicon and xenon are used as target materials in the upcoming computations. The most important properties of these nuclei and their naturally occuring isotopes are given in table 3.4. Obviously there are only four isotopes yielding a spin-dependent interaction namely ^{29}Si, ^{73}Ge, ^{129}Xe and ^{131}Xe. Since the natural abundances of the two isotopes used by the CDMS collaboration are exceedingly small this experiment has usually been considered to be neglectable analyzing spin-dependent interactions. However this is definitively not the case which will be shown later.

Finally a short comment on the possibility to distinguish the UED model from

experiment	element	Z	A	abundance	m_T in u	J
CDMS	silicon	14	28	0.922297	27.9769271	0
			29	0.046832	28.9764949	$\frac{1}{2}$
			30	0.030872	29.9737707	0
	germanium	32	70	0.2084	69.9242497	0
			72	0.2754	71.9220789	0
			73	0.0773	72.9234626	$\frac{9}{2}$
			74	0.3628	73.9211774	0
			76	0.0761	75.9214016	0
XENON10	xenon	54	124	0.0009	123.9058942	0
			126	0.0009	125.904281	0
			128	0.0192	127.9035312	0
			129	0.2644	128.9047801	$\frac{1}{2}$
			130	0.0408	129.9035094	0
			131	0.2118	130.905072	$\frac{3}{2}$
			132	0.2689	131.904144	0
			134	0.1044	133.905395	0
			136	0.0877	135.907214	0

Table 3.4: Isotopes used in the detectors of the CDMS and XENON10 collaborations with their most important properties for this work. (Data taken from [21].)

Supersymmetry which is by far the most extensively studied extension of the Standard Model. The authors of [18] argue that a potential distinction depends on the range of a measured cross section. Without going into details it is their main result that spin-independent cross sections from supersymmetric particles can usually be larger than those of particles arising from UED. So quite large cross sections would strongly disfavour the UED model whereas no conclusion can be drawn from the observation of small cross sections. However it should be kept in mind that a high degree of degeneracy or rather a small value of Δ could significantly raise the spin-independent cross section from the UED model as well. Therefor this can only be one hint for the underlying theory and additional information for example from collider experiments is of crucial importance.

Chapter 4

Form factors

As described in the previous chapter it is necessary to introduce form factors to modify the cross sections in order to incorporate non-zero momentum transfer which is inevitable considering heavy WIMPs of a few 10's of GeV or more. To be more precise the structure of the nucleon has to be taken into account when the momentum transfer q given by

$$q = \sqrt{2m_T E_R} \tag{4.1}$$

with the recoil energy E_R yields a corresponding de Broglie wave length $\lambda = \frac{h}{q}$ which is no longer large compared to the effective nuclear radius r_n. These form factors should be normalized to 1 for zero momentum transfer and smaller than 1 otherwise. Great reviews dealing with form factors and related nuclear shell model calculations necessary in the spin-dependent case are given in [13], [22] and [23].

Without going into the details of the underlying nuclear physics it can be shown that both kinds of form factors can be written in a similar form ensuring the normalization constraint namely

$$F_{SI}^2(q) = \frac{S_{SI}(q)}{S_{SI}(0)} \qquad \text{and} \qquad F_{SD}^2(q) = \frac{S_{SD}(q)}{S_{SD}(0)} \tag{4.2}$$

with

$$S_{SI}(q) = \sum_{L \text{ even}} |\langle J||\mathcal{C}_L(q)||J\rangle|^2 \simeq |\langle J||\mathcal{C}_0(q)||J\rangle|^2 \tag{4.3}$$

and

$$S_{SD}(q) = \sum_{L \text{ odd}} \left(|\langle J||\mathcal{T}_L^{el5}(q)||J\rangle|^2 + |\langle J||\mathcal{L}_L^5(q)||J\rangle|^2 \right) \tag{4.4}$$

where the double vertical lines denote the reduced matrix elements of the respective operators. In (4.4) $\mathcal{T}_L^{el5}$ and $\mathcal{L}_L^5$ denote the transverse electric and longitudinal multipole projections of the axial vector current respectively. $\mathcal{C}_L$ in (4.3) represents the so-called *coulomb projection*. The explicit forms of these operators can be found in any of the just mentioned review articles. The simplification in (4.3) is justified because the contribution from $L = 0$ dominates so that the rest can be neglected.

Since the form given in (4.2) will not be needed in the spin-independent case the subscript of S will be dropped in the following considerations. Therefor S always denotes the spin-dependent case from now on.

The following two sections deal with both types of form factors seperately starting with the much simpler spin-independent case.

4.1 Spin-independent form factors

As mentioned before the spin-independent case is rather easy to treat since then the WIMPs couple only to the number of nucleons in the nucleus. A short introduction to this topic can be found in [24].

So considering the first Born approximation the form factor F_{SI} is just given by the Fourier transformation of the mass density distribution ρ which in turn is usually assumed to be proportional to the charge density distribution. This is necessary because the latter is known to a much higher accuracy from low-energy elastic lepton scattering which in turn is observed to be isotropic justifying the ansatz $\rho(\vec{r}) = \rho(r)$ yielding $F_{SI}(\vec{q}) = F_{SI}(q)$. So F_{SI} can be computed using

$$F_{SI}(q) = \int \rho(r) e^{i\vec{q}\cdot\vec{r}} \mathrm{d}^3 r = \frac{4\pi}{q} \int_0^\infty r \sin(qr) \rho(r) \mathrm{d}r \ . \tag{4.5}$$

A lot of different density distributions have been proposed in the literature. According to [24] the most realistic one is the Fermi distribution given by

$$\rho(r) = \rho_0 \frac{1}{1 + e^{\frac{r-c}{a}}} \ . \tag{4.6}$$

However a proposal originally made by Helm in [25] half a century ago is usually preferred because its Fourier transformation can be evaluated analytically whereas the ansatz (4.6) demands numerical evaluation of (4.5). Moreover it turns out that both forms yield quite similar results. Helm considered a folded density distribution of the form

$$\rho(\vec{r}) = \int \rho_0(\vec{r'}) \, \rho_1(\vec{r} - \vec{r'}) \mathrm{d}^3 r' \ . \tag{4.7}$$

Observing that the scattering depends mainly on the charge distribution near the

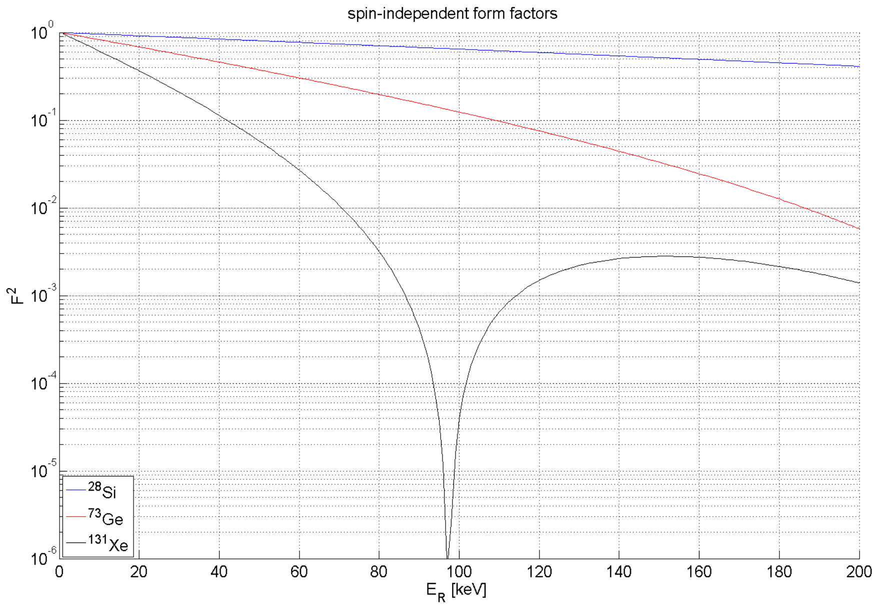

Figure 4.1: Spin-independent form factors of ^{28}Si, ^{73}Ge and ^{131}Xe. Obviously the latter drops down much faster than the other form factors.

surface and only slightly on the distribution inside the nucleus he decided to let ρ_0 define the radius of the nucleus and ρ_1 the surface thickness yielding a damping of the form factor. Assuming a spherical symmetric distribution he chose

$$\rho_0(r) = \begin{cases} \frac{3}{4\pi r_n^3} & , r < r_n \\ 0 & , r > r_n \end{cases} \tag{4.8}$$

and

$$\rho_1(r) = \frac{1}{(2\pi s^2)^{\frac{3}{2}}} e^{-\frac{(qs)^2}{2}} \tag{4.9}$$

with the effective nuclear radius r_n and the nuclear skin thickness s. Inserting this ansatz into (4.5) and performing the integration yields

$$F_{SI}(qr_n) = 3\frac{j_1(qr_n)}{qr_n} e^{-\frac{(qs)^2}{2}} \simeq 3\frac{\sin(qr_n) - qr_n\cos(qr_n)}{(qr_n)^3} e^{-\frac{(qs)^2}{2}} \tag{4.10}$$

where j_1 denotes the spherical Bessel function of index 1. Common values for the used parameters taken from [24] are $s = 1$ fm and

$$r_n = \sqrt{c^2 + \frac{7}{3}\pi^2 a^2 - 5s^2} \tag{4.11}$$

with $a = 0.52$ fm and

$$c = 1.23\sqrt[3]{A} - 0.60 \text{ fm} . \tag{4.12}$$

The just explained analysis highlights an important difference from the spin-dependent case considered in the next section: The spin-independent form factors F_{SI} are almost independent of the used target nuclei except for the values of their atomic masses A. In particular there is no dependence on the spin-independent WIMP-nucleon couplings f_p and f_n which turns out to be a great benefit determining cross section limits.

Finally figure 4.1 shows a comparison of spin-independent form factors for one silicon, one germanium and one xenon isotope. Obviously the form factor from the xenon isotope drops down much faster than the form factors from the silicon and the germanium isotopes partly compensating the xenon benefit from the $\sim A^2$ scaling. However considering really low thresholds the use of xenon seems to be more advantageous.

4.2 Spin-dependent form factors

Computing form factors in the spin-dependent case is considerably more complicated because the spin structure varies enormously between different target nuclei. Therefor they have to be computed separately for every single target isotope using extensive nuclear shell model calculations.

Considering zero momentum transfer (4.4) can be evaluated explicitely since most contributions to the sum vanish. The result is given by

$$S(0) = \frac{2J+1}{\pi} J(J+1)\Lambda^2 \tag{4.13}$$

with Λ given in (3.23). Obviously knowledge of the expectation values of the proton and neutron spins within the nucleus $\langle S_p \rangle$ and $\langle S_n \rangle$ as well as of the WIMP nucleon couplings a_p and a_n is necessary.

At finite momentum transfer it is inevitable to consider more complicated approaches. The applied formalism is in fact a generalization of the one accomplished for the investigation of weak and electromagnetic semi-leptonic interactions in nuclei. It is a common procedure to switch from the proton-neutron representation to the isospin representation. This is implemented by writing the isoscalar and isovector spin couplings a_0 and a_1 in terms of the WIMP-proton and WIMP-neutron couplings a_p and a_n.

$$\begin{aligned} a_0 &= a_p + a_n \\ a_1 &= a_p - a_n \ . \end{aligned} \tag{4.14}$$

Using this translation (4.4) can be written in the form

$$S(q) = a_0^2 S_{00}(q) + a_1^2 S_{11}(q) + a_0 a_1 S_{01}(q) \tag{4.15}$$

with the spin structure functions S_{00}, S_{11} and S_{01} representing an isoscalar, isovector and interference term respectively.

Considering the dependence of the WIMP-nucleon couplings it can be seen that the form of $S(q)$ is determined solely by the ratio $\frac{a_p}{a_n}$ whereas its magnitude is proportional to $a_p^2 + a_n^2$. Since according to (4.2) the squared form factor is given by (4.15) normalized to 1 for $q = 0$ it is clear that F^2 is solely determined by the ratio $\frac{a_p}{a_n}$. Knowledge of the absolute value of neither one of the WIMP-nucleon couplings is required.

Moreover it should already be noted at this stage that evaluating (4.15) at $q = 0$ can be very problematic since $S(0)$ can reach 0 for certain values of $\frac{a_p}{a_n}$ leading to a singularity in the expression (4.2) for F^2. Fortunately there is no problem using the WIMP-nucleon couplings from the UED model given in (3.26). However this problem occurs determining limits on WIMP-nucleon couplings as explained in a later chapter. It can partly be solved by using (4.13) in the denominator of (4.2) instead of evaluating (4.15) at $q = 0$. It should be kept in mind that in practice this substitution leads to a slight violation of the normalization constraint since evaluating (4.15) using fitted functions as explained below only approximately yields (4.13). Anyway this accomplishment makes it possible to avoid singularities. Nevertheless other difficulties especially in the case of the two xenon isotopes ^{129}Xe and ^{131}Xe remain. A detailed discussion can be found in the appropriate chapter.

As already mentioned both introduced quantities $\langle S_p \rangle$ and $\langle S_n \rangle$ as well as the three spin structure functions have to be determined evaluating (4.4) using nuclear shell models. Usually the results for the spin structure functions are presented as plots accompanied by analytic functions fitted to the curves. Mostly polynomial and exponential functions are applied.

Unfortunately it turns out that the results depend sensitively on the nuclear structure assumed. This is especially problematic for heavy nuclei since many nuclear states have to be considered. However the situation improves thanks to advances in computer power and storage.

In order to test the accuracy of the accomplished determinations it is useful to calculate some nuclear observables and compare the obtained values with measurements from experiments. A very convenient observable in this context is the nuclear magnetic moment given by

$$\mu = g_n^s \langle S_n \rangle + g_n^l \langle L_n \rangle + g_p^s \langle S_p \rangle + g_p^l \langle L_p \rangle \tag{4.16}$$

with the free particle g-factors

$$g_n^s = -3.826 \qquad g_n^l = 0 \qquad g_p^s = 5.586 \qquad g_p^l = 1 \tag{4.17}$$

given in nuclear magnetons and the expectation values of the angular momentum of the nucleons $L_{p,n}$ in the nucleus. The suitability is obvious since μ contains $\langle S_p \rangle$ and $\langle S_n \rangle$. Therefor the magnetic moment provides an appropriate benchmark to judge the validity of the considered shell model.

After this introduction the rest of this section focusses on appropriate results for the four isotopes of interest ^{29}Si, ^{73}Ge, ^{129}Xe and ^{131}Xe. For most isotopes used by dark matter experiments more than one paper has been puplished on computing spin structure functions. An extensive summary of all available publictions on this topic is given in [22] and [23]. As already mentioned problems occured considering certain values for the WIMP-nucleon couplings. Since these issues were not so significant for ^{29}Si and ^{73}Ge only the respective puplications accepted as being the most adequate by the community are considered. However in the case of xenon it seems appropriate to consider several possibilities.[1]

The results using ^{29}Si puplished in [26] in 1993 were obtained performing nuclear shell model calculations in large model spaces. The calculations were rather straight-forward since a well-defined and extensively tested Hamiltonian describing the nucleus was available. The spin structure functions in this and all other papers are not given as functions of the transfered momentum q but of the quantity

$$y = \left(\frac{bq}{2} \right)^2 \tag{4.18}$$

with the so-called oscillation parameter b given by

$$b = \sqrt[6]{A} \text{ fm} \approx 1.75 \text{ fm} . \tag{4.19}$$

After finishing the numerical shell model computations exponential functions were fitted to the three spin structure functions yielding

$$\begin{aligned} S_{00}(y) &= 0.00818\, e^{-4.428y} \\ S_{11}(y) &= 0.00818 \cdot 1.06\, e^{-6.264y} \\ S_{01}(y) &= 0.00818 \cdot (-2.06)\, e^{-5.413y} \end{aligned} \tag{4.20}$$

[1] Even though it turns out that none of the different nuclear shell models yields good results for all WIMP-nucleon couplings.

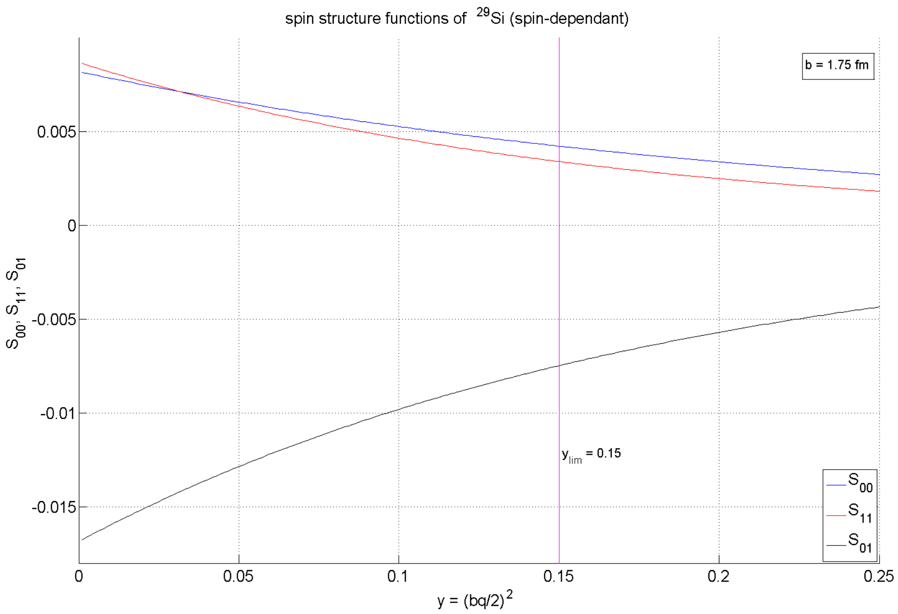

Figure 4.2: Spin structure functions of ^{29}Si as published in [26] The fits are valid up to $y < 1.5$.

valid for $y < 1.5$ which corresponds to a maximum recoil energy of $E_R = 140.86$ keV which is well above the interesting region of the CDMS experiment with an upper analysis limit of 100 keV. The fits are shown in figure 4.2.

Apart from that there are two interesting annotations in this paper. First of all the authors argue that serious issues occur in the case that $a_p \gg a_n$ or equivalently $a_0 \simeq a_1$ since then S_{00} and S_{11} cancel against S_{01}. This is exactly the problem mentioned before in this section and investigated further in a later chapter. None of the other papers contains any hint to similar problems with the authors' calculations even though it turns out that the issues using ^{29}Si are almost negligible whereas they get really severe in the case of xenon. However according to the authors this problem is not related to the general computation but to the accuracy of the exponential fits. Using the full result instead of the fits should yield more convenient structure functions in this case. So since the fits seem to be quite reasonable and the magnetic moment μ given in table 4.1 is in quite good agreement with experimental data other even more recent approaches considering this isotope are discarded.

The second remark worth mentioning is the authors' comment regarding uncertainties in these calculations. To be more precise they compared uncertainties in the WIMP-nucleon couplings arising from the determination of the parameters $\Delta^{p,n}q$ which are quite large to those due to the difficult modeling of nuclear shell processes. They argue that the uncertainties due to the former are usually much

experiment	isotope	method	$\langle S_p \rangle$	$\langle S_n \rangle$	μ	μ_{exp}
CDMS	^{29}Si	—	-0.002	0.13	-0.50	-0.555
	^{73}Ge	—	0.030	0.378	-0.920	-0.879
XENON10	^{129}Xe	Bonn A	0.028	0.359	-0.983 (-0.634)	-0.788
	^{129}Xe	Nijmegen II	0.0128	0.300	-0.701 (-0.379)	
	^{131}Xe	Bonn A	-0.009	-0.227	0.980 (0.637)	0.692
	^{131}Xe	Nijmegen II	-0.012	-0.217	0.979 (0.347)	
	^{131}Xe	QTDA	-0.041	-0.236	0.70	

Table 4.1: Summary of the expectation values of the proton and neutron spins within the nucleus $\langle S_p \rangle$ and $\langle S_n \rangle$ as well as the magnetic moments μ computed using nuclear shell models. All models relevant for this work are listed. If several models are considered for one isotope they are labeled appropriately. In the cases of the Bonn A and the Nijmegen II methods for the xenon isotopes two magnetic moments are given in the associated paper. As explained in the text the values in parenthesis belong to the use of effective g-factors. The last column presents the respective measured magnetic moments. Of course good agreement of the values in the last two columns indicates a reliable nuclear model. (Values taken from [22].)

larger than those of the latter. So even though the $\Delta^{p,n}q$'s are measured to a much better precision today it should be kept in mind that they still play a crucial role considering uncertainties.[2]

Even though the former paper also addressed modeling the nucleus of ^{73}Ge [27] using a hybrid model published in 1994 is commonly considered to be more adequate especially because the authors did not have to introduce a quenching factor to bring their computed value of the magnetic moment μ in good agreement with the measured value. As cognizable from table 4.1 the achieved agreement makes the computations look reliable. The oscillation parameter is defined in the same way as in [26] and yields

$$b = \sqrt[6]{A}\ \text{fm} \approx 2.04\ \text{fm} \tag{4.21}$$

in the case of ^{73}Ge. The three spin strucure functions were fitted using sixth-order

[2] The authors assume an error of ± 0.08 on all $\Delta^{p,n}q$'s which should be compared to those given in table 3.3.

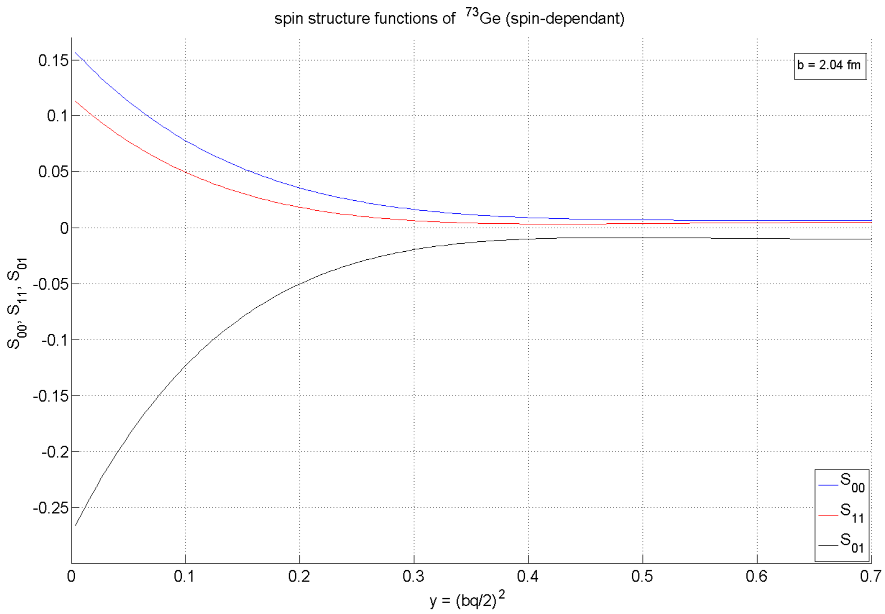

Figure 4.3: Spin structure functions of ^{73}Ge as published in [27].

polynomials which finally led to

$$\begin{aligned} S_{00}(y) &= 0.1606 - 1.1052y + 3.2320y^2 - 4.9245y^3 \\ &\quad + 4.1229y^4 - 1.8016y^5 + 0.3211y^6 \\ S_{11}(y) &= 0.1164 - 0.9228y + 2.9753y^2 - 4.8709^3 \\ &\quad + 4.3099y^4 - 1.9661y^5 + 0.3624y^6 \\ S_{01}(y) &= -0.2736 + 2.0374y - 6.2803y^2 + 9.9426y^3 \\ &\quad - 8.5710y^4 + 3.8310y^5 - 0.6948y^6 \end{aligned} \tag{4.22}$$

The authors do not mention an upper limit on the validity of these fits shown in figure 4.3. They just state that they should be useful "over the full range of relevant momenta".

Considering both xenon isotopes ^{129}Xe and ^{131}Xe the most recent computations even though ten years old are given in [28]. The authors accomplished these and two other nuclear shell model calculations which however are not of interest here using two different Hamiltonians describing the nuclei. These Hamiltonians are based on nucleon-nucleon potentials one named Bonn A the other one Nijmegen II which is the reason to use the terms Bonn A method and Nijmegen II method to distinguish them from each other.

In this paper the oscillation parameter is defined slightly different from the two cases before namely

	^{129}Xe					
	Bonn A			Nijmegen II		
k	C_k for S_{00}	C_k for S_{01}	C_k for S_{11}	C_k for S_{00}	C_k for S_{01}	C_k for S_{11}
0	0.0713238	−0.12166	−2.05825	0.046489	−0.0853786	−1.28214
1	−0.344779	0.644351	1.80756	−0.225507	0.453434	1.09276
2	0.755895	−1.52732	−1.27746	0.499045	−1.06546	−0.712949
3	−0.933448	2.02061	0.654589	−0.622439	1.3867	0.314894
4	0.690061	−1.57689	−0.221971	0.46361	−1.0594	−0.0835104
5	−0.302476	0.723976	0.0454635	−0.20375	0.47576	0.0105933
6	0.0765282	−0.190399	−0.00425694	0.0510851	−0.122077	0.000233709
7	−0.0103169	0.0263823	−0.000136779	−0.00670516	0.0164292	−0.000243292
8	0.000573919	−0.00148593	0.00004396	0.00035659	−0.000894498	0.0000221666
9	0.0	0.0	2.11016	0.0	0.0	1.32136

	^{131}Xe					
	Bonn A			Nijmegen II		
k	C_k for S_{00}	C_k for S_{01}	C_k for S_{11}	C_k for S_{00}	C_k for S_{01}	C_k for S_{11}
0	0.0296421	−0.0545474	0.0250994	0.0277344	−0.0497844	0.0223447
1	−0.133427	0.271757	−0.137716	−0.124487	0.247247	−0.122063
2	0.377987	−0.723023	0.366609	0.328287	−0.632306	0.319493
3	−0.579614	1.0545	−0.53851	−0.481399	0.896416	−0.466949
4	0.578896	−0.971333	0.492545	0.475646	−0.816445	0.428767
5	−0.345562	0.538422	−0.269903	−0.285177	0.452352	−0.236789
6	0.115952	−0.168988	0.0836943	0.0968193	−0.142686	0.0740837
7	−0.0201178	0.027416	−0.0133959	−0.0170957	0.0233463	−0.0119668
8	0.00141793	−0.00180527	0.000868668	0.00123738	−0.00156293	0.000787042
9	0.0	0.0	0.0	0.0	0.0	0.0

Table 4.2: Coefficients used in (4.25) fitting the spin structure functions for ^{129}Xe and ^{131}Xe. The Bonn A as well as the Nijmegen II method is considered. (Values taken from [28].)

$$b = \sqrt{\frac{41.467}{\hbar\omega}}\ \text{fm} = 2.29\ \text{fm} \tag{4.23}$$

where $\hbar\omega$ is given by

$$\hbar\omega = 45A^{-\frac{1}{3}} - 25A^{-\frac{2}{3}}\ \text{MeV}\ . \tag{4.24}$$

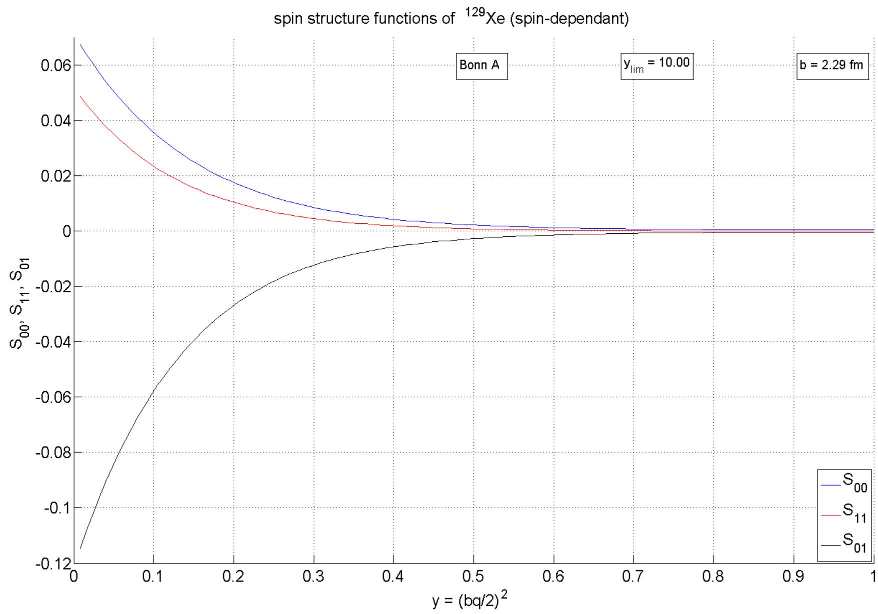

Figure 4.4: Spin structure functions of ^{129}Xe as published in [28] using the Bonn A method.

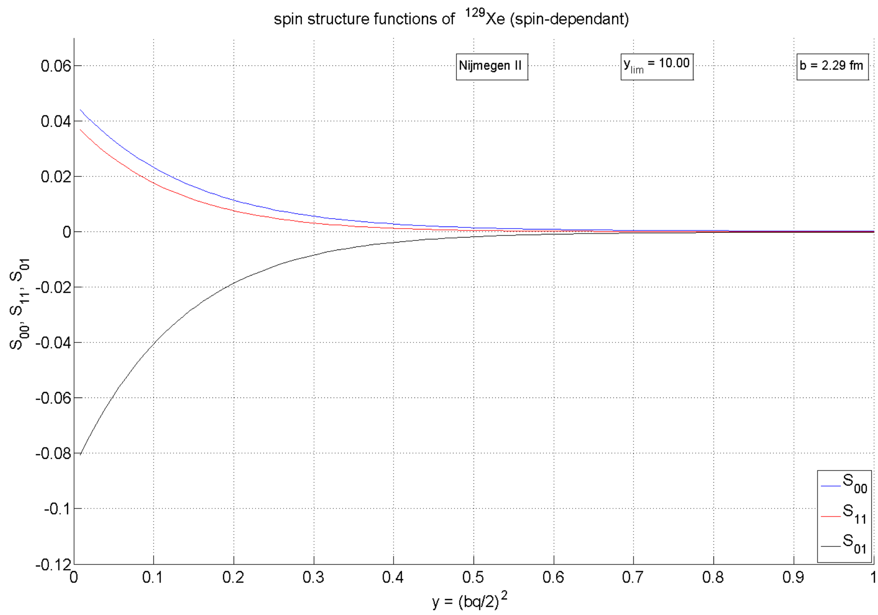

Figure 4.5: Spin structure functions of ^{129}Xe as published in [28] using the Nijmegen II method.

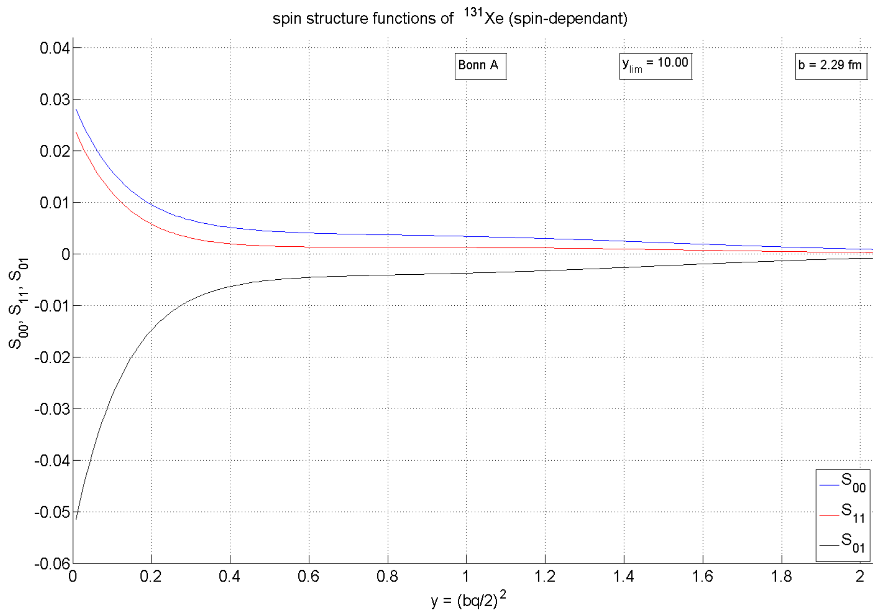

Figure 4.6: Spin structure functions of ^{131}Xe as published in [28] using the Bonn A method.

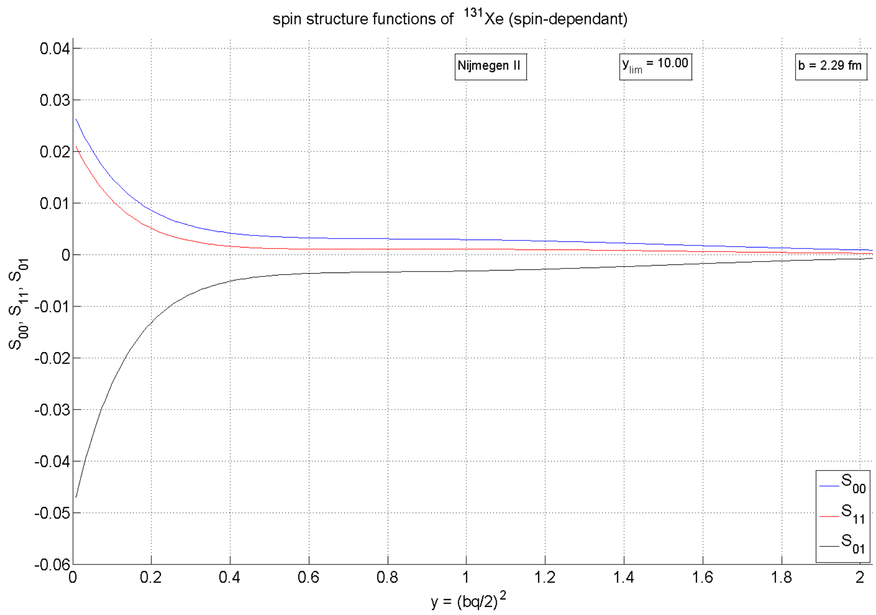

Figure 4.7: Spin structure functions of ^{131}Xe as published in [28] using the Nijmegen II method.

The result from (4.23) is valid for both isotopes up to the quoted accuracy. The fits were performed using eigth-order polynomials multiplied by a damping factor given by e^{-2y} and introducing another singular pole term in the case of ^{129}Xe necessary to handle the so called Goldberger-Trieman term arising from $\mathcal{L}_L^5$ in (4.4). So the fitted spin structure functions valid according to the authors up to $y = 10$ have the form

$$S_{ij}(y) = \left(\sum_{k=0}^{8} C_k y^k + \frac{C_9}{1+y} \right) e^{-2y} \tag{4.25}$$

with the corresponding coefficients given in table 4.2 and the plots shown in the figures 4.4, 4.5, 4.6 and 4.7. In order to obtain a better agreement with the experimentally determined magnetic moment the authors introduced effective g-factors given by

$$g_n^s = -2.87 \qquad g_n^l = -0.1 \qquad g_p^s = 4.18 \qquad g_p^l = 1.1 \tag{4.26}$$

which should be compared to (4.17) yielding an effective magnetic moment.[3] Table 4.1 contains the magnetic moments computed the usual way and using effective g-factors as well with the latter given in parenthesis. Obviously the Bonn A method yields a better agreement with the experimental value of μ considering the quenched results which is the reason for adopting this method throughout most parts of the upcoming analysis.

However there is another approach available for ^{131}Xe published in [29] which though from 1991 and hence using a less accurate model of the nucleus reproduces the magnetic moment with a higher precision as evident from table 4.1. Therefor the authors of [28] admit that it is not clear which calculation should be prefered. In this work the more recent computations are prefered. However due to the mentioned problems in the accomplishment of setting limits on WIMP-nucleon couplings this approach using the Quasiparticle Tamm-Dancoff approximation (QTDA) and henceforth called QTDA method is considered, too, but only for the computations aimed at setting limits.[4]

Unfortunately in [29] there is only a plot available showing the spin structure functions but no fitted analytic functions are given. However a table including some of the corresponding function values is given in the already mentioned review article [23]. It is reproduced in table 4.3. In order to obtain analytic spin structure functions functions of the form

[3] However according to the authors no quenching should be applied to the WIMP-nucleon couplings.

[4] Admittedly as already mentioned this approach does not solve the problem either.

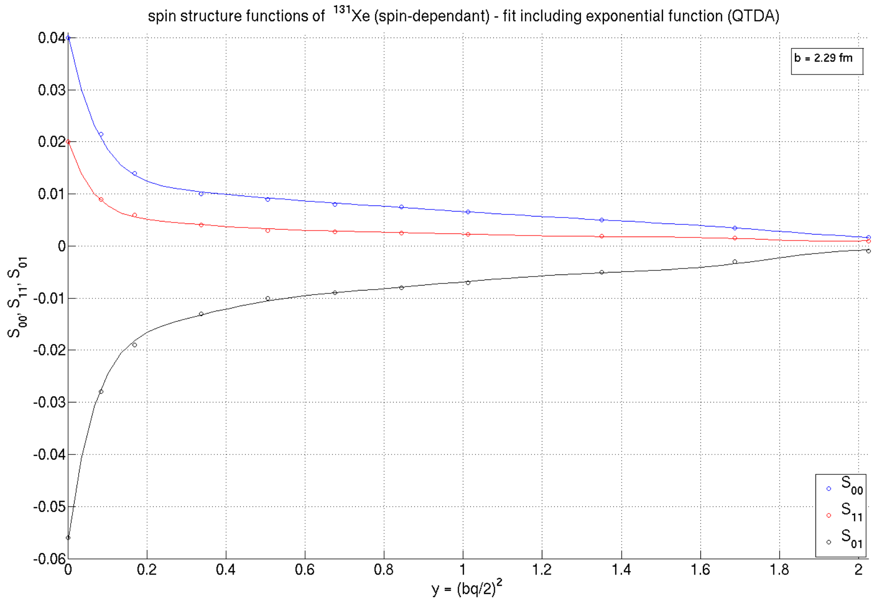

Figure 4.8: Spin structure functions of ^{131}Xe as published in [29] using the QTDA method.

q^2	S_{00}	S_{11}	S_{01}
0	0.04	0.020	−0.056
0.0025	0.0215	0.009	−0.028
0.005	0.014	0.006	−0.019
0.01	0.01	0.004	−0.013
0.015	0.009	0.003	−0.01
0.02	0.008	0.0027	−0.009
0.025	0.0075	0.0025	−0.008
0.03	0.0066	0.0023	−0.007
0.04	0.005	0.0019	−0.005
0.05	0.0035	0.0015	−0.003
0.06	0.0017	0.001	−0.001

	^{131}Xe – QTDA		
k	C_k for S_{00}	C_k for S_{01}	C_k for S_{11}
0	0.040652	−0.056981	0.020277
1	−0.29594	0.47334	−0.19368
2	1.5088	−2.7468	1.1657
3	−3.9086	8.2959	−3.6222
4	6.0746	−14.528	6.452
5	−5.7049	14.975	−6.7166
6	3.1674	−8.9254	4.0253
7	−0.95147	2.8295	−1.2806
8	0.11845	−0.36729	0.16692

Table 4.3: Left: Function values for the spin structure functions for ^{131}Xe computed using the QTDA method considering the dependence on the squared momentum transfer q^2. (Values taken from [23].) Right: Coefficients obtained by fitting (4.27) to the values from the left table.

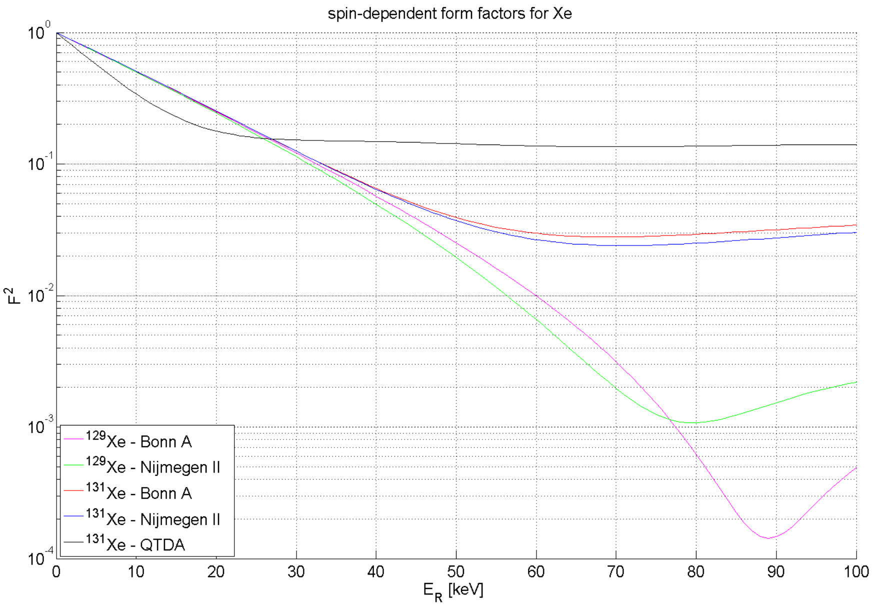

Figure 4.9: Squared spin-dependent form factors for ^{129}Xe and ^{131}Xe using the WIMP-nucleon couplings from the UED model given in (3.26). Obviously there is no big difference in any of these formfactors up to about 30 keV recoil energy except for the computation for ^{131}Xe using the QTDA method.

$$S_{ij}(y) = \left(\sum_{k=0}^{8} C_k y^k \right) e^{-2y} \tag{4.27}$$

are fitted to these values in a least square sense. So they are similar to (4.25) but neglecting the pole term. However tests including this term did not yield severe differences. The result of the fitting procedure is shown in figure 4.8 whereas the obtained coefficients are given in table 4.3. It should be mentioned that again definition (4.23) is used for the oscillation parameter.

Figure 4.9 shows a comparison of spin-dependent squared xenon formfactors for both considered isotopes and all explained methods using the WIMP-nucleon couplings from the UED model given in (3.26). Substituting formula (4.13) for the denominator in the definition of F^2 has not been accomplished in order to respect the normalization constraint.

Finally the figures 4.10, 4.11 and 4.12 show all form factors for all targets used in the following computations. In the case of xenon the Bonn A method is applied for the spin-dependent form factors. In figure 4.10 an upper limit on the validity of the spin-dependent form factor is shown whereas there is no limit in figure 4.11 and figure 4.12. This is due to the fact that there is no limit given in the paper considering ^{73}Ge and that the limit in the case of both xenon

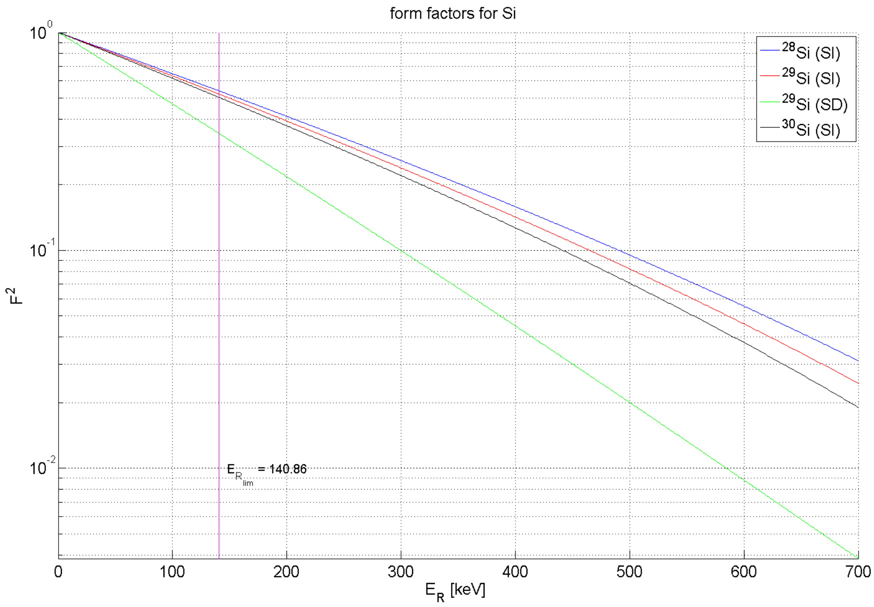

Figure 4.10: Squared spin-independent and spin-dependent form factors for all isotopes in natural silicon. The WIMP-nucleon couplings given in (3.26) are used for computing the spin-dependent form factors. $E_{\mathrm{R_{lim}}}$ denotes the upper limit of the validity of the fits to the spin structure functions and hence the validity of the corresponding spin-dependent form factor.

isotopes given by $y = 10$ is well beyond the scale shown. However the gap for the spin-dependent form factor of ^{129}Xe between approximately 420 and 520 keV arising from negative values implies that this limit might be considered as being optimistically high. Nevertheless the CDMS experiment only analyzes events up to a recoil energy of 100 keV whereas the XENON10 experiment only uses data up to 26.9 keV. Therefor it looks like using the given form factors is quite convenient at least for the WIMP-nucleon couplings of the UED model.

Besides in principle it should be possible to compute F^2 for any values of the WIMP-nucleon couplings a_p and a_n by inserting the obtained spin structure functions in (4.15) regarding the translation (4.14) and finally evaluating (4.2). However this turns out to be difficult for certain parameters.

Moreover it should be pointed out that the main difference from the spin-independent case apart from the fact that all target nuclei must be considered separately using very complicated nuclear shell models is that the form factors themselves depend on the WIMP-nucleon couplings. This will turn out to complicate the calculations of limits on cross sections and these couplings significantly.

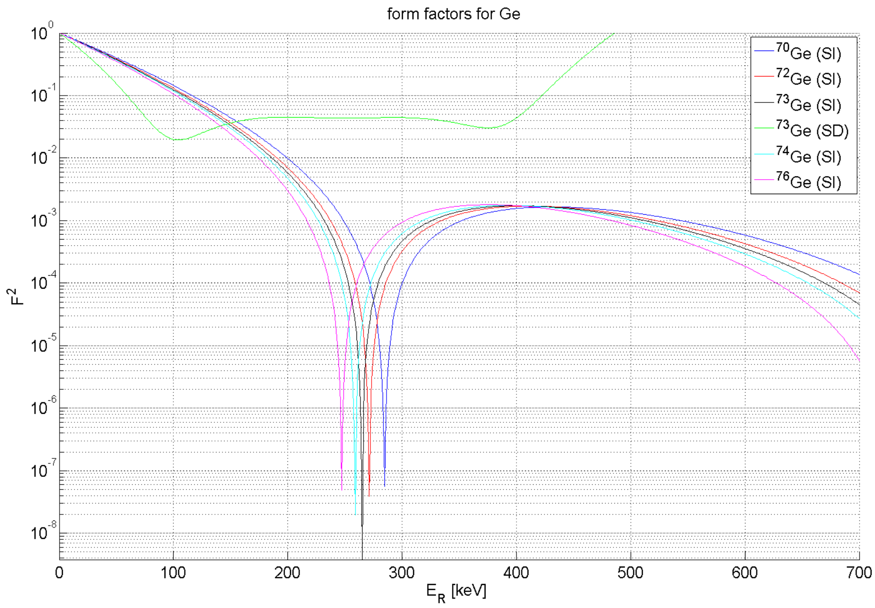

Figure 4.11: Squared spin-independent and spin-dependent form factors for all isotopes in natural germanium. WIMP-nucleon couplings taken from (3.26).

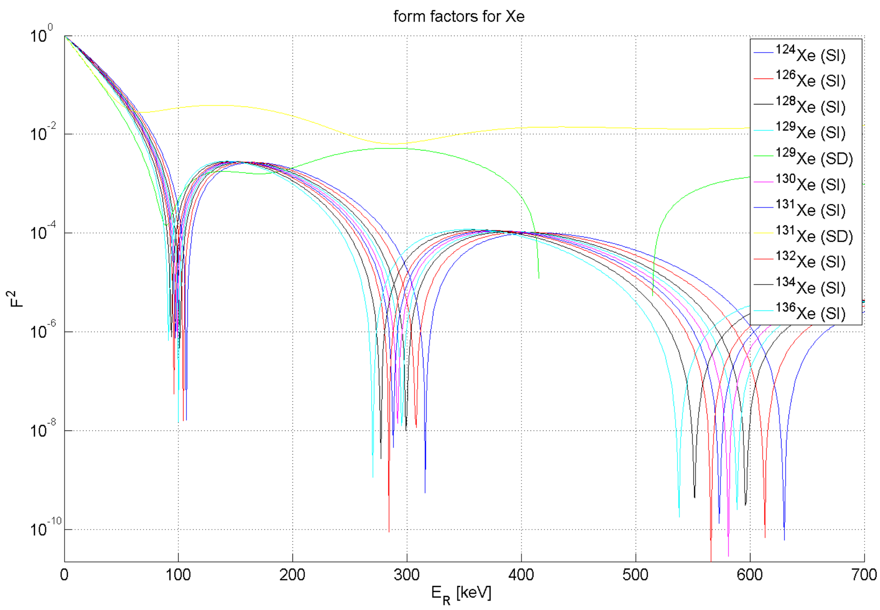

Figure 4.12: Squared spin-independent and spin-dependent form factors for all isotopes in natural xenon. WIMP-nucleon couplings taken from (3.26).

Chapter 5

Event rates from $B^{(1)}$-nuclei scattering

After these extensive investigations of the spin-independent and spin-dependent $B^{(1)}$-nuclei zero-momentum transfer cross sections and appropriate form factors to include the finite-momentum transfer all necessary information are available to compute theoretical predictions for expected event rates. The standard reference for this procedure is [24] which gives an excellent summary of this topic.

To come to grips with this problem it is necessary to make certain assumptions about the dark matter halo. It is a common procedure to assume an isothermal and isotropic sphere of WIMP gas obeying a yet to define velocity dispersion. Unfortunately reliability of this assumption is not secured at all. However detailed analysis shows that the uncertainties in modelizing the halo are rather small compared for example to theoretical uncertainties arising from calculations of the WIMP-nucleon cross sections.

However before actually proceeding with this issue it is convenient to discuss two other short topics first because they are important for the following calculations.

The first one is the velocity of the earth with respect to the galactic rest frame v_E which is its relative velocity to the motionless dark matter halo introduced above at the same time. In fact there are three contributions to this velocity namely the galactic rotation velocity $\vec{v}_r$, the velocity of the sun with respect to the moving galactic disc $\vec{v}_s$ which can be measured by investigating its motion relative to nearby stars and finally the velocity of the earth arising from its motion around the sun $\vec{v}_{orb}$. So it can be written as

$$\vec{v}_E = \vec{v}_r + \vec{v}_s + \vec{v}_{orb} \; . \tag{5.1}$$

Using galactic coordinates the first two contributions are given by

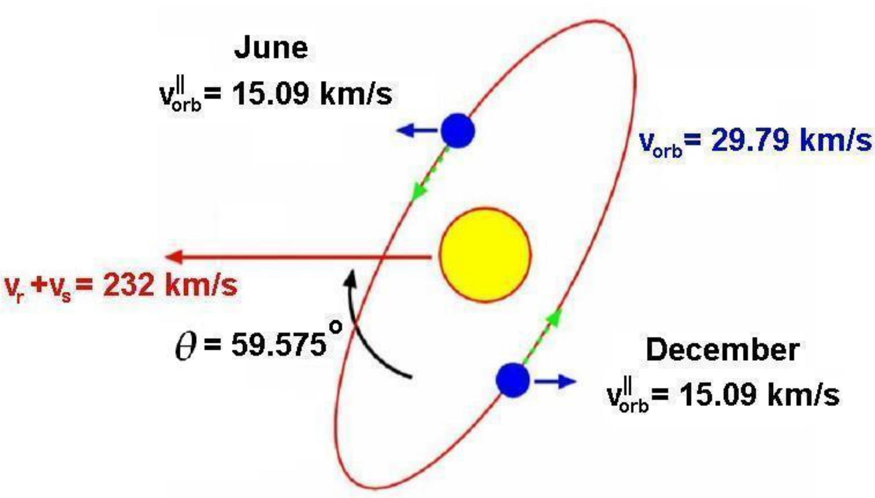

Figure 5.1: Motion of the earth around the sun. The galactic plane is perpendicular to the surface of the paper containing the vector denoting the velocity of the sun. The angle θ between the earth orbital plane and the galactic plane has to be taken into account to obtain the projection of the earth's velocity in the direction of the sun's velocity which yields its contribution to the dominant y-coordinate of $\vec{v}_E$. (Figure with some modifications taken from [30].)

$$\vec{v}_r = \begin{pmatrix} 0 \\ 220 \\ 0 \end{pmatrix} \frac{\mathrm{km}}{\mathrm{s}} \qquad \text{and} \qquad \vec{v}_s = \begin{pmatrix} 9 \\ 12 \\ 7 \end{pmatrix} \frac{\mathrm{km}}{\mathrm{s}} \,. \tag{5.2}$$

Since the y-coordinate of $\vec{v}_r$ is so large this component dominates and the others can be neglected. The last contribution is determined by the orbital velocity of the earth around the sun given by $v_{orb} = 29.79$ km/s. However as just mentioned only the y-component is of interested here. Therefor taking the angle between the earth orbital plane and the galactic plane into account which is given by $\theta = 59.575°$ the velocity of the earth in the galactic frame is given by

$$v_E(t) = v_r + v_s + v_{orb} \cos\theta \cos\left(2\pi \frac{t - t_0}{T}\right) \tag{5.3}$$

where the subscript y has been droped. t_0 denotes the day in a year corresponding to the 2$^{\text{nd}}$ June so $t_0 = 152.5$ and T denotes the number of days in a year so $T = 365.25$. Evaluating this expression yields

$$v_E(t) = 232 + 15.09 \cos\left(2\pi \frac{t - 152.5}{365.25}\right) \frac{\mathrm{km}}{\mathrm{s}} \tag{5.4}$$

which is illustrated in figure 5.1. Obviously this oscillation leads to a modulation of the mean velocity $\sim \pm 6.5\%$. It should be pointed out that the mean velocity of 232 km/s is burdened with a quite high degree of uncertainty of about ± 30 km/s whereas the 15.09 km/s amplitude of the modulation has negligible uncertainty. Moreover note that the modulation is not exactly sinusoidal.

In order to investigate effects caused by this annual modulation which is accomplished in the next chapter t is taken as a free parameter. However to compare theoretical predictions to the results of measurements from CDMS and XENON10 it is more useful to define a mean earth velocity $\langle v_E \rangle$.

In the case of the CDMS experiment all data of the runs 118 and 119 were available which made it possible to compute a live time weighted mean by

$$\langle v_E \rangle = \frac{\sum\limits_n v_E(t_n)\, l_n}{\sum\limits_n l_n} = 232.2 \frac{\mathrm{km}}{\mathrm{s}} \tag{5.5}$$

where the index n runs over all detected events and t_n and l_n denote the event time and the live time of the n$^{\text{th}}$ event respectively. The result which is almost equal to the mean of v_E averaged over a year given by 232 km/s is plausible considering the fact that run 118 lasted from October 11, 2003 until January 11, 2004 as stated in [31] whereas run 119 took data between March 25, 2004 and August 8, 2004 as stated in [32].

Considering the XENON10 experiment only the dates of the beginning and the end of the last run were available. According two [20] data were aquired between October 6, 2006 and February 14, 2007. Hence an average velocity was obtained by evaluating

$$\langle v_E \rangle = \frac{1}{t_{run}} \int_{t_{run}} v_E(t)\, \mathrm{d}t = \frac{1}{131.25} \left(\int_{279.5}^{365.25} v_E(t)\, \mathrm{d}t + \int_0^{45.5} v_E(t)\, \mathrm{d}t \right) = 220.1 \frac{\mathrm{km}}{\mathrm{s}}\ . \tag{5.6}$$

Obviously $t_{run} = 131.25$ denotes the duration of the run while 279.5 and 45.5 represent the day in the year of its beginning and its ending. The just obtained results are summarized in figure 5.2.

The second topic is a short discussion of the local dark matter density ρ_W which is of importance in the upcoming computations. Several groups have tried to restrict its value. An example is given in [34]. The authors started by constructing a large variety of models based on some fundamental ingredients like a bar or an asymmetric bulge, a disk with certain properties and isothermal cold dark matter and MACHO halos with finite radii and ellipsoidal density profiles. Then several parameters like the bulge mass and the halo radii were varied. Finally all models were rejected which did not give rise to certain measured values of for example

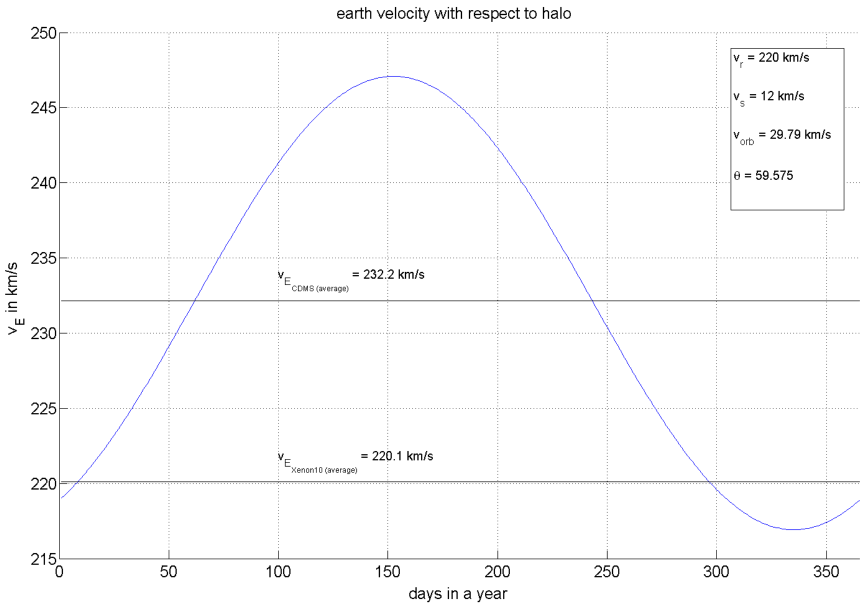

Figure 5.2: Sinusodial dependence of the earth velocity with respect to the motionless dark matter halo v_E on the day in the year. Besides the mean velocities of both considered experiments are shown.

the galactocentric distance of 7.0 kpc to 9.0 kpc or the local rotation speed of 200 km/s to 240 km/s. Afterwards the local densities of the remaining viable models were investigated. Finally the authors came to the conclusion that the total local dark matter density is expected to be in the range of

$$0.3\,\frac{\mathrm{GeV}}{\mathrm{cm}^3} < \rho_W < 0.7\,\frac{\mathrm{GeV}}{\mathrm{cm}^3}\,. \tag{5.7}$$

Since only the amount of non-baryonic dark matter is of interest here and a certain fraction of MACHOS lowers the density $\rho_W = 0.3\ \mathrm{GeV/cm}^3$ is considered as the dark matter density throughout all computations.[1] Even though it should be kept in mind that this value is burdened with considerable uncertainty and model-dependence other groups achieve similar results. Another important remark is that it is very likely that more than one particle constitute the non-baryonic dark matter which would further lower ρ_W. Finally it is important to know that there are several estimates considering the local dark matter density $\rho_W = m_W\, n_0$ yielding similar results whereas neither the WIMP mass m_W nor the particle number density n_0 are separately known.

After these annotations on the earth velocity with respect to the dark matter

[1]However remember that flattening of the halo leads to increasing values pf ρ_W.

halo and the local halo density proceeding with calculations of the expected event rates is rather easy. So considering the dark matter halo one has to assume a certain velocity distribution. Usually a distribution of the form

$$f(\vec{x}, \vec{v}, \vec{v}_E) \sim e^{-\frac{\frac{1}{2} m_W (\vec{v}+\vec{v}_E)^2 + m_W \phi(\vec{x})}{k_B T}} \tag{5.8}$$

with the velocity of the WIMPs $\vec{v}$ in the earth rest frame which is the target rest frame at the same time and the just introduced velocity of the earth with respect to the motionless galactic halo $\vec{v}_E$ is considered. Moreover m_W and T denote the WIMP mass and temperature and k_B not surprisingly the Boltzmann constant. Of course the WIMP will be identified with the $B^{(1)}$ below yielding $m_W = m_{B^{(1)}}$. However since the way event rates are computed is completely general this identification will be imposed later. Apart from that the velocity distribution contains the gravitational potential $\phi(\vec{x})$ but since this position dependent part is fixed at a certain location it can be incorporated in the normalization. Hence introducing the so-called characteristic velocity v_0 which is usually assumed to be equal to the galactic rotation velocity yieding $v_0 = v_r = 220$ km/s by

$$\frac{1}{2} m_W v_0^2 = k_B T \tag{5.9}$$

(5.8) reduces to the well known Maxwell-Boltzmann distribution

$$f(\vec{v}, \vec{v}_E) \sim e^{-\frac{(\vec{v}+\vec{v}_E)^2}{v_0^2}} \ . \tag{5.10}$$

One important annotation has to be made before continuing the investigations. As obvious from (5.10) the velocity distribution is isotropic in the galactic rest frame considering the galactocentric WIMP velocity $\vec{v} + \vec{v}_E$. However this distribution does not extract to infinity. Rather a cut-off which is also isotropic in the galactic rest frame has to be introduced in order to take care of the fact that WIMPs with a high velocity and accordingly high kinetic energy are able to escape the gravitational potential so that they would not contribute to the dark matter halo. This cut-off is defined by

$$|\vec{v} + \vec{v}_E| < v_{esc} \tag{5.11}$$

with the so-called escape velocity v_{esc}. A recent value for this quantity is given in [33]. The collaboration states a median likelihood of 544 km/s and a 90% confidence interval of 498 km/s $< v_{esc} <$ 608 km/s. In the following computations $v_{esc} = 544$ km/s is used which is significantly lower than earlier estimates that were mostly around 600 km/s or even higher so close to the upper limit of the new results. However it should be mentioned that theoretical predictions were

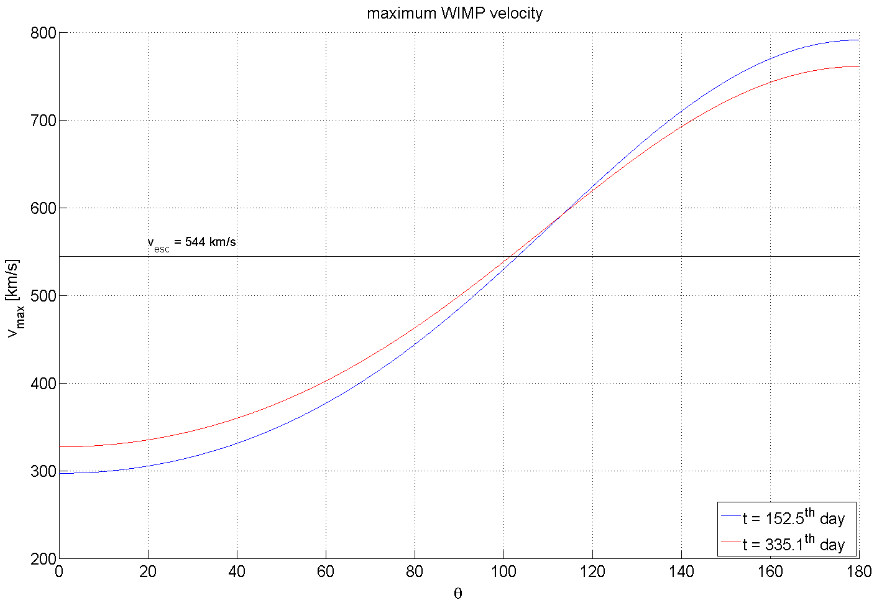

Figure 5.3: Dependence of v_{max} on the scattering angle in the galactic rest frame for the 2nd June and the 2nd December. Depending on θ v_{max} varies enormeously.

computed using $v_{esc} = 600$ km/s before this recent paper was brought to attention and differences were only slight. This is due to the fact that $v_{esc} \simeq 2.5\, v_0$ and hence its actual value only influences WIMPs with high velocities contributing to the Maxwell tail. Keeping in mind that due to its definition in (5.9) v_0 also corresponds to the most probable velocity it is clear that these particles give rise to a exiguous contribution to the expected spectrum computed below.

Since the maximum allowed WIMP velocity in the rest frame of the earth-borne target v_{max} is needed below (5.11) should be further investigated. The result is given by

$$v_{max}(\theta, t) = \sqrt{v_{esc}^2 - v_E^2(t)\,(1 - \cos^2\theta)} - v_E(t)\cos\theta \tag{5.12}$$

with v_E given in (5.4) and θ denoting the angle between $\vec{v}$ and $\vec{v}_E$ in this short section. So θ corresponds to the scattering angle in the galactic rest frame and not in the center of mass frame. Figure 5.3 displays (5.12) as a function of θ for the 2nd June ($t = t_0 = 152.5$) and the 2nd December ($t = 335.1$) which according to (5.4) and figure 5.2 correspond to the days in a year with the highest and lowest value of v_E. Obviously the dependence on the day in a year is only slight whereas the maximum possible velocity of a WIMP interacting with a target nucleus severly depends on the scattering angle θ.

In order to use v_{max} in the computations below considering the CDMS and

XENON10 experiment it is useful to define a mean maximum velocity $\langle v_{max} \rangle$ similar to $\langle v_E \rangle$. This is accomplished by substituting $v_E(t)$ in (5.12) by $\langle v_E \rangle$ given in (5.5) in the case of CDMS and (5.6) in the case of XENON10. Afterwards an averaging over the scattering angle is excecuted so that $\langle v_{max} \rangle$ is definded by

$$\langle v_{max} \rangle = \frac{1}{\pi} \int_0^{\pi} \left(\sqrt{v_{esc}^2 - \langle v_E \rangle^2 \left(1 - \cos^2 \theta\right)} - \langle v_E \rangle \cos \theta \right) \mathrm{d}\theta \tag{5.13}$$

leading to $\langle v_{max} \rangle = 518.3$ km/s for the CDMS experiment and $\langle v_{max} \rangle = 521.0$ km/s for the XENON10 experiment.

In order to actually adress the problem of event rates it is necessary to take a short look at the kinematics which is very instructive at the same time since it yields an idea about the energies involved in the scattering processes. This can be accomplished by considering simple Newtonian mechanics. Obviously this assumption is valid since only WIMPs with a velocity up to v_{esc} are considered. So assuming the WIMP-nuclei interaction to be a simple scattering process applying energy and momentum conservation directly yields

$$E_R = \frac{1}{2} Er(1 - \cos \theta) \tag{5.14}$$

with the WIMP energy E, the recoil energy E_R and the so-called kinematic factor

$$r = \frac{4 m_W m_T}{(m_W + m_T)^2} \ . \tag{5.15}$$

Moreover it is important to know that in this context θ denotes the scattering angle in the centre-of-mass frame. Since the non-relativistic limit is considered E is simply given by

$$E = \frac{1}{2} m_W v^2 \ . \tag{5.16}$$

So what is the magnitude of the expected recoil energy? This can be estimated by making some appropriate assumptions about the WIMP mass and its velocity. Obvioulsy a mass of $m_W = 500$ GeV consistent with the results from relic density computations shown in figure 2.6 and a velocity of $v = v_0 = 220$ km/s seems quite reasonable. Evaluating (5.16) yields an energy carried by the WIMP of about $E = 135$ keV. Considering scattering from a ^{73}Ge nuclei with $m_T = 68$ GeV yields a kinematic factor of $r = 0.4$ and hence according to (5.14) an expected recoil energy of about $E_R \simeq Er = 57$ keV. Obviously the expected recoil energy range is of order ~ 10 keV and even smaller for lighter WIMPs.

According to (5.14) and (5.16) the maximum recoil energy $E_{R_{max}}$ is given by

$$E_{R_{max}} = \frac{1}{2} m_W v_{max}^2 r \tag{5.17}$$

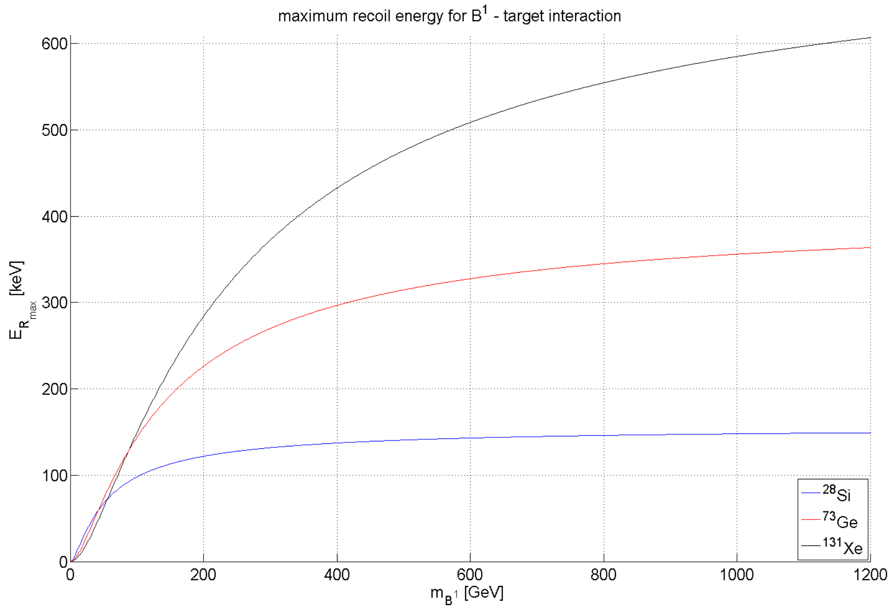

Figure 5.4: Dependence of $\langle E_{R_{max}} \rangle$ on the WIMP mass for ^{28}Si, ^{73}Ge and ^{131}Xe. Obviously it is increasing rapidly with m_W finally converging against $2\langle v_{max} \rangle^2 m_T$. Of course even though the x-axis is labeled $m_{B(1)}$ due to the fact that the UED model is considered in the actual computations below these results are clearly model independent.

with v_{max} given in (5.12). Introducing an averaged maximum recoil energy by substituting v_{max} with $\langle v_{max} \rangle$ yields the result shown in figure 5.4 where the WIMP mass dependence of $\langle E_{R_{max}} \rangle$ is compared for one silicon, one germanium and one xenon isotope. It should be kept in mind that this energy has been computed by using the averaged earth velocity and additionally averaging over the angle of incidence in the galactic rest frame meaning that there is a fraction of WIMPS which can give rise to a higher maximum recoil energy especially those which hit the detector in a head-on collision. It will be discussed below that this might be important for WIMPS with low masses.

After tantalizing the reader for such a long time the event rates are about to be computed in the upcomig paragraph without further interruptions.

The WIMP density dn in the halo can be written as

$$\mathrm{d}n = \frac{n_0}{k_1} f(\vec{v}, \vec{v}_E) \mathrm{d}^3 v \tag{5.18}$$

with the velocity distribution $f(\vec{v}, \vec{v}_E)$ given in (5.10). Besides n_0 denotes the mean dark matter partcle density given by

$$n_0 = \frac{\rho_W}{m_W} \tag{5.19}$$

obeying

$$n_0 = \int_0^{v_{max}} \mathrm{d}n \tag{5.20}$$

with $\rho = 0.3\ \mathrm{GeV/cm}^3$ while k_1 denotes the normalization constant. This constant is obviously given by

$$k_1 = \int_{|\vec{v}|<v_{max}(\theta)} f(\vec{v}, \vec{v}_E)\mathrm{d}^3 v = \int_0^{v_{max}(\theta)} \mathrm{d}v\, v^2 \int \mathrm{d}\Omega_v\, e^{-\frac{(\vec{v}+\vec{v}_E)^2}{v_0^2}} \tag{5.21}$$

which is rather complicated to evaluate because v_{max} defined in (5.12) is a function of $\theta\sphericalangle(\vec{v}, \vec{v}_E)$. However remembering that the velocity distribution is isotropic in the galactic rest frame and the corresponding definition of the cut-off given in (5.11) it is possible to avoid this difficult integration because obviously k_1 can also be computed evaluating

$$k_1 = \int_{|\vec{v}+\vec{v}_E|<v_{esc}} f(\vec{v}, \vec{v}_E)\mathrm{d}^3|\vec{v}+\vec{v}_E| = \int_0^{v_{esc}} \mathrm{d}|\vec{v}+\vec{v}_E|\, |\vec{v}+\vec{v}_E|^2 \int \mathrm{d}\Omega_v\, e^{-\frac{(\vec{v}+\vec{v}_E)^2}{v_0^2}} \,. \tag{5.22}$$

Since v_{esc} is constant it is easy to evaluate this integral which leads to

$$k_1 = k_0 \left[\mathrm{erf}\left(\frac{v_{esc}}{v_0}\right) - \frac{2}{\sqrt{\pi}} \frac{v_{esc}}{v_0} e^{-\frac{v_{esc}^2}{v_0^2}} \right] \tag{5.23}$$

where k_0 is defined in the same way as k_1 but with the integration evaluated for $v_{esc} = \infty$ which leads to

$$k_0 = \sqrt{\pi}\, \pi\, v_0^3 \,. \tag{5.24}$$

Besides erf denotes the so-called error function defined as

$$\mathrm{erf}(x) = \frac{2}{\sqrt{\pi}} \int_0^x \mathrm{d}u\, e^{-u^2} \,. \tag{5.25}$$

The fact that (5.21) and (5.22) yield the same results which has been explicitely tested is in principle also clear since the particle density should be independent of the earth velocity.

The differential event rate $\mathrm{d}R$ considering zero-momentum transfer is defined as

$$\mathrm{d}R = \frac{N_0}{A_u}\,\sigma\, v\,\mathrm{d}n \tag{5.26}$$

which has to be multiplied by the appropriate form factors discussed extensively in the last chapter to incorporate the finite-momentum transfer. $N_0 = 6.022 \cdot 10^{26}\mathrm{kg}^{-1}$ denotes the Avogadro constant while A_u represents the atomic mass in u which in fact is quite similar to A. Theoretical predictions for the cross sections have already been extensively described. Inserting (5.18) in (5.26) $\mathrm{d}R$ can be rewritten in the form

$$\mathrm{d}R = R_0 \frac{k_0}{k_1}\frac{1}{2\pi v_0^4}\, v\, f(\vec{v}, \vec{v}_E)\mathrm{d}^3v \tag{5.27}$$

with

$$R_0 = \frac{2}{\sqrt{\pi}}\frac{N_0}{A_u}\frac{\rho_W}{m_W}\,\sigma\, v_0 \tag{5.28}$$

which in fact is the total event rate assuming $v_E = 0$, $v_{esc} = \infty$ and integrating over recoil energies from $E_R = 0$ to $E_R = \infty$. However in the following computations it is only used as a convenient abbreviation.

Taking a look at (5.14) and assuming isotropic scattering in the center of mass frame it can be assumed that recoils are uniformly distributed in E_R over the range from 0 to the maximum recoil energy given by $E\,r$. Thus the differential event rate with respect to the recoil energy is given by

$$\frac{\mathrm{d}R}{\mathrm{d}E_R} = \int_{E_{min}}^{E_{max}} \frac{1}{Er}\,\mathrm{d}R(E) = \frac{1}{E_0 r}\int_{v_{min}}^{v_{max}} \frac{v_0^2}{v^2}\,\mathrm{d}R(v) \tag{5.29}$$

with the θ-dependent maximum velocity v_{max} given in (5.12) and E_0 defined as the energy carried by a WIMP with velocity v_0

$$E_0 = \frac{1}{2} m_W v_0^2 \,. \tag{5.30}$$

Moreover v_{min} is defined as the minimum velocity leading to a certain recoil energy E_R which yields

$$v_{min} = \sqrt{\frac{2E_{min}}{m_W}} = \sqrt{\frac{E_R}{E_0 r}}\, v_0 \tag{5.31}$$

since $E_{min} = \frac{E_R}{r}$. Inserting (5.27) into (5.29) leads to

$$\frac{\mathrm{d}R}{\mathrm{d}E_R} = \frac{R_0}{E_0 r}\frac{k_0}{k_1}\frac{1}{2\pi v_0^2}\int_{v_{min}}^{v_{max}}\frac{1}{v}\,f(\vec{v},\vec{v}_E)\mathrm{d}^3v\,. \tag{5.32}$$

Unfortunately the occuring integration cannot be simplified similar to the way computing the normalization constant k_1. Therefor the θ-dependence of v_{max} has to be carefully regarded. Nevertheless evaluation of the occuring integral finally yields the rather complicated result

$$\frac{\mathrm{d}R}{\mathrm{d}E_R} = \frac{R_0}{E_0 r}\frac{k_0}{k_1}\left[\frac{\sqrt{\pi}}{4}\frac{v_0}{v_E}\left[\mathrm{erf}\left(\frac{v_{min}+v_E}{v_0}\right) - \mathrm{erf}\left(\frac{v_{min}-v_E}{v_0}\right)\right] - e^{-\frac{v_{esc}^2}{v_0^2}}\right] \tag{5.33}$$

which energy dependence is approximately exponentially decreasing. This behaviour is evident from considering $v_E = 0$ and $v_{esc} = \infty$ which yields

$$\frac{\mathrm{d}R}{\mathrm{d}E_R}\Big|_{v_E=0}^{v_{esc}=\infty} = \frac{R_0}{E_0 r}e^{\frac{E_R}{E_0 r}} \tag{5.34}$$

It should be kept in mind that this expression depends on the day in the year via v_E which will be further discussed below.

Since R_0 is proportional to σ the differential rate is proportional to σ as well which is the only part of (5.33) depending on the kind of interaction and hence being related to the assumed UED model described in former chapters. Therefor and especially for latter purposes considering limit computations it is convenient to define $\frac{\mathrm{d}R}{\mathrm{d}E_R}|_\sigma$ denoting the whole expression given in (5.33) except for the cross section σ. Using this abbreviation the spin-independent and if applicable the spin-dependent differential event rates including the form factors for finite-momentum transfer are given by

$$\frac{\mathrm{d}R}{\mathrm{d}E_R}|_{SI} = \sigma_{SI}\,\frac{\mathrm{d}R}{\mathrm{d}E_R}|_\sigma\,F_{SI}^2 \tag{5.35}$$

$$\frac{\mathrm{d}R}{\mathrm{d}E_R}|_{SD} = \sigma_{SD}\,\frac{\mathrm{d}R}{\mathrm{d}E_R}|_\sigma\,F_{SD}^2\,. \tag{5.36}$$

Hence the total differential event rate for scattering from a certain nuclei can be computed using

$$\frac{\mathrm{d}R}{\mathrm{d}E_R}|_{total} = \frac{\mathrm{d}R}{\mathrm{d}E_R}|_{SI} + \frac{\mathrm{d}R}{\mathrm{d}E_R}|_{SD} = \sigma_{SI}\,\frac{\mathrm{d}R}{\mathrm{d}E_R}|_\sigma\,F_{SI}^2 + \sigma_{SD}\,\frac{\mathrm{d}R}{\mathrm{d}E_R}|_\sigma\,F_{SD}^2\,. \tag{5.37}$$

Finally if the considered target consists of more than one element which is the case in both experiments since only natural silicon, germanium and xenon is used the respective abundances f have to be taken into account. Admittedly this is not really of crucial importance in the spin-independent case where all isotopes contribute since they are all quite similar considering a certain detector. So even though this accomplishment is much more import in the spin-dependent case and for example in the spin-independent case using a NaI target it should be incorporated for convenience. Marking the total differential event rates given by (5.37) with another label i to distinguish between different isotopes the total differential event rate for a whole target is given by

$$\frac{\mathrm{d}R}{\mathrm{d}E_R}\Big|_{total}^{target} = \sum_i f_i \, \frac{\mathrm{d}R}{\mathrm{d}E_R}\Big|_{total}^{i} \,. \tag{5.38}$$

Now the differential event rates can be evaluated. Just as a reminder the spin-dependent form factors are evaluated without substituting (4.13) in the denominator of (4.2) defining F^2. The averaged earth velocities $\langle v_E \rangle$ for both experiments are given in (5.5) and (5.6) for the CDMS and XENON10 experiment respectively. Moreover generally used values are $v_0 = 220$ km/s, $v_{esc} = 544$ km/s and $\rho_W = 0.3$ GeV/cm^3. The abundances used to evaluate (5.38) are given in table 3.4.

Besides some more information about the experiments is given in table 5.1 like the energy interval considered for the analysis, the minimal WIMP mass yielding recoil energies above the threshold, the exposure of the respective runs and the corresponding efficiencies. $\mathrm{q}_{\min}$ and $\mathrm{q}_{\max}$ denote the lower and upper limit of the energy interval considered for the analysis. So the former denotes the energy threshold. Moreover $m_{W_{\min}}$ labels the minimal WIMP masses yielding recoil energies above the threshold. They are computed using (5.17) incorporating $\langle v_{max} \rangle$ and setting $\langle E_{R_{max}} \rangle = \mathrm{q}_{\min}$. Moreover it is important to know that the exposure given for the XENON10 experiment already contains the (constant) efficiency which is the reason for setting the efficiency factor in the upcoming computations to 1. Setting the efficiency to 0.4 for CDMS is due to the fact that the estimation of its actual energy dependence has not been finished yet. Experience from earlier analysis shows that the constant value 0.4 is a reasonable assumption for most energies except for those close to the threshold where its value is significantly lower. After the efficency is computed properly the scripts incorporating its value should be run again.

As a first example figure 5.5 shows spin-independent differential event rates

experiment	target	$\mathrm{q}_{\min}$ in keV	$\mathrm{q}_{\max}$ in keV	$m_{W_{\min}}$ in GeV	exposure in kg · days	efficiency
CDMS	Si	20	100	15	43.1	0.4
	Ge	7	100	11	102.9	0.4
XENON10	Xe	4.5	26.9	11	136.1	1

Table 5.1: Basic facts about the CDMS and XENON10 experiments. See text above for details. Some values are taken from [32] for CDMS and from [20] for XENON10.

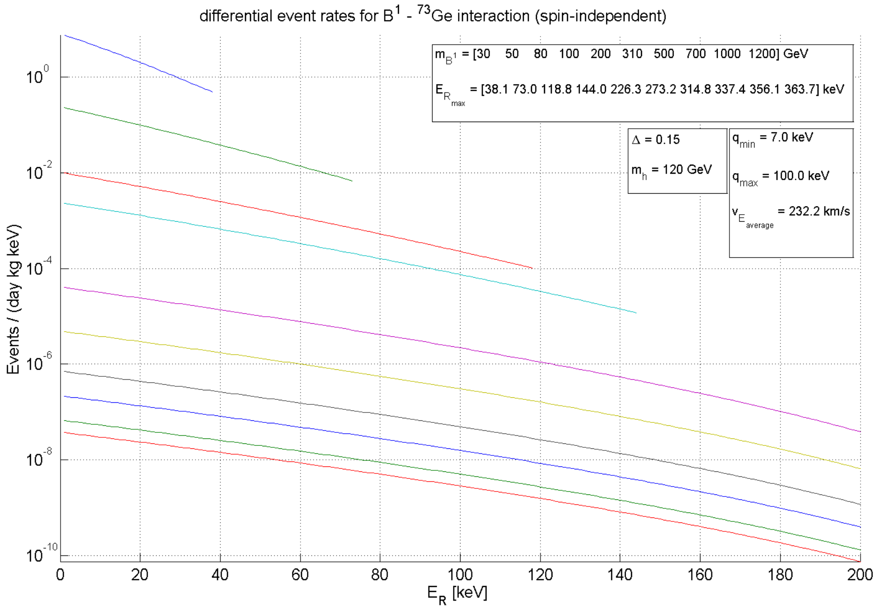

Figure 5.5: Spin-independent differential event rates for $B^{(1)}$-^{73}Ge scattering. All important parameters like the used Higgs mass m_H and degeneracy parameter Δ are given. Since the differential event rates depend only slightly on the Higgs mass the value $m_H = 120$ GeV is used throughout the whole analysis. Obviously higher WIMP masses yield lower differential event rates. Moreover the almost exponentially decreasing is evident.

from $B^{(1)}$-^{73}Ge scattering obtained by evaluating $(5.35)^2$ using the values $m_H = 120$ GeV and $\Delta = 0.15$ and a semilogarithmic y-axis. Each curve is related to different WIMP masses given in the upper box which also contains the corresponding averaged maximum recoil energies $\langle E_{R_{max}} \rangle$ computed using (5.17) and displayed in figure 5.4. As already explained before the highest (blue) curve belongs to the first value in the list of WIMP masses which is $m_{B^{(1)}} = 30$ GeV. Each curve is tructated at the just mentioned averaged maximum recoil energy. However as already mentioned it should be kept in mind that it is very likely that a certain scattering process can give rise to a higher recoil energy especially in a head-on collision. But since the differential rates are decreasing approximately exponential this cut-off is actually only important for low WIMP masses. This is due to the fact that the range directly behind the threshold given for each kind of detector in table 5.1 clearly contributes the most important part to the spectrum.

In conjunction with this first example figure 5.6 shows the corresponding spin-dependent differential event rates computed with $(5.36)^2$ using the same degen-

[2]So the corresponding abundance factor is not included.

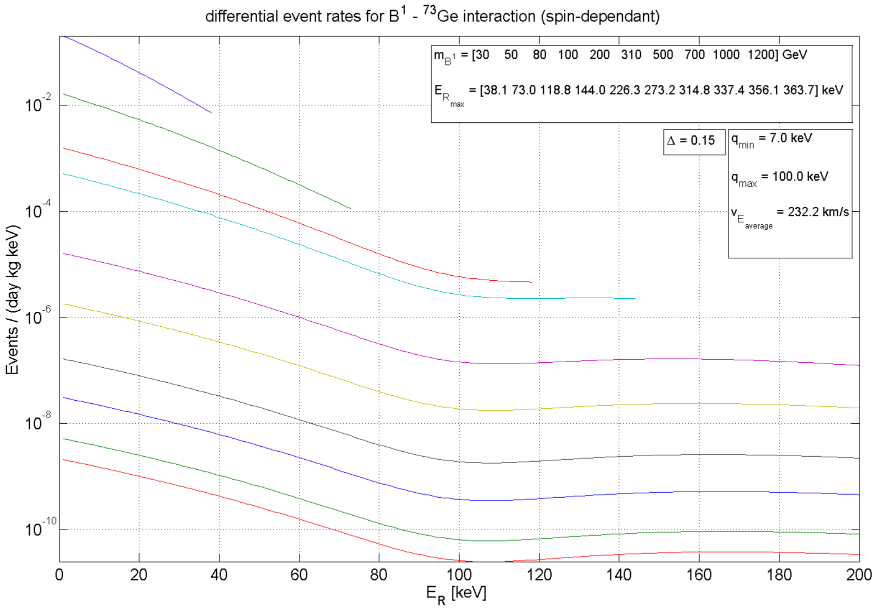

Figure 5.6: Spin-dependent differential event rates for $B^{(1)}$-^{73}Ge scattering. All important parameters like the used Higgs mass m_H and degeneracy parameter Δ are given. Obviously higher WIMP masses yield lower differential event rates. Moreover the almost exponentially decreasing is evident.

eracy parameter as before namely $\Delta = 0.15$.[3] The obtained rates are smaller compared to the corresponding spin-independent rates approximately by a factor of 10. So since the spin-independent rates dominate scattering from a single isotope it is clear that considering the whole silicon, germanium and xenon targets spin-dependent scattering contributes only negligible to the total differential event rate. This is clear since only a few isotopes contribute to this kind of interaction.

Figure 5.7 shows total differential event rates for certain silicon, germanium and xenon isotopes computed using (5.37) and a WIMP mass of $m_{B^{(1)}} = 1000$ GeV. Obviously the use of xenon targets seem to be more promising considering low recoil energies due to the $\sim A^2$ scaling of the spin-independent cross sections whereas it is less advantageous for higher recoil energies since the spin-independent formfactors of xenon isotopes drop down much faster than those of silicon and germanium isotopes as evident from figure 4.1. And as already explained it is the spin-independent contribution which dominates the interaction.

Plots showing the total differential events rates obtained by evaluating (5.38) summing over all occuring isotopes in the respective detectors and incorporating the abundance factors can be found in the figures 5.8, 5.9 and 5.10 for silicon, germanium and xenon targets. The used parameters are still $m_H = 120$ GeV and

[3] As already explained the spin-dependent results are independent from the Higgs mass.

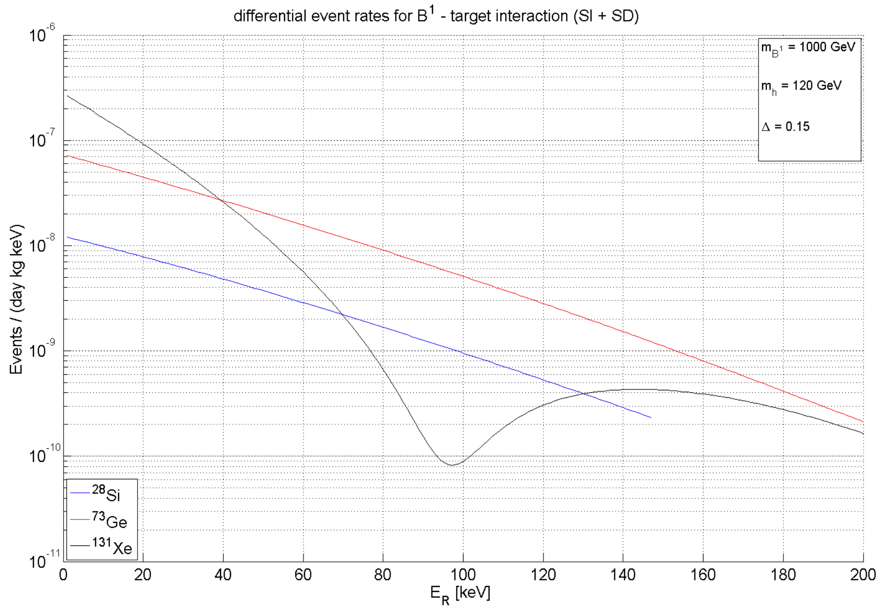

Figure 5.7: Comparison of differential event rates scattering from ^{28}Si, ^{73}Ge and ^{131}Xe.

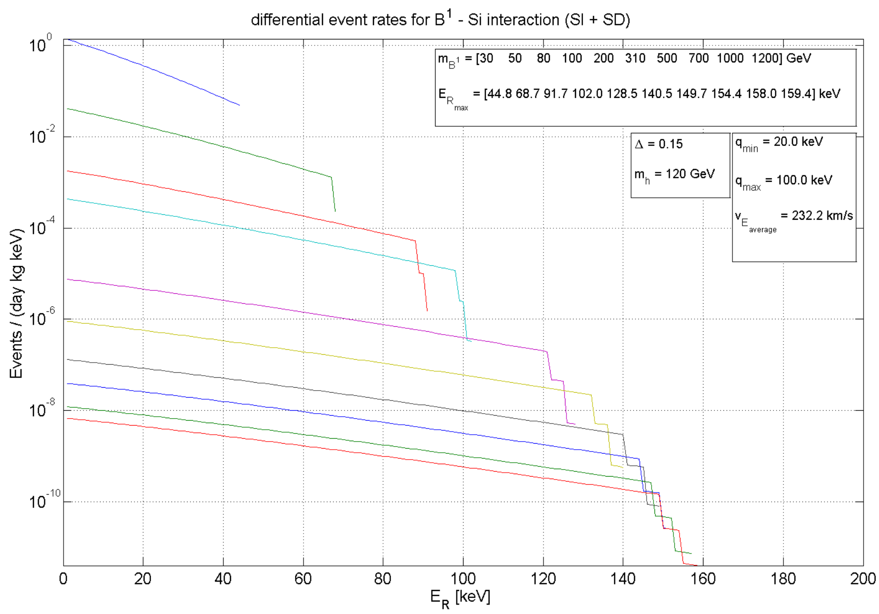

Figure 5.8: Differential event rates for $B^{(1)}$-Si scattering.

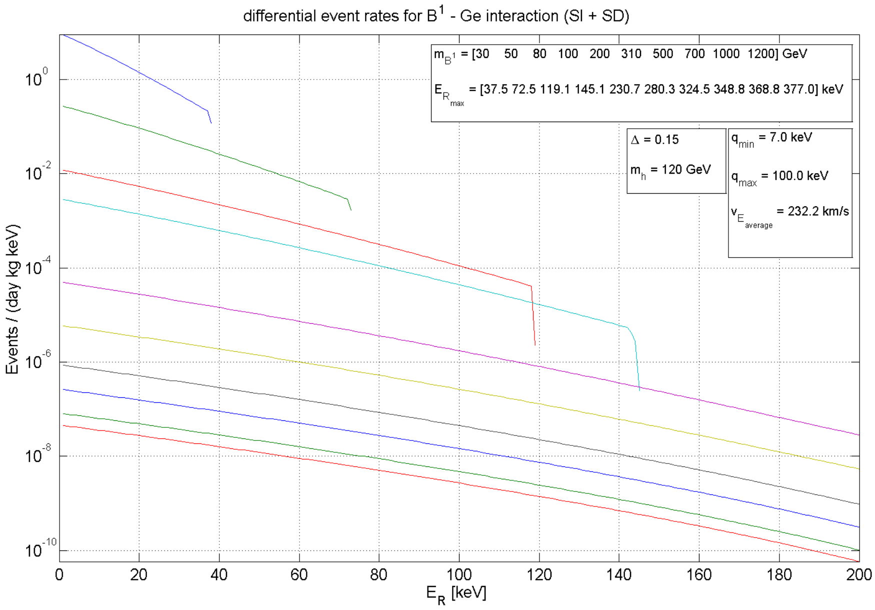

Figure 5.9: Differential event rates for $B^{(1)}$-Ge scattering.

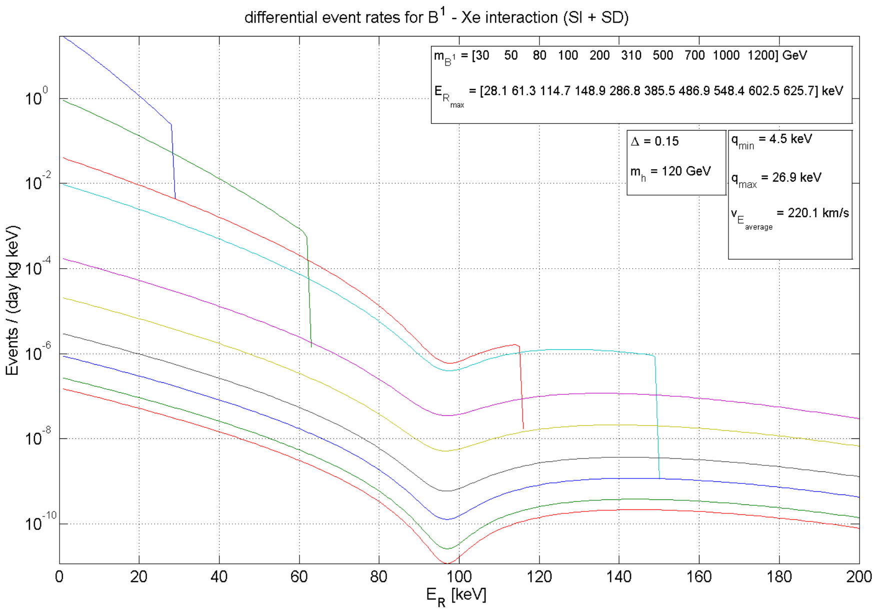

Figure 5.10: Differential event rates for $B^{(1)}$-Xe scattering.

$\Delta = 0.15$.[4] The given values of $\langle E_{R_{max}} \rangle$ correspond to the heaviest used isotopes so according to table 3.4 to ^{30}Si, ^{76}Ge and ^{136}Xe. Except for very small WIMP masses up to about 50 GeV this always corresponds to the maximum value of $\langle E_{R_{max}} \rangle$ for the whole target. Really striking is the bend down at the end of each curve. This is related to the fact that isotopes with similar masses as present in each detector also have similar but not exactly the same averaged maximum recoil energy $\langle E_{R_{max}} \rangle$. Consider for example a WIMP with a mass of $m_{B^{(1)}} = 500$ GeV and a silicon target where the three occuring isotopes ^{28}Si, ^{29}Si and ^{30}Si give rise to values of 140.7 keV, 145.3 keV and 149.7 keV for $\langle E_{R_{max}} \rangle$. Taking a look at table 3.4 it is clear that ^{28}Si contributes by far the most important part to the differential event rate since its abundance is about 92 %. So recoil energies of more than 140.7 keV can only arise from the other two isotopes with almost negligible abundance. Of course, however these effects are not observable especially because they are calculated using averaged recoil energy cut-offs. In reality the behaviour at the cut-off is expected to be smeared out due to measured recoils with different scattering angels and at different days in a year which leads to a damping near the calculated cut-off. Nevertheless this uncertainty about the cut-off behaviour is not really of crucial importance except for really low WIMP masses due to reasons already stated.

Moreover as already explained these plots are almost identical to those obtained by considering only the spin-independent contribution neglecting spin-dependent scattering which is the reason not to show them here. In contrast showing contributions arising only from spin-dependent interactions is clearly of interest. So plots similar to the figures 5.8, 5.9 and 5.10 but using only spin-dependent contributions can be found in B.2. In the case of silicon and germanium this amounts to evaluating (5.36) and multiplying by the appropriate abundance of ^{29}Si and ^{73}Ge. In the case of xenon there are two isotopes which are sensitive to spin-dependent interactions meaning that (5.38) has to be used but neglecting the spin-independent contribution to $\frac{\mathrm{d}R}{\mathrm{d}E_R}|_{total}$.

After having discussed the differential event rates the next step is obviously the computation of the total event rates. Therefor the differential event rates have to be integrated. The lower limit for these integrations is clearly given by the threshold $\mathrm{q_{min}}$ whereas the upper limit is chosen to be the minimum of the upper analysis limit $\mathrm{q_{max}}$ and the averaged maximum recoil energy $\langle E_{R_{max}} \rangle$ with the latter being computed for every isotope separately. This means that

$$R = \int_{\mathrm{q_{min}}}^{\min\left(\mathrm{q_{max}}, \langle E_{R_{max}} \rangle\right)} \mathrm{d}E_R \, \frac{\mathrm{d}R}{\mathrm{d}E_R}|_{total}^{target} \tag{5.39}$$

with the differential event rate given in (5.38) has to be evaluated. Again it is clear that only results for very small WIMP masses depend on the actual value of

[4] Similar plots for various values of Δ considerng scattering from germanium can be found in section B.1 of the appendix.

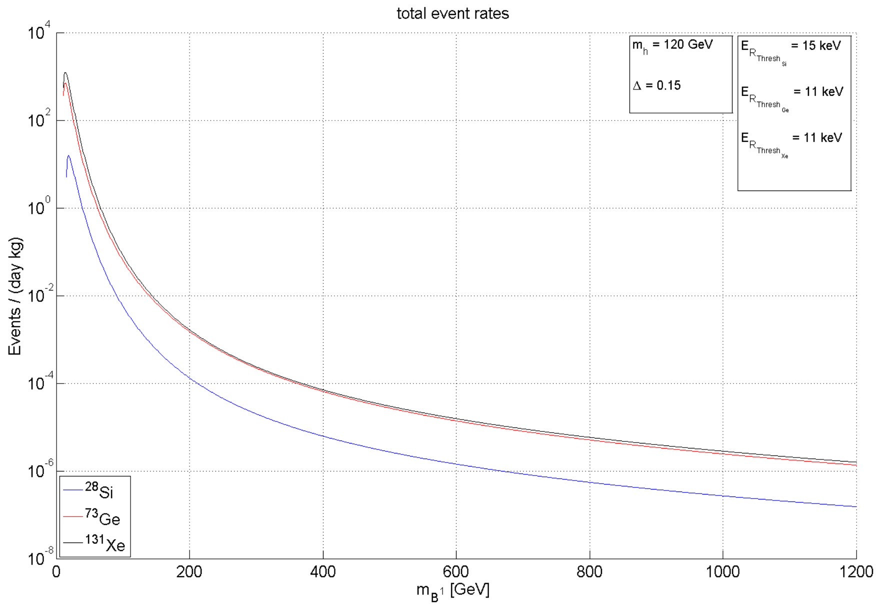

Figure 5.11: Comparison of total event rates scattering from ^{28}Si, ^{73}Ge and ^{131}Xe.

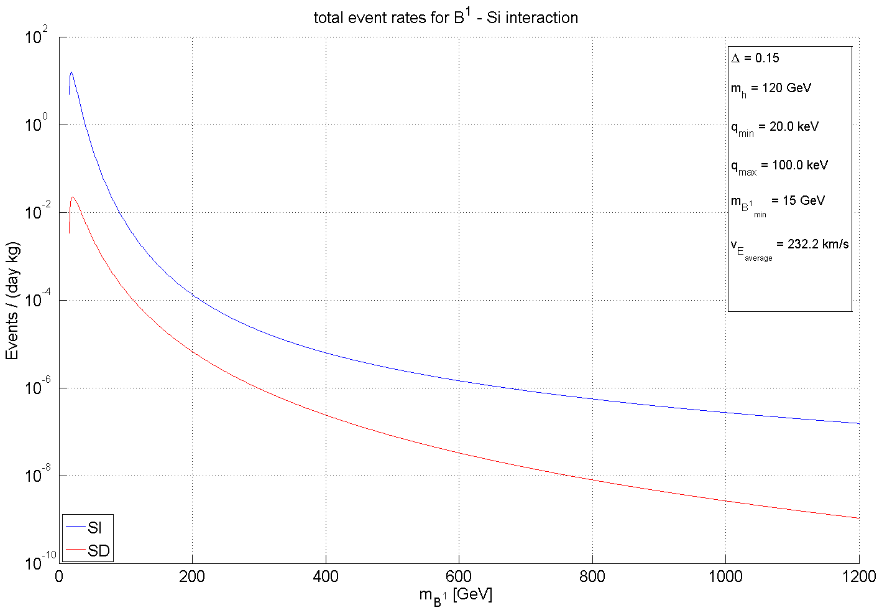

Figure 5.12: Total event rates for $B^{(1)}$-Si scattering.

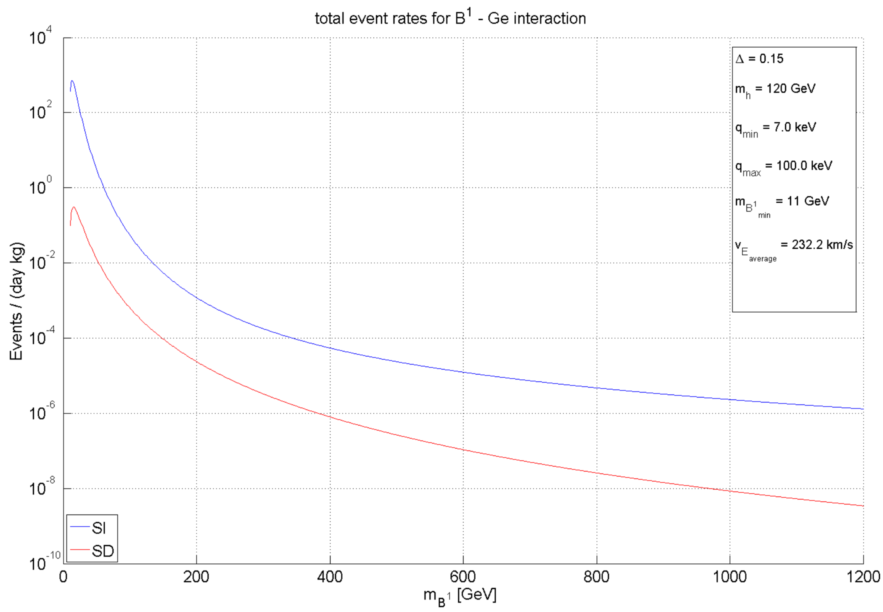

Figure 5.13: Total event rates for $B^{(1)}$-Ge scattering.

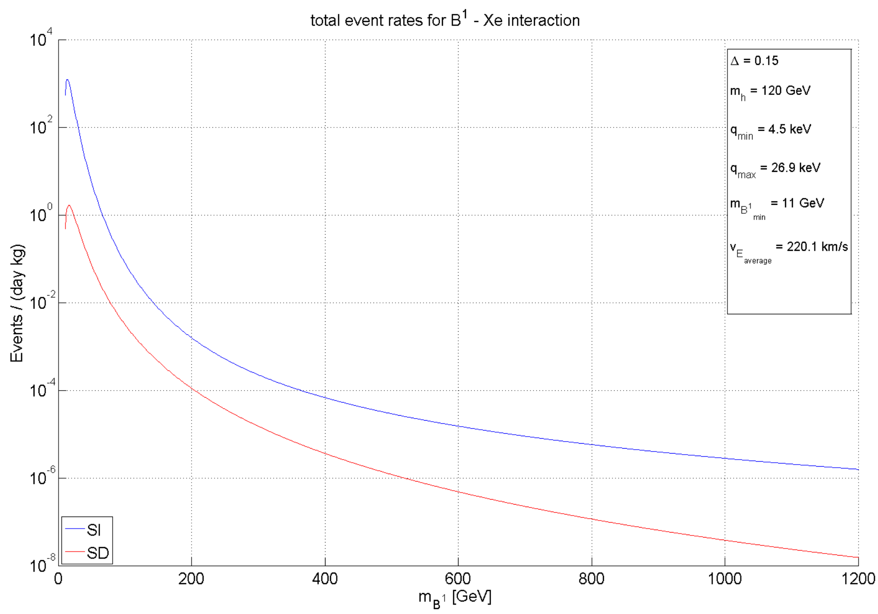

Figure 5.14: Total event rates for $B^{(1)}$-Xe scattering.

the upper limit.

But before considering rates from the whole targets a short comparison of total event rates obtained by considering only single isotopes is shown in figure 5.11. No abundance factors are incorporated here. Therefor this figure is closely related to figure 5.7 since the results in the former for a WIMP mass of $m_{B^{(1)}} = 1000$ GeV are obtained by integrating over the corresponding curves in the latter. Remember that according to table 5.1 the recoil energy interval considered for the analysis of germanium is $7 - 100$ GeV whereas the corresponding interval for xenon is $4.5 - 26.9$ GeV. So even though according to figure 5.7 the differential event rate from the xenon isotope lies clearly above the differential event rate from the germanium isotope for low energies it looks like the larger interval considered for germanium can almost completely compensate the lower germanium rates despite the exponential drop-down. Nevertheless it must be admitted that the xenon isotope is achieving slightly better results. However in any case it is clear that the results from the silicon target are far behind.

At this stage the total event rates for whole targets are about to be studied. In practice it is more convenient to show plots distinguishing between the spin-independent and the spin-dependent case. The obtained total event rates for $\Delta = 0.15$ and $m_H = 120$ GeV as functions of the WIMP mass $m_{B^{(1)}}$ are shown in the figures 5.12, 5.13 and 5.14 for silicon, germanium and xenon targets.[5]

Obviously the total rate drops down significanlty for higher WIMP masses which makes it more difficult to detect corresponding WIMPs in an experiment. Moreover the rates arising from spin-independent interactions are usually about a factor of 10 or even 100 higher than the spin-dependent counterparts which again makes the contribution of the latter almost negligible.

There are two more useful annotations considering the low mass behaviour of the total event rates. First of all the cut-off at low masses is due to the fact that WIMPs with lower masses would not give rise to recoil energies above the threshold. The corresponding minimum masses $m_{W_{\min}}$ for each target are given in table 5.1.

The second remark is about the cause of the bend of the curves at low masses In order to investigate this issue figure 5.15 shows the differential event rates for the lowest five masses yielding recoil energies above the threshold considering scattering from ^{130}Xe.[6] It is obvious that for these low masses the total event rates significantly depend not only on the threshold but also on the maximum recoil energy. In contrast, for high masses the maximum recoil energy is so high that the total event rate does not significantly depend on it either because it exceeds the energy interval considered or because the differential event rate drops down very fast. Apart from the maximum recoil energy the fact that differential event rates for different masses have a point of intersection also contributes to the

[5]Similar to the case of differential event rates the corresponding plots using various values of Δ and considering scattering from germanium can be found in B.3.

[6]Only integers have been used.

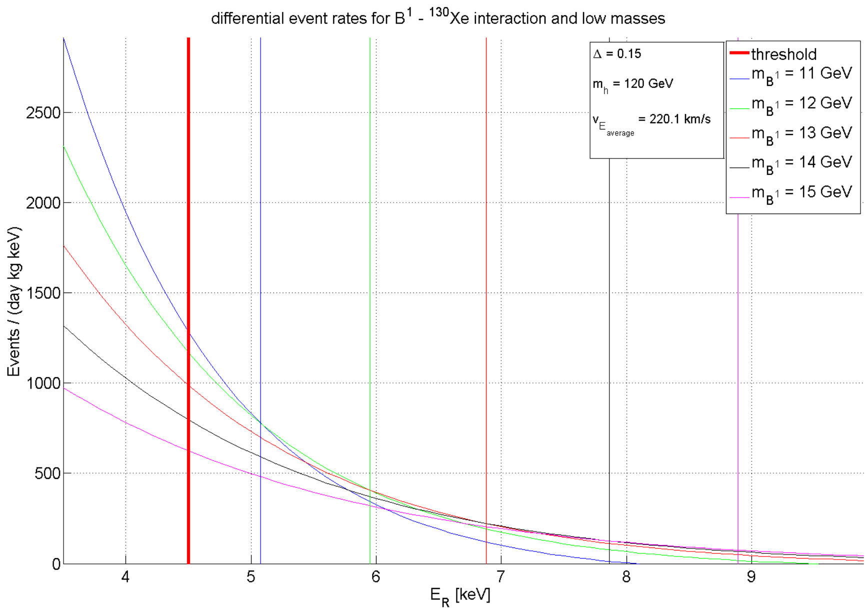

Figure 5.15: Differential event rates for the lowest five masses yielding recoil energies above the threshold using only integers for the masses and considering scattering from ^{130}Xe.

bend. For example the area under the upper blue curve between the vertical red line representing the threshold and the vertical blue line representing the averaged maximum recoil energy for the corresponding WIMP mass is smaller than the area under the green curve between the vertical red and green lines. Hence the total rate for a WIMP mass of $m_{B(1)} = 11$ GeV is smaller than for a WIMP mass of $m_{B(1)} = 12$ GeV. As cognizable from the plot the intersection points of two adjacent rates move to higher recoil energies for higher WIMP masses. This also contributes to the fact that except for low WIMP masses the total rate always decreases with increasing WIMP masses. However as already stated this bend should not be taken too serious due to the mentioned uncertainties of the cut-off behaviour of the differential rates. Moreover this bend disappears if a detector has a very low threshold close to 0 keV because then the part of the differential event rate directly above the threshold dominates by far. This is shown in a plot in B.4 where a threshold of 0.1 keV is assumed.

Chapter 6

Annual modulation

As explained in the previous chapter the differential and total event rates depend on the day in a year via the velocity v_E due to the earth's motion around the sun. However this time dependence was neglected by replacing v_E with appropriate averaged values given in (5.5) for the CDMS and in (5.6) for the XENON10 experiment. The main topic of this chapter is a short investigation of annual modulation effects which are related to this time dependence. Therefor the averaged values are replaced by the general expression (5.4).

To start with the investigation of this topic it is the best to take a look at the figures 6.1, 6.2 and 6.3 where each shows two differential event rate curves considering scattering from ^{73}Ge and the standard parameters $\Delta = 0.15$ and $m_H = 120$ GeV.[1] The difference in these plots is the considered WIMP mass which is chosen to be 30 GeV in the first, 200 GeV in the second and 1000 GeV in the third figure. The two curves belong to two different days in a year namely the blue one labeled 152.5$^{\text{th}}$ day to June 2$^{\text{nd}}$ and the red one labeled 335.1$^{\text{th}}$ day to December 2$^{\text{nd}}$ which are related to the maximum and the minimum value of v_E in a year respectively. Obviously both curves have a point of intersection called crossover recoil energy $E_{R_{cross}}$. In other words the differential event rates at high energies are always in phase with the motion of the earth around the sun whereas a phase reversal occurs for low recoil energies. Note that the y-axis scales differently in each plot whereas the x-axis remains the same. Therefor it is easy to see that $E_{R_{cross}}$ is increasing with the Wimp mass.

To further investigate the consequences remember that the threshold of the germanium detectors is set to 7 keV. So considering a low WIMP mass like 30 GeV it is clear from figure 6.1 that the differential event rate on June 2$^{\text{nd}}$ is higher than the corresponding rate on December 2$^{\text{nd}}$ for the whole considered energy range. Consequently roughly speaking the total event rates obtained by integration are always higher in summer compared to those in winter. So the total event rate is in phase with the earth velocity as well peaking in summer. But as already observed

[1] Note that the investigated crossover recoil energy is independent of the cross section and so it is especially independent of Δ and m_H.

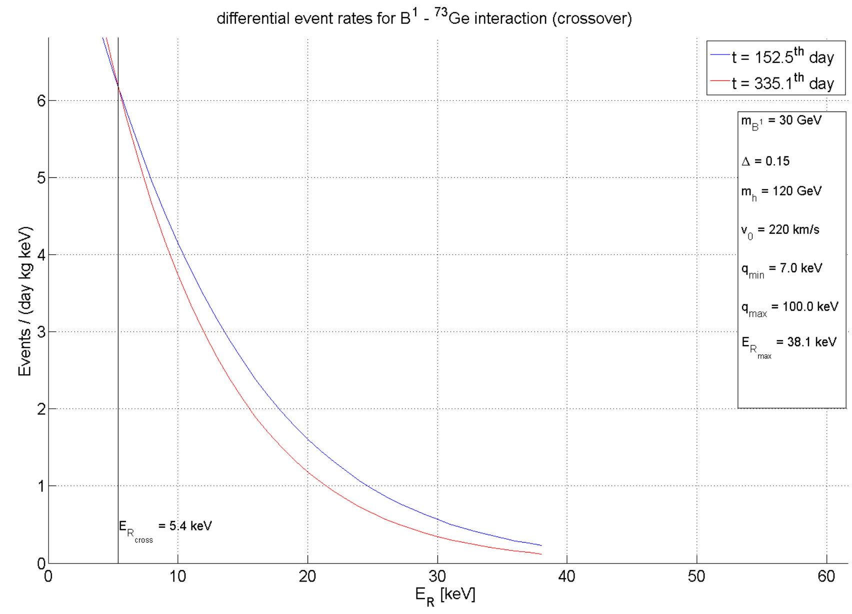

Figure 6.1: Differential Event rates for June 2$^{\text{nd}}$ and December 2$^{\text{nd}}$ considering $m_{B^{(1)}} = 30$ GeV.

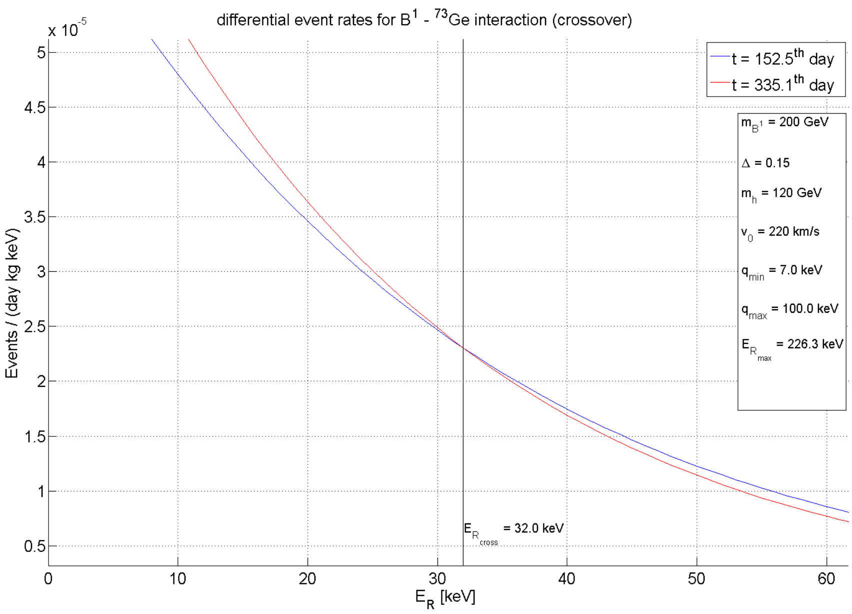

Figure 6.2: Similar to figure 6.1 but using $m_{B^{(1)}} = 200$ GeV.

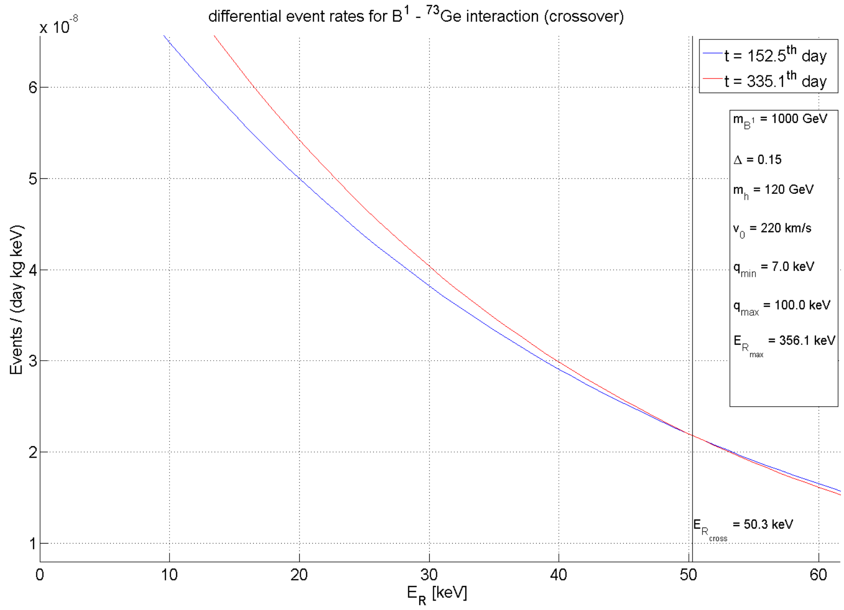

Figure 6.3: Similar to figure 6.1 but using $m_{B^{(1)}} = 1000$ GeV.

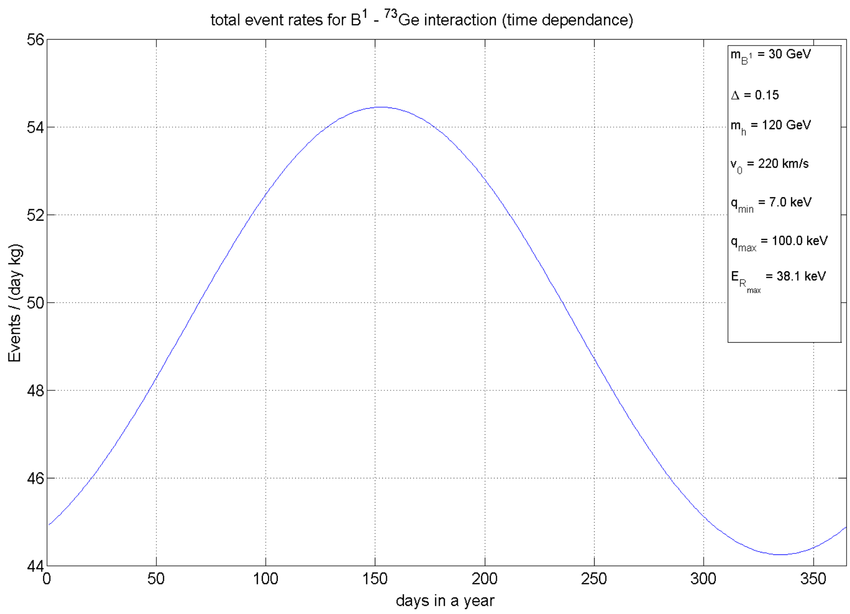

Figure 6.4: Time dependence of the total event rate considering $m_{B^{(1)}} = 30$ GeV.

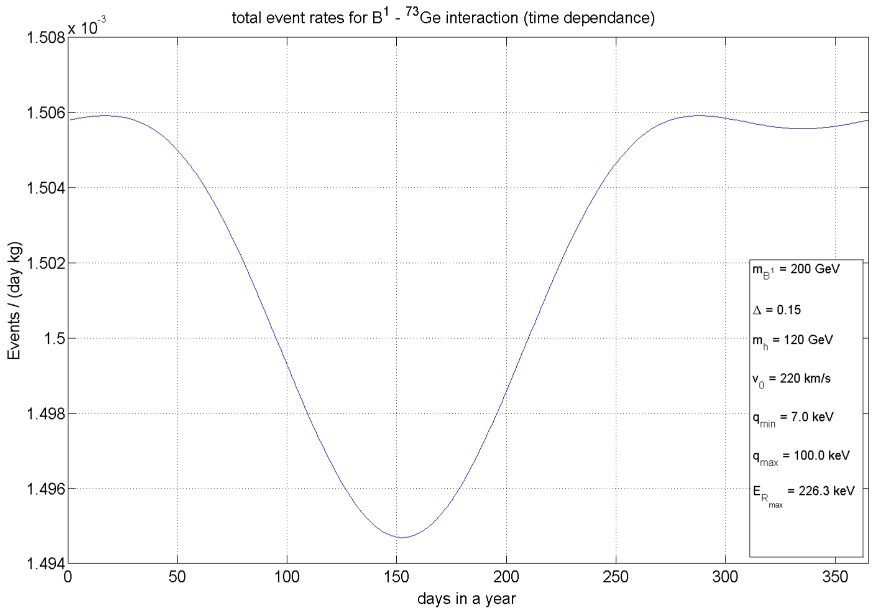

Figure 6.5: Similar to figure 6.4 but using $m_{B^{(1)}} = 200$ GeV.

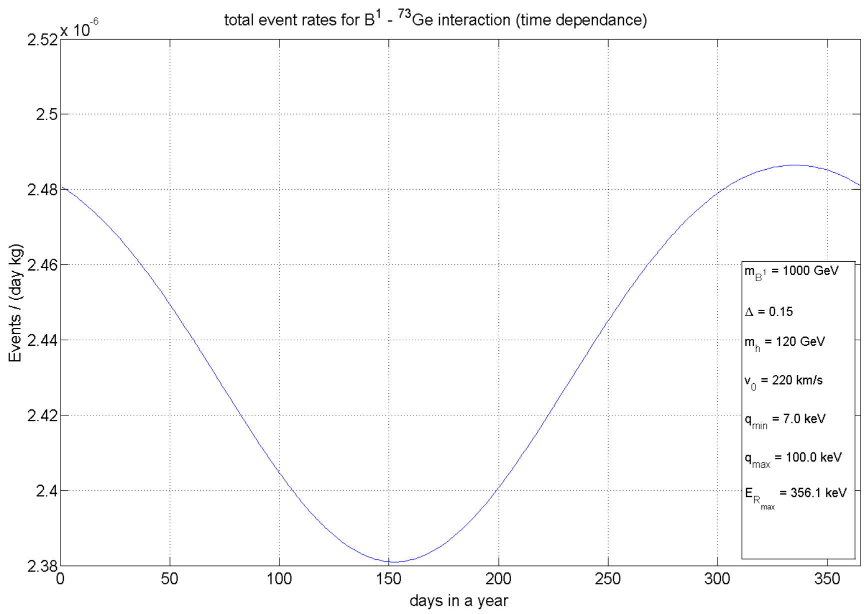

Figure 6.6: Similar to figure 6.4 but using $m_{B^{(1)}} = 1000$ GeV.

the crossover recoil energy increases to higher values with increasing WIMP masses. So it is clear that the recoil energy interval between the threshold and $E_{R_{cross}}$ yields a higher contribution to the total event rate in winter whereas the interval between $E_{R_{cross}}$ and the end of the analysis region still gives rise to higher contributions of the total event rate in summer.[2] Hence the total event rate considered as a function of the day in a year peaks in summer for low WIMP masses but undergoes a phase reversal with increasing WIMP masses. This behaviour can be seen in the figures 6.4, 6.5 and 6.6 which show the time dependence of the total event rate for the same three masses and parameters used in the figures 6.1, 6.2 and 6.3. The actual mass interval where the phase reversal takes place depends on each isotope and the considered energy intervals. For example considering ^{73}Ge the phase reversal occurs at a WIMP mass of about $\simeq$ 175 GeV whereas it already occurs approximately at $\simeq$ 60 GeV using ^{131}Xe. In the case of silicon no phase reversal can be observed up to a WIMP mass of 1200 GeV which is mostly due to its high threshold of 20 keV.

Even though the just discussed mass interval where the phase reversal takes place clearly depends not only on the WIMP mass and the target mass but also on the theoretical framework considered. However the actual value of the crossover recoil energy is independent of the WIMP model, the form factor and even the local halo density ρ_W which makes it a really interesting quantity. To understand the just stated properties just take a look at the way it can be computed:

$$\begin{aligned} 0 &\stackrel{!}{=} \frac{\mathrm{d}R}{\mathrm{d}E_R}|_{t_0} - \frac{\mathrm{d}R}{\mathrm{d}E_R}|_{t_1} \qquad (6.1) \\ &= \left[\frac{\sqrt{\pi}}{4}\frac{v_0}{v_E(t_0)}\left[\mathrm{erf}\left(\frac{v_{min}+v_E(t_0)}{v_0}\right) - \mathrm{erf}\left(\frac{v_{min}-v_E(t_0)}{v_0}\right)\right] - e^{-\frac{v_{esc}^2}{v_0^2}}\right] \\ &\quad - \left[\frac{\sqrt{\pi}}{4}\frac{v_0}{v_E(t_1)}\left[\mathrm{erf}\left(\frac{v_{min}+v_E(t_1)}{v_0}\right) - \mathrm{erf}\left(\frac{v_{min}-v_E(t_1)}{v_0}\right)\right] - e^{-\frac{v_{esc}^2}{v_0^2}}\right] \end{aligned}$$

with the formulae for the differential event rates taken from (5.33) and t_0 denoting June 2$^{\mathrm{nd}}$ whereas t_1 denotes December 2$^{\mathrm{nd}}$. Plots of the term on the right side of this equation as a function of the recoil energy considering scattering from ^{73}Ge can be found in figure 6.7 for various masses.[3] The target properties only enter the formula via the m_T-dependence of v_{min} given in (5.31). Computing of its respective roots is rather easy since the curves are obviously negative for low recoil energies as expected and increase monotonously to positive values until they reach a maximum and decrease asymptotically towards 0.

Figure 6.8 shows the result of the whole computation for one silicon, one germanium and one xenon isotope considered to be the target. Obviously the

[2] Of course it is possible that $E_{R_{cross}}$ exceeds the energy interval used in the analysis.

[3] Even though the masses are labeled $m_{B^{(1)}}$ the results shown in these figures are independent of the WIMP model.

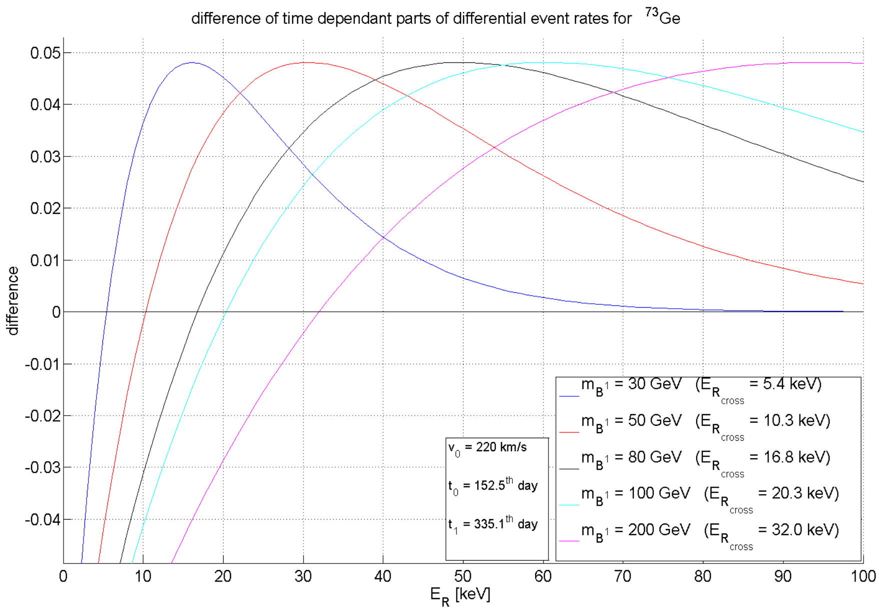

Figure 6.7: Computing the crossover recoil energy.

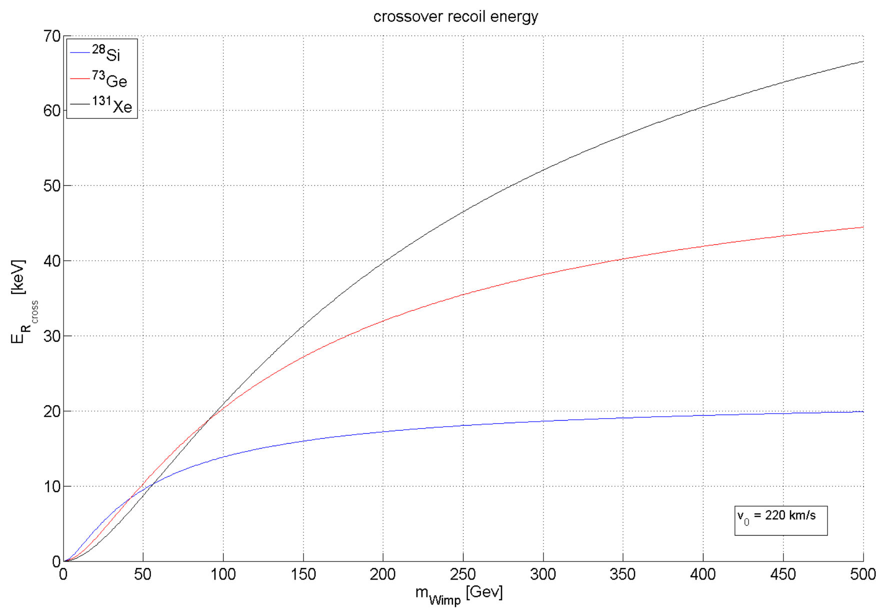

Figure 6.8: Mass dependence of the crossover recoil energy for ^{28}Si, ^{73}Ge and ^{131}Xe.

crossover recoil energy is a monotonically increasing function of the WIMP mass. Therefor an observation of an annual modulation signal can be used to constrain the WIMP mass. Consider for example an observed annually modulated signal with a peak in June in an energy range $E_{R_1} - E_{R_2}$. Hence it is clear that the cross over recoil energy must be below E_{R_1} or otherwise a peak in December would have been observed. Since it turned out that the crossover recoil energy is monotonically increasing function of the WIMP mass this in turn directly places an upper limit on the WIMP mass. For example if CDMS would observe such a signal in their germanium detectors in energy bins close to the threshold of 7 keV an upper limit of about 40 GeV could be set for the WIMP mass. Of course a direct measurement of $E_{R_{cross}}$ itself would direcctly determine the WIMP mass.

However the expected modulation is very small so that excellent energy resolution and a really long exposure would be necessary in order to have a chance to potentially detect it at all. The authors of [35] estimated the required exposures for several experiments. For example considering the germanium detectors used by CDMS they argue that an exposure of about 80 kg $\cdot$ years would be required assuming perfect energy resolution which leads to the conclusion that observing the annual modulation is not very likely with this experiment. Considering large scale liquid xenon detectors as in XENON10 their results are much more encouraging but only for a very narrow WIMP mass range of about $100 - 150$ GeV for which they estimated a necessary exposure of about 25 kg $\cdot$ years making it possible to detect the annual modulation within a single year of continous running. However outside of this narrow interval the situation gets even worse than in the case of CDMS. So annual modulation is not very likely to be detected by neither CDMS nor XENON10 if the dark matter is really made up of the $B^{(1)}$ which is expected to have a mass of about $500 - 600$ GeV. Of course the obtained results have to be modified considering different halo models with different velocity distributions.

To finish the topic of annual modulation the figures 6.9 and 6.10 show differential event rates for a WIMP mass of $m_{B^{(1)}} = 500$ GeV and the ususal values for the parameters Δ and m_H considering scattering from ^{73}Ge. What distinguishes these two plots from all other plots showing differential event rates before is that here the recoil energy E_R is fixed and the dependence of the day in a year is investigated. The crossover recoil energy for this combination of WIMP and target mass is given by 44.5 keV. Needless to say that from the phase of the curves it is clear that figure 6.9 shows results obtained by using a recoil energy below the cross over recoil energy namely $E_R = 22.2$ keV whereas a recoil energy above given by $E_R = 66.6$ keV is used in figure 6.10.

As a final investigation which however is not really related to the annual modulation effect figure 6.11 explores the dependence of differential event rates on the characteristic velocity of the velocity distribution v_0. Throughout this whole analysis its value was set to $v_0 = 220$ km/s but its value is burdened with a high degree of uncertainty. Therefor the differential event rate is plotted for five different values of v_0 from 220 km/s to 270 km/s. Scattering from ^{29}Si and a WIMP mass of $m_{B^{(1)}} = 500$ GeV is considered. Obviously there is a point of intersection

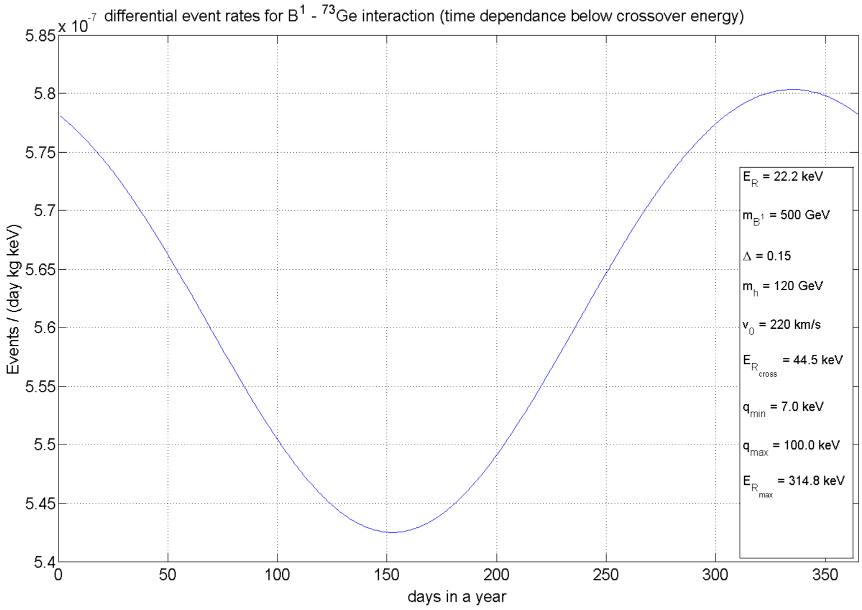

Figure 6.9: Computing the crossover recoil energy.

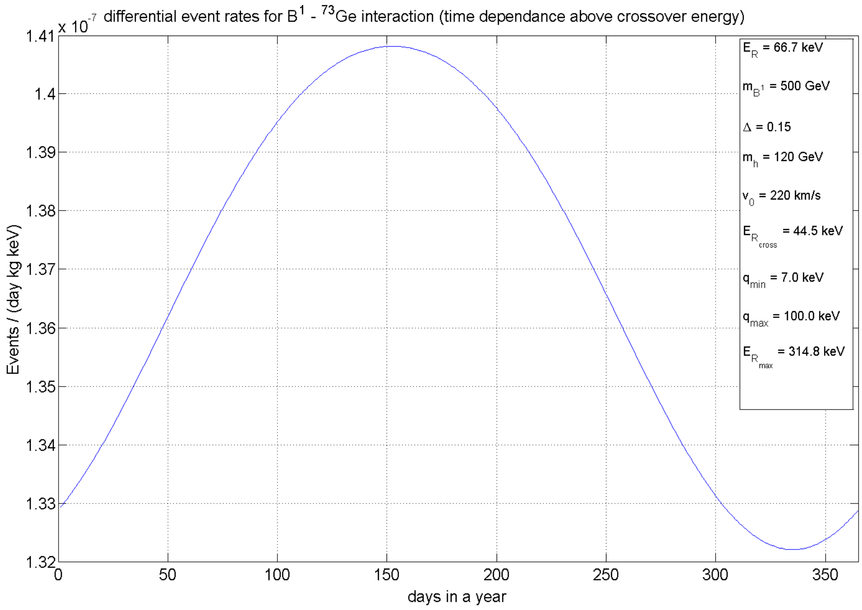

Figure 6.10: Mass dependence of the crossover recoil energy for ^{28}Si, ^{73}Ge and ^{131}Xe.

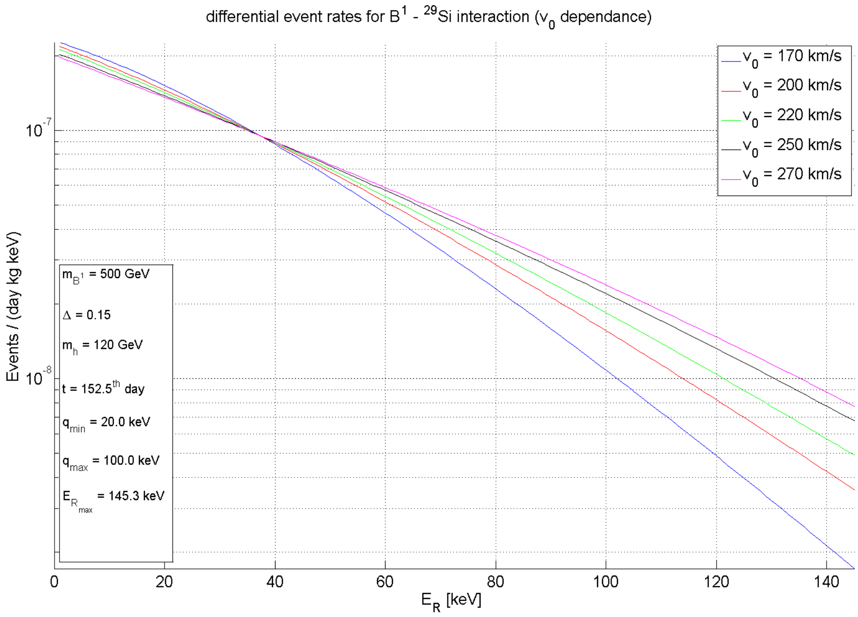

Figure 6.11: Dependence of the differential event rate on v_0 considering a WIMP mass of $m_{B^{(1)}} = 500$ GeV and scattering from ^{29}Si.

near $E_R = 50$ keV. However more important is the observation that the differential event rates only depend very slightly on v_0 for low recoil energies. Remembering that this is the by far most important energy range it seems that the uncertainties are not so crucial even though they are quite large.

Chapter 7

Limits on cross sections and WIMP-nucleon couplings

In the previous chapters the UED model was used in order to determinine predictions for the spin-independent and spin-dependent WIMP-nucleon coulings $f_{p,n}$ and $a_{p,n}$ and hence for the respective cross sections σ_{SI} and σ_{SD}. Unfortunately to this day no experiment except for the widely doubted DAMA has ever claimed to have detected dark matter neither in direct detection experiments discussed here nor accomplishing different approaches. Hence it is not possible to compare any kind of measured signal to theoretical predictions. Even though this is of course disappointing and the community is eagerly waiting for a positive result it is at least possible to compute upper limits on the mentioned quantities. As already mentioned the parameter space considering direct detection can be described by the four WIMP-nucleon coulings and the WIMP mass. So in this chapter these quantities are assumed to be a priori unknown.

Setting limits it is usually assumed that one of the two types of interaction dominates by far so that the other one can be neglected. Similar to the discussions of cross sections and form factors the spin-independent case is the one considered first since it is much easier and even straight forward to deal with. The spin-dependent case considered afterwards turns out to be much more complicated.

7.1 Limits on spin-independent cross sections

Computing limits on the WIMP-nucleon cross sections in the spin-independent case is comparatively simple for two reasons.

First of all there is no relationship between the actual cross section and the form factors which is different in the spin-dependent case where not only the spin-dependent cross section depends on the WIMP-nucleon couplings but also the corresponding form factors. Therefor investigating spin-independent interactions it is possible to compute limits on the cross sections from target nuclei without even considering the properties of the WIMP-nucleon couplings f_p and f_n.

The second reason concerns the normalization from cross section limits considering target nuclei to the limits from scattering of single nucleons. As already mentioned in the chapter on cross sections it is appropriate for most dark matter candidates to assume that the interaction is isospin-independent which means that $f_p \approx f_n$ yielding the simple normalization given in (3.19). Even though this normalization is used throughout this whole chapter it is useful to think about the consequences if the just made assumption does not hold. This is discussed for example in [36]. Consider for example the extreme case that $f_p = -f_n$. From (3.9) it is clear that this would result in a strongly suppression of the spin-independent interaction with the advantegeous $\sim A^2$ scaling from the isospin-independent case switching to a $\sim (N-Z)^2$ scaling. Of course this would be disastrous especially for experiments with comparatively low target masses where $N \approx Z$. So taking a look at table 3.4 reveals that for example ^{73}Ge would end up with only 9 nucleons effectively participating in the interaction whereas ^{131}Xe would still constitute at least 23 effective nucleons. Hence the sensitivity of these targets would be suppressed by factors of approximately 66 and 32 respectively. For the general case of arbitrary WIMP-nucleon couplings an analysis similar to the approach presented for spin-dependent interactions constraining f_p and f_n would be necessary which however would be still less complicated due to the almost target-independent form factors. Nevertheless as already mentioned the simple case assuming isospin-independent interactions is investigated here.

So how are cross section limits computed? In order to answer this question the arrangement is made to start by calculating limits for every target isotope seperately and combining them afterwards. The general procedure is rather simple. First of all the number of events N has to be considered. It can be calculated by multiplying the total event rate with the respective abundance factor f given in table 3.4 as well as the exposure exp and efficiency eff given in table 5.1. So using the expression for the spin-independent differential event rate considering scattering from only one single isotope given in (5.35) and directly replacing σ_{SI} by the cross section normalized to a neutron given in (3.19) yields[1]

$$N = f \cdot exp \cdot eff \cdot \sigma_{SI}^n \, A^2 \, \frac{\mu_T^2}{\mu_n^2} \int_{\mathrm{q_{min}}}^{\min\left(\mathrm{q_{max}}, \langle E_{R_{max}} \rangle\right)} \frac{\mathrm{d}R}{\mathrm{d}E_R}|_\sigma \, F_{SI}^2 \, \mathrm{d}E_R \,. \tag{7.1}$$

All factors in front of the integral are clearly independent of the recoil energy. However in the general case the efficiency is also energy dependent which has to be taken into account. (7.1) directly yields an expression for the cross section. N clearly has to be estimated by analyzing data from the respective experiments. After this is done the corresponding normalized cross section can be computed using

[1] Of course normalizing to scattering from a proton would yield almost exactly the same results.

$$\sigma_{SI}^n = \frac{N}{f \cdot exp \cdot eff \cdot A^2 \frac{\mu_T^2}{\mu_n^2} \int_{\mathrm{q_{min}}}^{\min\left(\mathrm{q_{max}}, \langle E_{R_{max}} \rangle\right)} \frac{\mathrm{d}R}{\mathrm{d}E_R}|_\sigma F_{SI}^2 \,\mathrm{d}E_R} \,. \tag{7.2}$$

which can also be used to set constrains on it. It is important to note that the denominator of 7.2 is constant for a given WIMP mass. Thus the obtained limits for all isotopes can be combined by considering that (7.2) yields results which are in fact overestimated by a factor of $1/f$. From now on a label lim is added to the obtained limits. Since clearly

$$\sigma_{SI}^n|^{\mathrm{lim}} \sim \frac{1}{f} \tag{7.3}$$

holds for all isotopes it is a common procedure to define this constant of proportionality to be the overall limit. Therefor adding another label i to the cross sections and abundance factors in order to distinguish between the different isotopes and considering that obviously

$$\sum_i f_i = 1 \tag{7.4}$$

holds the final limit can be computed using

$$\frac{1}{\sigma_{SI}^n|^{\mathrm{lim}}_{\mathrm{total}}} = \sum_i \frac{1}{\sigma_{SI}^n|^{\mathrm{lim}}_i} \,. \tag{7.5}$$

The last open issue is the estimation of the number of events N. In order to approach this problem it is the best way to start with the simplest example considering that no events were observed which is the case for the silicon target as evident fom table 7.1. Since direct detection experiments always deal with a very small number of observed events it is a common assumption that this process obeys a Poisson statistic with the familiar probability distribution

experiment	target	detected events	E_R of detected events in keV	expected events	μ from FC method
CDMS	Si	0	—	0	$0 \ldots 2.44$
	Ge	1	64.0	1	$0 \ldots 3.36$
XENON10	Xe	10	$4.5, 15.4, 16.7, 16.9, 19.6, 20.2, 23.7, 24.0, 25.4, 26.2$	7	$0 \ldots 9.50$

Table 7.1: Expected and detected events from the CDMS and XENON10 experiments. Values are taken from [31] for CDMS and from [20] for XENON10. The last column shows the Poisson signal mean μ used in the Feldman & Cousins method taken from [37].

$$P(k|\mu) = \frac{\mu^k}{k!}e^{-\mu} \tag{7.6}$$

where μ denotes the expectation value. Usually a 90 % confidence limit is given on the cross sections. In the case that no events were observed or rather $k = 0$ this is easily evaluated.

$$P(0|\lambda) = e^{-\mu} \stackrel{!}{=} 1 - 0.9 \tag{7.7}$$

directly yields $\mu = \ln 10 \approx 2.30$ which henceforth is used as the number of events N in (7.2). To summarize this procedure using $N = \ln 10$ in (7.2) yields a 90 % upper confidence limit on the cross section.

Nevertheless usually a small number of events is detected and moreover estimations on the occuring background should be included in the computations if possible. Therefor more advanced analysis techniques are necessary. In the following two different approaches are investigated which are called the Feldman & Cousins method presented in [37] and the Maximum Gap method from Steve Yellin published in [38].

The Feldman & Cousins method is distinguished from other classical approaches of setting limits especially by the fact that the decision whether upper limits or two-sided confidence intervals should be computed is not made by the person doing the analysis but rather intrinsically by the procedure itself. This is very promising because the authors of [37] showed that the obtained limits are not really confidence intervals if the choice is based on the data obtained. Moreover this method avoids the possible occurance of unphysical or empty intervals. In order to briefly explain the method consider a Poisson process with an unknown expectation value μ and a background with known mean b

$$P(k|\mu) = \frac{(\mu + b)^k}{k!}e^{-(\mu+b)}\,. \tag{7.8}$$

The used procedure amounts to the accomplishment of a certain ordering principle. So considering the fixed background b and a fixed value of μ the corresponding propability (7.8) is computed for several observed events k starting from $k = 0$. Hence the ratio

$$R = \frac{P(k|\mu)}{P(k|\mu_{\text{best}})} \tag{7.9}$$

is computed for all k with $P(k|\mu_{\text{best}})$ denoting the use of that value of μ which gives rise to the maximum possible value of $P(k|\mu)$. This parameter R defines the ordering principle. So the value of n with the highest corresponding value of R is the first value put into the acceptance region. Thus values of n are added to this region in decreasing order of R until the sum of $P(k|\mu)$ finally meets or exceeds the considered confidence level which is 90 % in this case.

Fortunatelly the authors were so kind to provide some tables with prepared results for certain confidence levels including 90 %. Therefor having observed a certain number of events and estimated the number of expected background events the only thing to do is take a look at these tables and find the already computed confidence level for the signal mean μ. The results considering the CDMS and XENON10 experiments can be found in table 7.1. Obviously it turns out that all limits are upper limits and not central confidence intervals as it was expected. Hence the given upper values have to be inserted into (7.2) so for example $N = 2.44$ for silicon. So the modification in the case where the pure Poisson approach is valid as well since no events are detected the Feldman & Cousins method amounts to replace $N = 2.30$ by $N = 2.44$. A disadvantage of this method is that it only incorporates the pure number of events and not their energy distribution. Moreover apart from the normalization even the expected shape of the event distribution is known. The Maximum Gap method incorporates these information finally yielding more stringent limits.

The Maximum Gap method can be used to compute cross section limits in a slightly different way. Unlike the Feldman & Cousins method it is also applicable if there is a certain unknown background contaminating the data. The basic procedure is to find a certain energy range yielding an especially stringent limit. Therefor an interval has to be chosen where the sum of the signal and the background is particularly small. However this is not done manually which would be very subjective since for example low energy ranges are usually dominated by background signals which would result in a weaker upper limit but included in the procedure. It works as follows:

The unbinned data is considered and for every interval between two adjacent measured events the expected number of events is computed which is clearly given by (7.1) but with the the integration limits replaced by the recoil energies of these two events. Since the cross section is unknown this means that the right side of the equation without considering σ_{SI}^n has to be evaluated. Of course the upper and lower analysis limits serve as integration limits as well. So for example taking a look at the germanium data given in table 7.1 it is clear that two intervals have to be considered namely $7 - 64$ keV and $64 - 100$keV. Moreover there is obviously only one interval in the silicon case and eleven considering xenon. It should be self-evident that these integrations might have to be cut-off at the averaged maximum recoil energy. After executing all these computations the one with the highest resulting number of expected events labeled x is chosen which defines the so-called Maximum Gap. It is this interval which is used to compute the upper limit. Remember that the actual expected number of events in the Maximum Gap is still not known since the obtained result still has to be multiplied with the cross section so it would be more precise to write $x(\sigma_{SI}^n)$. However the author of [38] derived a formula for the propability C_0 that the maximum gap is smaller than a certain value of x. It is only dependent on x and μ with the latter clearly being obtained by integrating over the whole energy range:

$$C_0(x,\mu) = \sum_{k=0}^{m} = \frac{(kx-\mu)^{k-1}e^{-kx}}{k!}\Big(k(x-1)-\mu\Big) \tag{7.10}$$

m denotes the greatest integer $\leq \frac{\mu}{x}$. Therefor a 90 % confidence level can be obtained increasing σ_{SI}^n until $C_0 = 0.9$. An interesting case occurs when no events are detected so for example considering the silicon detectors. Then $x = \mu$ gives rise to

$$C_0(\mu,\mu) = 1 - e^{\mu}\,. \tag{7.11}$$

Demanding $C_0 = 0.9$ directly yields $\mu = \ln 10 \approx 2.30$ which is nothing but the pure Poisson limit. This has been used to check the correctness of the Maximum Gap code.

To summarize some of the properties of this method it is clear that it is not very sensitive to the boundaries of the whole energy range considered. Moreover it does not use any kind of binning. Besides it uses information about the shape of the event distribution and it is possible to include unknown background which is different from the Feldman & Cousins method which only incorporates the actual number of events and requires information about the expected background. Therefor the obtained results are usually more stringent. Finally it is important to know that this method is excellent to compute upper limits but it cannot be used to analyze a positive WIMP search signal.

As an annotation the author also published a generalization of the Maximum Gap method in the same paper called Optimum Interval method. This procedure is similar to the Maximum Gap method however not only empty intervals are considered but intervals with an arbitrary number of events. For example in the case of germanium there are three different intervals namely the two already mentioned $7-64$ keV and $64-100$ keV containing no event at all and the whole analysis range from $7-100$ keV containing one event. Unfortunately these investigations do not yield an analytic formula to compute a limit similar to (7.10). Instead Monte Carlo methods are needed to evaluate occuring functions. Fortunately resulting tables and several routines are published on the internet [39]. This method was used to compute spin-independent cross section limits as well. The results can be found in C.1. However since they totally agree with the results obtained using the Maximum Gap method considering silicon and germanium only the latter is accomplished in the spin-dependent case described in the next chapter. The reason for the bend around 50 GeV using xenon is unfortunately not known.

Finally the results of the computations for each target after using (7.5) including the Feldman & Cousins method as well as the Maxmum Gap method can be found in the figures 7.1, 7.2 and 7.3. Since the ansatz for the cross section (3.9) is model-independent these limits are clearly model-independent as well. However

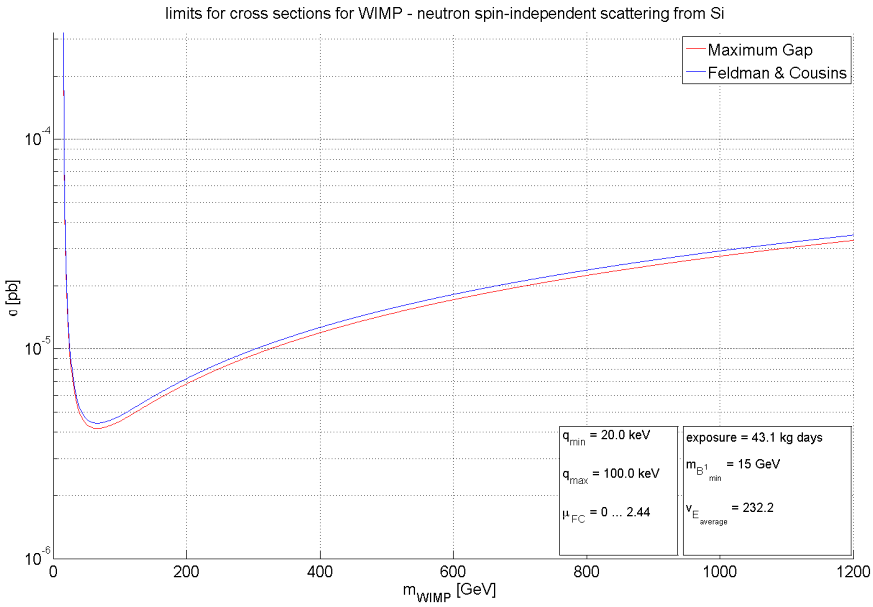

Figure 7.1: Spin-independent cross section limits from silicon detectors used by CDMS.

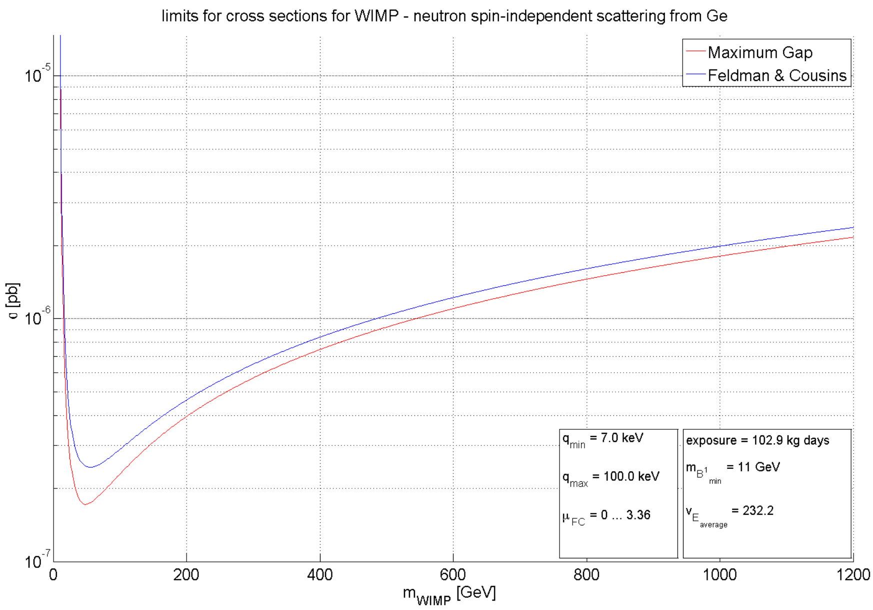

Figure 7.2: Spin-independent cross section limits from germanium detectors used by CDMS.

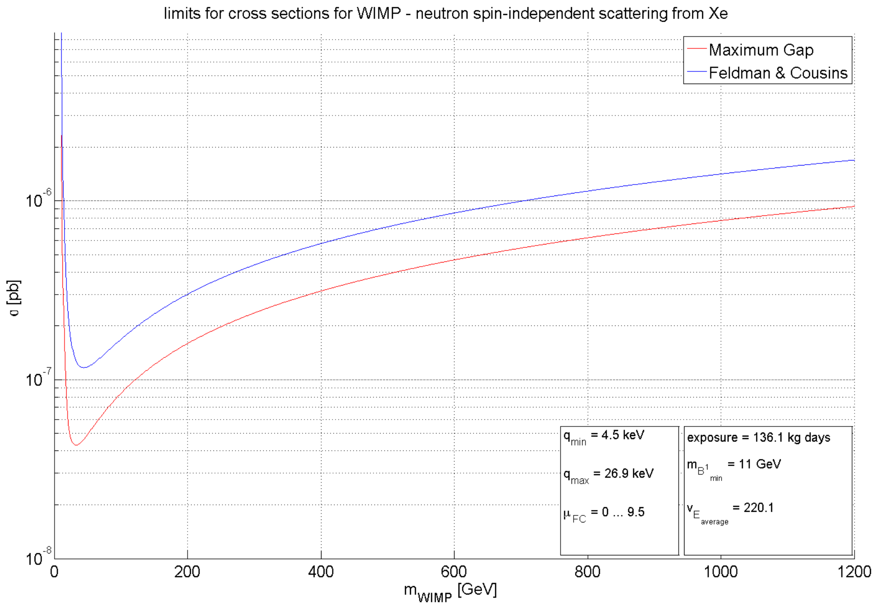

Figure 7.3: Spin-independent cross section limits from XENON10.

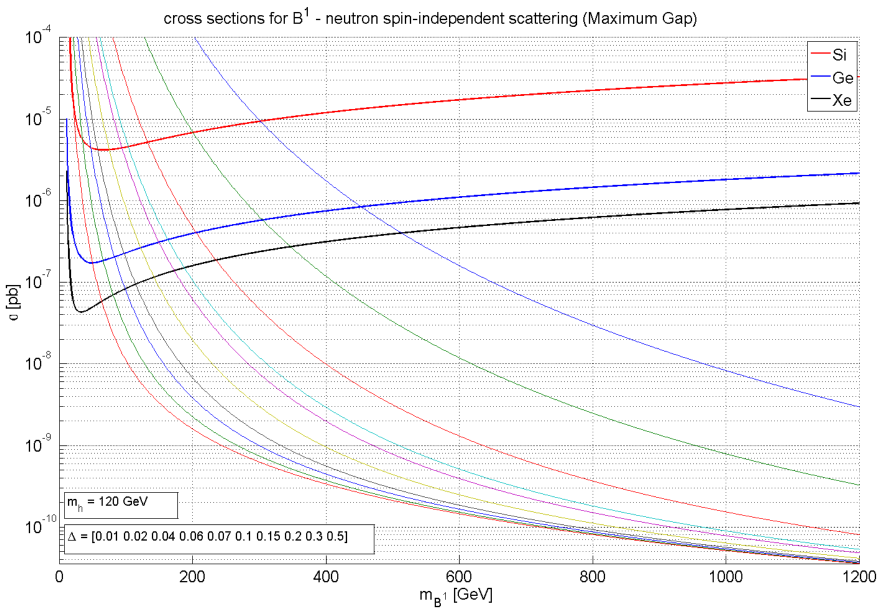

Figure 7.4: Comparison of all spin-independent cross section limits using the Maximum Gap method and theoretical predictions using $m_H = 120$ GeV.

experiment	target	m_W in GeV	σ_{SI} in pb
CDMS	Si	66	$4.17 \cdot 10^{-6}$
	Ge	48	$1.72 \cdot 10^{-7}$
XENON10	Xe	33	$4.31 \cdot 10^{-8}$

Table 7.2: Minimum spin-independent cross section limits computed using the Maximum Gap method and the corresponding WIMP masses.

it should be kept in mind that computing limits for the CDMS experiment a constant efficiency of 0.4 is used which is definitely to high for small recoil energies. Thus these limits surely are a little bit to restrictive.

As expected the results from the Maximum Gap method yield more stringent results in each case. The slightest difference can be observed in the case of Si which is no surprise since as already explained in this case the only difference between both methods is the use of $N = 2.30$ for the Maximum Gap method and $N = 2.44$ for the Feldman & Cousins method.

As another annotation the limits at low masses become significantly larger due to the fact that WIMPs with such masses hardly lead to events with recoil energies above the threshold. Hence the cross sections have to increase significantly to account for the observed signal. Moreover limits in this mass region also depend comparatively severe on the parameters of the velocity distribution used to describe the WIMPs.

For a better comparison between the three used targets and with theoretical predictions figure 7.4 shows all maximum gap limits and the predictions for a Higgs mass of $m_H = 120$ GeV already given in figure 3.3 in one plot. Obviously the xenon target from XENON10 yields the strongest limits. Besides it is encouraging that this experiment just starts to probe the paramter space for 500 GeV WIMPs which accoring to the explained relic density computations is the preferred mass region for dark matter arising from Universal Extra Dimensions.

Before proceeding with the spin-dependent case table 7.2 summarizes the minimum cross section limits obtained using the Maximum Gap method and the corresponding masses.

7.2 Limits on spin-dependent WIMP-nucleon couplings and cross sections

Since it turned out that spin-independent cross sections are expected to dominate WIMP-nuclei interactions the question arises why it should be useful to deal with this problem at all. The first reason is of course that any information concerning WIMP-nucleon couplings would help to identify the nature of the WIMP so especially whether it turns out to be a Kaluza-Klein particle, a particle proposed by Supersymmetry or maybe something completely different. Furthermore it is possible that the spin-independent interaction is strongly suppressed which has already been addressed in the former section. Of course in this case any analysis based on spin-independent cross sections would be useless.

As an annotation before starting with the actual computations it should be mentioned that the power of any experiment to yield limits on WIMP-nucleon interactions strongly depends on the kind of target material via the corresponding form factors and spin expectation values. So of course even-even nuclei are definitely not useful in this context since their spin-dependent sensitivity is clearly negligible though in general not completely vanishing. The four isotopes with spin-dependent sensitivity ^{29}Si, ^{73}Ge, ^{129}Xe and ^{131}Xe used here are all odd-neutron isotopes which is evident from table 3.4. Hence they yield quite strong limits on the WIMP-neutron interactions whereas those considering WIMP-proton interactions are really weak. It will turn out that the fact that no odd-proton isotope is used here leads to the result that it is only slightly possible to diminish the parameter space combining the respective limits. Hence the combination with the results from the analysis of at least one odd-proton isotope would be really advantageous. However this will be explained in more detail below.

As evident from table 3.4 the natural abundance of the target isotopes contributing to spin-dependent interactions is rather low in the case of the CDMS experiment which is the reason for the fact that the corresponding limits were often considered to be negligible. However it turns out that the data is so clean and background free enough to compensate for the low abundances. In contrast the abundances of the two appropriate xenon isotopes are significantly higher and thus clearly yield iinteresting results..

So as alreay pointed out a few times before the spin-dependent case is rather difficult to deal with.

First of all this is due to the fact that the cross sections and the form factors cannot be handled seperately since they are both dependent on the unknown WIMP-nucleon couplings a_p and a_n which in turn can differ by several order of magnitude. Therefor in principle a 3-dimensional parameter space consisting of the WIMP mass and the WIMP-nucleon couplings must be considered. Remember the spin-independent case where after certain reasonable assumptions it was possible to consider a 2-dimensional parameter space using only the WIMP mass and the cross section. In particular it was not necessary to work with the WIMP-nucleon couplings directly. However this problem is a little bit tricky to deal with but it can be solved satisfactorily.

The second problem turns out to be much more severe. It is related to the fact that all form factors computed using the spin structure functions extensively discussed before do not yield reasonable results for all values of the WIMP-nucleon couplings a_p and a_n. This problem can be diminished but not solved properly and discomfort about the obtained results remains.

Besides it should be clear that since the ansatz for the spin-dependent cross section given in (3.22) depends on Δ via $m_{q^{(1)}}$ it is only valid for the discussed UED model and hence the results considering for example neutralino-nucleon scattering in a supersymmetric framework have to be computed separately. This should be contrasted to the spin-independent case where (3.9) gave rise to model-independent results.

In order do accomplish all upcoming computations in an adequate the problem with the form factors should be considered first since it leads to a slight modification of the form factors which actually has already been addressed on page 50. So taking a look at the definition of the form factors (4.2) with (4.15) and (4.14) it is obvious that its nominator and denominator are quadrics considering the functional dependence on the WIMP-nucleon couplings. Therefor it turns out to be very useful to consider polar coordinates in the subspace containing a_p and a_n:

$$\begin{aligned} a_p &= r \sin\theta \\ a_n &= r \cos\theta \end{aligned} \tag{7.12}$$

Clearly pure proton coupling is obtained by setting $\theta = 90°$ whereas the case of pure neutron coupling is given by setting $\theta = 0°$. Inserting this ansatz in (4.15) yields

$$S(q) = r^2 \Big((\sin\theta + \cos\theta)^2 \, S_{00}(q) + (\sin\theta - \cos\theta)^2 \, S_{11}(q) - \cos(2\theta) \, S_{01}(q) \Big) \tag{7.13}$$

which in turn leads to

$$F^2_{SD}(q) = \frac{(\sin\theta + \cos\theta)^2 \, S_{00}(q) + (\sin\theta - \cos\theta)^2 \, S_{11}(q) - \cos(2\theta) \, S_{01}(q)}{(\sin\theta + \cos\theta)^2 \, S_{00}(0) + (\sin\theta - \cos\theta)^2 \, S_{11}(0) - \cos(2\theta) \, S_{01}(0)} \tag{7.14}$$

an expression depending only on the polar angle θ. So in order to investigate the behaviour of these form factors the next step is to scan over the polar angle theta from $0° - 360°$ and see what happens.

The results for the case of ^{129}Xe using the Nijmegen II method can be found in C.2. However any of the considered isotopes ^{29}Si, ^{73}Ge, ^{129}Xe and ^{131}Xe and using any method in the case of the xenon isotopes yields similar outcomes. They are postponed to the appendix because it seems reasonable to show quite a few plots to illuminate the occuring problem. These plots show the respective spin-dependent form factors for $\theta = 0°$ so pure neutron coupling and some angles around $\theta = 90°$. It is quite obvious that there are severe issues for some angles in the latter case. What is already quite obvious is the occurance of two problems. First of all the denominator $S(0)$ can get very close to 0 making F^2 increase dramatically. This problem can be avoided as explained below but apart from that also the general shape of the form factor gets strange e.g. it sometimes increases immediately considering finite momentum-transfer and it can even get negative sometimes which considering the given example is the case for $\theta = 93°$. Of course this behaviour is totally absurd. It should be mentioned that the same problems occur with a phase shift of $\theta = 180°$ and that there are no noticeable problems at other angles. These issues seem to be related to the fact that all considered isotopes are odd-neutron isotopes. This idea can be underpinned by taking a look at an odd-proton isotope like ^{127}I with spin structure functions taking from [28]. In this case the same problems occur but for angles around $\theta = 180°$. Finally it should be mentioned that in the case of ^{131}Xe the QTDA method which is prefered by some authors indeed yields a more reasonable form factor for pure WIMP nucleon coupling than the Bonn A method and the Nijmegen II method but negative results for angles over a $15°$ range from $95° - 110°$.

In order to avoid dividing by values close to 0 take a look at the product of the zero-momentum transfer cross section σ_{SD} given in (3.22) and F_{SD}^2:

$$\sigma_{SD}\, F_{SD}^2 = \frac{2}{3\pi}\mu_T^2 g_1^4 \frac{\Lambda^2 J(J+1)}{(m_{B^{(1)}}^2 - m_{q^{(1)}}^2)^2} \frac{S(q)}{S(0)} \tag{7.15}$$

Obviously the expression (4.13) for $S(0)$ rewritten in the form

$$\frac{J(J+1)}{\pi}\Lambda^2 \frac{1}{S(0)} = \frac{1}{2J+1} \tag{7.16}$$

turns out to be very useful here since now (7.15) can be written as

$$\sigma_{SD}\, F_{SD}^2 = \frac{2}{3}\mu_T^2 g_1^4 \frac{1}{(m_{B^{(1)}}^2 - m_{q^{(1)}}^2)^2} \frac{1}{2J+1} S(q)\,. \tag{7.17}$$

To check the validity of this substitution figure 7.5 shows a comparison of both sides of equation (7.16) with $S(0)$ obtained by evaluating (4.15) at zero-momentum transfer for ^{131}Xe using the Bonn A method.[2] Obviously the substitution seems appropriate for all angles of θ except for the troublesome angles just mentioned. So it can be used as an adequate way to avoid problems related to dividing by values close to zero.

However as already mentioned this does not solve all of the problems since not only the denominator of F^2 which has just been removed is troublesome but also the numerator yielding its shape. This is shown in C.3 where the energy dependence of the differential event rates for ^{129}Xe using the Nijmegen II method and a WIMP mass of 50 GeV for the same angles of θ used in C.2 can be found. Admittedly actually the factor R_0 is missing but since it is clearly independent of the recoil energy this only effects the magnitude of the plots but not their general shape which is clearly inherited from the corresponding form factors. From these plots in the appendix it is quite obvious that the energy dependence of the differential rate shows some strange behaviour in the mentioned angle intervals even after substituting the denominator $S(0)$. Without showing the plots for other isotopes it should be mentioned that this behaviour is worst for the two

[2]Needless to say that the results from all other isotopes look very similar.

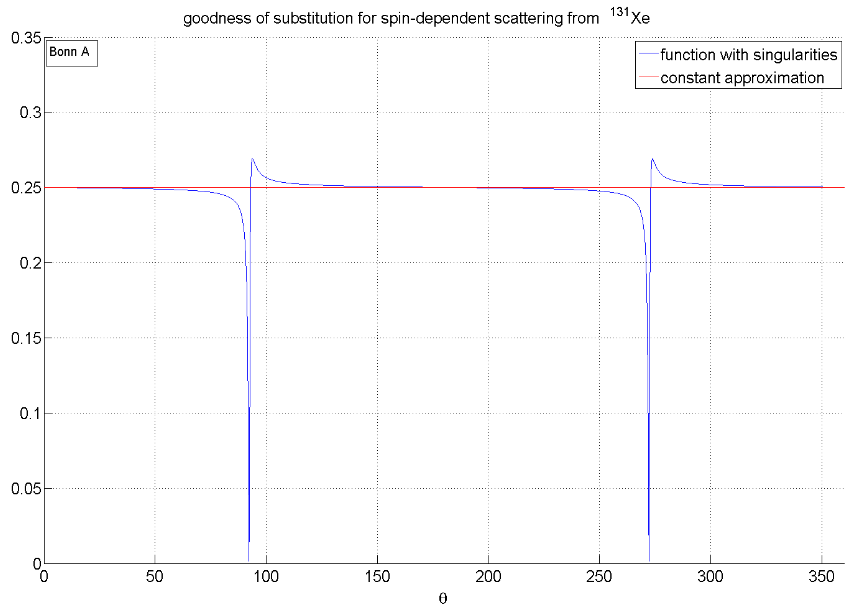

Figure 7.5: Test of the substitution (7.16) in the case of ^{131}Xe using the Bonn A method. "function with singularities" clearly denotes the left side of the equation whereas "constant approximation" denotes the right one. As expected the substitution looks adequate for all angles except those around 90° and 270°.

xenon isotopes especially because as cognizable from the given example the rate drops down significantly at energies slightly above the threshold which naturally contribute the most important part to the total event rate. In the case of silicon and germanium the form factors look a little bit wierd for the mentioned angles as well however the deformation is much less significant.

Keeping these issues in mind the rest of the computation is similar to the spin-independent case and in principle straight forward. The procedure is extensively described in [40]. First of all the number of events has to be considered which is calculated in the same way as in the spin-independent case. The result comparable to (7.1) which is obtained by multiplying the total event rate given in (5.36) with the exposure, the efficency and the appropriate abundence factor in order to consider only one single isotope taking (7.17) into account is

$$N = f{\cdot}exp{\cdot}eff{\cdot}\,\frac{2}{3}\mu_T^2\,g_1^4\,\frac{1}{(m_{B^{(1)}}^2 - m_{q^{(1)}}^2)^2}\,\frac{1}{2J+1}\int_{\mathrm{q_{min}}}^{\min\left(\mathrm{q_{max}},\langle E_{R_{max}}\rangle\right)} \frac{\mathrm{d}R}{\mathrm{d}E_R}|_\sigma\, S(q)\,\mathrm{d}E_R \tag{7.18}$$

with the unknown coefficents a_p and a_n contained in $S(q)$. Since the latter is a quadric considering the functional dependence on the former coefficients N can be written in the form

$$N = A\,a_p^2 + 2\,B\,a_p a_n + C\,a_n^2 \tag{7.19}$$

with the values A, B and C which are constant for a given WIMP mass which will be assumed at the moment:

$$\begin{aligned}
A &= f \cdot exp \cdot eff \cdot \frac{2}{3}\mu_T^2\, g_1^4 \frac{1}{(m_{B^{(1)}}^2 - m_{q^{(1)}}^2)^2}\frac{1}{2J+1} \\
&\quad \cdot \int_{\mathrm{q_{min}}}^{\min\left(\mathrm{q_{max}},\langle E_{R_{max}}\rangle\right)} \frac{\mathrm{d}R}{\mathrm{d}E_R}|_\sigma \left(S_{00}(q) + S_{11}(q) + S_{01}(q)\right) \mathrm{d}E_R \\
B &= f \cdot exp \cdot eff \cdot \frac{2}{3}\mu_T^2\, g_1^4 \frac{1}{(m_{B^{(1)}}^2 - m_{q^{(1)}}^2)^2}\frac{1}{2J+1} \\
&\quad \cdot \int_{\mathrm{q_{min}}}^{\min\left(\mathrm{q_{max}},\langle E_{R_{max}}\rangle\right)} \frac{\mathrm{d}R}{\mathrm{d}E_R}|_\sigma \left(S_{00}(q) + S_{11}(q) - S_{01}(q)\right) \mathrm{d}E_R \\
C &= f \cdot exp \cdot eff \cdot \frac{2}{3}\mu_T^2\, g_1^4 \frac{1}{(m_{B^{(1)}}^2 - m_{q^{(1)}}^2)^2}\frac{1}{2J+1} \\
&\quad \cdot \int_{\mathrm{q_{min}}}^{\min\left(\mathrm{q_{max}},\langle E_{R_{max}}\rangle\right)} \frac{\mathrm{d}R}{\mathrm{d}E_R}|_\sigma \left(S_{00}(q) - S_{11}(q)\right) \mathrm{d}E_R\,.
\end{aligned} \tag{7.20}$$

In order to get a certain idea about the different types of solutions which are possible it is appropriate to remember that the quadric (7.19) describes a conic in the a_p vs. a_n-plane. However since there are no linear terms in a_p or a_n this is not the general form of a second degree polynomial and only three different types of solutions are possible which are furthermore all centered at the origin. These are ellipses, hyperbolas and two parallel straight lines[3] which can be written in the following forms respectively:

$$\frac{x^2}{a^2} + \frac{y^2}{b^2} = 1\,, \qquad \frac{x^2}{a^2} - \frac{y^2}{b^2} = 1\,, \qquad x^2 = a^2 \tag{7.21}$$

where all cross terms leading to a rotation in the x vs. y-plane have been suppressed. However from taking a look at (7.19) rotations definitely occur. The actual type of conic is clearly determined by the relative magnitudes of the coefficients A, B and C which crucially depend on the WIMP mass and the structure functions. Mathematically the shape can be determined by computing

$$D := \det\begin{pmatrix} B & C \\ A & B \end{pmatrix} = B^2 - AC\,. \tag{7.22}$$

$D < 0$ corresponds to an ellipse whereas $D = 0$ correponds to two parallel straight

[3]Two parallel straight lines are in fact called a degenerate conic.

lines and $D > 0$ to a hyperbola. Considering all isotopes for the masses discussed below negative values were obtained so that the only occuring shape is an ellipse. Hence the eigenvectors of the matrix given in (7.22) yield the direction of the major axis and the inverse eigenvalues their lengths.

However it turns out to be much more appropriate to use the polar coordinates introduced in (7.12) which gives rise to

$$N = r^2 \Big(A \, \sin^2 \theta + 2 \, B \, \sin \theta \cos \theta + C \, \cos^2 \theta \Big) \,. \tag{7.23}$$

This in turn can be rewritten as

$$r^2 = \frac{N}{\Big(A \, \sin^2 \theta + 2 \, B \, \sin \theta \cos \theta + C \, \cos^2 \theta \Big)} \tag{7.24}$$

which should be compared to (7.2). The most important difference between these two expressions apart from the troublesome form factors determining A, B and C is that even for a fixed WIMP mass the right side of (7.24) is clearly not constant due to the dependence on θ.

So computing limits on the WIMP-nucleon couplings is accomplished as follows: For any WIMP mass of interest perform a scan over the angle θ from $0° - 360°$ which leads to a constant denominator in (7.24). Hence a limit on r^2 can be computed in exactly the same way as in the spin-independent case using the Feldman & Cousins method as well as the Maximum Gap method. Thus since the determinante D given in (7.22) yielded negative values each time the results are expected to be ellipses in the a_p vs. a_n plane for each considered WIMP mass. So the a_p-a_n parameter space is restricted to the inner region of these ellipses. If a WIMP signal would be observed this analysis would yield two concentric ellipses with the obtained band representing the permitted region and its thickness being defined by the uncertainty in the observed signal.

Of course for a proper analysis it is necessary to scan over a reasonable interval of WIMP masses as well starting with the minimal WIMP masses yielding recoil energies above the threshold given in table 5.1. Since ellipses are obtained for each fixed WIMP mass the result is clearly a closed surface shaped as a tube considering the full 3-dimensional parameter space.[4] However a more useful form is to only consider the ellipses for a few fixed WIMP masses since it is difficult to extract proper results from 3-dimensional plots. Several plots showing the obtained results can be found below after the discussion of another though less exact method to compute limits in the a_p vs. a_n plane.

But before proceeding with the description of this method a short insertion. Apart from the computation of limits on WIMP-nucleon couplings for a given WIMP mass it is quite interesting to calculate limits on the WIMP-neutron cross

[4] A plot like this can be found in C.6 but for neutralino-nucleon scattering. The reason to consider this model as well is discussed later on.

sections considering coupling solely to neutrons which means setting $a_p = 0$ and the other way around setting $a_n = 0$ to compute cross section limits for pure WIMP-proton coupling. However this can be achieved rather easily by remembering that the former case is equivalent to setting $\theta = 0°$ yielding $a_n = r$ and the latter to setting $\theta = 90°$ yielding $a_p = r$. Hence the computed limits on r^2 for $\theta = 0°$ and $\theta = 90°$ directly yield the important limits on pure WIMP-nucleon couplings which can be converted to corresponding cross section limits using the normalization given in (3.27). It is important to note that the obtained limits on the pure WIMP-nucleon cross sections are model independent which is evident from (3.27).

Since obtained results considering pure coupling to protons differ very much from the corresponding results considering pure coupling to neutrons both cases have to be shown separately. This is accomplished in the figures 7.6 and 7.7 for silicon, in 7.8 and 7.9 for germanium and 7.10 and 7.11 for xenon using the Bonn A method with the results from both xenon isotopes combined using (7.5). As expected the limits considering pure coupling to neutrons are much more stringent than the limits related to pure coupling to protons with a difference of about a factor of $100 - 1000$. General annotations about the shape of the curves and the comparison of the Feldman & Cousins method and Maximum Gap method can be found in the corresponding discussion of limits on spin-independent cross sections.

Of course in order to accomplish a comparison between these computed limits and theoretical predictions it is useful to plot all results in two figures one for the coupling to neutrons and another one for the coupling to protons. The theoretical predictions are taken from the figures 3.7 and 3.6 respecively. Moreover similar to the spin-independent case the results considering the Maximum Gap method are used for the comparisons. They can be found in the figures 7.12 and 7.13 respectively. Obviously the XENON10 experiment yields the most stringent limits on these cross sections in both cases. However the results from germanium targets are quite good as well despite of the low abundance of ^{73}Ge. However they are weaker approximately by a factor of 10. An important observation is the fact that even considering the results from XENON10 and pure coupling to neutrons the limits are about a factor of 100 to high to probe the interesting parameter space for WIMP masses of 500 GeV. Before proceeding an important annotation has to be made considering the spin-dependent limits assuming pure coupling to protons or rather $\theta = 90°$. Taking a look at the corresponding differential event rate for ^{129}Xe using the Nijmegen II potential given in C.3 indicates that this curve is to high due to the mentioned form factor problems. Of course this leads to a lower upper limit on the corresponding cross section. An appropriate form factor would certainly yield less stringent results. Since the cross section limits corresponding to this kind of interaction are generally less interesting since odd-proton isotopes naturally yield better results this does not seem to be a real problem. However they are a crucial input to the other method used to compute limits in the a_p vs. a_n plane just mentioned which is described below. This will turn out to be an important problem of this procedure.

experiment	target	method	m_W in GeV	σ_{SI} in pb	m_W in GeV	σ_{SI} in pb
CDMS	Si	—	66	1.02	98	787.77
	Ge	—	46	0.06	50	4.98
XENON10	Xe	Bonn A	28	0.005	32	0.63
		Nijmegen II	30	0.007	32	1.94

Table 7.3: Minimum spin-dependent cross section limits computed using the Maximum Gap method and the corresponding WIMP masses considering pure coupling to neutrons and protons.

To finish the analysis of cross sections the figures 7.16 and 7.17 show a comparison of the respective cross sections obtained from XENON10 accomplishing the Maximu Gap method for three cases using the Nijmegen II and the Bonn A method for both isotopes and the Bonn A method for ^{129}Xe and the QTDA method for ^{131}Xe. Obviously the obtained results differ about a factor of ~ 2 in the case of pure coupling to neutrons and a about a factor of ~ 6 considering pure coupling to protons. Since the former results are clearly more important since they yield more stringent results the difference between using different structure functions is not so severe. Nevertheless it should be kept in mind.

Finally table 7.3 shows the obtained minimum spin-dependent cross section limits obtained using the Maximum Gap method and the corresponding masses.

At this stage the already mentioned other method to calculate limits on the WIMP-nucleon couplings should be presented. It was published in [41] by Tovey et al. which is the reason to call it Tovey method abbreviatoryly. Since the paper considered the theoretical framework of supersymmetry it is the best to explain it using this model as well. So the interaction of interest in this case is the scattering of neutralinos from target nuclei. The corresponding spin-dependent cross section at zero-momentum transfer is given by

$$\sigma_{SD} = 4\, G_F^2\, \mu_T^2\, C_A \tag{7.25}$$

introducing the so called enhancement factor C_A defined as

$$C_A = \frac{8}{\pi}\Lambda^2 J(J+1) \tag{7.26}$$

with Λ given in (3.23).

As an annotation before proceeding it should be noted that all collaborations involved in dark matter experiments usually compute and puplish limits on the WIMP-nucleon couplings accomplishing this supersymmetric framework which was the reason to calculate these limits as well. They are given in C.6. However switching between both frameworks is rather easy because it simply amounts to the substitution

$$
\begin{array}{ccc}
\text{Susy} & \longleftrightarrow & \text{UED} \\
 & & \\
G_F^2 & \longleftrightarrow & \dfrac{1}{48}\dfrac{g_1^4}{(m_{B^{(1)}}^2 - m_{q^{(1)}}^2)^2}
\end{array}
\tag{7.27}
$$

which is evident from comparing (7.25) to (3.22).

In order to continue the discussion of the Tovey method the enhancement factor can be written as

$$
C_A = \frac{8}{\pi}\Big(|a_p\langle S_p\rangle| \pm |a_n\langle S_n\rangle|\Big)^2 \frac{J+1}{J} = \Big(\sqrt{C_A^p} \pm \sqrt{C_A^n}\Big)^2 \tag{7.28}
$$

where the relative sign inside the square is given by the sign of $\frac{a_p\langle S_p\rangle}{a_n\langle S_n\rangle}$ and the proton and neutron contributions are defined as

$$
\begin{aligned}
C_A^p &= \frac{8}{\pi}\big(a_p\langle S_p\rangle\big)^2 \frac{J+1}{J} \\
C_A^n &= \frac{8}{\pi}\big(a_n\langle S_n\rangle\big)^2 \frac{J+1}{J}\,.
\end{aligned}
\tag{7.29}
$$

Using these definitions the contributions of both nucleons to the cross section (7.25) can be separated similarly using

$$
\begin{aligned}
\sigma_A^p &= 4\,G_F^2\,\mu_T^2\,C_A^p \\
\sigma_A^n &= 4\,G_F^2\,\mu_T^2\,C_A^n
\end{aligned}
\tag{7.30}
$$

yielding

$$
\sigma_{SD} = \Big(\sqrt{\sigma_A^p} \pm \sqrt{\sigma_A^n}\Big)^2\,. \tag{7.31}
$$

Note that the quantities σ_A^p and σ_A^n are nothing but convenient auxiliary quantities which however do not represent measurable cross sections. Hence (7.28) and (7.25) can be evaluated for single nucleons leading to

$$
\begin{aligned}
C_p &= \frac{6}{\pi}a_p^2 \\
C_n &= \frac{6}{\pi}a_n^2
\end{aligned}
\tag{7.32}
$$

and thus to

$$\begin{aligned}
\sigma_p &= \sigma_A^p \frac{\mu_p^2}{\mu_T^2} \frac{C_p}{C_A^p} \\
\sigma_n &= \sigma_A^n \frac{\mu_n^2}{\mu_T^2} \frac{C_n}{C_A^p}
\end{aligned} \tag{7.33}$$

Now comes an approximation which obviously is not necessary accomplishing the θ scan explained before. Since as already mentioned the quantities introduced in (7.30) are not measurable quantities the authors made the assumptions

$$\sigma_A^p \approx \sigma_{SD} \qquad \text{and} \qquad \sigma_A^n \approx \sigma_{SD} \tag{7.34}$$

independently which together with the renamings $\sigma_p \to \sigma_p^A$ and $\sigma_n \to \sigma_n^A$ in this case leads to

$$\begin{aligned}
\sigma_p^A &= \sigma_A \frac{\mu_p^2}{\mu_T^2} \frac{C_p}{C_A^p} \\
\sigma_n^A &= \sigma_A \frac{\mu_n^2}{\mu_T^2} \frac{C_n}{C_A^p}
\end{aligned} \tag{7.35}$$

So the quantities σ_p^A and σ_n^A denote the WIMP-nucleon cross sections assuming that it is dominated by the proton and neutron contribution respectively. Comparing (7.33) and (7.35) directly yields the two relations

$$\frac{\sigma_p}{\sigma_p^A} = \frac{\sigma_A^p}{\sigma_{SD}} \qquad \text{and} \qquad \frac{\sigma_n}{\sigma_n^A} = \frac{\sigma_A^n}{\sigma_{SD}} \tag{7.36}$$

Expressing σ_p and σ_n in terms of the WIMP-nucleon couplings and neglecting the difference between the proton and neutron mass inserting (7.36) into (7.31) leads to the final result given by

$$\left(\frac{a_p}{\sqrt{\sigma_p^A}} \pm \frac{a_n}{\sqrt{\sigma_n^A}} \right)^2 = \frac{\pi}{24 G_F^2 \mu_n^2} \tag{7.37}$$

which can be translated to the UED framework using (7.27):

$$\left(\frac{a_p}{\sqrt{\sigma_p^A}} \pm \frac{a_n}{\sqrt{\sigma_n^A}} \right)^2 = \frac{2\pi (m_{B^{(1)}}^2 - m_{q^{(1)}}^2)^2}{g_1^4 \mu_n^2} \tag{7.38}$$

Note that the sign in the brackets of both equations is given by the sign of $\frac{\langle S_p \rangle}{\langle S_n \rangle}$.

According to their definition limits on σ_p^A and σ_n^A are set by the already discussed cross section limits considering pure coupling to protons and neutrons respectively. Since (7.27) and (7.38) actually define two parallel lines it is clear that the exterior of these two lines is excluded. Taking a closer look at the definitions of these lines it is clear that the method only puts straight lines through the points of pure coupling in the a_p vs. a_n plane. Moreover their slope m is given by

$$m = -\,\mathrm{sign}\left(\frac{\langle S_p\rangle}{\langle S_n\rangle}\right)\sqrt{\frac{\sigma_p^A}{\sigma_n^A}} \approx -\frac{\langle S_n\rangle}{\langle S_p\rangle} \tag{7.39}$$

The authors argue that the last "≈" holds exactly. In fact it can be derived by using the expression (3.28) assuming that the obtained cross section limit is equal for pure proton and pure neutron coupling. However it is not which is clear due to the accomplishment of different form factors in each case. Nevertheless using a form factor which is constant with respect to the couplings leads to their result. This is accomplished for example by the Zeplin-II collaboration as stated in [42]. According to this paper they used a form factor arising from higgsino interactions which is particularly small so that the resulting limits are expected to be conservative.

Finally it should be mentioned that it seems that all collaborations searching for dark matter using direct detection use the just explained Tovey method.

After this extensive discussion it is time to take a look at the final results of the computation of setting limits on the WIMP-nucleon couplings. The figures 7.18, 7.19, 7.20 and 7.21 show these results for a fixed WIMP mass of $m_{B^{(1)}} = 50$ GeV and a degeneracy parameter of $\Delta = 0.15$ for all odd-nucleon targets. Moreover the theoretical predictions given in (3.26) are included in these plots as well.

The θ scan and the Tovey method combined with the Feldman & Cousins method as well as the Maximum Gap method are used. Again the results obtained by the Maximum Gap method are more stringent than those using the Feldman & Cousins method. Moreover it is clear that the CDMS limits are a little bit to severe due to the accomplishment of an efficiency of 0.4. Especially from the silicon results it is obvious that the limits from the Tovey method and the θ scan are equal in the cases of pure nucleon coupling as expected. Moreover it is obvious that ^{29}Si is the only isotope where the lines determined by the Tovey method have a positive slope. This can be explained by taking a look at the spin expectation values given in table 4.1.

The general orientation of the obtained ellipses or rather parallel lines is also clear. Since all isotopes have an unpaired neutron limits on a_p are much weaker than on a_n. Hence the allowed regions are almost aligned with the a_p-axis. This alignment is not exact since each isotope has only a little but nevertheless not a vanishing sensitivity to pure WIMP-proton coupling. Note that allowing non-vanishing values of both a_n and a_p the limits on each can be considerably weakened. Consider for example the shown limits computed using ^{73}Ge. Assuming

$a_p = 0$ sets an upper limit on the WIMP-neutron coupling of $a_n \approx 1$. However if the WIMP-proton coupling is considered to be for example $a_p = -10$ the corresponding limit on a_n is approximately doubled.

An important annotation is that the angles of θ leading to unphysical form factors determine the length of the ellipses. This is particularly obvious from both xenon isotopes where the ellipses are degenerate to quadrangles. As a reminder in these cases the problems with the form factors are really significant. In general the problematic angle intervals though small dominate a huge part of the ellipses near the “apexes”. So taking up the position that the form factors are not reliable there limits for these angles must be rejected which means rejecting a huge part of the ellipses. Especially a combination with odd proton isotopes would be very useful here because then only a certain angle interval would be necessary to yield a combined result.

However before taking a look at combined limits from all isotopes figure 7.22 shows ellipses using the θ scan and the Maximum Gap method for a WIMP mass of $m_{B^{(1)}} = 50$ GeV and several values of Δ using ^{73}Ge. Obviously the limits get weaker increasing the degeneracy parameter.

Combined limits using the same configuration as in the last plot can be found in figure 7.23.[5] The overlap of all ellipses marked red clearly yields the region in the a_p vs. a_n plane allowed by all isotopes. Obviously the limits are determined by the results from ^{73}Ge and ^{129}Xe. Even though the orientation of these ellipses is only slight with respect to each other it is sufficent to cut off the “apexs” yielding an overall result which is more reliable. However as already stated a combination with an odd-proton isotope would be even more desirable. Moreover it looks like that considering the used degeneracy parameter $\Delta = 0.15$ a $B^{(1)}$ with a mass of 50 GeV can be excluded.

A comparison of the Bonn A and the Nijmegen II method is shown in C.5.

[5]Combined limits for different values of Δ can be found in C.4.

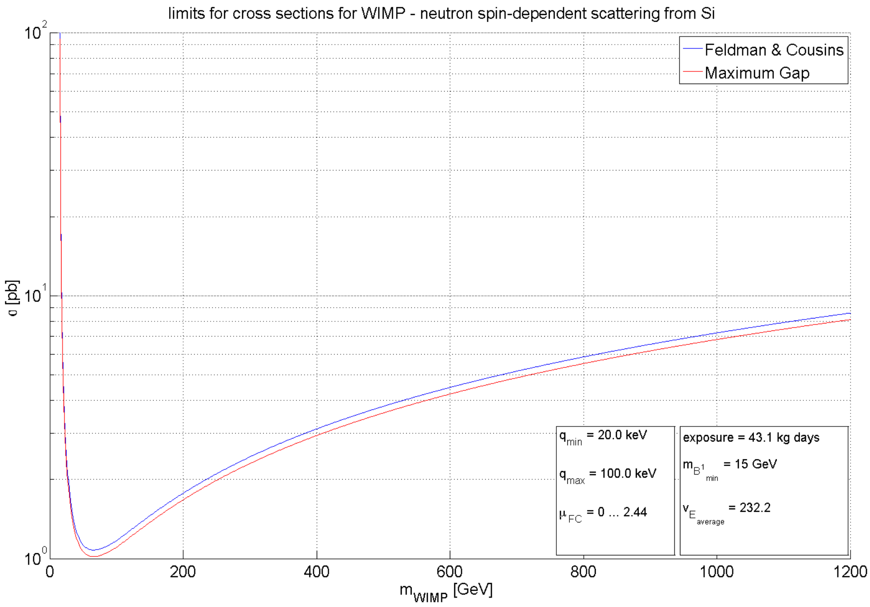

Figure 7.6: Spin-dependent cross section limits from ^{29}Si considering pure coupling to neutrons.

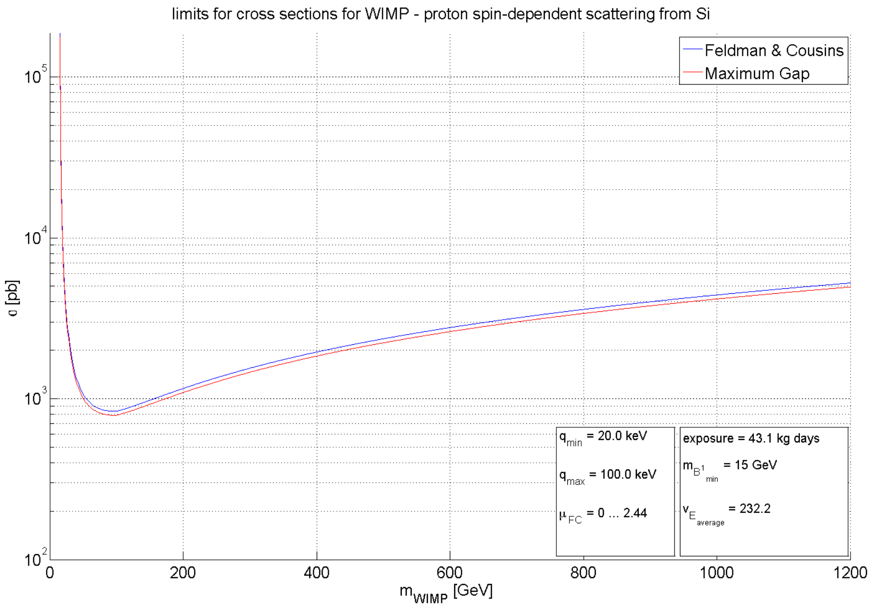

Figure 7.7: Spin-dependent cross section limits from ^{29}Si considering pure coupling to protons.

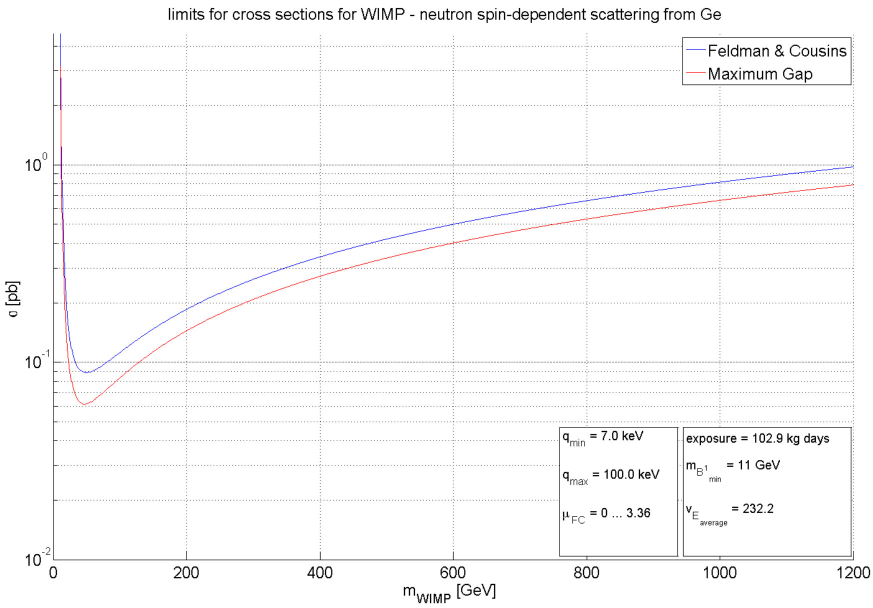

Figure 7.8: Spin-dependent cross section limits from ^{73}Ge considering pure coupling to neutrons.

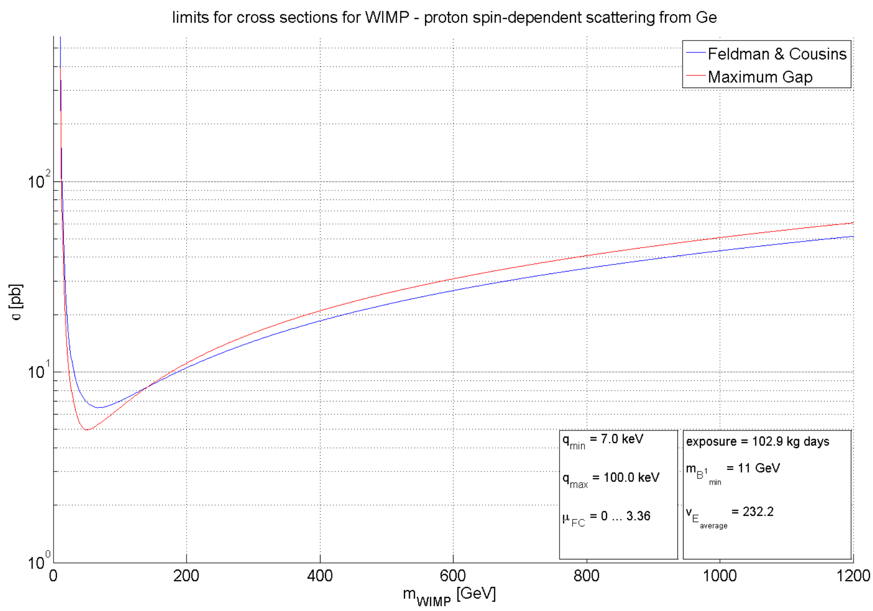

Figure 7.9: Spin-dependent cross section limits from ^{73}Ge considering pure coupling to protons.

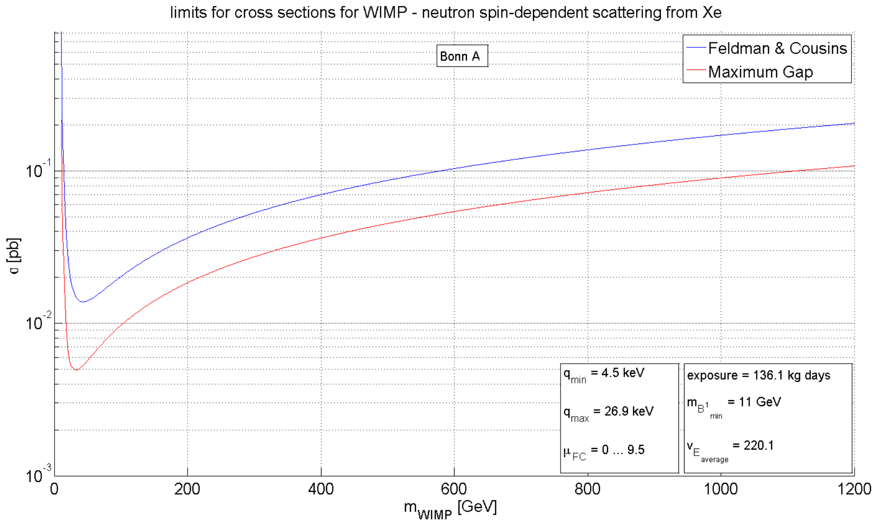

Figure 7.10: Spin-dependent cross section limits from ^{129}Xe and ^{131}Xe considering pure coupling to neutrons.

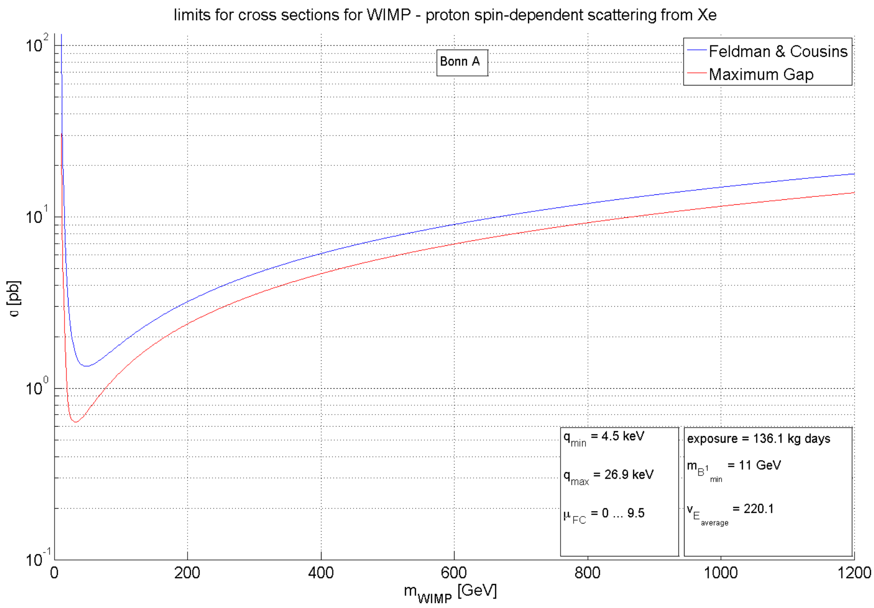

Figure 7.11: Spin-dependent cross section limits from ^{129}Xe and ^{131}Xe considering pure coupling to protons.

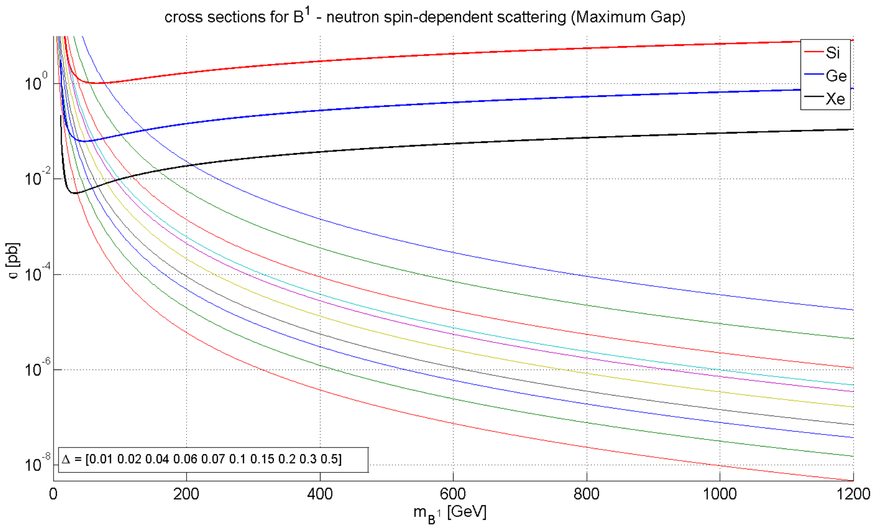

Figure 7.12: Comparison of all spin-dependent cross section limits using the Maximum Gap method and theoretical predictions considering pure coupling to neutrons.

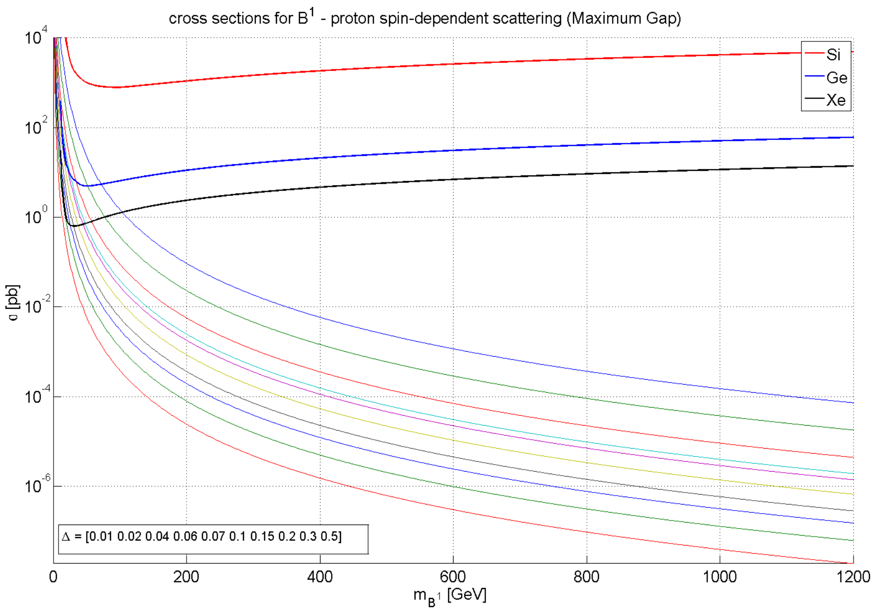

Figure 7.13: Comparison of all spin-dependent cross section limits using the Maximum Gap method and theoretical predictions considering pure coupling to protons.

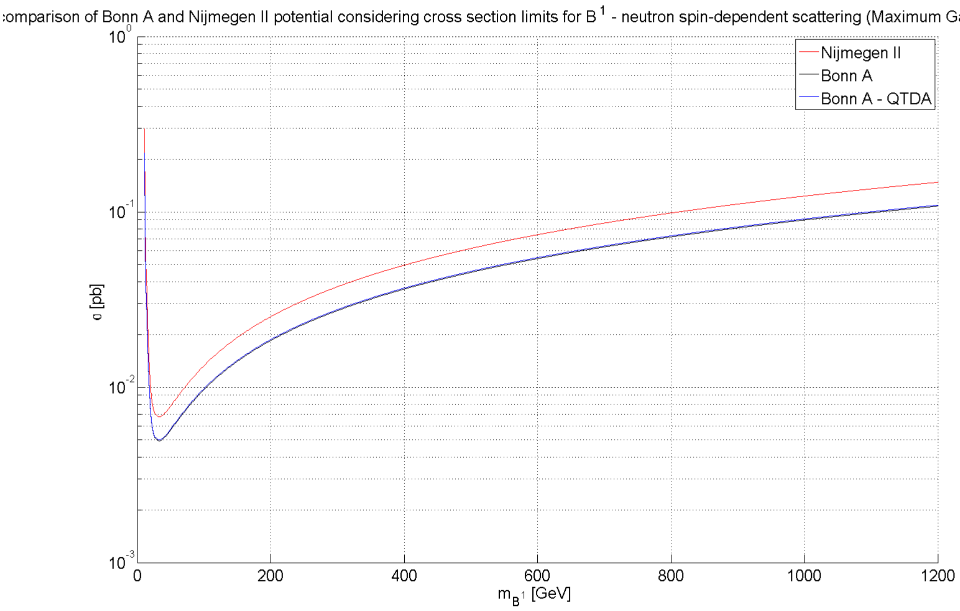

Figure 7.14: Comparison of spin-dependent cross section limits from XENON10 using the Maximum Gap method and different spin structure functions considering pure coupling to neutrons.

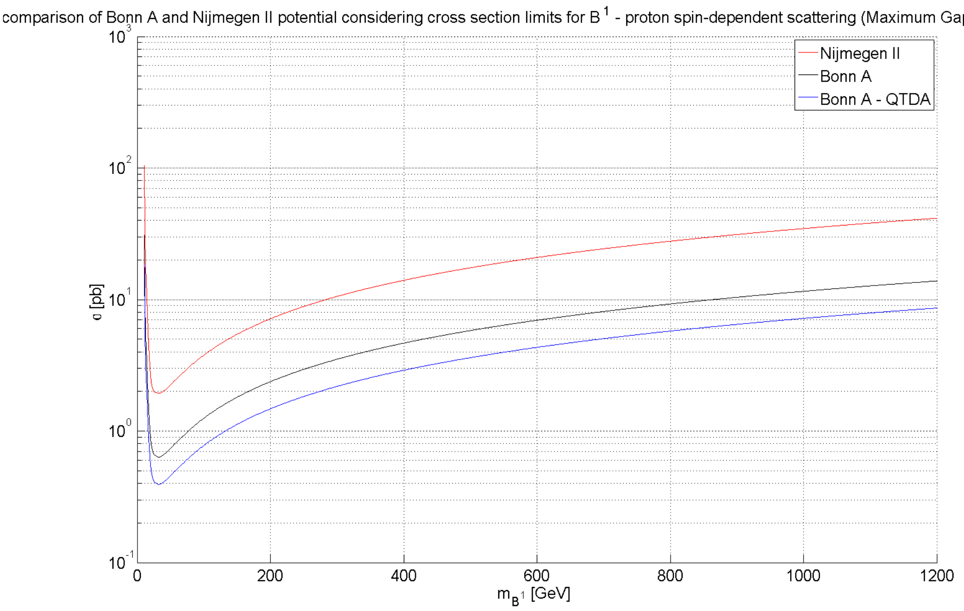

Figure 7.15: Plot similar to figure 7.16 but considering pure coupling to protons.

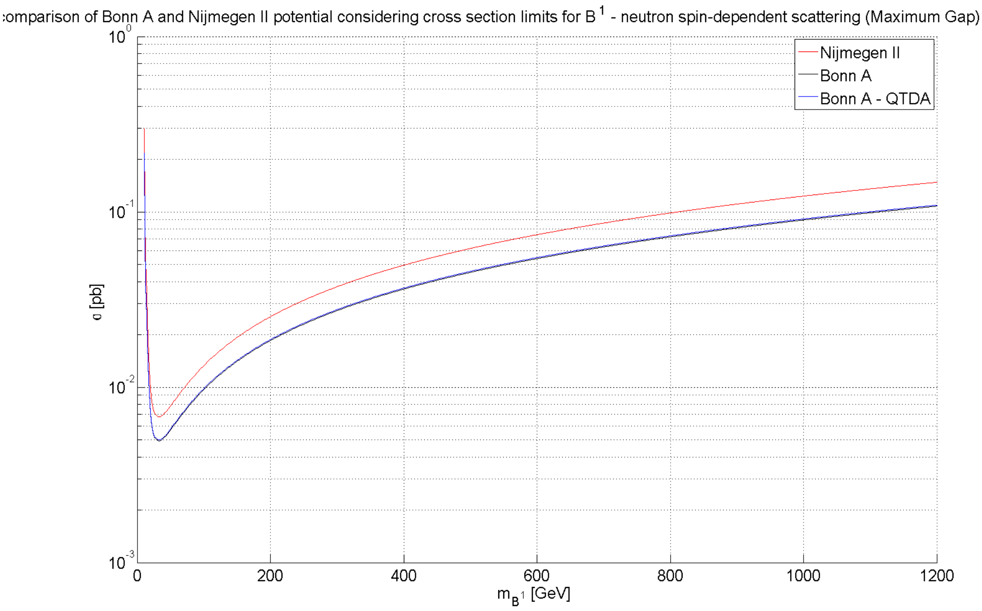

Figure 7.16: Comparison of spin-dependent cross section limits from XENON10 using the Maximum Gap method and different spin structure functions considering pure coupling to neutrons.

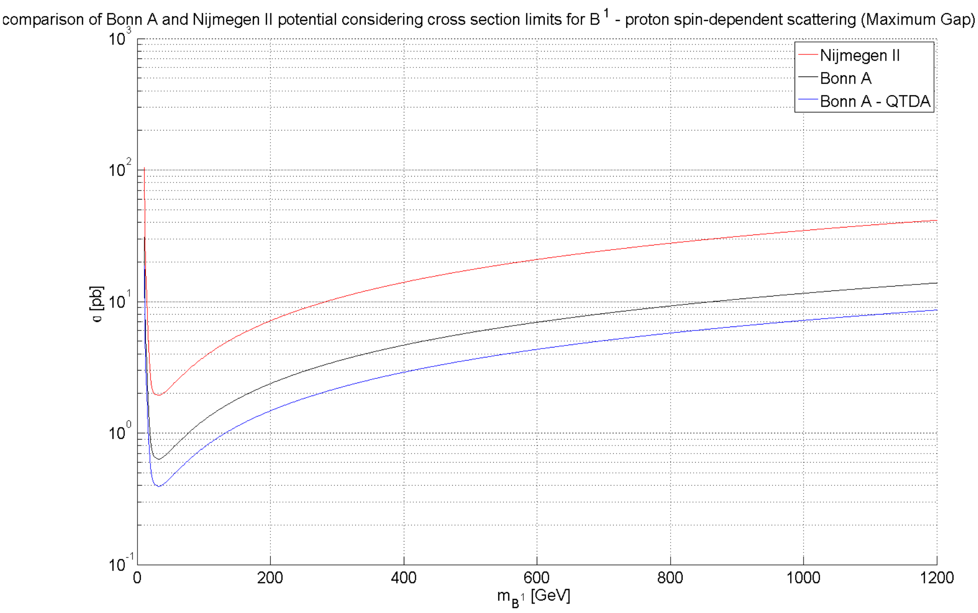

Figure 7.17: Plot similar to figure 7.16 but considering pure coupling to protons.

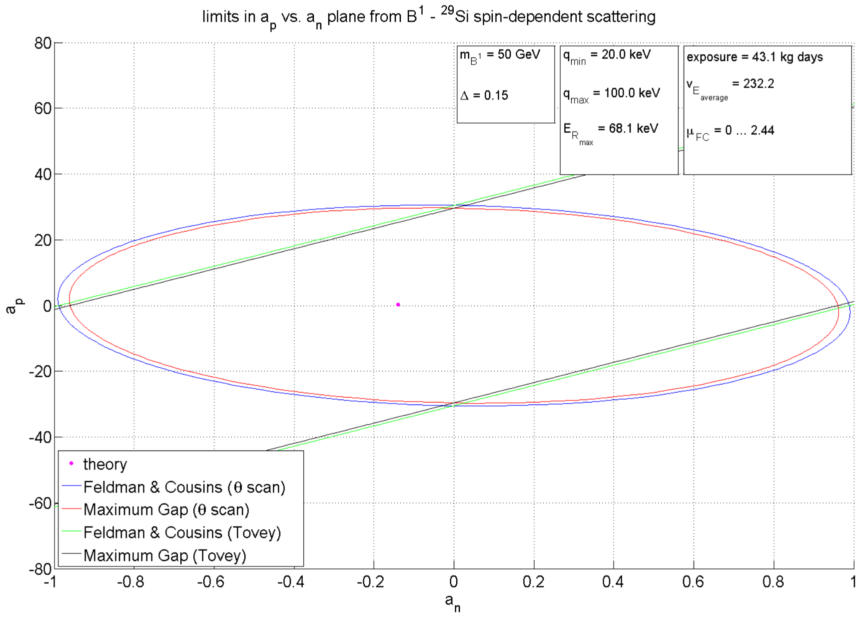

Figure 7.18: Limits on WIMP-nucleon couplings from ^{29}Si using $\Delta = 0.15$ and a WIMP mass of $m_{B^{(1)}} = 50$ GeV.

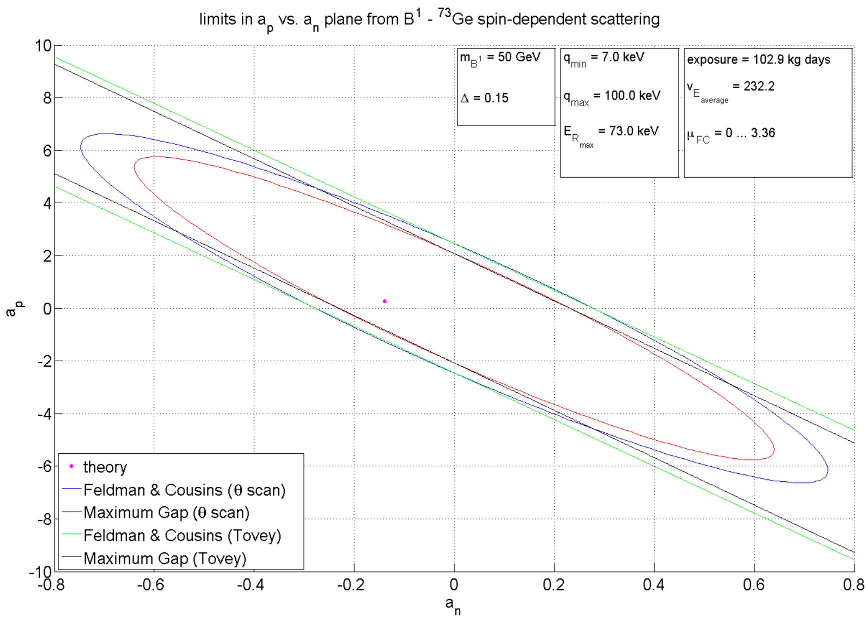

Figure 7.19: Limits on WIMP-nucleon couplings from ^{73}Ge using $\Delta = 0.15$ and a WIMP mass of $m_{B^{(1)}} = 50$ GeV.

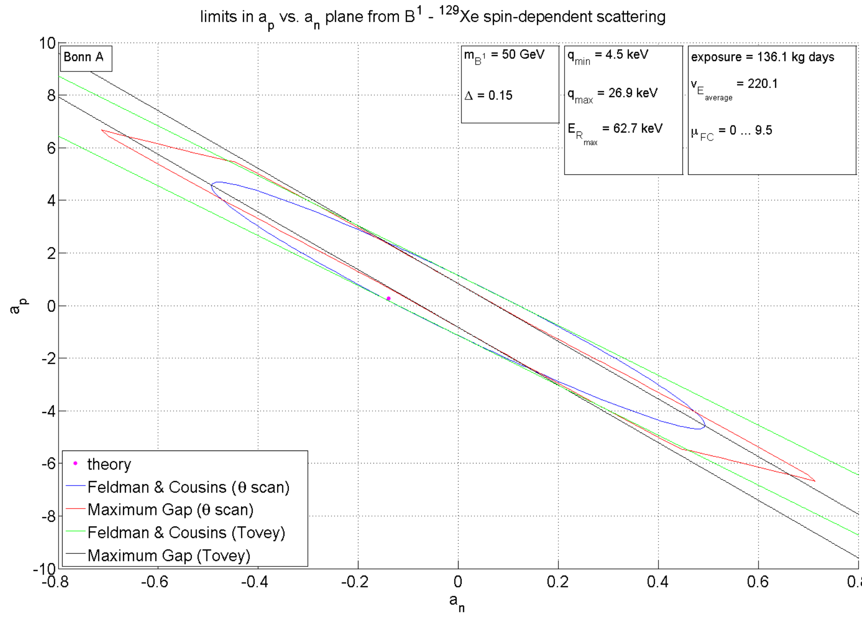

Figure 7.20: Limits on WIMP-nucleon couplings from ^{129}Xe using $\Delta = 0.15$ and a WIMP mass of $m_{B^{(1)}} = 50$ GeV.

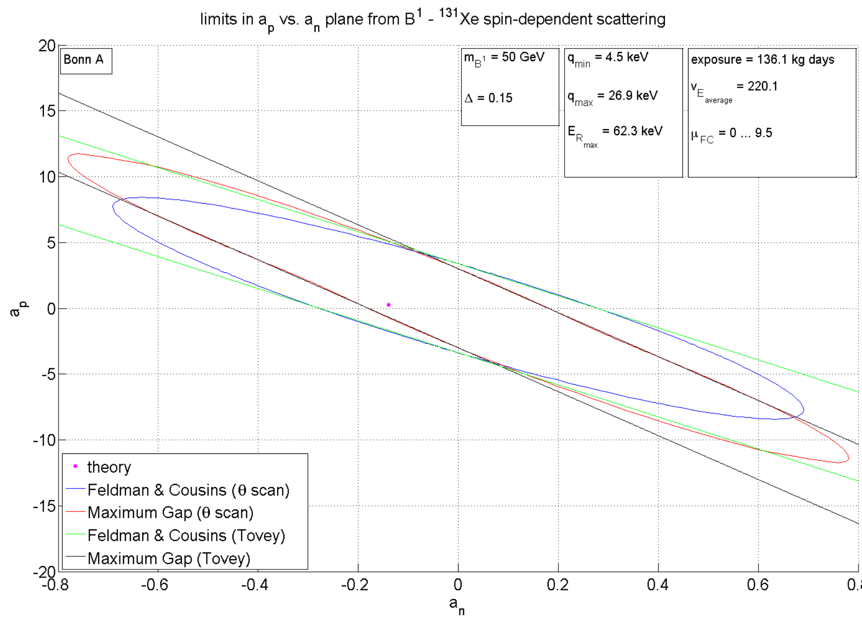

Figure 7.21: Limits on WIMP-nucleon couplings from ^{131}Xe using $\Delta = 0.15$ and a WIMP mass of $m_{B^{(1)}} = 50$ GeV.

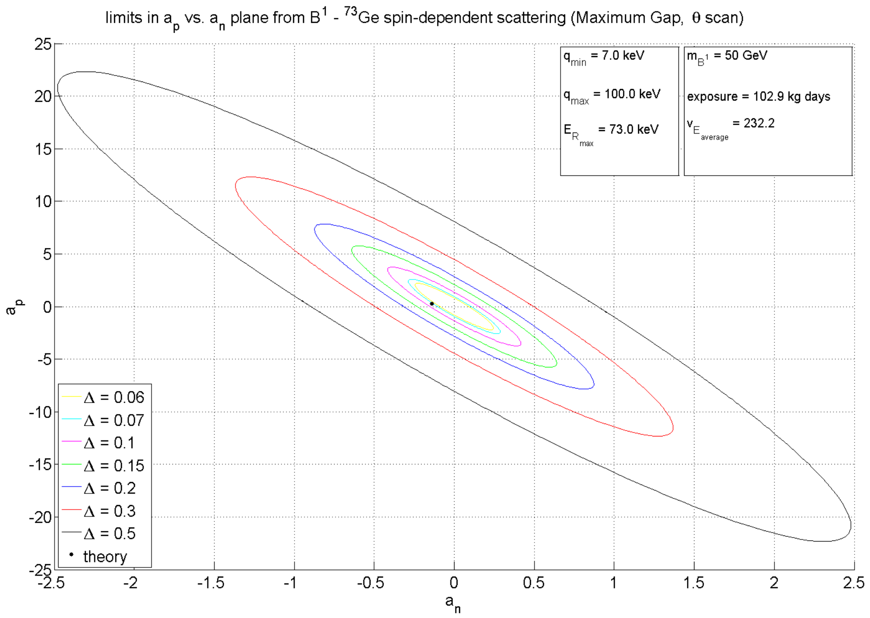

Figure 7.22: Limits on WIMP-nucleon couplings from ^{73}Ge using a WIMP mass of $m_{B^{(1)}} = 50$ GeV and comparing different values of Δ. The accomplished method is a combination of θ scan and Maximum Gap method.

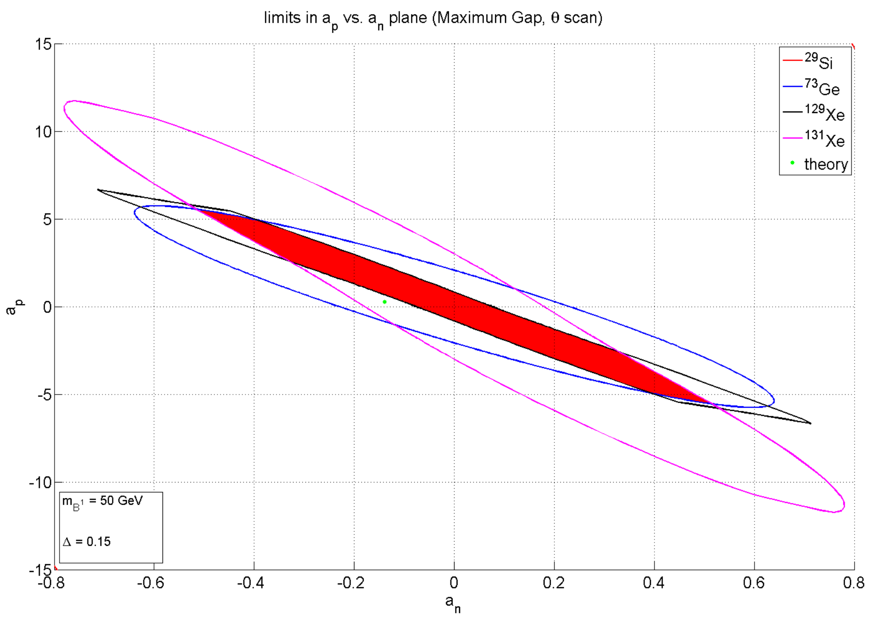

Figure 7.23: Combined limits on WIMP-nucleon couplings using $\Delta = 0.15$ and a WIMP mass of $m_{B^{(1)}} = 50$ GeV.

Chapter 8

Conclusion

In this diploma thesis theoretical predictions from Universal Extra Dimensions and limits on cross sections and WIMP-nucleon couplings were presented. It was shown that in the spin-independent case the considered experiments in particular XENON10 are just starting to probe the parameter space of WIMPs with masses predicted by relic density computations which is a really encouraging result. However much higher exposures are necessary in order to test the interesting spin-dependent parameter space. In this context it is important to know that the CDMS collaboration is already analyzing data from a more recent WIMP search run with five towers and thus with a much higher exposure.

Nevertheless the presented analysis will also have to be redone after the corresponding efficiency is estimated properly. This will change the accomplished constant value of 0.4 to an energy dependent efficiency leading to less stringent limits.

However another important result is that models for the spin-dependent form factors available in the literature are not reliable for certain parameters. This is especially problematic if there are unphysical form factors for pure WIMP-nucleon couplings. Consider the Tovey method which is used by almost all experiments which basically puts a straight line through the points of pure Wimp nucleon couplings. Then how reliable is a limit depending on two points in parameter space from which one is really questionable? Surely using alternative form factors as discussed considering the ZEPLIN-II results is a possibility to avoid these problems. However this is of course undesirable. So new calculations of the spin structure functions are necessary in order to properly investigate the whole parameter space.

In any case the introduced θ scan should be preferred to the Tovey method. First of all this is due to the fact that no additional simplifying assumptions have to be made. Moreover due to unphysical form factors only the lengths of the occuring ellipses are uncertain. However using the Tovey method might lead to wrong slopes of the constraining parallel lines and hence to a wrong shape of the whole allowed region. Obviously the problem with the lengthes of the ellipses can be easily avoided combining the results presented here with other results from odd-proton isotopes. However this clearly cannot compensate wrong slopes of the parallel lines.

Appendix A

Spin-independent cross sections

A.1 Spin-independent cross sections for fixed m_H

In this part of the appendix some plots showing spin-independent $B^{(1)}$-neutron cross sections for fixed values of the Higgs mass can be found. These figures are similar to figure 3.3 so an appropriate description of these plots can be found there. Obviously the dependence of the Higgs mass is rather weak.

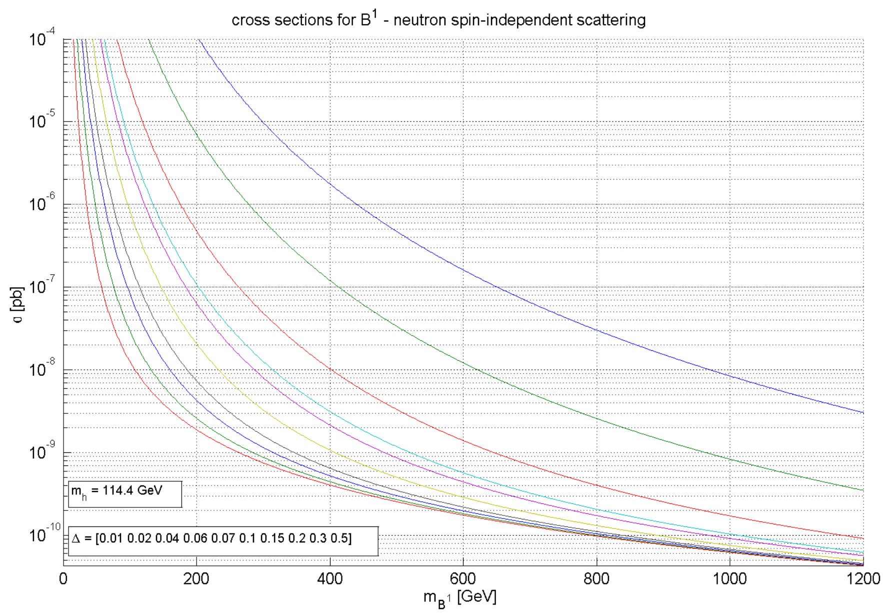

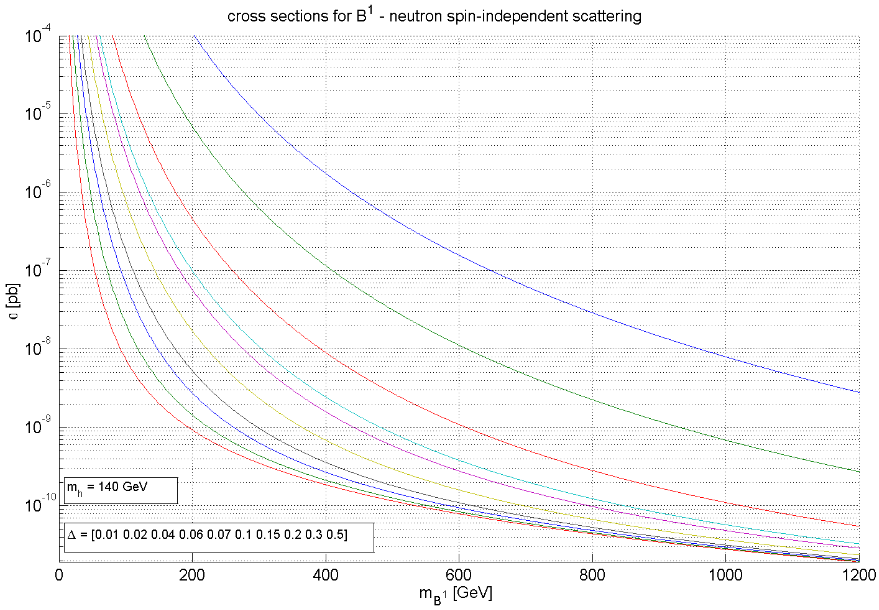
cross sections for B^1 - neutron spin-independent scattering
σ [pb]
m_{B^1} [GeV]
m_h = 140 GeV
Δ = [0.01 0.02 0.04 0.06 0.07 0.1 0.15 0.2 0.3 0.5]

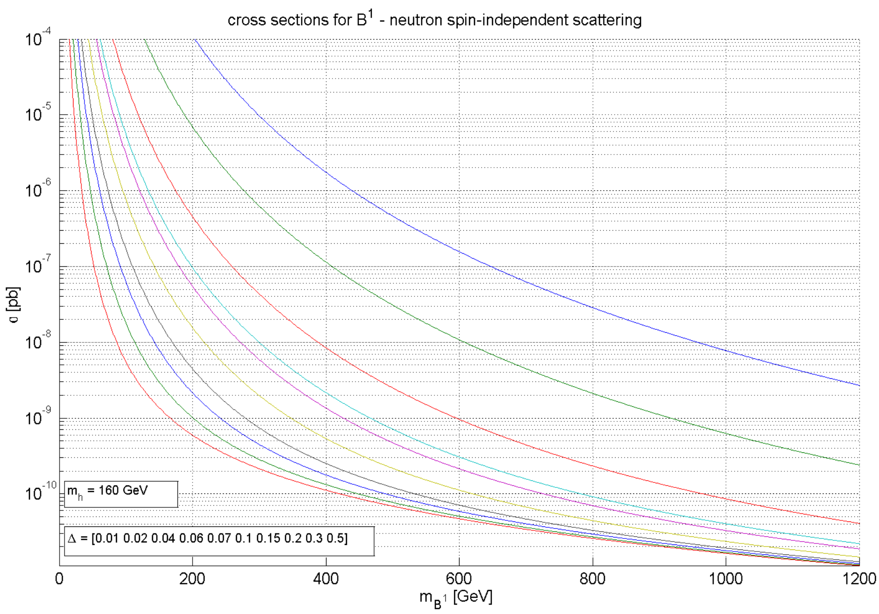
cross sections for B^1 - neutron spin-independent scattering
σ [pb]
m_{B^1} [GeV]
m_h = 160 GeV
Δ = [0.01 0.02 0.04 0.06 0.07 0.1 0.15 0.2 0.3 0.5]

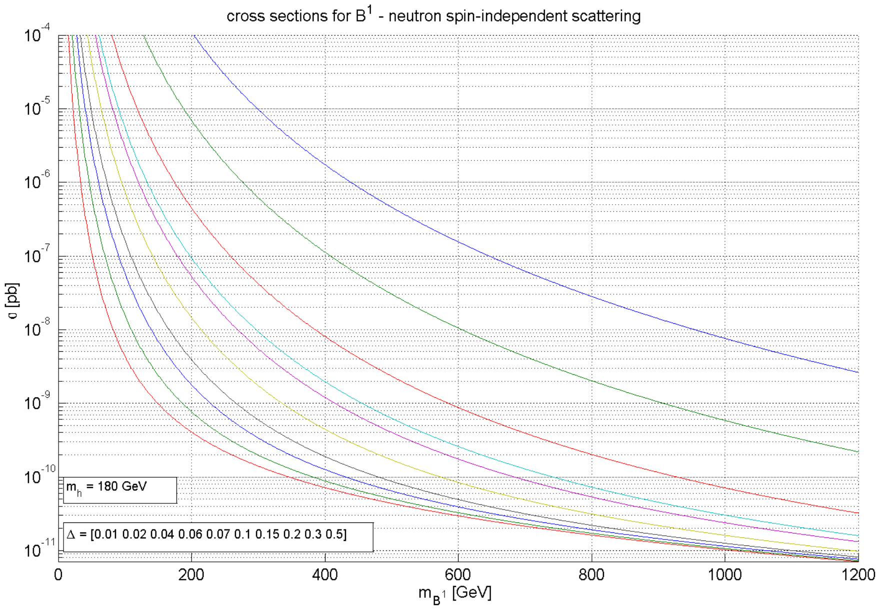
cross sections for B1 - neutron spin-independent scattering
σ [pb]
m_h = 180 GeV
Δ = [0.01 0.02 0.04 0.06 0.07 0.1 0.15 0.2 0.3 0.5]
m_B1 [GeV]

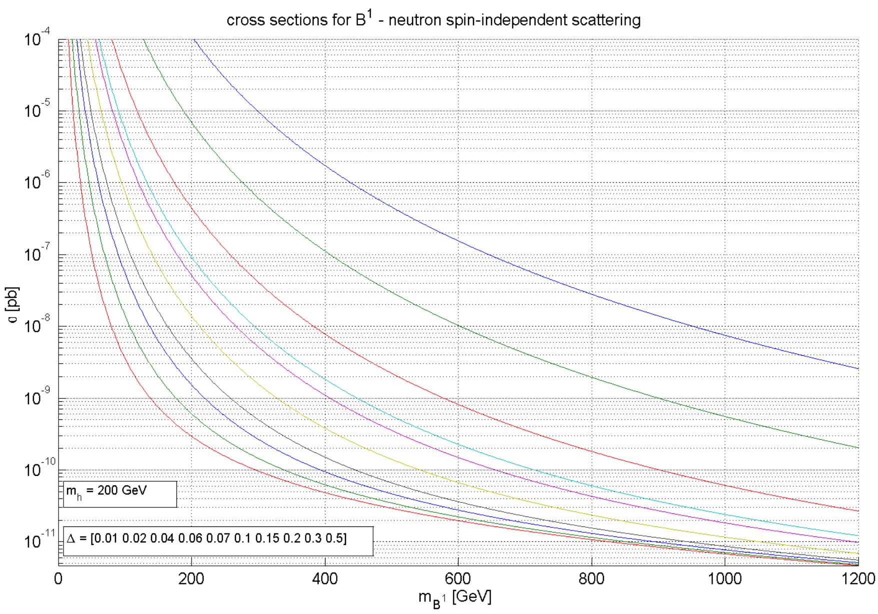
cross sections for B1 - neutron spin-independent scattering
σ [pb]
m_h = 200 GeV
Δ = [0.01 0.02 0.04 0.06 0.07 0.1 0.15 0.2 0.3 0.5]
m_B1 [GeV]

A.2 Spin-independent cross sections for fixed Δ

The plots in this part of the appendix are related to those from A.1 but with a fixed value of Δ instead of a fixed Higgs mass. So they are similar to Figure 3.4. Of course more information about them can be found in the corresponding chapter.

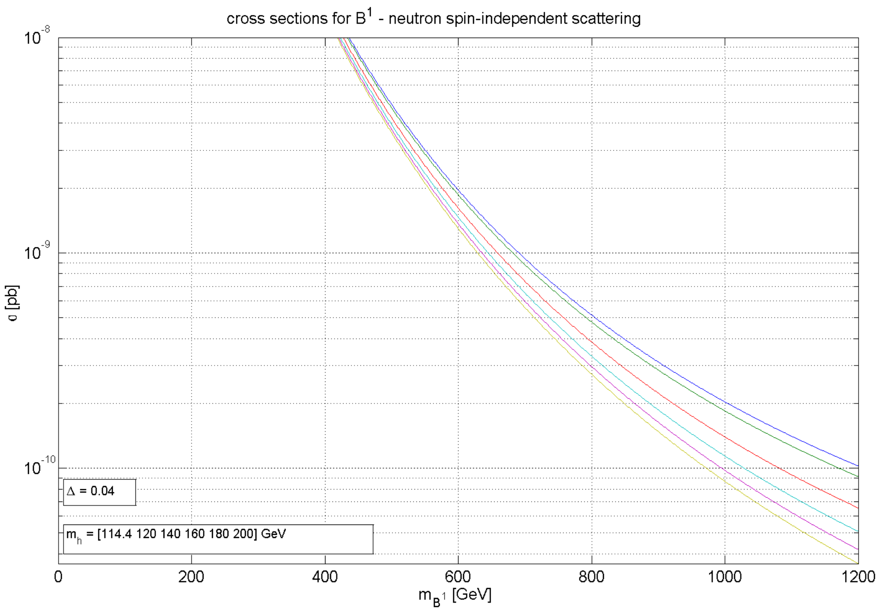

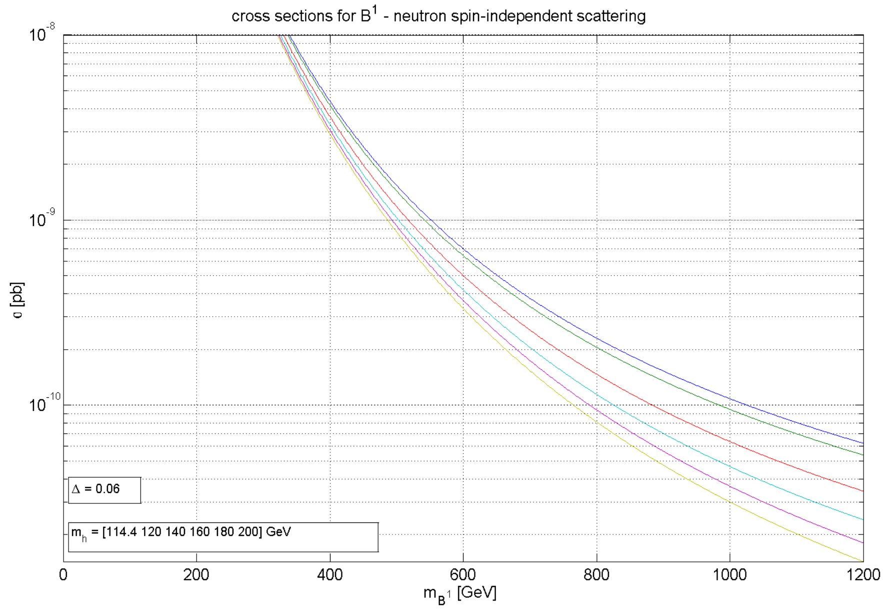
cross sections for B1 - neutron spin-independent scattering
σ [pb]
m_B1 [GeV]
Δ = 0.06
m_h = [114.4 120 140 160 180 200] GeV

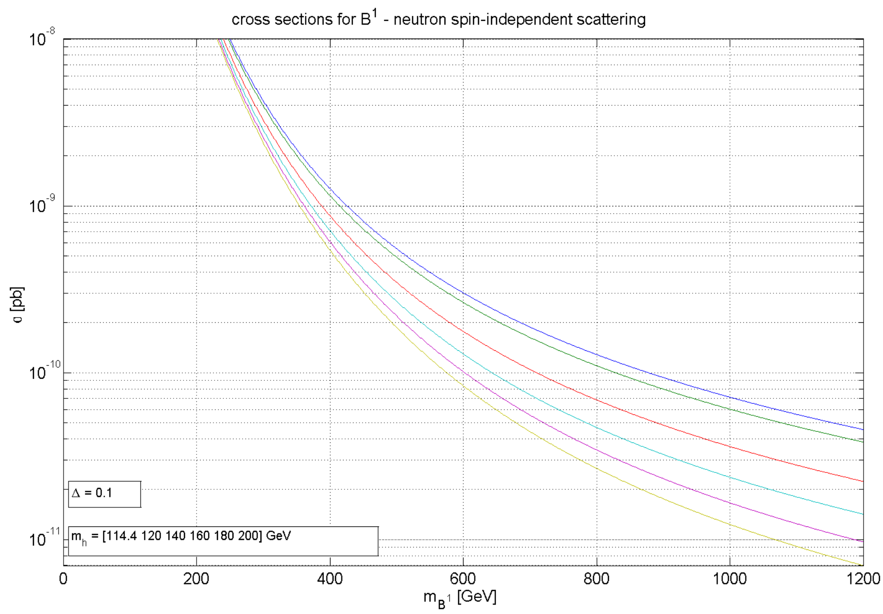
cross sections for B1 - neutron spin-independent scattering
σ [pb]
m_B1 [GeV]
Δ = 0.1
m_h = [114.4 120 140 160 180 200] GeV

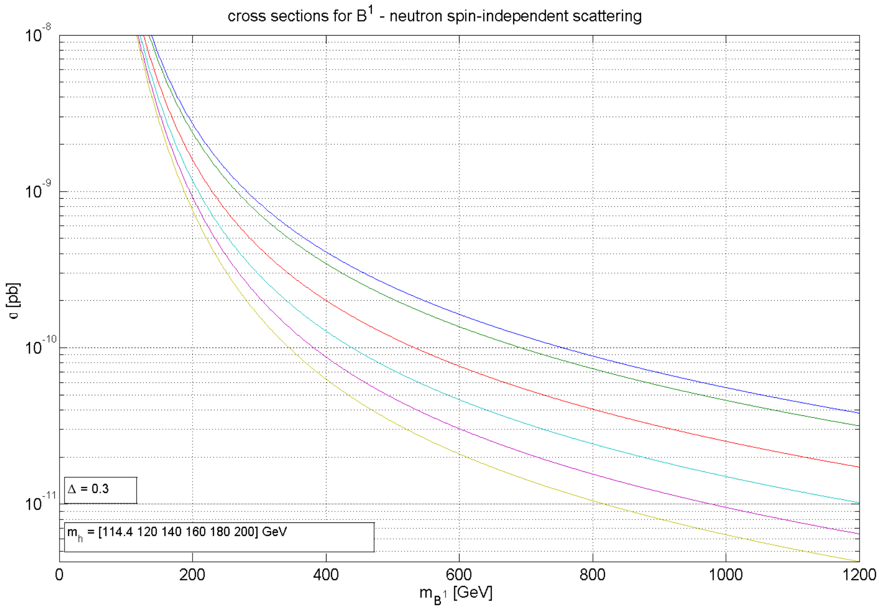
cross sections for B^1 - neutron spin-independent scattering
10^{-8}
10^{-9}
10^{-10}
10^{-11}
σ [pb]
Δ = 0.3
m_h = [114.4 120 140 160 180 200] GeV
0
200
400
600
800
1000
1200
m_{B^1} [GeV]

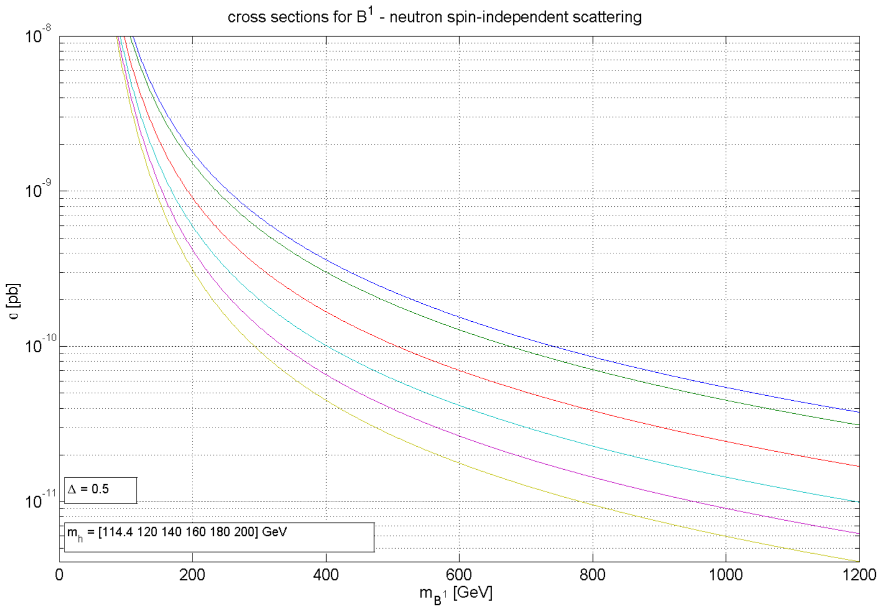
cross sections for B^1 - neutron spin-independent scattering
10^{-8}
10^{-9}
10^{-10}
10^{-11}
σ [pb]
Δ = 0.5
m_h = [114.4 120 140 160 180 200] GeV
0
200
400
600
800
1000
1200
m_{B^1} [GeV]

Appendix B

Event rates

B.1 Differential event rates for various values of Δ

The three plots in this part of the appendix show differential event rates considering scattering from germanium for $\Delta = 0.01$, $\Delta = 0.07$ and $\Delta = 0.30$. These figures are similar to figure 5.9 so an appropriate description of these plots can be found there. As expected the magnitude of the rates depends crucially on the degeneracy parameter.

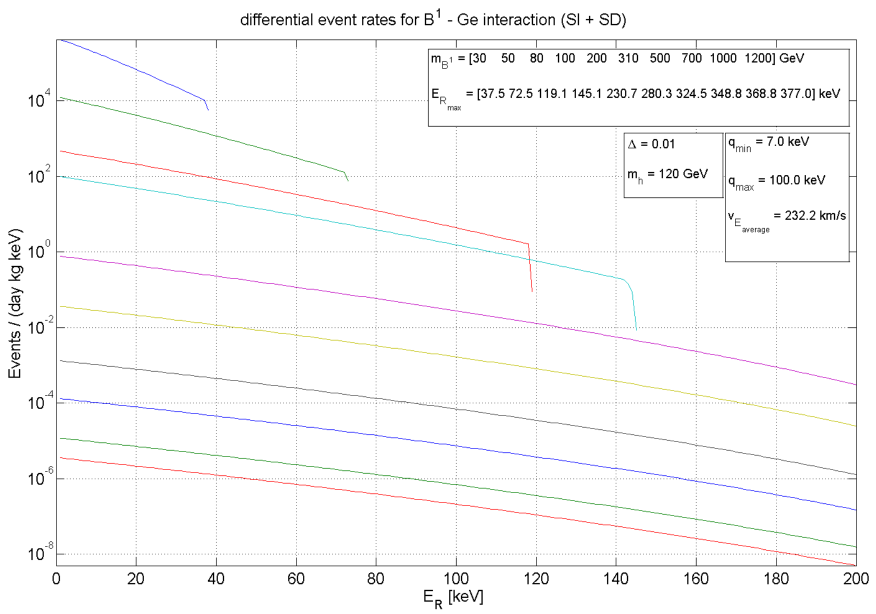

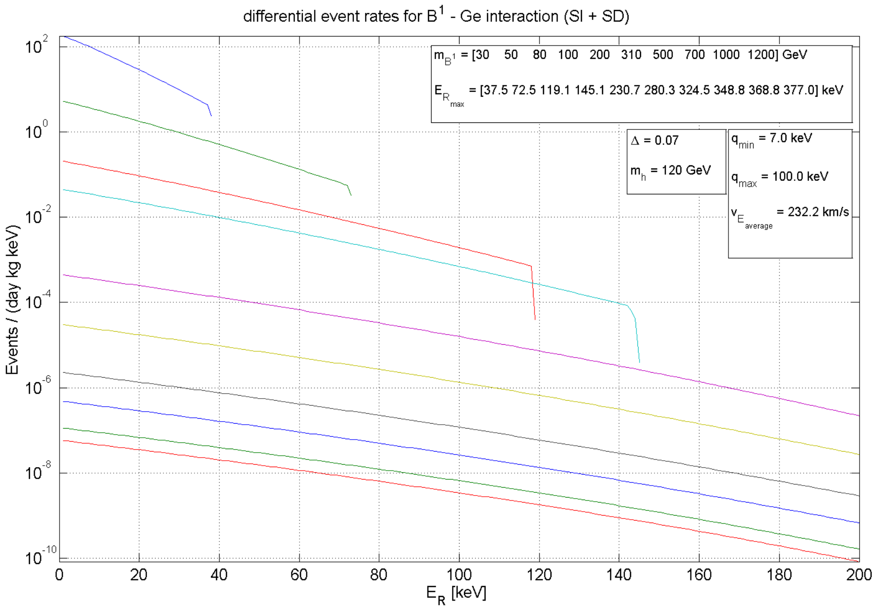
differential event rates for B1 - Ge interaction (SI + SD)
m_B1 = [30 50 80 100 200 310 500 700 1000 1200] GeV
E_Rmax = [37.5 72.5 119.1 145.1 230.7 280.3 324.5 348.8 368.8 377.0] keV
Δ = 0.07
m_h = 120 GeV
q_min = 7.0 keV
q_max = 100.0 keV
v_E average = 232.2 km/s
Events / (day kg keV)
E_R [keV]

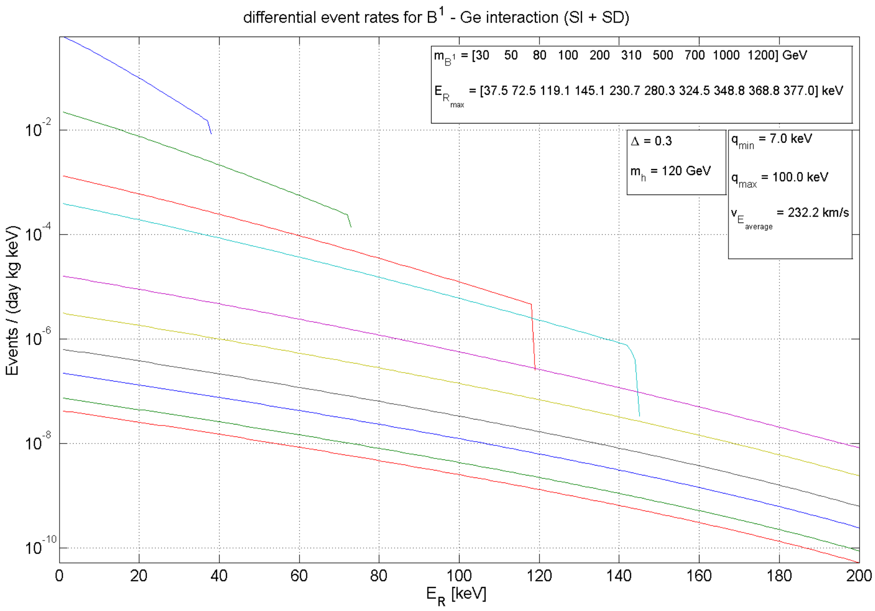
differential event rates for B1 - Ge interaction (SI + SD)
m_B1 = [30 50 80 100 200 310 500 700 1000 1200] GeV
E_Rmax = [37.5 72.5 119.1 145.1 230.7 280.3 324.5 348.8 368.8 377.0] keV
Δ = 0.3
m_h = 120 GeV
q_min = 7.0 keV
q_max = 100.0 keV
v_E average = 232.2 km/s
Events / (day kg keV)
E_R [keV]

B.2 Spin-dependent differential event rates

In this section spin-dependent differential event rates considering scattering from silicon, germanium and xenon can be found. Abundance factors are included. These figures correspond to the figures 5.8, 5.9 and 5.10 whereas both types of interaction are incorporated in the latter. Note that the rates shown here are much lower than in the related figures just mentioned.

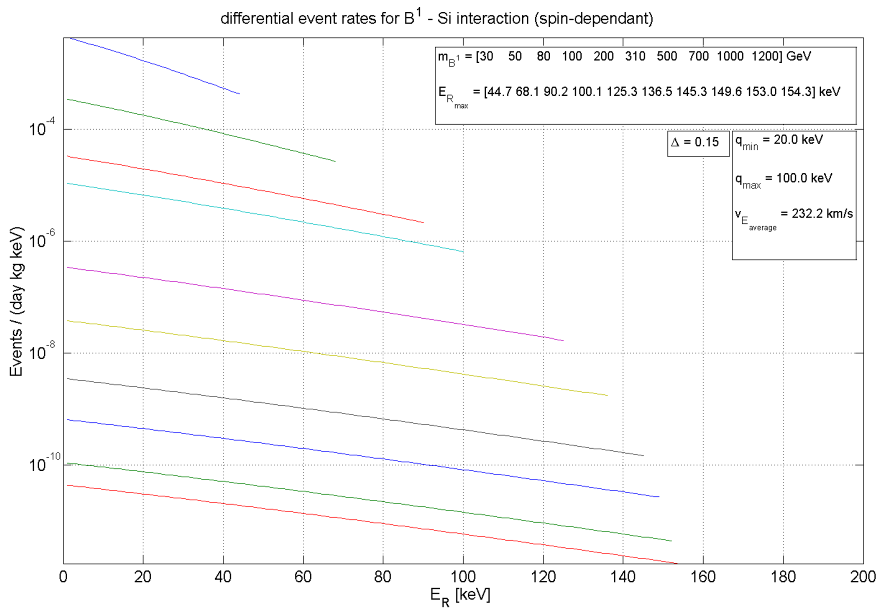

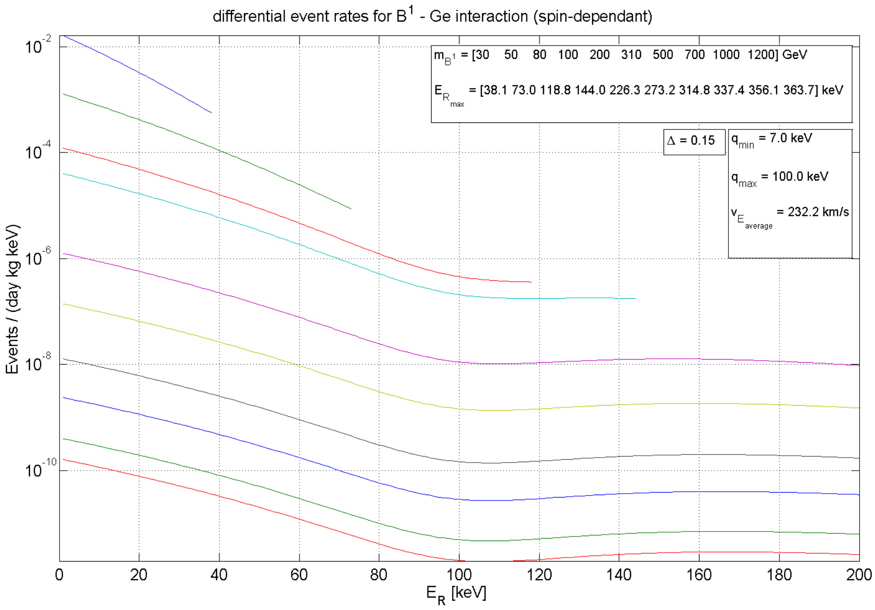
differential event rates for B1 - Ge interaction (spin-dependant)
m_B1 = [30 50 80 100 200 310 500 700 1000 1200] GeV
E_R max = [38.1 73.0 118.8 144.0 226.3 273.2 314.8 337.4 356.1 363.7] keV
Δ = 0.15
q_min = 7.0 keV
q_max = 100.0 keV
v_E average = 232.2 km/s
Events / (day kg keV)
E_R [keV]

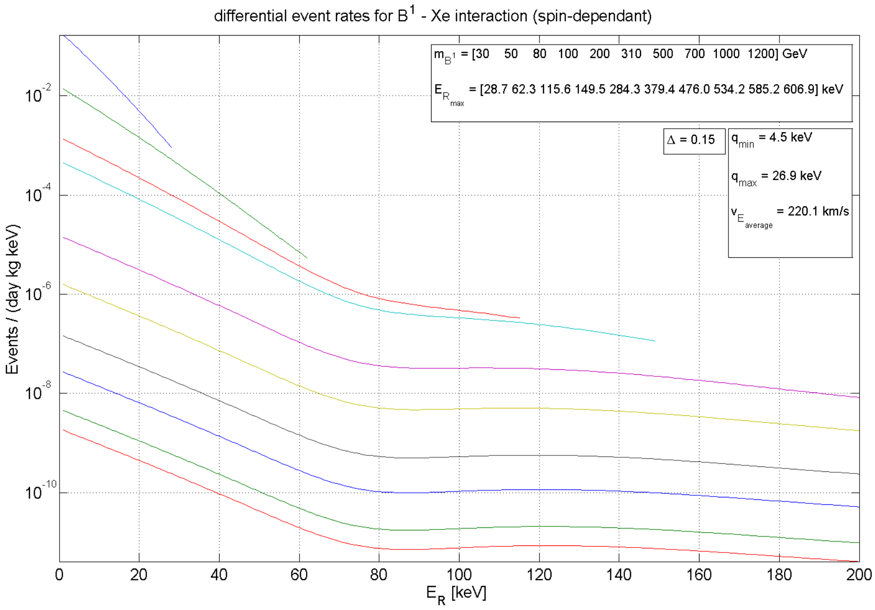
differential event rates for B1 - Xe interaction (spin-dependant)
m_B1 = [30 50 80 100 200 310 500 700 1000 1200] GeV
E_R max = [28.7 62.3 115.6 149.5 284.3 379.4 476.0 534.2 585.2 606.9] keV
Δ = 0.15
q_min = 4.5 keV
q_max = 26.9 keV
v_E average = 220.1 km/s
Events / (day kg keV)
E_R [keV]

B.3 Total event rates for various values of Δ

The following three plots show total event rates considering scattering from germanium for $\Delta = 0.01$, $\Delta = 0.07$ and $\Delta = 0.30$. These figures are similar to figure 5.13 so an appropriate description of these plots can be found there. As expected the magnitude of the rates depends crucially on the degeneracy parameter.

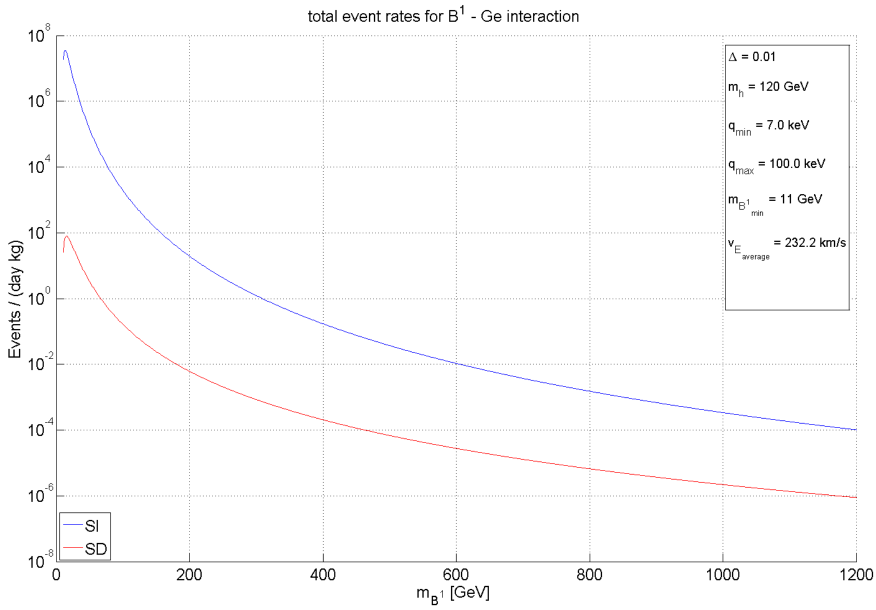

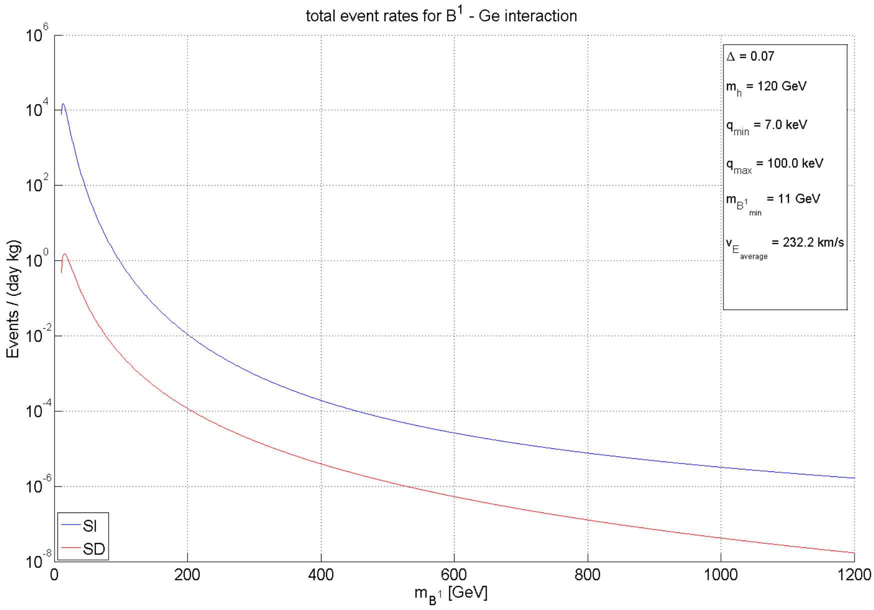
total event rates for B^1 - Ge interaction
Δ = 0.07
m_h = 120 GeV
q_{min} = 7.0 keV
q_{max} = 100.0 keV
$m_{B^1_{min}}$ = 11 GeV
$v_{E_{average}}$ = 232.2 km/s
Events / (day kg)
m_{B^1} [GeV]
SI
SD

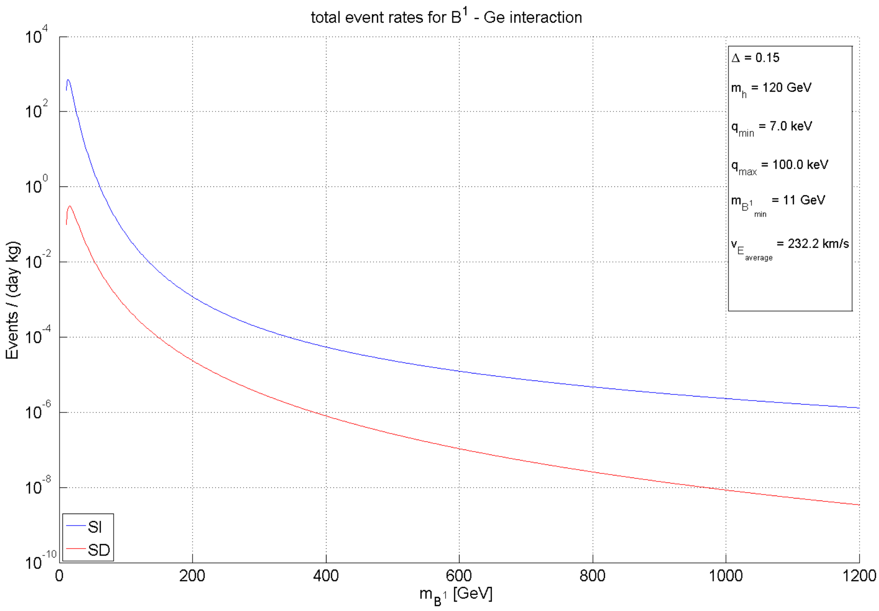
total event rates for B^1 - Ge interaction
Δ = 0.15
m_h = 120 GeV
q_{min} = 7.0 keV
q_{max} = 100.0 keV
$m_{B^1_{min}}$ = 11 GeV
$v_{E_{average}}$ = 232.2 km/s
Events / (day kg)
m_{B^1} [GeV]
SI
SD

B.4 Total event rates for negligible threshold

This plot shows spin-independent and spin-dependent total event rates considering scattering from ^{73}Ge using the usual parameters $\Delta = 0.15$ and $m_H = 120$ GeV and a really low threshold of only 0.01 keV. This negligible threshold leads to the disappearence of the bend at low masses as shown for example in the corresponding figure 5.13.

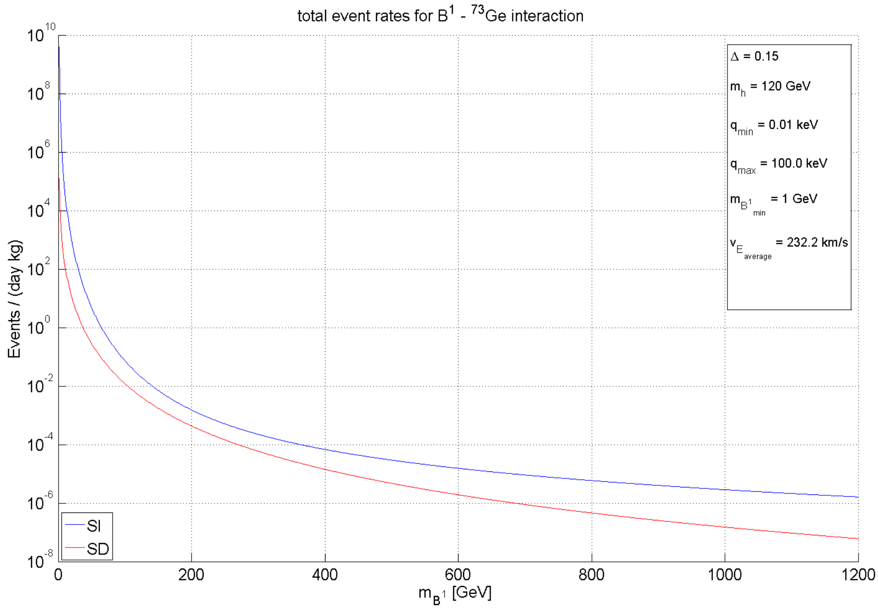

Appendix C

Limits on cross sections and WIMP-nucleon couplings

C.1 Limits on spin-independent cross sections using the Optimum Interval method

This section shows results from the computations of spin-independent cross section limits for silicon, germanium and xenon using the Feldman & Cousins, Maximum Gap and Optimum Interval method. In fact the two former results are already shown in the figures 7.1, 7.2 and 7.3. In the case of silicon and germanium it is really difficult to see the curves from the Optimum Interval method because they are almost totally equal to the ones obtained using the Maximum Gap method. As an annotaion the reason for the bend at a WIMP mass of around 50 GeV unfortunately could not be revealed. However since the Maximum Gap method and the Optimum Interval method clearly lead to very similar results only the former is used in the spin-dependent case.

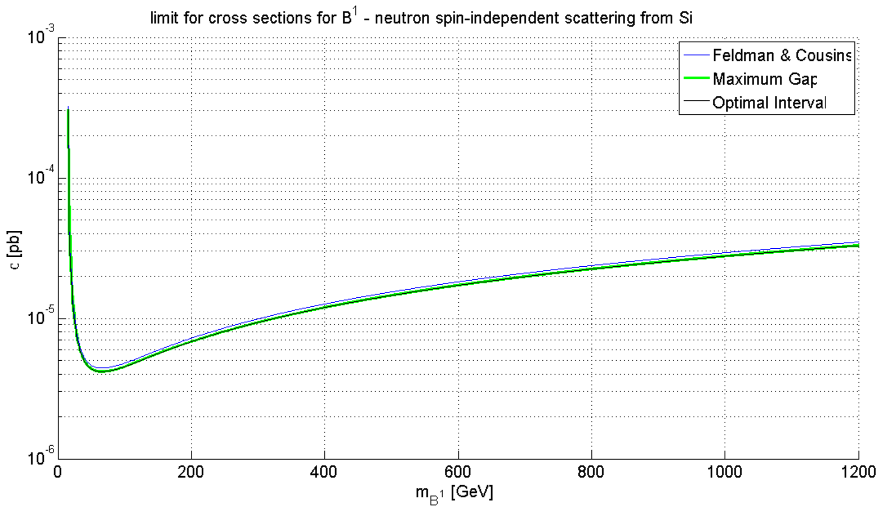
limit for cross sections for B1 - neutron spin-independent scattering from Si
Feldman & Cousins
Maximum Gap
Optimal Interval
c [pb]
m_B1 [GeV]

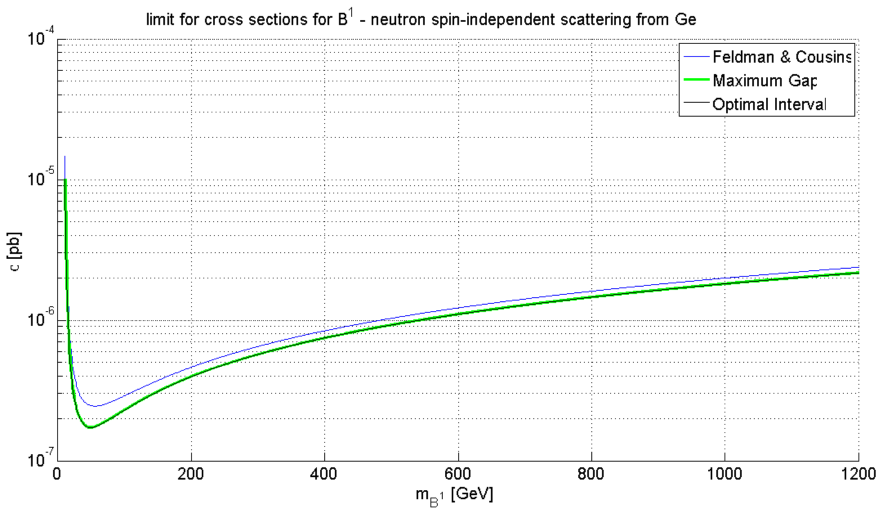
limit for cross sections for B1 - neutron spin-independent scattering from Ge
Feldman & Cousins
Maximum Gap
Optimal Interval
c [pb]
m_B1 [GeV]

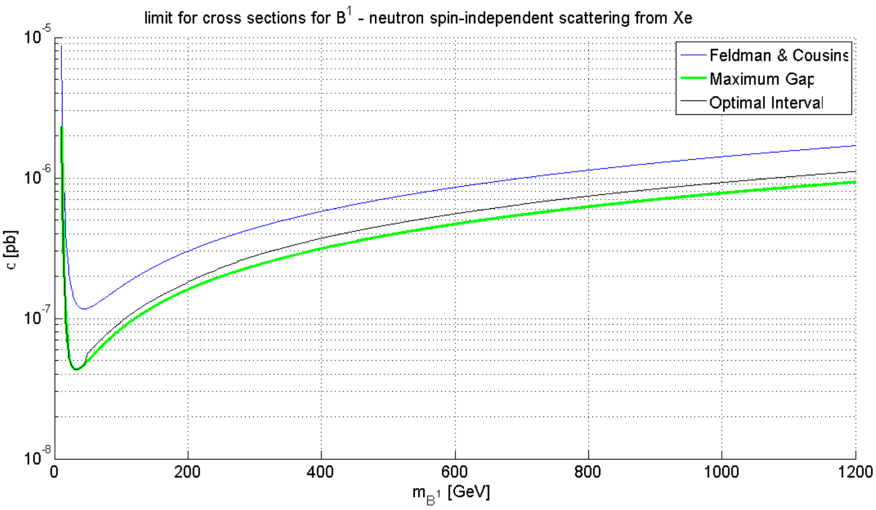
limit for cross sections for B1 - neutron spin-independent scattering from Xe
Feldman & Cousins
Maximum Gap
Optimal Interval
c [pb]
10-5
10-6
10-7
10-8
0
200
400
600
800
1000
1200
mB1 [GeV]

C.2 θ scan for the spin-dependent form factor of ^{129}Xe using the Nijmegen II method

The figures in this section show some spin-dependent form factors of ^{129}Xe using the Nijmegen II method obtained by evaluating (7.14) for different angles θ. In the first one on this side $\theta = 0°$ was used which yields a quite reasonable result. The others show angles around $\theta = 90°$. The occuring problems scaning over θ in this region are obvious. A more detailed discussion can be found on page 103.

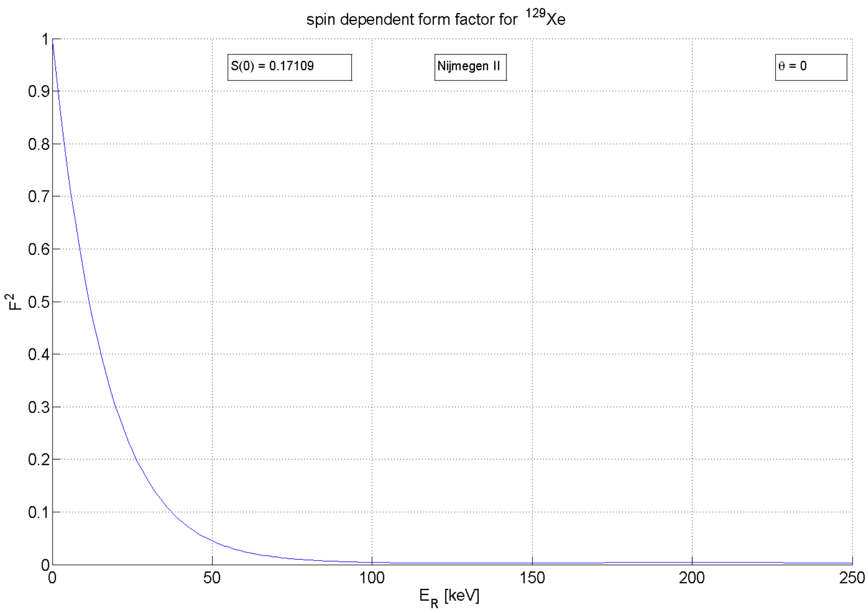

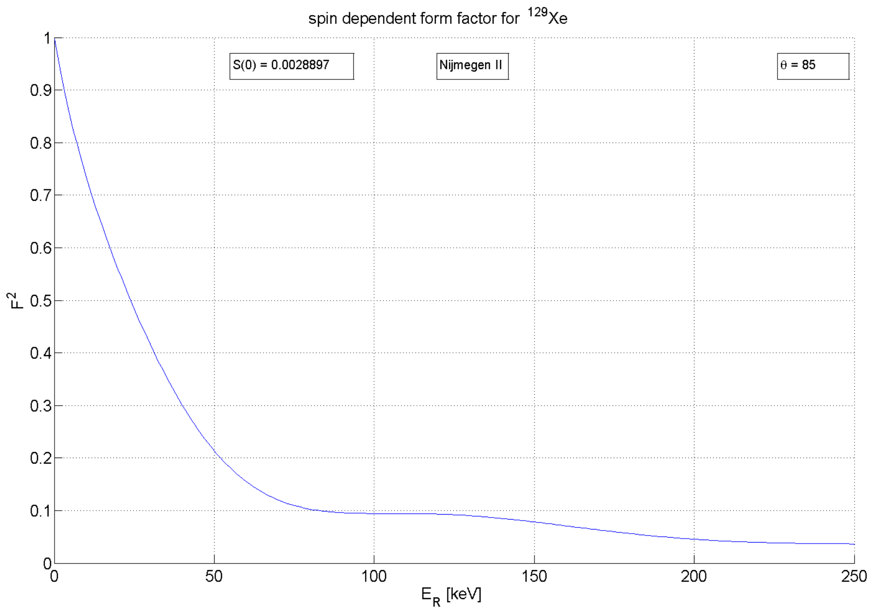
spin dependent form factor for 129Xe
S(0) = 0.0028897
Nijmegen II
θ = 85
F2
ER [keV]
0
0.1
0.2
0.3
0.4
0.5
0.6
0.7
0.8
0.9
1
0
50
100
150
200
250

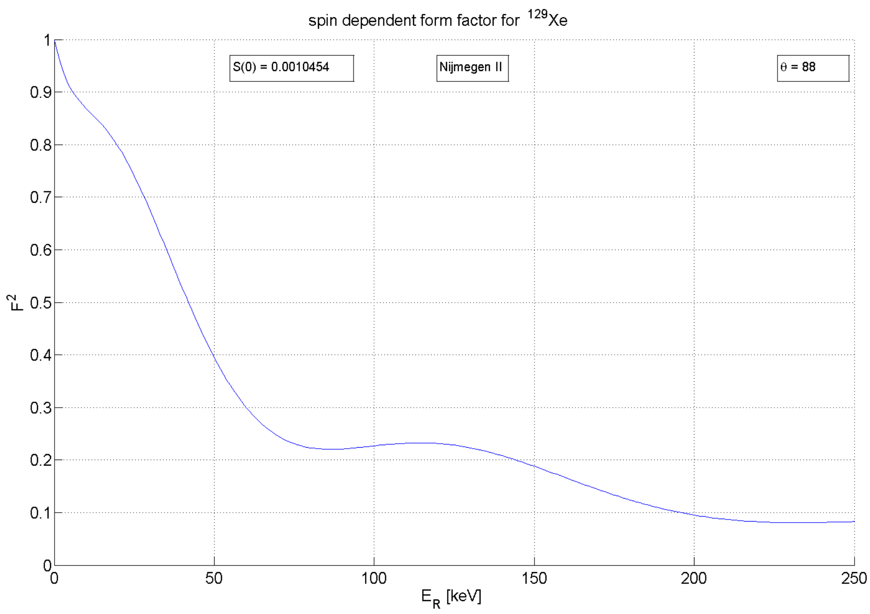
spin dependent form factor for 129Xe
S(0) = 0.0010454
Nijmegen II
θ = 88
F2
ER [keV]
0
0.1
0.2
0.3
0.4
0.5
0.6
0.7
0.8
0.9
1
0
50
100
150
200
250

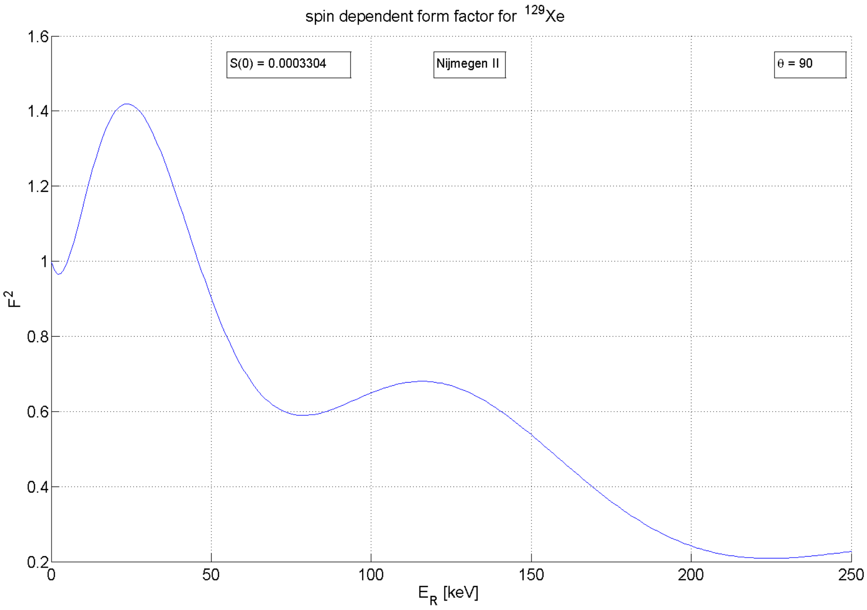
spin dependent form factor for 129Xe
S(0) = 0.0003304
Nijmegen II
θ = 90
F2
ER [keV]
0
50
100
150
200
250
0.2
0.4
0.6
0.8
1
1.2
1.4
1.6

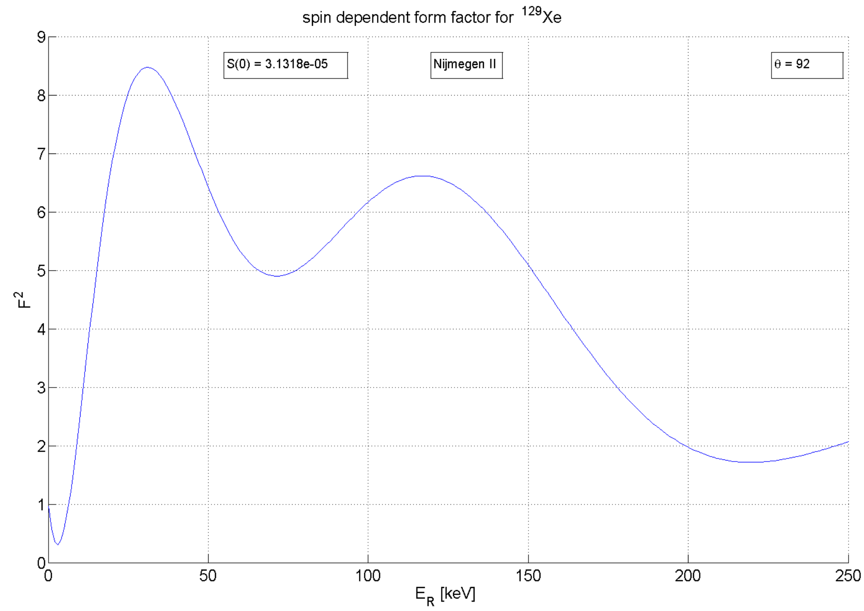
spin dependent form factor for 129Xe
S(0) = 3.1318e-05
Nijmegen II
θ = 92
F2
ER [keV]
0
50
100
150
200
250
0
1
2
3
4
5
6
7
8
9

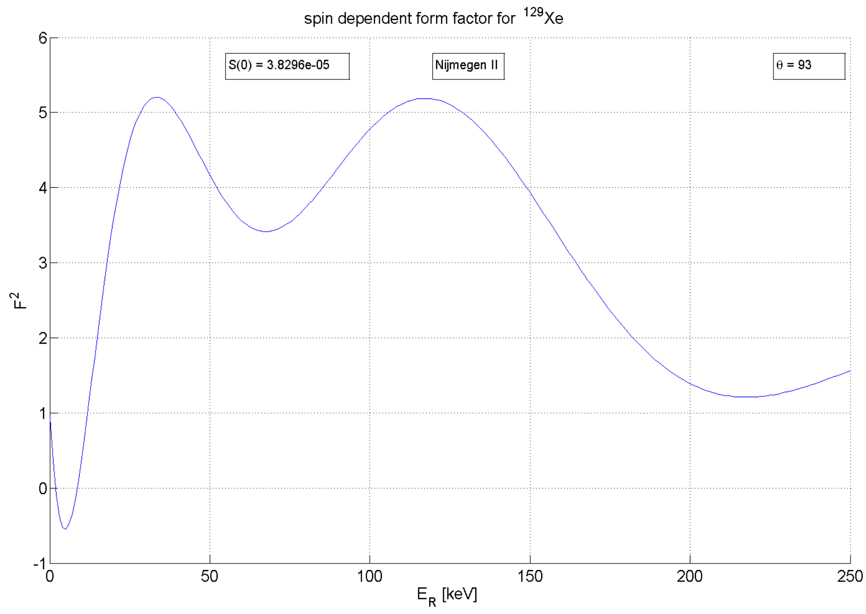
spin dependent form factor for 129Xe
S(0) = 3.8296e-05
Nijmegen II
θ = 93
F2
ER [keV]
0
50
100
150
200
250
-1
0
1
2
3
4
5
6

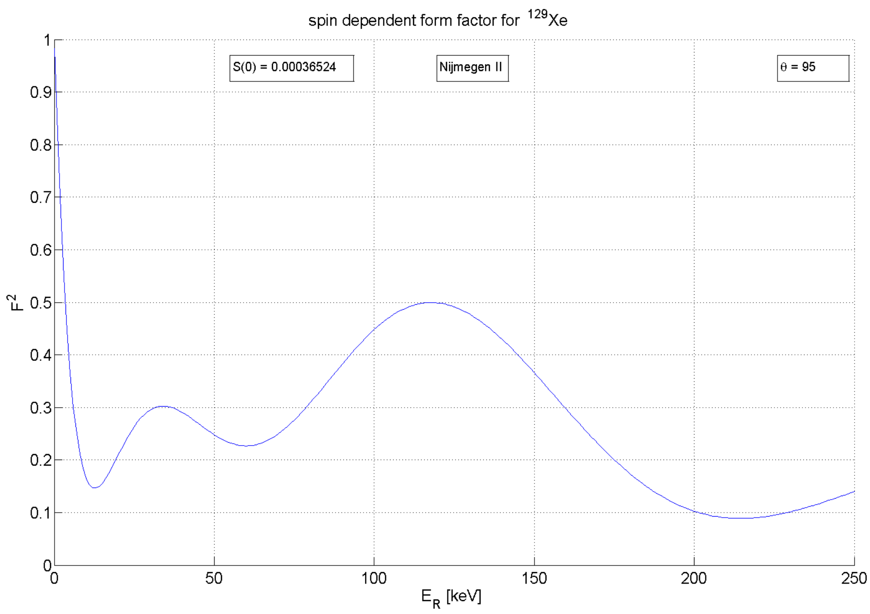
spin dependent form factor for 129Xe
S(0) = 0.00036524
Nijmegen II
θ = 95
F2
ER [keV]
0
50
100
150
200
250
0
0.1
0.2
0.3
0.4
0.5
0.6
0.7
0.8
0.9
1

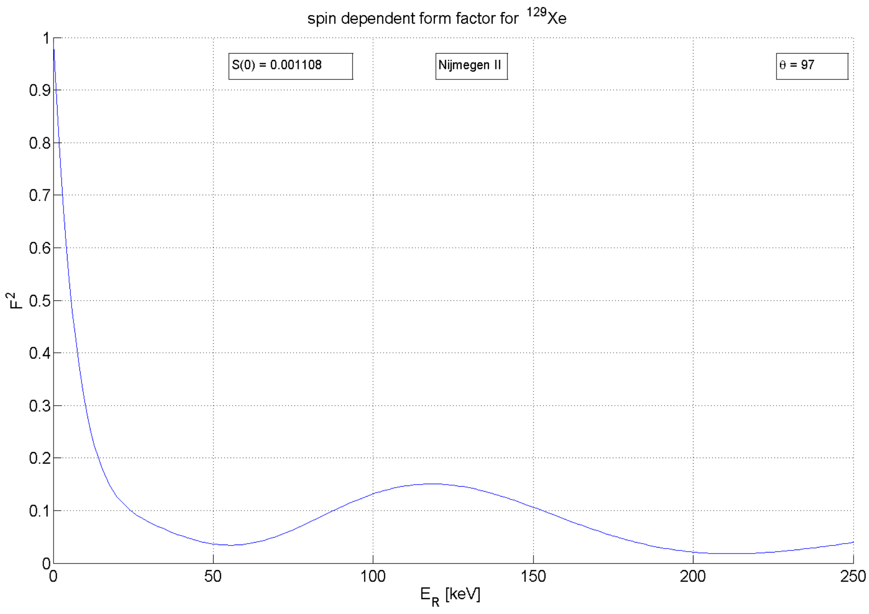
spin dependent form factor for 129Xe
S(0) = 0.001108
Nijmegen II
θ = 97
F2
ER [keV]

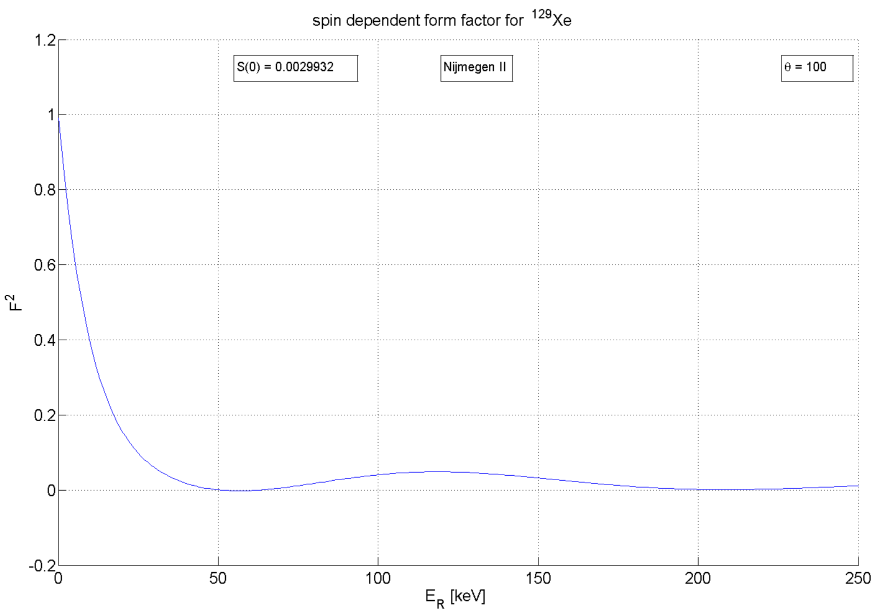
spin dependent form factor for 129Xe
S(0) = 0.0029932
Nijmegen II
θ = 100
F2
ER [keV]

C.3 θ scan for the spin-dependent differential event rates of ^{129}Xe using the Nijmegen II method

In this section of the appendix some spin-dependent differential event rates omitting the energy independent factor R_0 for ^{129}Xe using the Nijmegen II method for the same angles θ used in C.2 except 0° can be found. Obviously there are still issues considering angles around 90° however this interval seems to be smaller. The recoil energy interval used in the analysis is marked. A more detailed discussion can be found on page 104.

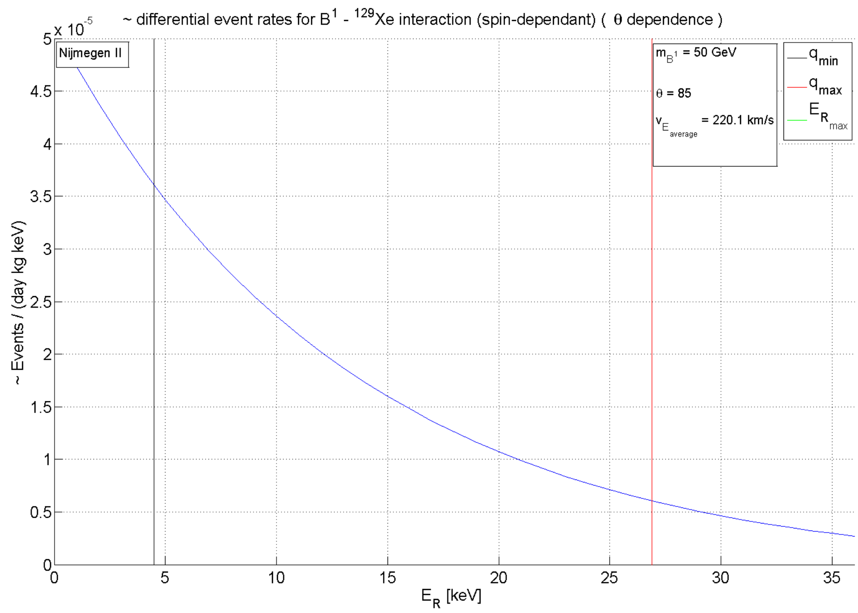

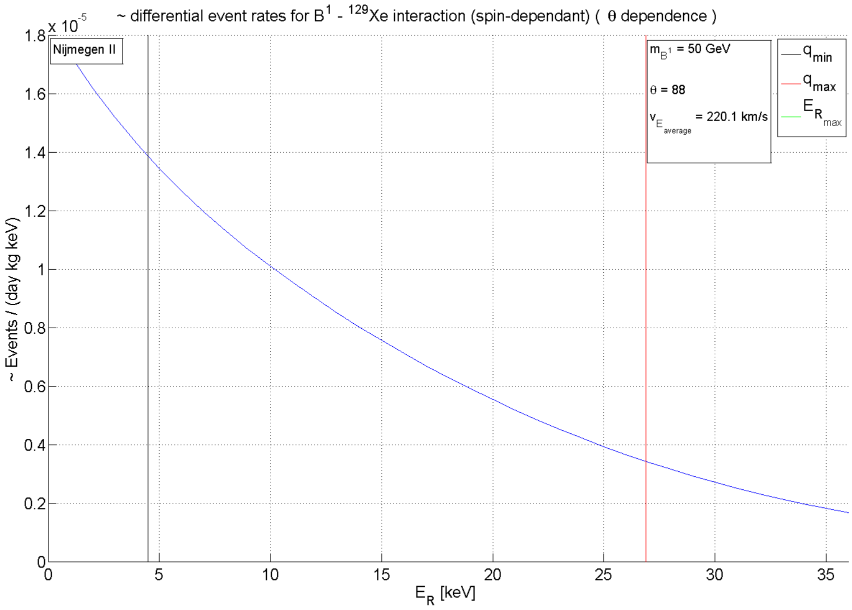
~ differential event rates for B1 - 129Xe interaction (spin-dependant) (θ dependence)
x 10-5
Nijmegen II
mB1 = 50 GeV
θ = 88
vE average = 220.1 km/s
qmin
qmax
ERmax
~ Events / (day kg keV)
ER [keV]

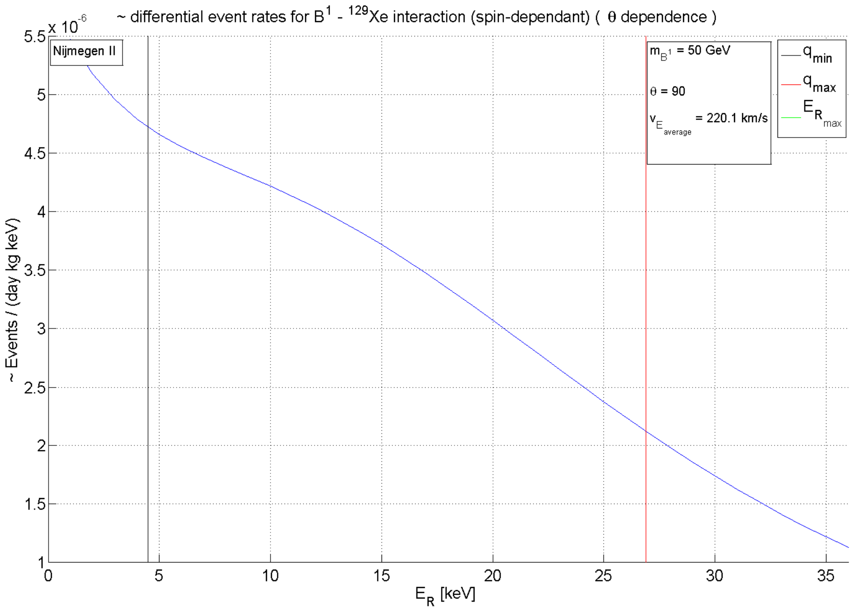
~ differential event rates for B1 - 129Xe interaction (spin-dependant) (θ dependence)
x 10-6
Nijmegen II
mB1 = 50 GeV
θ = 90
vE average = 220.1 km/s
qmin
qmax
ERmax
~ Events / (day kg keV)
ER [keV]

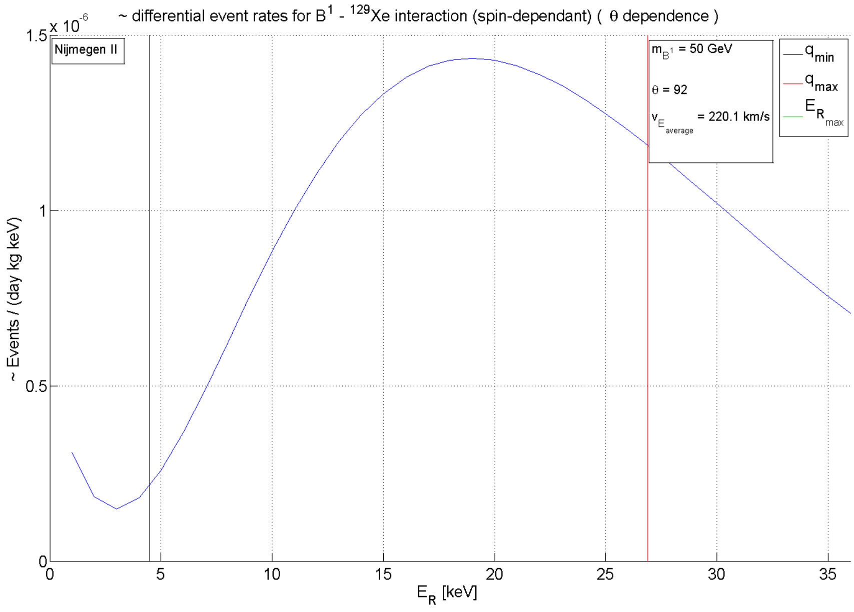
~ differential event rates for B1 - 129Xe interaction (spin-dependant) (θ dependence)
x 10-6
Nijmegen II
mB1 = 50 GeV
θ = 92
vE average = 220.1 km/s
qmin
qmax
ER max
~ Events / (day kg keV)
ER [keV]

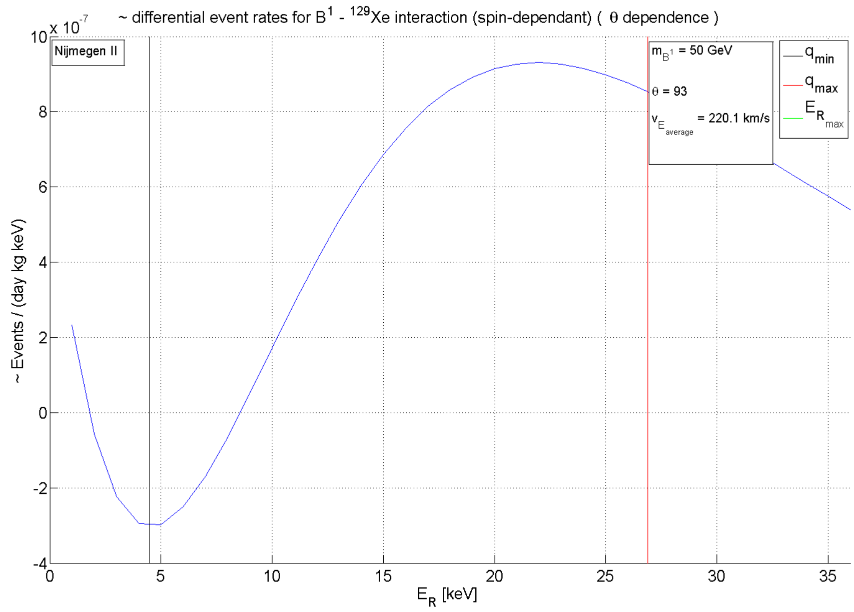
~ differential event rates for B1 - 129Xe interaction (spin-dependant) (θ dependence)
x 10-7
Nijmegen II
mB1 = 50 GeV
θ = 93
vE average = 220.1 km/s
qmin
qmax
ER max
~ Events / (day kg keV)
ER [keV]

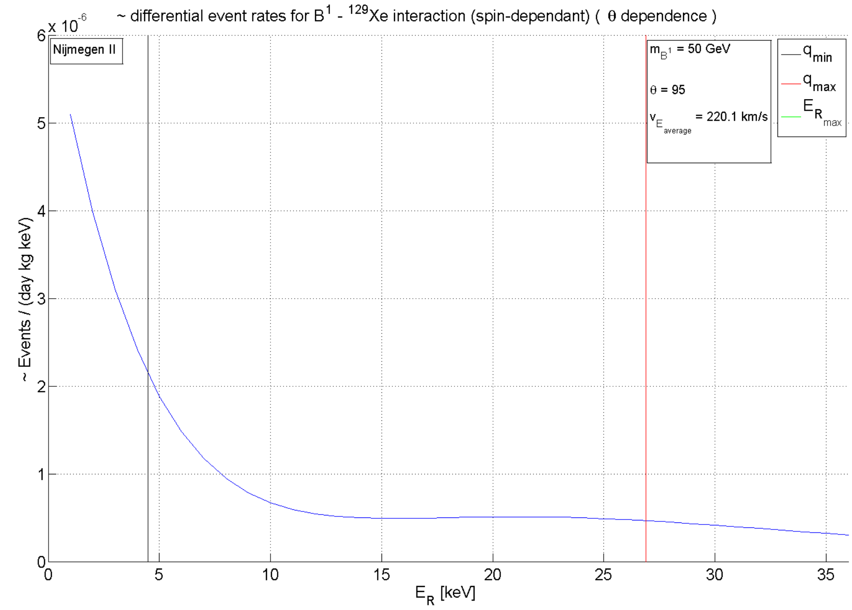
~ differential event rates for B1 - 129Xe interaction (spin-dependant) (θ dependence)
x 10-6
Nijmegen II
mB1 = 50 GeV
θ = 95
vE average = 220.1 km/s
qmin
qmax
ERmax
~ Events / (day kg keV)
ER [keV]

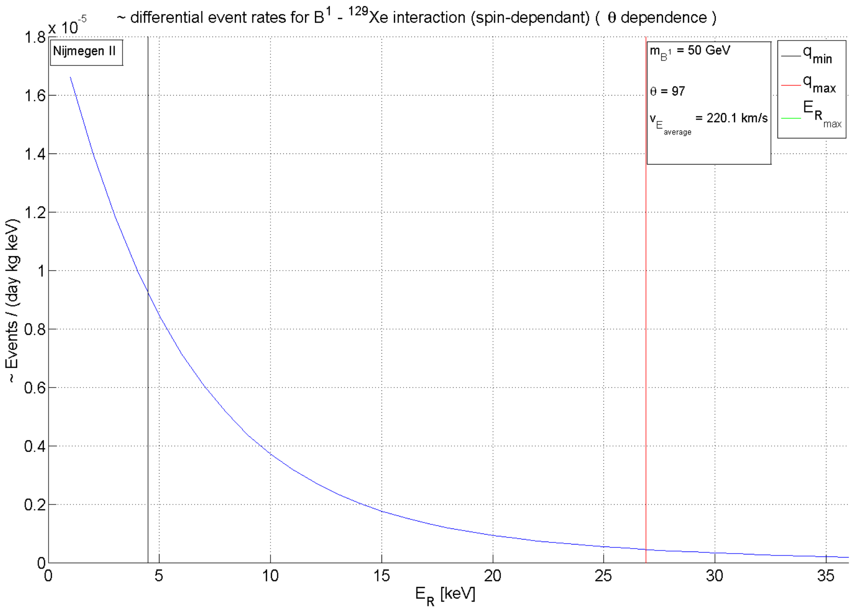
~ differential event rates for B1 - 129Xe interaction (spin-dependant) (θ dependence)
x 10-5
Nijmegen II
mB1 = 50 GeV
θ = 97
vE average = 220.1 km/s
qmin
qmax
ERmax
~ Events / (day kg keV)
ER [keV]

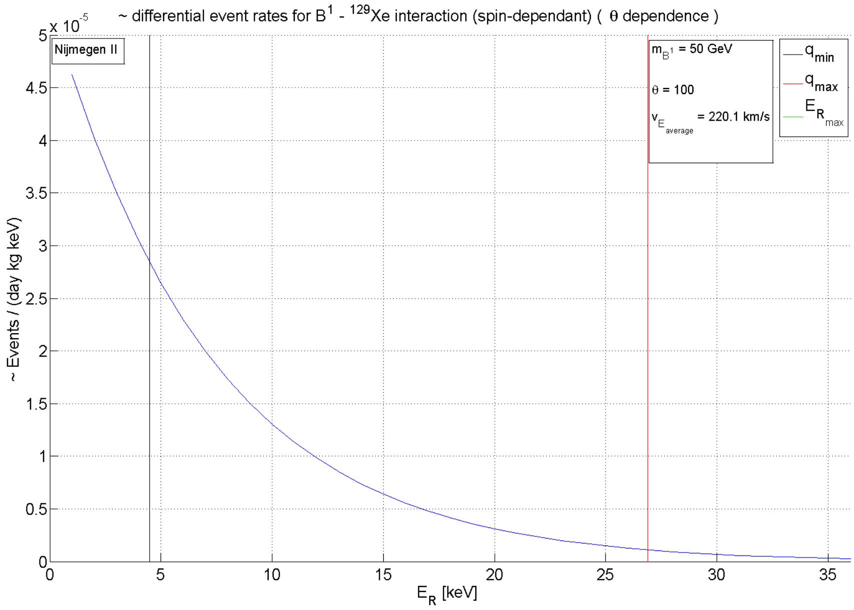
~ differential event rates for B1 - 129Xe interaction (spin-dependant) (θ dependence)
x 10-5
Nijmegen II
mB1 = 50 GeV
θ = 100
vEaverage = 220.1 km/s
qmin
qmax
ERmax
~ Events / (day kg keV)
ER [keV]
0
0.5
1
1.5
2
2.5
3
3.5
4
4.5
5
0
5
10
15
20
25
30
35

C.4 Combined limits on WIMP-nucleon couplings for different Δs

The three figures in this section show combined limits on WIMP-nucleon couplings from all isotopes using $m_{B^{(1)}} = 50$ GeV and different values of Δ. The accomplished method is a combination of the θ scan and the Maximum Gap Method. The figures are similar to the plot shown in figure 7.23.

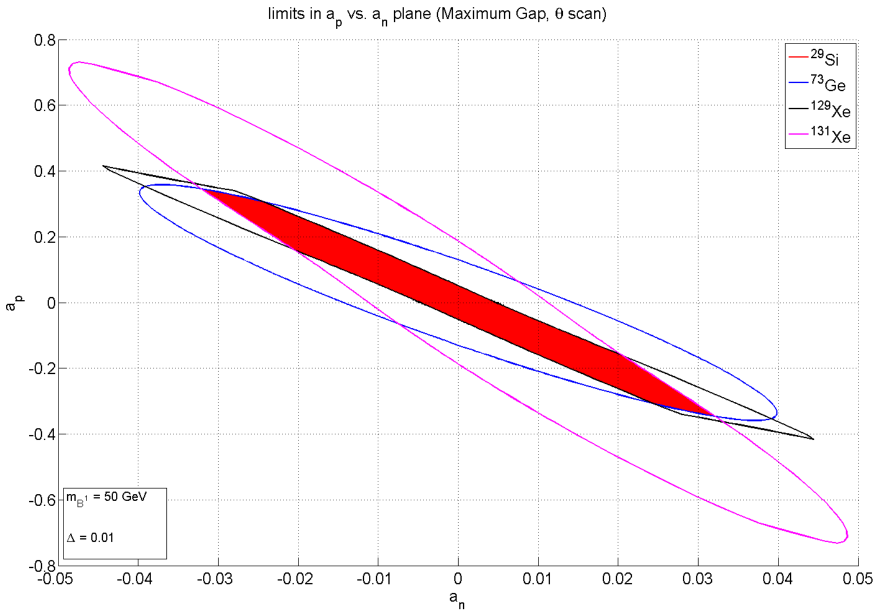

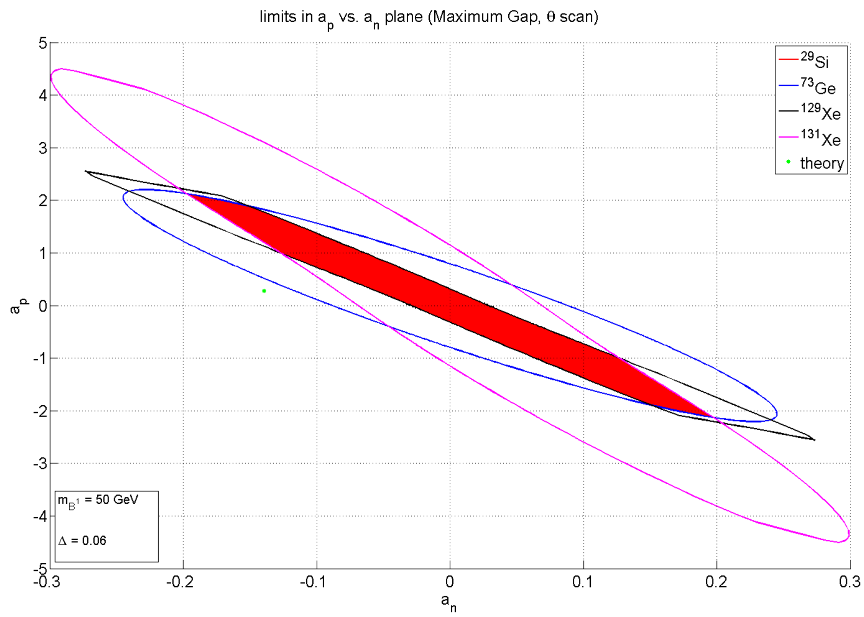
limits in a_p vs. a_n plane (Maximum Gap, θ scan)
29Si
73Ge
129Xe
131Xe
theory
m_B1 = 50 GeV
Δ = 0.06
a_p
a_n

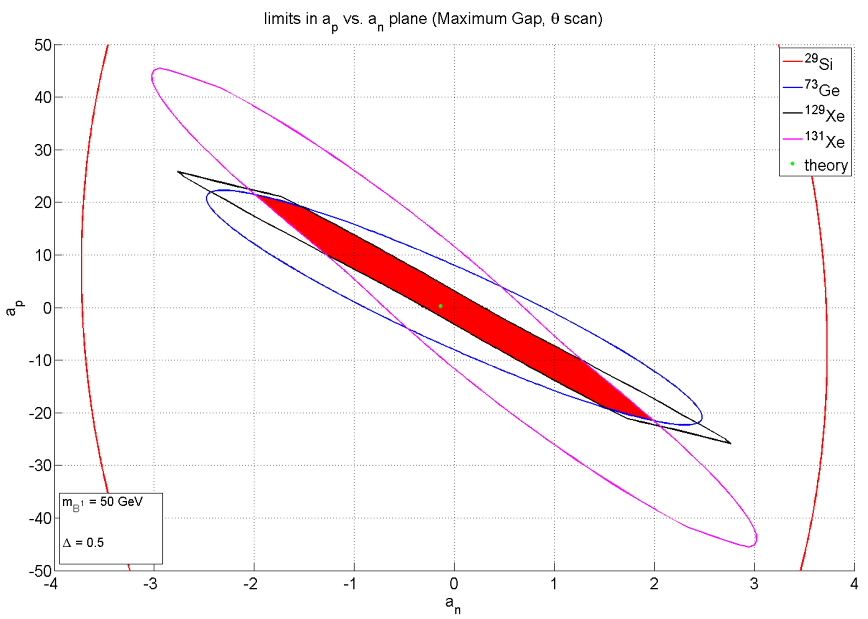
limits in a_p vs. a_n plane (Maximum Gap, θ scan)
29Si
73Ge
129Xe
131Xe
theory
m_B1 = 50 GeV
Δ = 0.5
a_p
a_n

C.5 Comparison of limits on WIMP-nucleon couplings from the xenon isotopes using the Bonn A and the Nijmegen II method

The plot below shows a comparison of limits on the WIMP-nucleon coulings from ^{129}Xe and ^{131}Xe using $m_{B^{(1)}} = 50$ GeV and $\Delta = 0.15$. Obviously the ellipses are rotated with respect to each other.

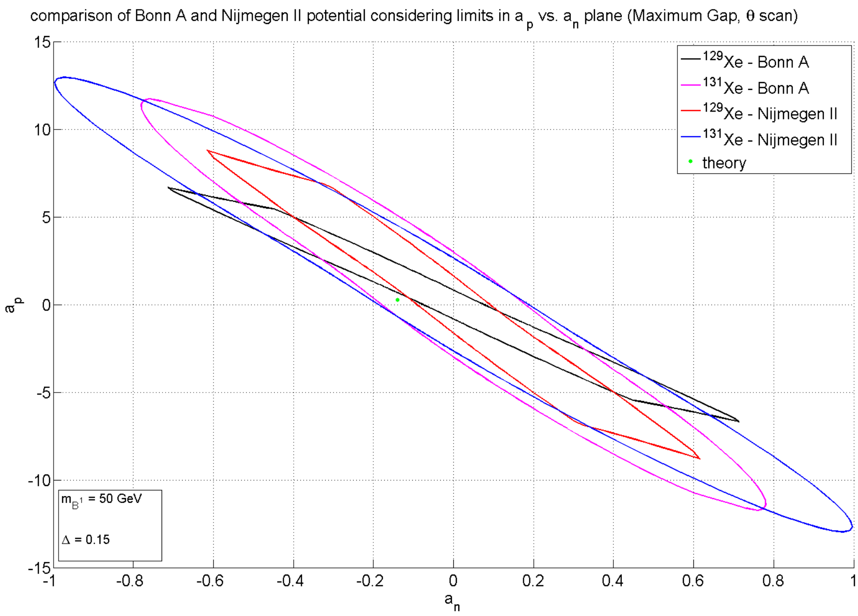

C.6 Supersymmetry

This section shows two limit plots for WIMP-nucleon couplings based on a supersymmetric model where the neutralino constitutes the WIMP. So the cross section is determined by (7.25). The first plot on this side is particularly interesting since it shows the allowed region in the 3-dimensional parameter space of the WIMP-nucleon couplings and the WIMP mass. The second one shows combined limits similar to figure 7.23.

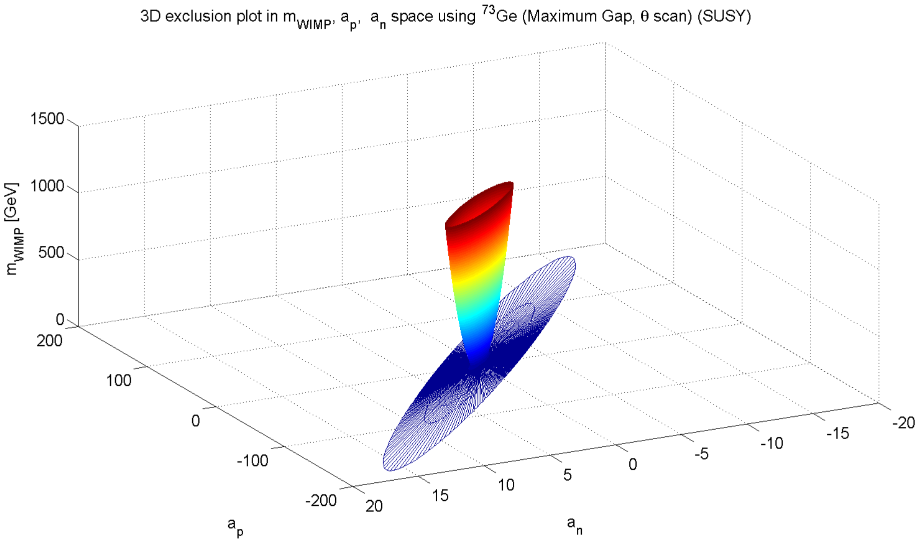

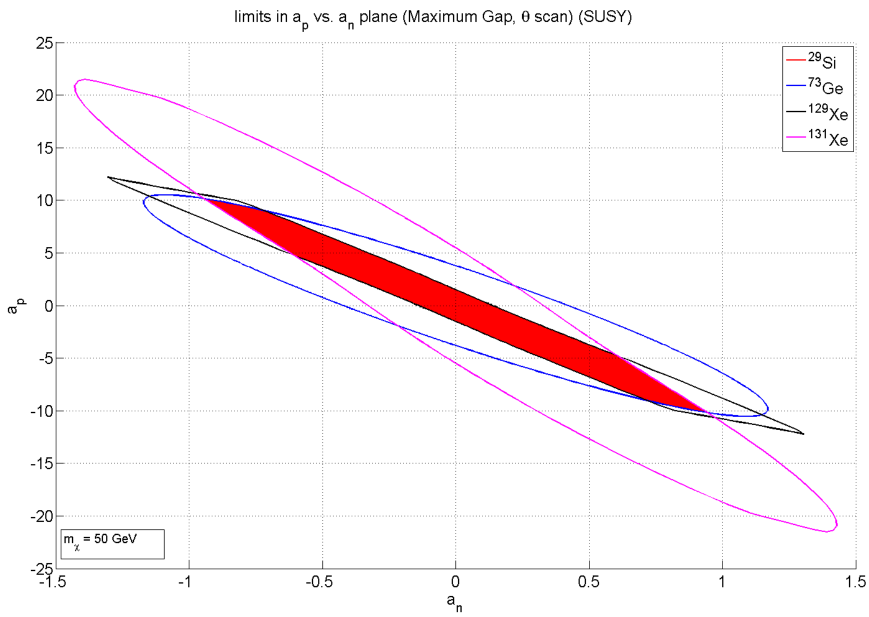

Bibliography

[1] T. Kaluza, Zum Unitätsproblem der Physik, Sitzungsber. Preuss. Akad. Wiss., Phys. Math. Kl. 966, 1921

[2] J. v. Dongen, Einstein and the Kaluza-Klein particle, arxiv:gr-qc/0009087

[3] L. O'Raifeartaigh, N. Strauman, Early history of Gauge Theories and Kaluza-Klein Theories, with a Glance at Recent Developments, arxiv:hep-ph/9810524

[4] O. Klein, Quantenthorie und fünfdimensionale Relativitätstheorie, Z.Phys. 37, 895, 1926

[5] K.R. Dienes, New directions for new dimensions: An introduction to Kaluza-Klein theory, large extra dimensions and the brane world, 2002 TASI lectures

[6] D. Hooper, S. Profumo, Dark Matter and Collider Phenomenology of Universal Extra Dimensions, arxiv:hep-ph/0701197

[7] G. D. Kribs, TASI 2004 Lectures on the Phenomenology of Extra Dimensions, arxiv:hep-ph/0605325

[8] T. Appelquist, H.-C. Cheng, B. A. Dobrescu, Bounds on Universal Extra Dimensions, arxiv:hep-ph/0012100

[9] H.-C. Cheng, K. T. Matchev, M. Schmaltz, Radiative Corrections to Kaluza-Klein Masses, arxiv:hep-ph/0204342

[10] G. Servant, T. M.P. Tait, Elastic Scattering and Direct Detection of Kaluza-Klein Dark Matter, arxiv:hep-ph/0209262

[11] D. N. Spergel et al., Wilkinson Microwave Anisotropy Probe (WMAP) Three Year Observations: Implications for Cosmology, arxiv:astro-ph/0603449

[12] K. Kong, K. T. Matchev, Precise Calculation of the Relic Density of Kaluza-Klein Dark Matter in Universal Extra Dimensions, arxiv:hep-ph/0509119

[13] J. Engel, S. Pittel, Nuclear Physics of Dark Matter Detection, Int. J. Mod. Phys. E Vol. 1 No. 1 (1992) 1-37

[14] G. Jungman, M. Kamionkowski, K. Griest, Supersymmetric dark matter, Phys. Rept. 267 (1996)

[15] A. Kurylov, M. Kamionkowski, Generalized Analysis of Weakly-Interacting Massive Particle Searches, arxiv: hep-ph/0307185

[16] Particle Data Group, The Review of Particle Physics, http://pdg.lbl.gov

[17] H.-C. Cheng, J. L. Feng, K. T. Matchev, Kaluza-Klein Dark Matter arxiv:hep-ph/0207125

[18] D. Hooper, G. Zaharijas, Distinguishing Supersymmetry From Universal Extra Dimensions or Little Higgs Models With Dark Matter Experiments, arxiv:hep-ph/0612137

[19] L. Baudis, The XENON10 WIMP Search Experiment at the Gran Sasso Underground Laboratory, arxiv:astrp-ph/0703183

[20] J. Angle et al., First Results from the XENON10 Dark Matter Experiment at the Gran Sasso National Laboratory, arxiv:/0706.0039

[21] http://webelements.com/

[22] V. A. Bednyakov, F. Šimkovic, Nuclear spin structure in dark matter search: The zero momentum transfer limit, arxiv:/hep-ph/0406218

[23] V. A. Bednyakov, F. Šimkovic, Nuclear spin structure in dark matter search: The finite momentum transfer limit, arxiv:/hep-ph/0608097

[24] J. D. Lewin, P. F. Smith, Review of mathematics, numerical factors and corrections for Dark Matter experiments based on elastic nuclear recoil, Astropart. Phys. 6, 87 (1996)

[25] R. H. Helm, Phys. Rev. 104 (1956) 1466

[26] M. T. Ressell et al., Nuclear shell model calculations of neutralino-nucleus cross sections for ^{29}Si and ^{73}Ge, Phys. Rev. D 48 5519 (1993)

[27] V. Dimitrov, J. Engel, S. Pittel, Scattering of weakly interacting massive particles from ^{73}Ge, arxiv:/hep-ph/9408246

[28] M. T. Ressell, D. J. Dean, Spin-Dependent Neutralino-Nucleus Scattering for $A \sim 127$ Nuclei, arxiv:/hep-ph/9702290

[29] J. Engel, Nuclear form factors for the scattering of weakly interacting massive particles, Phys. Lett. B 264 114 (1991)

[30] J. D. Vergados, On the Direct Detection of Dark Matter - Exploring all the signatures of the neutralino-nucleus interaction, arxiv:/hep-ph/0601064

[31] D. S. Akerib et al., Exclusion limits on the WIMP-Nucleon Cross-Section from the First Run of the Cryogenic Dark Matter Search in the Soudan Underground Lab, arxiv:/astro-ph/0507190

[32] D. S. Akerib et al., Limits on spin-independent WIMP-nucleon interactions from the two-tower run of the Cryogenic Dark Matter Search, arxiv:/astro-ph/0509259

[33] M. C. Smith et. al, The RAVE Survey: Constraining the Local Galactic Escape Speed, arxiv:/astro-ph/0611671

[34] E. I. Gates, G. Gyuk, M. S. Turner, The local halo density, arxiv:/astro-ph/9505039

[35] M. J. Lewis, K. Freese, The Phase of the Annual Modulation: Constraining the WIMP mass, arxiv:/astro-ph/0307190

[36] F. Giuliani, Are Direct Search Experiments Sensitive to All Spin-Independent Weakly Interacting Massive Particles?, arxiv:/hep-ph/0504157

[37] G. J. Feldman, R. D. Cousins, Unified approach to the classical statistical analysis of small signals, Phys. Rev. D 57, 3873 (1998)

[38] S. Yellin, Finding an upper limit in the presence of an unknown background, Phys. Rev. D 66, 032005 (2002)

[39] http://titus.stanford.edu/Upperlimit/

[40] C. Savage, P. Gondolo, K. Freese, Can WIMP Spin Dependent Couplings explain DAMA data in the light of Null Results from Other Experiments?, arxiv:/astro-ph/0408346

[41] D. R. Tovey et al., A New Model-Independent Method for Extracting Spin-Dependent Cross Section limits from Dark Matter Searches, arxiv:/hep-ph/0005041

[42] G. J. Alner et al. Limits on spin-dependent WIMP-nucleon cross-sections from the first ZEPLIN-II data, arxiv:/0708.1883

Acknowledgement

Hiermit möchte ich mich bei einigen Menschen bedanken, die entscheidend bei der Durchführung dieser Arbeit geholfen haben. Zunächst möchte ich dabei natürlich Laura danken, insbesondere auch dafür, dass ich in Zürich meine Doktorarbeit machen kann. Desweiteren danke ich meinen Bürokollegen Stefan, Tobi und Michael für ein sehr interessantes Jahr. Abgesehen davon natürlich meiner Mutter, Jihye und schliesslich Ssico.

Statement

Hiermit versichere ich, dass ich die vorliegende Arbeit selbstständig und ohne Benutzung anderer als der angegebenen Quellen und Hilfsmittel angefertigt habe.
Aachen, den 02. Oktober 2007